Theoretical and Numerical Evaluations of Electromagnetic Waves Energy Deposition within the Human Body Due to Exposure to Existent and Emerging Wireless Technologies

by

Muhammad Rafaqat Ali Qureshi

A thesis submitted in partial fulfilment of the requirements
for the degree of Doctor of Philosophy

School of Electronic Engineering and Computer Science
Queen Mary University of London
London E1 4NS, United Kingdom

November, 2017

I, Muhammad Rafaqat Ali Qureshi, confirm that the research included within this thesis is my own work or that where it has been carried out in collaboration with, or supported by others, that this is duly acknowledged below and my contribution indicated. Previously published material is also acknowledged below.

I attest that I have exercised reasonable care to ensure that the work is original, and does not to the best of my knowledge break any UK law, infringe any third party's copyright or other Intellectual Property Right, or contain any confidential material.

I accept that the College has the right to use plagiarism detection software to check the electronic version of the thesis.

I confirm that this thesis has not been previously submitted for the award of a degree by this or any other university.

Signature:

Date:

Details of collaboration and publications:

Journal Papers

- **M.R.A. Qureshi**, Y. Alfadhl, X. Chen, A. Peyman, M. Maslanyj, and S. Mann, "Assessment of exposure to radio frequency electromagnetic fields from smart utility meters in GB; part II) Numerical assessment of induced SAR within the human body", *Bioelectromagnetics*, DOI:10.1002/bem.22094, 2017.

Conference Papers

- **M.R.A. Qureshi**, Y. Alfadhl, X. Chen, "Assessment of the Induced SAR within human head due to exposure from LTE MIMO Mobile Handset", *Joint Meeting of Bioelectromagnetics Society and the European Bioelectromagnetics Association (BioEM)*, June 2017, Hangzhou, China.
- **M.R.A. Qureshi**, Y. Alfadhl, X. Chen, "Numerical assessment of the heterogeneous tissues mass density values in liquid phantoms", *Joint Meeting of Bioelectromagnetics Society and the European Bioelectromagnetics Association (BioEM)*, June 2017, Hangzhou, China.
- **M.R.A. Qureshi**, Y. Alfadhl, X. Chen, and A.Peyman, "Effect of Dispersive and High Precision Age-Dependent Dielectric Properties on SAR Assessments", *European Conference on Antennas and Propagation (EuCAP)*, April 2016, Davos, Switzerland.
- **M.R.A. Qureshi**, Y. Alfadhl, X. Chen, "The influence of children's weight on the absorption of electromagnetic fields", *IEEE Antennas and Propagation Society International Symposium (AP-S)*, June 2016, Fajardo, Puerto Rico, USA.
- A. Kothandaraman, **M.R.A. Qureshi**, Y. Alfadhl, X. Chen, A. Harker, Y. Ventikos, M. Edirisinghe, "Novel Preparation of Monodisperse Microbubbles by Integrating Oscillating Electric Fields with Microfluidics", *Int. Conference of Nanochannels, Microchannels & Minichannels (ICNNMM)*, July 2016, Washington DC, USA.
- **M.R.A. Qureshi**, Y. Alfadhl, X. Chen, "Numerical assessment of the induced SAR within humans due to EM radiations from Smart Meters", *Joint Meeting of Bioelectromagnetics Society and the European Bioelectromagnetics Association (BioEM)*, June 2015, California, USA.

Project Reports

- **M.R.A. Qureshi**, Y. Alfadhl, and X. Chen, "Smart meters modelling project", *Final Project Report*, Submitted to Public Health England, Oxford, UK, October 2015.

To My Parents and My Family

Abstract

In this thesis, a comprehensive investigation of the state-of-the-art guidelines for the conducted schemes in the near vicinity of the human body has been provided. The primary objectives of this work have been mainly focused on the electromagnetic (EM) wave exposure at both the microwave and millimetre-wave (mm-wave) frequency bands, along with their thorough analyses for a number of wireless technologies, such as the smart meters (SMs) and multiple-input multiple-output (MIMO) antennas. This work has undertaken a detailed theoretical and numerical modelling, as well as experimental measurements to propose the frameworks for the exposure conditions regarding the advanced wireless systems and applications. The employed numerical methods have been validated using the finite integration technique (FIT)-based simulations. The specific absorption rate (SAR) distributions have been determined using the anatomically realistic human models at various frequency bands. In this regard, each human model is assigned with the age- and frequency-dependent (AFD) dielectric properties, based on the novel expressions. This has then resulted in the representation of dispersive and age-dependent dielectric properties, in order to potentially improve the accuracy of the current assessment methods. Moreover, a number of generalised exposure conditions involving the standing and sleeping postures have been assessed for the home area network operating at the microwave band. The obtained results on the study on the SMs have been partly used by the Public Health England to provide the practical guidelines for the improvement of the services provided for the public. Furthermore, an assessment of the MIMO mobile handset has been performed in two exposure conditions, involving calling and body worn postures. Some aspects of this MIMO study has shown higher absorption levels in comparison with the basic restriction limits. A new SAR estimation approach has also been adopted to address the compliance assessment issues at the mm-wave bands. Finally, this work has identified a number of key factors that cause the high absorption levels in the human body and has provided insight into the efficient techniques in order to reduce such effects.

Acknowledgments

It is my greatest pleasure to express sincere appreciation and gratitude to my supervisor Dr. Yasir Alfadhl for his beneficial discussions, encouragement, valuable advice and guidance throughout the course of this work. I would also like to thank Prof. Xiaodong Chen, Dr. Akram Alomainy and Dr. Robert Donnan for their positive and constructive comments during my research.

I am also greatly indebted to Dr. Azadeh Peyman, Dr. Myron Maslanyj and Dr. Simon Mann from Public Health England for their formative discussions and invaluable advice regarding the part of this work. Special thanks to Mr. Ho Huen and Dr. Max Munoz Torrico for his help in antenna fabrications and measurements respectively.

I would also take this opportunity to thank all my friends especially Dr. Manmohan Sharma, Dr. Masood Ur Rehman, Dr. Qammer Abbasi, Dr. Deepak Singh Nagarkoti, Ms. Syeda Fizzah Jilani, Dr. Min Zhou, Dr. Xiang Li, Dr. Guangwei Jiang, Dr. Yang Zeng, Dr. Jiandong Lang, Dr. Jing Tian, Mr. Qiao Cheng, Ms. Qianyun Zhang, Dr. Zhijin Qin, Mr. Dingliang Wen, Dr. Yuan Ma, Mr. Xingjian Zhang, Ms. Lanting Zha, Mr. Li Cheng and Mr. Ardavan Rahimian who encouraged me at each and every step throughout the time. I am grateful to my wife, brothers and sisters for their continuous support and encouragement. Above all, I am deeply obliged to my parents, whose love and upbringing have been instrumental behind every success I achieved in my life.

Last but not the least; all the praises to the God Almighty who bestowed me with His unending blessings and made me reach to this point.

Table of Contents

List of Figures

List of Tables

List of Abbreviations

1G	First Generation (Mobile Networks)
2G	Second Generation (Mobile Networks)
3G	Third Generation (Mobile Networks)
4G	Fourth Generation (Mobile Networks)
5G	Fifth Generation (Mobile Networks)
AC	Adaptive Cube
AP	Access Point
ABC	Absorbing Boundary Condition
AFD	Age- and Frequency-Dependent
Comms-Hub	Communication Hub
CFIT	Conformal Finite Integration Technique
DECC	Department of Energy and Climate Change
E-field	Electric Field
EM	Electromagnetic
EMF	Electromagnetic Field
FAC	Fixed Adjustable Cube
FCA	Fixed Cube Algorithm
FCC	Federal Communications Commission Office
FDM	Finite Difference Method
FDTD	Finite Difference Time Domain
FEM	Finite Element Method
FIT	Finite Integral Technique
GSM	Global System for Mobile
HAN	Home Area Network
HEECM	Human Eye-Equivalent Cube Model
HHECM	Human Head-Equivalent Cube Model
ICNIRP	International Commission on Non-Ionising Radiation Protection
ICRP	International Commission on Radiological Protection
IEEE	Institute of Electrical and Electronics Engineers
IEC	International Electro-technical Commission
IFAC	Nello Carrara Institute of Applied Physics
IHD	In-Home Display

IoT	Internet of Things
IPD	Incident Power Density
ISM	Industrial Scientific and Medical
LTE	Long Term Evolution
LTE-A	Long Term Evolution Advanced
MIMO	Multiple Input Multiple Output
MWS	Microwave Studio
mmW	Millimetre Wave
MoM	Method of Moments
PEC	Perfectly Electric Conductor
PD	Power Density
PHE	Public Health England
PML	Perfectly Matched Layers
RF	Radio Frequency
rms	Root mean square
S11	Reflection Coefficient
S21	Transmission Coefficient
SAM	Specific Anthropomorphic Mannequin
SAR	Specific Absorption Rate
SARrm	SAR on averaged reference mass
SISO	Single Input Single Output
SMs	Smart Meters
TAPS	Time-Averaged Simultaneous Peak SAR
TLM	Transmission Line Matrix
UMTS	Universal Mobile Telecommunications System
Voxel	Volume Cells
WAN	Wide Area Network
WBSAR	Whole-Body SAR
WHO	World Health Organisation

List of Symbols

α	Alpha Dispersion Region
β	Beta Dispersion Region
γ	Gamma Dispersion Regions
ε^*	Complex Relative Permittivity
ε'	Relative Permittivity
ε''	Imaginary part of Permittivity
σ	Conductivity
σ_d	Displacement Electric Conductivity
σ_I	Ionic Conductivity
E	E-fields
ρ	Mass Density
C	Specific Heat Capacity
ΔT	Change in Temperature
Δt	Change in Time
R_n	Real Constant
θ_n	Phase
$\hat{\varepsilon}$	Complex Relative Permittivity of Cole-Cole model
A	Relaxation Time Distribution of Cole-Cole model
τ_{relax}	Relaxation Time
ε_s	Static Dielectric Constant
ε_0	Free Space Permittivity
ω	Angular Frequency
δ	Penetration Depth
Γ	Reflection Coefficient

Chapter 1
Introduction

1.1 Overview

The last few decades has seen an unprecedented growth in the use of wireless communication devices. The compact designs of modern devices (smart wireless devices) have been driven by the advances in wireless technology at several fronts [1–4]. The wide availability of such electronic devices raises concern toward the human health.

Human exposure to EM radiation is of concern to individuals, and to professional operating EM emitting devices worldwide. Various organisations and countries have developed radiofrequency (RF) energy exposure limits to prevent overexposure to the EM fields (EMFs), present in our environment.

These standards favour safe levels of exposure, for both the public, and for occupational workers. International organisations namely Institution of Electrical and Electronic Engineering (IEEE)/International Electro-Technical Commission (IEC) 62704-1 [5], Federal Communications Commission Office (FCC) [6], and the International Commission on Non-Ionising Radiation Protection (ICNIRP) [7, 8], formally recognised by World Health Organisation (WHO), recommends limits for human exposure to non-ionising radiations. The ICNIRP exposure guidelines diagnose the same threshold levels, while FCC and IEEE

exposure guidelines threshold levels are stricter at which harmful biological effects may occur (details given in Section 2.2).

The understanding of the interactions of EMFs with human body is a complicated topic due to the inhomogeneous nature of biological tissues, and the operating environment which has a direct influence on the way in which EM waves behave. Across the mobile frequency bands, the human body behaves as a lossy dielectric material and the EM waves penetrate through the human tissues [9]. The induced energy within the human tissues increases as a function of time, when exposed by EM energy. If this energy is sufficiently high, then temperature of the tissue will increase linearly as shown in Figure 1-1. This rise in temperature can be determine by power deposition on human body [10]. At some particular frequencies human body absorb more energy due to the resonances [11, 12].

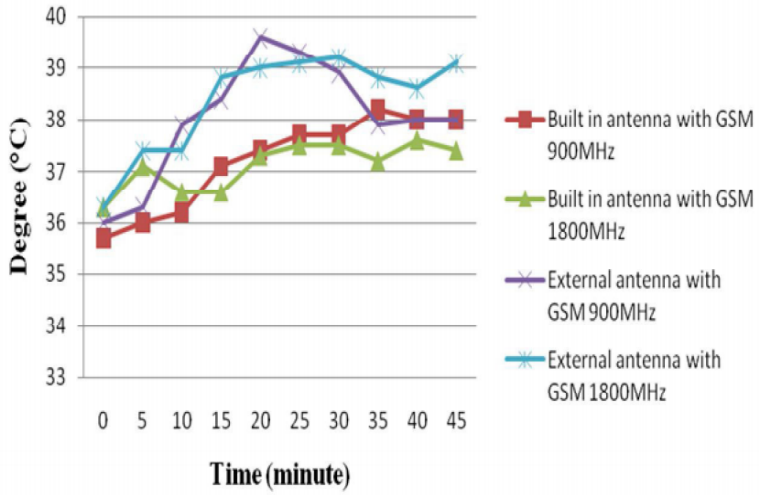

Figure 1-1. Comparison on temperature changes cause by traditional GSM 900 and 1800 MHz mobile handset with different models (source: [10]).

Thermal effects such as; dielectric heating are the prominent effect of EM waves. As a measure of the rate at which energy is absorbed by the human body, SAR define as a metric to estimate the exposure of human body to RF EMFs below 6 GHz for FCC and 10 GHz for ICNIRP [7, 8]. Beyond these frequencies, SAR may no longer be valid, hence power density (PD) has been adopted as the merit to limit the over exposure at higher frequencies [6–8].

There are few open research challenges relating to the numerical and practical scientific methods for the estimation of the EM exposure levels. The major limitations in EM exposure assessments require a number of important issues on the successful conduct of the exposure evaluations. These limitations primarily include: age-dependent dielectric tissue properties,

computational power to numerically consider the exposure configurations, e.g., smart homes and offices, numerical human body models with high resolution to bring confidence in assessments, and experimental facilities to consider heterogeneous phantoms for the exposure evaluations.

In this thesis, numerical dosimetry techniques used in order to study the interaction of EMFs produced from modern wireless devices with human body of different age groups. The outcome of these assessments will provide the guidelines to minimise the EM exposure. The conclusions drawn from this study will further demonstrate the possible aspects of EM exposure with human body in both near- and far-fields. It also provides the knowledge to improve accuracy in SAR assessment using AFD dielectric properties. A brief study is also conducted to analyse the compliance issues beyond 6 GHz. More specifically, the studies presented in this thesis will elucidate: (i) the EM exposure from traditional communication systems (SMs) on sample of population by considering AFD dielectric properties; (ii) the EM exposure from next-generation communication systems, i.e., MIMO mobile handset antenna, on voxel-based human head model; (iii) compliance assessment issues at higher frequencies (above 6 GHz).

1.2 Research Focus

Wireless communication is not only restricted to the telecommunication sector, but rather is applied in a number of other areas such as smart homes, smart offices, smart cities, healthcare and also for IoT applications. At present, machine-to-machine communication is become major research area such as SMs interact with electronic devices, handheld mobile phones connected with base station, and provides modern way of communication.

The widespread impact of these new technologies has raised concerns about safety of human exposure to EM waves emitted by wireless access point (AP) at homes/offices, telecommunication devices (smart mobile handsets, MIMO Wi-Fi devices), SMs at homes etc. In this study, EM exposure from wireless devices investigation divided into two sections. Section 1.21: EM exposure from traditional communication systems. Section 1.2.2: EM exposure from next generation communication systems.

1.2.1 Electromagnetic Exposure from Traditional Communication System

Due to the recent advancement in mobile communication systems, smart wireless communication devices have become widely available in all fields of our daily life, including homes, offices, healthcare, railway stations, airports and many more places. The primary purpose of smart homes in particular are to improve home automation and facilitate energy management. The introduction of wireless communication systems at homes has prompted the improvements in home automation to monitor energy usage at any time.

Smart grid technology used for communication. The important aspects of smart grid used is to control the production and distribution of electricity. SMs act as an interface between smart grid and home appliances and are typically connected through wireless communication systems. This technology allows remote readings of gas and electricity meters, and is expected to be used the majority of households in the near future [13–17].

The home area network (HAN) technology is used to monitor the utility meters, which involves networking of several devices in the household premises. A wide area network (WAN) system is also utilised to transmit and receive data wirelessly between the meter and a central server. The widespread use of wireless devices in the near vicinity has drawn great amount of attention due to the EM absorption within the humans of all age groups. The excessive interaction between SMs architecture units with the human body raises health concerns.

Since the introduction of mobile communication growth and success, concern over the potential health hazards resulting from exposure to RF EMFs has captured public and media interests. In response, governments and industries worldwide have commenced and steered numerous research programs to address the public health concerns.

1.2.2 Electromagnetic Exposure from Emerging Communication System

Smartphones have become extremely complex due to integration of high quality cameras, music, and video play back, touch screen, email, texting and many more. Since 1985, wireless communication systems have rapidly emerged from the analogue systems (1G: first-generation systems), to digital systems (2G: second-generation systems), and later to third-

generation systems (3G), which can realise multimedia transmission. In order to further increase the data transmission rate and reduce interference, MIMO technology has become a vital feature in fourth-generation (4G) wireless communication systems. In future, 5G expected to use MIMO technology that promise higher bandwidth and data transmission rates. [18].

MIMO technique improves communications performance between the transmitter and receiver by either resist or capitalise on multipath scattering in the communication channels. MIMO systems have drawn much attention, due to effectiveness in linearly increasing the channel capacity with multiple antennas, without requiring more frequency spectrum or power [19]. However, MIMO systems technology world widely used in wireless communication devices. The excessive and continues exposure from such devices in near vicinity of humans raise health concern. This research conducted to investigate the possible harmful effects from wireless devices mainly SM devices and MIMO antennas for mobile handsets, and to investigate 5G compliance issues. The resultant exposure values compared with international exposure guidelines as basic restriction levels.

1.3 Motivation

Evaluation of EM waves interactions with the human body is a complex topic due to the variation in body parameters such as heterogeneous nature of biological tissues, height, weight, ages etc. The associated challenges vary from numerical modelling to experimental difficulties and are typically dependent on number of sources involved in assessment.

Due to the recent advancement of technology such as SMs, MIMO technology based mobile handsets and there continues exposure to humans of all age group has raised concern among public about possible health concern. These wireless devices operates on different frequencies such as 2G GSM networks, WLAN, 3G, 4G long term evolution (LTE) and long term evolution advanced (LTE-A) networks and 5G networks. SMs uses GSM and WLAN frequencies and the operating procedure is slightly different as compared to the standard wireless devices such as mobile handset or AP.

SM devices continuously connected with in-home display (IHD) device within the house which enhance the possibility of EM exposure towards humans of all age groups and also impose a challenge in assessment configuration. There could be number of configurations consider where humans are exposed with network of SM devices in both near- and far-fields

either from one or multiple sources over the long periods of time. This impose a challenge and also increase complexity in numerical dosimetry where accurate age-dependent dielectric data and fine resolution voxel models are required to successfully estimate the level of absorption within the human body. Therefore, a study is conducted to analyse human exposure from SM devices in all possible exposure configurations by considering age dependencies.

Similarly mobile handsets are generally operate very close to human body within 5 mm of distance. The use of MIMO technology in mobile handsets and their different sizes impose challenge toward the EM exposure assessments. MIMO technique is currently used in 3G and 4G systems and expected to be used in 5G systems. Due to various operating modes of this technology, the absorption levels are expected to be different for individuals including children's and adults. In addition, the position of mobile handset on human head and body plays a vital role in identifying the highest and lowest levels of absorption. Therefore, mobile handset exposure assessment on voxel model is performed in all operating modes and in possible exposure configurations. A method is identified to lower the absorption levels under the different exposure configurations.

At higher frequencies, beyond 6 GHz for FCC and 10 GHz for ICNIRP, SAR is not valid to limit the EM exposure. Due to the shallow penetration depth in biological materials SAR levels are significantly higher in comparison with those at microwave frequencies with same incident PD. Several international guidelines have emphasis to use PD as merit to limit the over exposure at before mentioned frequencies. But there are still some question that need to be address.

According to [20], PD is not useful as SAR or temperature for assessing safety in mmW devices, especially in near field. Assessment based on PD are not dependent on the knowledge of the distribution of fields or power absorption in the biological material but only rely on the density of power travelling towards the biological material. Therefore, an attempt is made to use SAR in order to identify the penetration depth within the body at higher frequencies in both heterogeneous and homogenous biological materials.

1.4 Organisation of the thesis

The thesis is organised in six chapters as follows:

Chapter 2: This chapter provides a brief knowledge on the EM spectrum and the behaviour of biological tissues over the communication band part of the spectrum. Four different type of SAR averaging methods can be used in numerical techniques are addressed. In order to reduce SAR measurements time different measurement techniques that are used to calculate SAR are discussed. Details about the safety international standards from different organisations to limit the excessive exposure are discussed in detail.

Chapter 3: In this chapter, details about the three different heterogeneous voxel models are presented which are used for SAR assessment in chapter 4 and 5. A novel technique used to calculate the AFD dielectric properties, which used in child model is also addressed. The validity of FIT method is performed by comparing the calculations over a homogenous muscle equivalent sphere with analytical Mie-series solution for homogenous sphere.

Chapter 4: SAR performance of SM antennas is assessed in detail. In total 24 different exposure scenarios study in this work. The results are critically analysed and discuss in detail. The SAR assessment is performed on three different models by using AFD tissue types. The E-field and PD is calculated for each case when models assumed standing or sleeping under grounded or in isolated condition and results are compared with recent studies and measurements as a validation.

Chapter 5: SAR performance of 2 element MIMO antennas is assessed under various modes by considering the commercially available handset dimensions. The standalone mode, simultaneous mode or real MIMO mode and beam forming mode of MIMO antenna for mobile handset is examined under extreme conditions by setting the maximum transmission power in compliance with FCC, IEEE and ICNIRP. The resultant SAR levels are validated by validating the numerical technique used in this chapter.

Chapter 6: In this chapter, SAR assessment is performed on head and eyes equivalent cube models to investigate the invalidity of SAR at mmW and also how SAR can be effectively use to identify the penetration depth. Number of exposure scenarios considered including single layer, multilayer models exposure from plane wave source. Conclusions are drawn through critical analysis. Safety international standards to limit the excessive exposure at mmW are also discuss in detail.

Chapter 7: This chapter concludes the research have been done in this thesis. Suggestions for future work are also given in this chapter.

References

[1] F. Gozasht, M. D. Hossain, and A. S. Mohan, "Miniaturized E-shaped PIFA antenna for wideband implantable biomedical applications," International Conference in Electromagnetics in Advanced Applications (ICEAA), pp. 832 – 835, 2013.

[2] Y. Chi, and F. Chen, "On-body Adhesive Bandage-like Antenna for Wireless Medical Telemetry Service," IEEE Transactions on Antennas and Propagation, vol. 62, pp. 2472 – 2480, 2014.

[3] J. Carter, J. Saberin, T. Shah, P. R. Sai Ananthanarayanan, and C. Furse, "Inexpensive fabric antenna for off-body wireless sensor communication," in Antennas and Propagation Society International Symposium (APSURSI), pp. 1 – 4, 2010.

[4] S. Movassaghi, M. Abolhasan, J. Lipman, D. Smith, and A. Jamalipour, "Wireless Body Area Networks: A Survey," Communications Surveys & Tutorials, vol. 16, pp. 1658 – 1686, 2014.

[5] CST Microwave Studio - 3D EM Simulation Software 2015 version: SAR Calculation, [Online]. Available: http://www.edatop.com/cst/CST2013/30278.html, (Accessed Feb 2016).

[6] R. F. Cleveland, D. M. Sylvar, and J. L. Ulcek, "Evaluating Compliance with FCC Guidlines for Human Exposure to Radiofrequency Electromagnetic Fields," Federal Communication Commission Office of Engineering & Technology, Washington D.C. August 1997.

[7] ICNIRP, "International Commission on Non-Ionizing Radiation Protection: Guidelines for limiting exposure to time-varying electric, magnetic and electromagnetic fields (up to 300GHz)," Heal. Phys. Soc., vol. 74, pp. 494 – 522, 1998.

[8] ICRNIRP, "Exposure to high frequency electromagnetic fields, biological effects and health consequences (100 kHz-300 GHz)," 2009.

[9] A. Kaur, H. Malik, A. Lather, and V.K.Lamba, "Effect of communication frequency on specific absorption rate of electromagnetic radiations in human body," Int. J. Soft Comp. Eng., vol. 2, pp. 272 – 274, 2012.

[10] M. A. Bhat, and D. V. Kumar, "Calculation of SAR and measurement of temperature change of human head due to the mobile phone waves at frequencies 900 MHz and 1800 MHz," Advances in Phy. Theories & Applicat. vol. 16, pp. 54 – 64, 2013.

[11] A. Hirata, K. Yanase, I. Laakso, K. H. Chan, O. Fujiwara, T. Nagaoka, et al., "Estimation of the whole-body averaged SAR of grounded human models for plane wave exposure at respective resonance frequencies," Phys. Med. Biol., vol. 57, pp. 8427 – 8442, 2012.

[12] P. Dimbylow, "Resonance behaviour of whole-body averaged specific energy absorption rate (SAR) in the female voxel model, NAOMI," Phys. Med. Biol., vol. 50, pp. 4053 – 4053, 2005.

[13] 2010 to 2015 government policy: household energy, [Online]. Available: https://www.gov.uk/government/policies/helping-households-to-cut-their-energy-bills/supporting-pages/smart-meters (Accessed Feb 2016).

[14] Transition to smart meters, [Online]. Available: https://www.ofgem.gov.uk/electricity/retail-market/metering/transition-smart-meters (Accessed Feb 2015).

[15] Smart meter, [Online]. Available: http://www.scottishpower.co.uk/energy-efficiency/smart-meters/ (Accessed Feb 2015).

[16] DECC, "Department of Energy and Climate Change: Smart Metering Implementation Programme," [Online]. Available: https://www.gov.uk/government/uploads/system/uploads/attachment_data/file/209840/SMIP_E2E_SMETS2_govt_consultation_response_part_2_final.pdf (Accessed Feb 2015).

[17] Smart metering: a guide for local authorities and third sector organisations, [Online]. Available: https://www.gov.uk/government/publications/smart-metering-a-guide-for-local-authorities-and-third-sector-organisations (Accessed Feb 2015).

[18] F. W. Vook, A. Ghosh, and T. A. Thomas, "MIMO and beamforming solutions for 5G technology," in 2014 IEEE MTT-S International Microwave Symposium (IMS), pp. 1 – 4, 2014.

[19] S. Zhang, K. Zhao, Z. Ying, and S. He, "Adaptive Quad-Element Multi-Wideband Antenna Array for User-Effective LTE MIMO Mobile Terminals," IEEE Trans. on Antennas and Propagation, vol. 61, pp. 4275 – 4283, 2013.

[20] T. Wu, T. S. Rappaport, and C. M. Collins, "Safe for Generations to Come: Considerations of Safety for Millimeter Waves in Wireless Communications," IEEE Microwave Magazine, vol. 16, pp. 65 – 84, 2015.

Chapter 2
EMF Exposure Assessment: Fundamentals and Methods

2.1 Introduction

Accurate assessment of the interaction of EMFs with the human body is of a fundamental importance for establishing clearer understanding and for establishing valid EM exposure limits. RF EMF's exposure estimation can be classified into two categories: 1) incident field assessment, i.e., quantification of the incident EMF, or the field characteristics at the exposed location of bodies; and 2) dosimetry, i.e., amount of the EMF induced in biological tissues, or bodies. In most cases of compliance assessment verification, the actual exposure levels are marginally or significantly below a basic restriction levels. These exposure levels are vital to accurate determination of individual exposure levels.

Numerical dosimetry has been widely used on anatomical computer models representing the human body to overcome the experimental limitation [1, 2]. In numerical dosimetry studies, one of the major factor that influences the assessment of human body exposure from EMFs is the use of accurate dielectric properties to represent the organs within the body. The human body is composed of number of different tissue types and each tissue type interact differently with the EMFs based on the differences in dielectric properties.

There are many factors affecting the dielectric properties of tissue such as frequency, temperature [3], water content, age and local tissue variability. The variations in dielectric

properties of biological materials can be categories in three major dispersion regions (α, β, and γ). Each region describes the behaviour of biological tissue on molecular level under the influence of electric field (E-field).

Various numerical assessment techniques are available and widely adopted for accurate EMF's exposure estimation. In support there are number different averaging methods are available that are used for compliance assessment verifications. However, due to the complexity of the exposure scenarios such as exposure from MIMO devices, empirical techniques can be applied in relation with measurements to estimate SAR in experimental dosimetry.

2.2 Public Electromagnetic Exposure Limit Guidelines

There are number of international bodies that provides global protection guidelines for exposure to EM and RF fields such as ICNIRP, FCC, NCRP and IEEE [4–6]. These organisations set basic restriction limits for both general public and occupational users. There basic restriction limits vary among each other due to difference in their averaging size of volume.

In the UK, ICNIRP guidelines have been adopted. These guidelines set limits for human exposure based on SAR and E-field strength in the body. The human body absorbs energy from EMFs at frequencies between 100 kHz to 100 GHz [4–6]. The main limits are set in terms of basic restrictions on the basis of established biological and health effects, and through experimental or computational dosimetry techniques. The basic restriction limits for frequencies 100 kHz to 100 GHz is define in two different assessment benchmarks i.e SAR and PD. These basic restriction limits for lower and higher frequencies are given in Table 2-1and

Table 2-2, respectively.

Table 2-1. Basic restriction levels for general public at lower frequency.

Standards	Frequency Range	Whole Body SAR (Wkg^{-1})	Spatial Peak SAR (Wkg^{-1})	Localised SAR (Limbs) (Wkg^{-1})	Averaging Time (Minutes)
ICNIRP	10 MHz – 10 GHz	0.08	2 (10 g)	4 (10 g)	6

IEEE	10 MHz – 3 GHz	0.08	2 (10 g)	4 (10 g)	N/A
FCC	10 MHz – 6 GHz	0.08	1.6 (1 g)	4 (10 g)	30

Table 2-2. Basic restriction levels for general public at higher frequency (f: frequency).

Standard	**Frequency (GHz)**	**E-field (V/m)**	**Power Density (mW/cm^2)**	**Averaging Surface (cm^2)**	**Averaging Time (min)**
ICNIRP	10-100	61	1	20	$68/f^{1.05}$
			20	1	
IEEE	3-30	N/A	10	$100\lambda^2$	150/f
	30-100			100	$25.24/f^{0.476}$
FCC	6-100		1	N/A	30

For lower frequencies, ICNIRP points out that "*established biological and health effects are equivalent to more than 1˚C rise in body temperature. This level of temperature increase results from exposure of individuals under environmental conditions to whole-body (WB) SAR of approximately 4 Wkg^{-1} for about 30 minutes. Therefore, a WB averaged SAR of 0.4 Wkg^{-1} averaged over 6 minutes has been chosen as the basic limit that provides satisfactory protection for occupational exposure. Moreover, an additional safety factor of 5 is introduced for exposure of the public, where the WB averaged SAR limits is 0.08 Wkg^{-1}*" [7].

ICNIRP recommends limits on local SAR (or peak/maximum SAR) as values that shall not be exceeded as average over any 10 g mass of contiguous tissue. While it is evident that smaller volumes allow more precise determination of SAR distribution, at the expenses of increasing difficulty and cost of dosimetry, the choice of 10 g mass represents a reasonable compromise based on biological considerations [8].

On the other hand, IEEE established the localised exposure basic limits to protect against excessive temperature rise in any part of the body that might result from, localised or non-uniform exposure. When SAR averaged over a 10 g volume of tissue in the extremities, and the pinnae, only SAR values for that tissue may be considered. If any cubic volume contains tissue from both the body and the extremities or pinna, each must be considered separately. Specifically, when determining the average SAR in a 10 g cube of tissue in the body, any lack of tissue contained in the cube from the extremities or pinna should be treated as air, i.e., mass = 0 and SAR =0 [4].

In addition to above, according to CST MWS, IEEE/IEC 62704-1 is an averaging method according to the current dual logo standard draft IEEE/IEC 62704-1 "draft recommended practice for determining the peak spatial-average SAR in the human body from wireless communications devices, 30 MHz - 6 GHz: General Requirements for using the FIT/finite-difference time-domain (FDTD) method for SAR calculations" (Formerly known as IEEE P1528.1). Compared to the IEEE C95.3 method it uses an additional criterion that limits the air volume in valid averaging cubes to 10 % [9].

IEC recommended practice ensures good tissue contiguity, as well as the separation of the tissues from body and extremity regions in the cases when cubic volumes contain tissue from both regions. The proposed manner of voxel selection, their status labelling and the building of cubes provide good accuracy of the 10 g mass target for any cubic volumes, as well as good peak SAR assessment. Moreover, a conservative assessment of peak SAR at interfaces is achieved. Therefore, the averaging method proposed by IEC 62704-1 standard is suitable for SAR assessment according to ICNIRP requirements.

For higher frequencies, ICNIRP use PD as merit to limit the EM exposure beyond 10 GHz. The possible reason of using PD as basic restriction limit could be due to shallow penetration of EM waves inside the human body. The penetration depth at 10 GHz within the human skin is between 4–6 mm according to [10] as shown in Figure 2-1. The penetration depth of EM waves decrease with the increase in frequency or in other words it is inversely proportional to the frequency.

Skin is the largest tissue among the other human tissues and organ. The average weight of human skin is about 10,886 grams which varies according to the size and weight of the human beings. Skin is composed of three layers: epidermis, dermis and subcutaneous tissues and its thicknesses varies among the public from gender to gender. Generally, epidermis and dermis thickness varies from 0.05 mm on eyelids to 1.5 mm on the soles of the feet and palms of the hand and, 0.6 mm on the eyelids to 3 mm on the back, palm and soles, respectively. It is well understood that tissues with high concentration of water absorb more energy. Therefore; eyes and skin are major concern beyond 10 GHz.

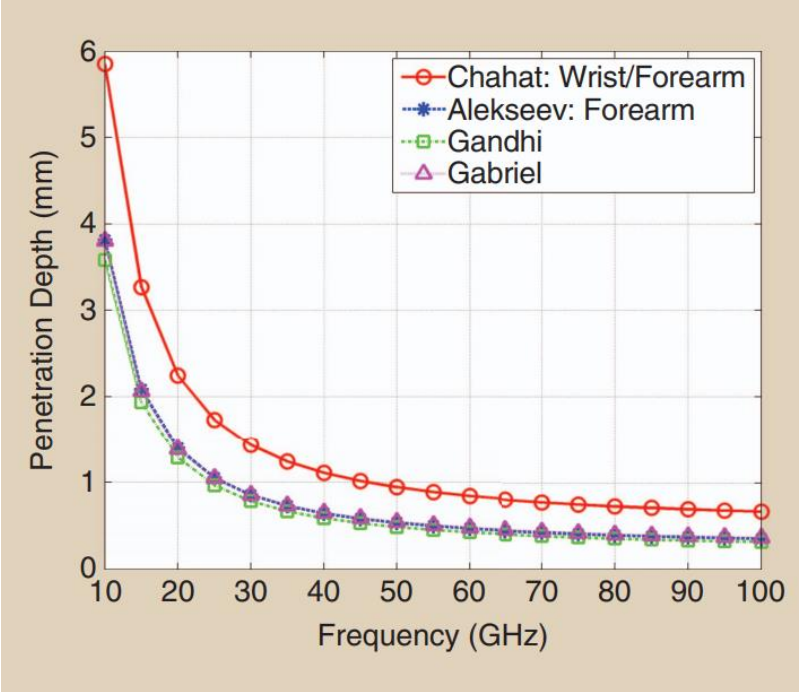

Figure 2-1. The penetration depth in the human skin with the increase of exposure frequencies [10].

2.3 Dielectric Properties of Biological Tissues

The study of dielectric properties of human tissues is topic of interest from more than five decades. The assessment of dielectric properties of biological tissues belongs to basic as well as applied science. An intense literature review on the dielectric properties of biological tissues has been done in reference [11]. The author reviewed the Schwan 1957, Schwan and Foster 1980, Pethig 1984, Pethig and Kell 1987, Foster and Schwan 1989 and Stuchly 1980, the theoretical aspects and the main findings in this subject in detail.

The dielectric properties play a vital role in dosimetry studies in accessing the EMFs exposure on human bodies. It also determines the interaction between the human body and EMFs. Accurate knowledge of dielectric properties of human tissues is required, in order to calculate the energy deposition when they are exposed to EMFs [12].

The dielectric properties of tissues are frequency-dependent. The electric behaviour of tissues over a wide frequency range are usually described by two properties relative permittivity (ε') and conductivity (σ). These two parameters represent the charge and current densities respectively induced in response to an applied E-field of unit amplitude [13]. The physical condition of these parameters can be affected by change in temperature, frequency

and other factors. The dielectric properties of materials are typically obtained from measured complex relative permittivity, (ε^*) as shown in equation 2.1.

$$\varepsilon^* = \varepsilon' - j\varepsilon'' \quad \text{(Equation 2.1)}$$

Where ε' is the relative permittivity of the material, a measure of the charge displacement and energy stored in the material, and ε'' is the imaginary part of permittivity which is commonly known as loss-factor, a measure of the electrical energy dissipated [13]. In a perfect dielectric material, losses are due to displacement currents and, loss factor (ε'') is related to and can be expressed as displacement electric conductivity (σ_d), whereas in biological material the conductivity is given by equation 2.2.

$$\sigma = \sigma_d + \sigma_i \quad \text{(Equation 2.2)}$$

Where σ_i is the ionic conductivity of material. The total conductivity of a biological material is a combination of ionic and displacement currents induced by the applied E-fields as shown in equation 2.2 [13]. The conductivity (σ) of material is also related to the loss factor, absolute permittivity (ε_o = 8.85 x 10-12 F/m) and the angular frequency ($\omega = 2\pi f$) as shown in equation 2.3.

$$\varepsilon'' = \sigma/\omega\varepsilon_o \quad \text{(Equation 2.3)}$$

The variation in dielectric properties under the wide temperature range (20–40^o C) is well studied in [13]. It has been reported that permittivity and conductivities values of several tissues for most frequencies increases about +1.5% and +2% per Celsius respectively up to 50 MHz. The negative change in dielectric behaviour was also observed between 400 MHz to 1 GHz.

2.3.1 Dielectric Spectrum Response of Biological Tissues

The dielectric properties of biological tissues can be determined when EM radiations interact with biological tissues. They exhibit systematic changes due to the physiological state of the tissue; for instance, the intactness of the cellular membrane and the water content of the tissue.

It has been reported from many years that children have high level of water content in biological tissues as compared to adults [15]. The water level inside the biological tissues varies with tissue types and variation in dielectric properties may be attributed to the water content [13]. The dielectric spectra of tissues consist of three main dispersions regions predicted by known interaction mechanisms as shown in Figure 2-2.

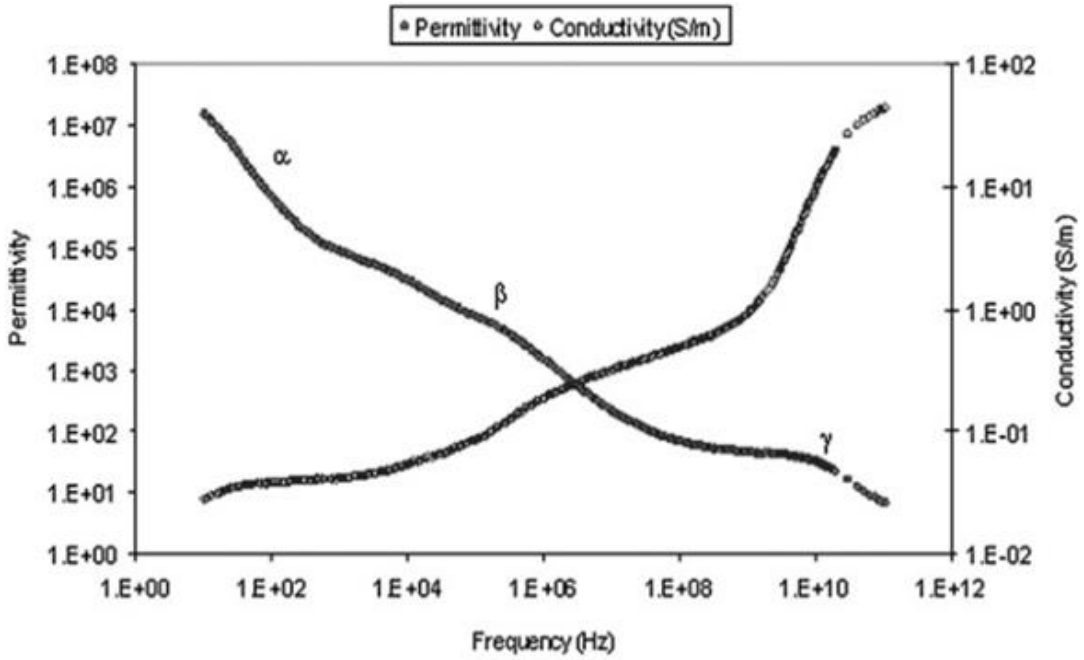

Figure 2-2. Dielectric spectrum of ovine liver, where three different dispersion represents the electric behaviour of biological tissues when interact with EM radiations [12].

2.3.2 Dielectric Dispersion Regions

The dispersion regions are also called relaxation regions [16, 17] that are defined on the bases of the electrical behaviour of biological tissues when interact with EM radiations. The dielectric spectrum of biological tissues is determined by a number of dispersion phenomena which are described in the following sections. The three main dispersion regions are given below:

1) α –dispersion region

The frequency below few kHz is defined as Alpha (α) dispersion region as shown in Figure 2-2. This region is characterised by very large permittivity values of biological tissues. The high permittivity values of the biological tissues are produced due to the ionic diffusion process at the cellular membrane [11, 12, 18].

2) β – dispersion region

The intermediate frequency or radio frequency region is defined as Beta (β) dispersion region as shown in Figure 2-2. In this region, the polarisation of cellular membranes occurs. This polarisation of membrane at cellular level acts as a barrier, to the flow of ions between intra and extra cellular media. The polarisation of proteins and other organic macromolecules can be described in this region [10, 11, 17].

3) γ – dispersion region

The gigahertz or microwave frequency region is defined as Gama (γ) dispersion region as shown in Figure 2-2. This region occurs due to the polarisation of water molecules inside the tissues [10, 11, 17].

2.4 Review of Numerical Assessment Techniques

The use of wireless communication devices has augmented worldwide brings about a public concern as to whether continuous utilisation of such devices is safe or not. Various numerical analysis techniques are available such as finite-difference method (FDM), finite-element method (FEM), the method of moments (MoM), transmission-line-matrix (TLM), FIT and FDTD. The detail information about all these methods and comparison between them is presented in this reference [19].

The TLM and FDTD methods have become the most important time domain simulation techniques which are used in wide range of EM assessments. The TLM method is a discrete model, in space and time, of the EM phenomena. The TLM method has been introduced in the year 1971 as a two dimensional method [20], and extended to three dimensional method in 1987 with the development of symmetrical condensed node [21]. In TLM method, EMFs are modelled by wave pulses propagation in a mesh of transmission line, and afterwards scattered in the mesh nodes. The TLM method is based on the network theory, and each cell is divided into 12 incident voltage pulses, and that are related by a scattering matrix to 12 reflected voltage pulses. More information about TLM method can be found in the reference [22–24].

However, FDTD method uses field theory [25–27]. It relies on the discretisation of Maxwell equations in time domain analysis. The FIT technique is a discretisation method, which convert Maxwell's equations onto a dual grid cell complex, which results in a set of discrete matrix equations. The FDTD and FIT methods are almost equivalent [27]. The

FDTD/FIT schemes uses perfectly matched layer (PML) absorbing conditions, and conformal path techniques (similar to conformal finite integration technique (CFIT)) undoubtedly are powerful tools for EM exposure assessments [27].

The FDTD method have been selected with adequate meshing techniques for fast and accurate SAR analysis from many years [9, 25]. CST microwave studio (MWS) has adopted FIT proposed by Weiland in 1976 [25]. The evaluation of SAR with different materials is performed by FIT method in CST MWS [9]. The FIT methods allows to use computationally adequate and easy to generate structured Cartesian, i.e, orthogonal, grid complexes. Moreover, this method is more suitable for volumetric dielectric bodies' analysis.

2.5 Numerical Dosimetry

The PD of any source of EM radiation is not only related to power level at the source, but rises rapidly as the distance reduce from the source. Some studies suggest that potential health hazards could be linked to excessive exposure to high PD's of non-ionizing radiation. A number of biological effects and established adverse health effects from severe exposure to RF fields have been investigated [30–32]. These effects are related to localise heating of any body organ or stimulation of excitable tissues.

The specific biological responses to RF fields are generally related to the rate of specific energy absorbed by body or usually refer as SAR, the strength of internal E-fields (voltage gradients) and currents. The rate and distribution of RF energy absorption in the human body depends on many factors such as operating frequency, boundary conditions, dielectric properties of human tissues, size and age of the human body and, strength and orientations of the incident field. However, SAR measurements are required to assess the compliance of mobile phones or smart devices with existing standards and recommendations.

2.5.1 Specific Absorption Rate (SAR) Theory

Absorption of RF energy is commonly described in terms of SAR, which is a measure of the rate of energy deposition per unit mass of body tissue of a person using a EMFs, and is usually expressed in units of watts per kilogram (Wkg^{-1}). The SAR can be calculated using equation 2.4.

$$SAR = \frac{\frac{\partial W}{\partial t}}{\rho_m} \quad (\text{Wkg}^{-1}) \qquad \text{(Equation 2.4)}$$

Where ρ_m is the mass density.

However, the rate of change of energy $\frac{\partial W}{\partial t}$, is equivalent to PD. Hence equation 2.4 can be represented as:

$$SAR = \frac{PD}{\rho_m} \quad (\text{Wkg}^{-1}) \qquad \text{(Equation 2.5)}$$

Equation 2.5 can be reproduced to present SAR in relation to internal E-fields [4]:

$$SAR = \frac{\sigma |E|^2}{\rho_m} \quad (\text{Wkg}^{-1}) \qquad \text{(Equation 2.6)}$$

Where

σ is the conductivity of the tissue (S/m).

ρ_m is the mass density of the tissue (kg/m^3).

E is the induced E-field in the biological tissue (V/m).

The whole body averaged SAR, is defined as the time rate of change of the total energy transferred to the dielectric body, divided by total mass of the body. In the IEEE standard C95.1 [4], the SAR is defined as the time derivation of the incremental energy (dW) dissipated in an incremental mass (dm) contained in a volume element (dV) of a given density (ρ).

$$SAR = \frac{d}{dt}\left(\frac{dW}{dm}\right) = \frac{d}{dt}\left(\frac{dW}{\rho . dV}\right) \quad (\text{Wkg}^{-1}) \qquad \text{(Equation 2.7)}$$

The SAR is also related to heat capacity, in terms of the rate of change of temperature within the test object as shown below [4]:

$$SAR = c.\frac{\Delta T}{\Delta t} \quad (\text{Wkg}^{-1}) \qquad \text{(Equation 2.8)}$$

Where

ΔT is the specific heat capacity (°C).

Δt is the change in temperature (s).

C is change in time (J/kg °C).

This equation is based on the consideration that any heat transfer mechanisms are negligible.

2.5.2 SAR Averaging Methods

As a matter of fact, quite large number of averaging algorithms are available for numerical estimation of SAR [33–41] and in this section, a brief overview on the most commonly used averaging algorithms are presented and discussed. One of the frequently adopted approaches [34, 36], for instance, computes the SAR on averaged reference mass (SARrm) on a certain point by considering the fact that contribution comes from the cells, which belongs to a cube centred in that point and this algorithm is called fixed cube algorithm (FCA) [42].

In this strategy, the size of the cube is calculated in a pre-processing phase. This is based on used spatial discretisation step, the average value of the biological tissues density, and the desired rm. Once the size of the reference cube has been estimated, the centre of the cube is moved up, and down in the discretised target. Therefore, in this process those cells are selected whose contribution is used for the SARrm calculation. A schematic and simplified two dimensional representation of the FCA is presented in Figure 2-3. This method comes with some advantages and disadvantages. It can be observed that, the non-modifiability of the volume shape significantly simplifies the algorithm implementation.

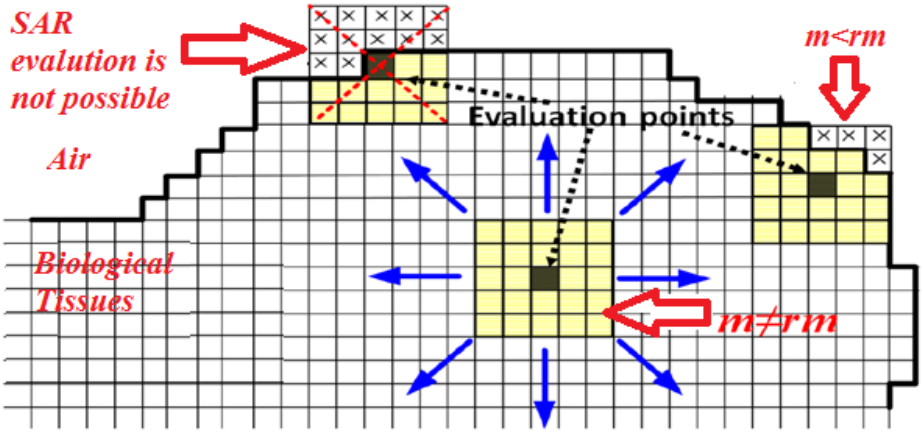

Figure 2-3. Two dimensional representation of fixed cube algorithm, reference cube needs to evaluate and then centre of the fixed cube is moved up, and down in the discretised target and then calculate the SAR [35].

However, on the other hand many drawbacks arise. First of all, it is worth mentioning that it is practically impossible to identify a cube volume that selects exactly the same number

of cells require to obtain a mass equivalent to rm. The detailed working of this method can be found in reference [42]. Moreover, when the FCA is used to select the SAR evaluation in a cell which is close to the external surface, cells of air are also selected, thus changed the averaging mass. In order to avoid the overestimation of the SAR in cases, where a selected cube volume doesn't contain dielectric tissues, a maximum tolerable percentage of air is implemented; if the percentage of air is greater than the fixed limit then SAR remains undetermined. This approach limits the algorithm to evaluate average SAR with some approximation. This approach does not allow the estimation of the SAR in the most external points of the exposed target where, though, high SAR values or even the peak/maximum SAR itself, are located.

In reference [37] a very first improvement in FCA is obtained by using the specific cubical volume, which dynamically adjusts its size, in order to consider the desired value of rm. This approach names as fixed adjustable cube (FAC), and it is presented in Figure 4. More specifically this algorithm constructs a sequence of cubes in order to evaluation each point and the dimension of cube continuously expanding until a mass superior to rm is reached. The percentage of air is estimated at each evaluation step and if it is greater than a prefixed limit then the SAR in that particular point remains undetermined. Similarly, the last cube of the sequence with mass less than rm is used as the central point for the SAR evaluation, and only a correct evaluated portion of the adjacent cells (peripheral cells of the cube) is added, in order to accurately reach rm.

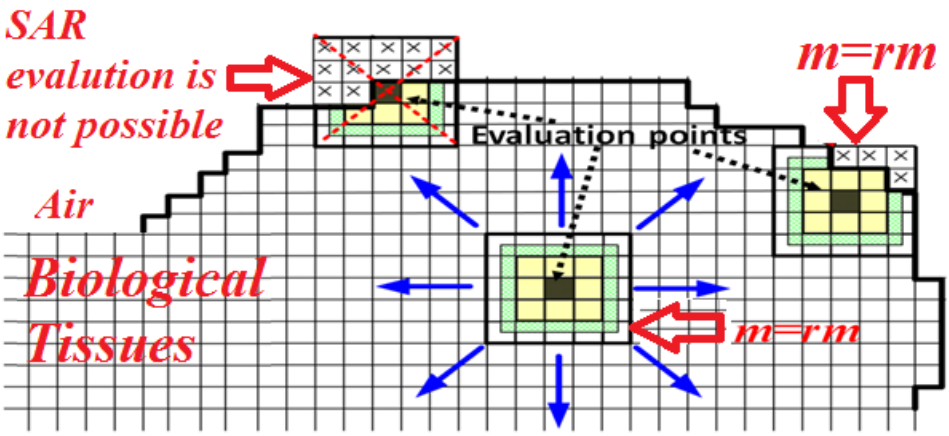

Figure 2-4. Two dimensional representation of fixed adjustable cube algorithm, percentage of air is estimated at each evaluation step and if it is greater than a prefixed limit then the SAR in that particular point remains unknown [35].

More specifically, the peripheral cells contribution to the SAR estimation is proportional to the portion of their mass in order to reach rm. However, a major limit of this

algorithm still remains; the incapability to identify the SAR in points closed to the surface of the exposed object [35].

The limitations of previous algorithms are addressed in reference [38], and further improvements are proposed. According to reference [38] the concept of a perfect cubical shape volume is not considered indispensable anymore; the cells are joined around the reference point, in one by one manor in order to establish benchmark and excludes air. This algorithm is called adaptive cube (AC) and represented in Figure 2-5..The AC algorithm stops adding the new cells, when the total mass of cubical volume reached to rm. Due to this technique the resultant averaging volume belongs to the combination of a cube and the non-tissue points; which is given by the set of cells. In such a way, the SAR can be estimated in every point, including those points that belong to the most external biological object.

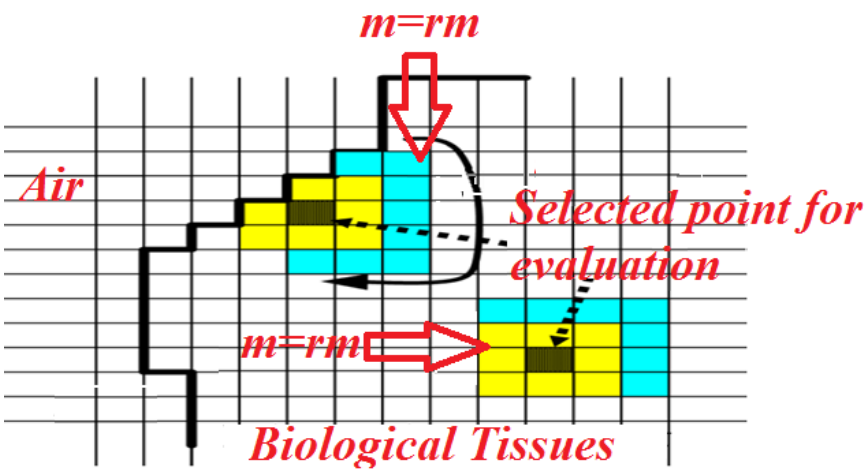

Figure 2-5. Two-dimensional representation of adaptive cube algorithm, the cells are joined around the reference point in one by one manor to established benchmark and exclude air [35].

Another alternative algorithm is reported in reference [39]. It is called **C95.3** IEEE standard. This averaging standard widely used around the globe. Various numerical analysis tools such as CST microwave studio implement IEEE averaging standard. The two dimensional representation is presented in Figure 2-6, though recommended in reference [43].

In C95.3, SAR is evaluated in three different steps. In the first step, the SAR_{rm} is calculated, wherever possible, by using a FCA. The maximum acceptable air limit in SAR calculation is set to zero, and only if reference mass is reached with tolerance of 5%. In the second step, the SAR in each unevaluated point is introduced as the maximum of the already assessed SAR among those whose cube contained that point. Finally, third step is applied in the remaining points (usually belongs to extremities); the point becomes the centre evaluation

point of a new cube. New selected point can contain air and extends until rm equivalent mass is selected. This algorithm allows the estimation of the SAR in every single point. Nevertheless, the second step of the algorithm, referred to a very crucial points close to the target surface, and assigns to such points SAR values which referred to more internal points, and hence causing a possible underestimation of the peak/maximum SAR [35].

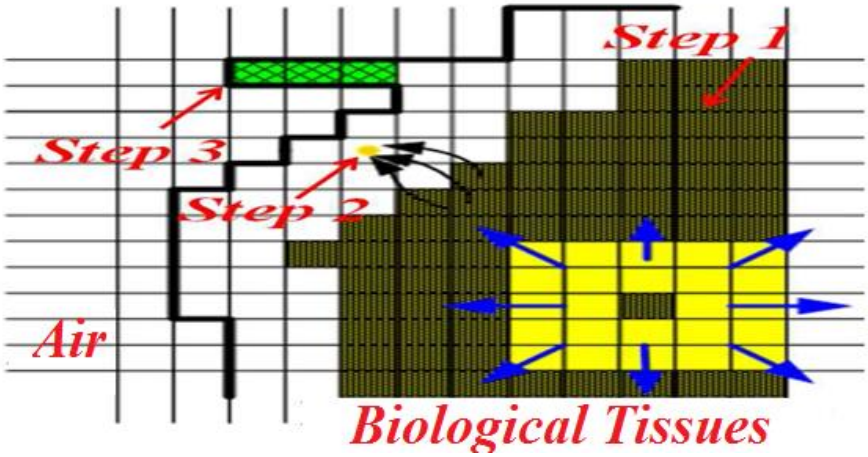

Figure 2-6. Two dimensional representation of C95.3 algorithm [34], three step process of estimating SAR at any point in biological tissue, where tolerable air percentage is set to zero.

The fair comparisons among the presented numerical techniques shows that these radically different averaging methods for SAR evaluation can give few indications in biological target object reported in RF safety guidelines. Despite the fact that, these averaging methods gives only the estimation of SAR, slight variations in results can be easily predicted that could generate discrepant results. Moreover, all methods are based on a cubical volume shape which allows easy implementation.

2.6 Experimental Dosimetry

Dosimetry plays vital role in the experimental studies to investigate possible effects of EMFs. Dosimetry means “metrology” of dose. It is defined as the amount of energy absorb by a substance when it come in contact with EMFs. The human body is reasonably a good conductor and can act like a receiving antenna. Dosimetry studies shows how human tissues and cells get affected from EMFs due to continuous exposure. For such kind of assessment very few standard experimental setups are available. These setups are applied to calculate the SAR either by measuring temperature change or calculating the E-field absorption in a sample of liquid (human tissue-equivalent).

The most important aspects of dosimetry measurements are the requirements for the performance and accuracy of the test system and also the method of carrying out the measurement. Most of the SAR compliance assessments are carried out by using a miniature and sensitive electric probe in order to measure the E-field distribution by scanning the sample or phantom which is filled with liquid simulating tissue-equivalent material. According to IEC standards [44], the SAR estimation should be performed using a miniature probe that can automatically positioned itself to measure the internal E-field distribution in a phantom when exposed to EMFs produced by any smart device.

There are several other important requirements to the measuring probe. It must be very small in order to have no resonances over the frequency of interest. Due to small size it allows a very precise and accurate spatial registration of the fields around it. The probe must not disturb the field structure significantly in the liquid phantom. The measurement centre of the probe must be very close to its tip, to minimise the in accuracies. The standards [44] recommends that the probe diameter should be no more than 8mm. Probe size is critical for higher frequencies (above 3 GHz) SAR assessment and the probe should be linear, isotropic and sensitive.

Furthermore, phantom should be a representation of human head model in the case of mobile handset exposure. From the measured E-field values, the SAR distribution and maximum averaged SAR values over 1 g or 10 g can be calculated using the standard SAR equations. The experimental setup consists of positioning robot and holder, E-field measuring probe and phantom which are filled with liquid which is equivalent to muscle or head tissues as shown in Figure 2-7.

The complexity of above explained system increase when a device contains multiple antennas such as MIMO. MIMO systems has multiple operating modes such as standalone mode, simultaneous excitation mode and beam steering mode. The details about the different operating modes are comprehensively discussed in chapter 5. MIMO enable devices including mobile handsets are required to comply with standards for limiting human exposure to EMFs.

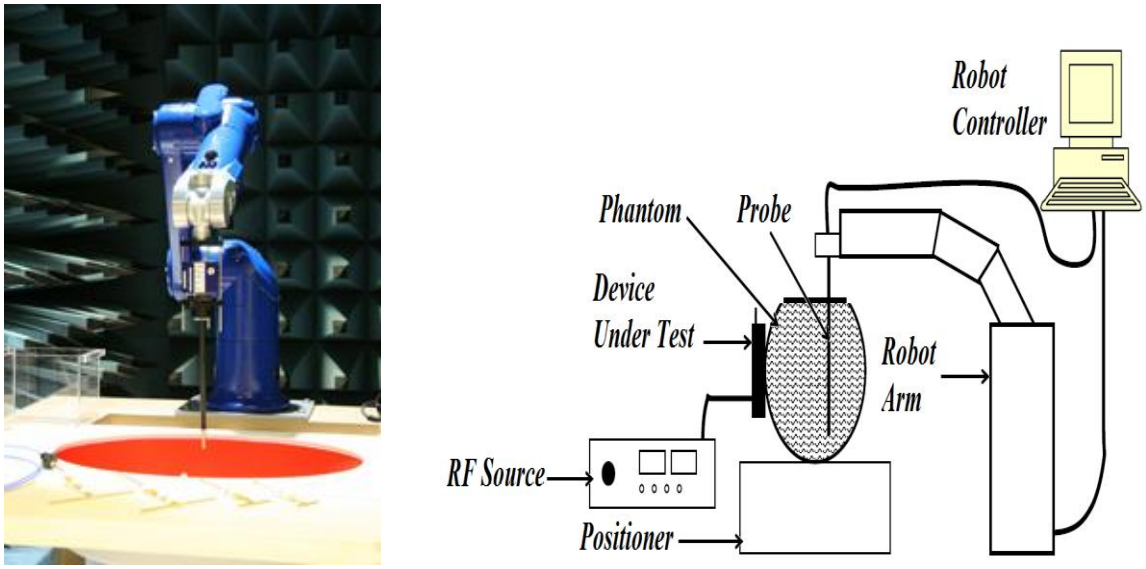

Figure 2-7. Measurement of SAR from body mounted device [45].

It is difficult to measure SAR under complex configuration such as simultaneous excitation by considering relative phase variations. So in order to reduce the complexity of SAR measurements in above mentioned configurations very few methods are available in literature [46–47]. The assessment of SAR due to exposure from single antenna element is relatively simple as compared to more than one antenna elements configuration as mentioned before.

In reference [47], an attempt is made to estimate the SAR when MIMO enable devices operates in simultaneous excitation mode. According to this method, prediction can be made on SAR values, in order to simplify the assessment procedure, when MIMO devices operates in simultaneous excitation mode based on the prior knowledge of SAR values in standalone mode. The peak of the standalone SAR for each antenna elements in MIMO system should be smaller than the limit (L) specified by the international organisations (ICNIRP and FCC). For example, for hand-held devices, the SAR limit is L = $2Wkg^{-1}$ when averaged over 10 g tissue according to ICNIRP guidelines and the SAR limit is L = $1.6Wkg^{-1}$ when averaged over 1 g tissue according to FCC guidelines.

Consider MIMO enabled device with ‘n’ antenna elements and ‘m’ number of antennas operating in simultaneous excitation mode where $1< m \leq n$. The power allocated to the *n*th antenna element is given by:

$$P_n = R_n P_{\text{total}} \qquad \text{(Equation 2.9)}$$

Where R_n is a real constant with $0 \leq R_n \leq 1$, $\sum_{n=1}^{m} R_n = 1$. Since the square of the E-field magnitude is directly proportional to the input power. Therefore, the total E-field can be represented by:

$$\vec{E}_{\text{total}} = \sum_{n=1}^{m} \sqrt{R_n}\, \vec{E}_n\, e^{j\theta_n} \qquad \text{(Equation 2.10)}$$

Where θ_n is the phase of the E-field generated by nth antenna element, with θ_n range from 0^o to 360^o. Now applying Euler's identity on above equation,

$$|\, \vec{E}_{\text{total}}\, |^2 = |\, \sum_{n=1}^{m} \sqrt{R_n}\, \vec{E}_n \cos\theta_n + \text{j} \sum_{n=1}^{m} \sqrt{R_n}\, \vec{E}_n \sin\theta_n\, |^2 \qquad \text{(Equation 2.11)}$$

Since power allocation and phase variations are independent from each other, assuming rapid and uniformly, distributed phase variation within 0^o to 360^o. Then, the time averaged total E-field is described by,

$$|\, \vec{E}_{\text{total}}\, |^2_{\text{avg}} = \sum_{n=1}^{m} R_n\, |\vec{E}_n|^2 \qquad \text{(Equation 2.12)}$$

By equating equation 2.12 into the equation 2.6, the averaged SAR can be represented by,

$$\text{SAR}_{\text{avg}} = \frac{\sigma}{\rho} |\, \vec{E}_{\text{total}}\, |^2_{\text{avg}} = \sum_{n=1}^{m} R_n \frac{\sigma}{\rho} |\vec{E}_n|^2 = \sum_{n=1}^{m} R_n\, \text{SAR}_n \qquad \text{(Equation 2.13)}$$

Where SAR_n is the standalone SAR for each antenna element, whose peak value max (SAR_n) $\leq$ L. Hence, time-averaged simultaneous peak SAR (TASPS) = max (SAR_{avg}) satisfies:

$$\text{TASPS} \leq \sum_{n=1}^{m} R_n \max\,(\text{SAR}_n) \leq \sum_{n=1}^{m} R_n\, \text{L} = \text{L} \qquad \text{(Equation 2.14)}$$

Where the first equality is only obtained, when all peak standalone SAR values appear at the same location. The second inequality represents the SAR limit max (SAR_n) $\leq$ L. So equation 2.14 depicts that TASPS always meets the SAR limits if standalone SAR from each

antenna elements meets the limit. It is worth mentioning that this method is only applicable to estimate simultaneous SAR values without considering relative phase among antenna elements if standalone SAR values from each antenna elements are less than the limit. Moreover, it is also found that TASPS under estimate the SAR values as compared to the literature [47].

2.7 Chapter Summary

This chapter summarise the brief introduction about the fundamental aspects of electromagnetic fields (EMFs) exposure assessments. Some of the major international guidelines requirements are discussed in detail in order to limit the public exposure below the health hazard levels. The behaviour of dielectric properties of materials (biological tissues) is analysed over a wide frequency spectrum. The interaction of EMFs with biological matter has been defined in three different dispersion or relaxation regions. The assessment of EMFs interaction with biological matters can be evaluated using a fundamental estimation method. Time domain analysis techniques such as finite difference time domain (FDTD), finite integral technique (FIT) and transmission line method (TLM) are briefly reviewed. However, few relevant methods are explained with possible comparisons and CST Microwave Studio (MWS) numerical assessment software has been chosen as final choice for assessment, which is based on finite integral technique (equivalent to finite difference time domain) method.

The fundamental parameters such as specific absorption rate (SAR) and power density (PD) are used for analysing the possible health effects of EMFs interaction with human bodies are briefly explained. Numerical averaging algorithms are used to successfully estimate SAR quantity. The detailed analysis is provided on their implementation in numerical domain. In addition, comparison are made among the adopted and several other averaging algorithms. Standard state-of-the-art experimental setup discussed in detail in order to limit the EM exposure below the recommend levels. Experimental dosimetry techniques for EM exposure assessment are complex, therefore, few reliable techniques are reviewed in detail which could be implemented to reduce the experiment time for simple and complicated assessment configurations in case of multiple-input-multiple-output (MIMO) systems.

References

[1] P. Dimbylow, "Development of the female voxel phantom, NAOMI, and its application to calculations of induced current densities and electric fields from applied low frequency magnetic and electric fields," Phys. Med. Biol., vol. 50, pp. 1047–1070, 2005.

[2] A. Christ, W. Kainz, E. G. Hahn, K. Honegger, M. Zefferer, E. Neufeld, et al., "The Virtual Family-development of surface-based anatomical models of two adults and two children for dosimetric simulations," Phys. Med. Biol., vol. 55, pp. 23–38, 2010.

[3] C. Rossmann and D. Haemmerich, "Review of temperature dependence of thermal properties, dielectric properties, and perfusion of biological tissues at hyperthermic and ablation temperatures," Critical reviews in biomedical engineering, vol. 42, pp. 467–492, 2014.

[4] IEEE, "IEEE Recommended Practice for Determining the Peak Spatial-Average Specific Absorption Rate (SAR) in the Human Head from Wireless Communications Devices: Measurement Techniques," IEEE Std. 1528 – 2013 (Revision of IEEE Std 1528 – 2003), pp. 1–246, 2013.

[5] R. F. Cleveland, "Compliance with FCC exposure guidelines for radiofrequency electromagnetic fields," in Int. Symp. EMC, pp. 1030–1035, 2004.

[6] NCRP, "National Council on Radiation Protection and Measurements: Advicing the Public about Radiation Emergencies," 1994.

[7] ICNIRP, "International Commission on Non-Ionizing Radiation Protection: Guidelines for limiting exposure to time-varying electric, magnetic and electromagnetic fields (up to 300 GHz)," Heal. Phys. Soc., vol. 74, pp. 494–522, 1998.

[8] ICRNIRP, "Exposure to high frequency electromagnetic fields, biological effects and health consequences (100 kHz-300 GHz)," 2009.

[9] CST Microwave Studio - 3D EM simulation software 2016 version, [Online]. Available: https://www.cst.com/Products/CSTMWS (Accessed Jun 2016).

[10] T. Wu, T. S. Rappaport, and C. M. Collins, "Safe for Generations to Come: Considerations of Safety for Millimeter Waves in Wireless Communications," IEEE Microwave Magazine, vol. 16, pp. 65 – 84, 2015.

[11] C. Gabriel, S. Gabriely, and E. Corthout, "The dielectric properties of biological tissues: I. Literature survey," Phys. Med. Biol., vol. 41, pp. 2231–2249, 1996.

[12] A. Peyman, "Dielectric properties of tissues; variation with age and their relevance in exposure of children to electromagnetic fields; state of knowledge," Phys. Med. Biol, vol. 107, pp. 434–438, 2011.

[13] F. A. Duck, *Physical Properties of Tissue: A comprehensive Reference Book*, pp. 1–360, 2012.

[14] A. Peyman, S. Holden, and C. Gabriel, "Dielectric Properties of Tissues at Microwave Frequencies," MTHR 2005.

[15] A. Peyman, C. Gabriel, E. H. Grant, G. Vermeeren, and L. Martens, "Variation of the dielectric properties of tissues with age: the effect on the values of SAR in children when exposed to walkie–talkie devices," Phys. Med. Biol, vol. 54, pp. 227 – 241, 2009.

[16] S. Gabriel, R. W. Lau, and C. Gabriel, "The dielectric properties of biological tissues: III. Parametric models for the dielectric spectrum of tissues," Phys. Med. Biol., vol. 41, pp. 2271–2293, 1996.

[17] O. G. Martinsen, S. Grimnes, H. P. Schwan, "Interface Phenomena and Dielectric Properties of Biological Tissue," Encyclopaedia of Surface and Colloid Science, pp. 2643–2652, 2002.

[18] A. Peyman, S. J. Holden, S. Watts, R. Perrott, and C. Gabriel, "Dielectric properties of porcine cerebrospinal tissues at microwave frequencies: in vivo, in vitro and systematic variation with age," Phys. Med. Biol, vol. 52, pp. 2229–2245, 2007.

[19] M. N. O. Sadiku, and A. F. Peterson, "A comparison of numerical methods for computing electromagnetic fields," Southeastcon '90, vol.1, pp. 42-47, 1990,

[20] P. B. Jhons, and R. L. Beurle, "Numerical solution of 2-dimensional scattering problems using a transmission-line matrix," Proceedings of the Institution of Elec. Engin., vol. 118, pp. 1203–1208, 1971.

[21] P. B. Johns, "A Symmetrical Condensed Node for the TLM Method," IEEE Trans. on Microwave Theory and Techniques, vol. 35, pp. 370–377, 1987.

[22] P. Russer, and J. Russer, "Transmission Line Matrix (TLM) and network methods applied to electromagnetic field computation," Microwave Symposium Digest (MTT), pp. 1–4, 2011.

[23] P. Enders, and C. Vanneste, "Huygens' principle in the transmission line matrix method (TLM). Local theory," Int. J. Numer. Model, vol. 16, pp. 175–178, 2003.

[24] M. O. Ozyalcin, F. Akleman, and L. Sevgi, "SAR Simulations in Wireless Communication and Safety Discussions in the Society," Turk. J. Elec. Engin., vol. 10, pp. 411–426, 2002.

[25] H.-H. Chou, H.-T. Hsu, H.-T. Chou, K.-H. Liu, and F.-Y. Kuo, "Reduction of Peak SAR in Human Head for Handset Applications with Resistive Sheets (R-Cards)," PIER, vol. 94, pp. 281–296, 2009.

[26] FDTD Method, [Online]. Available: http://www.remcom.com/xf7-fdtd-method/ (Accessed May 2017).

[27] D. M. Sullivan, "*Electromagnetic Simulation Using the FDTD Method*," 2nd Edition Hoboken, New Jersey: John Wiley & Sons, 2013.

[28] M. Clemens, and T. Weiland, "Discrete Electromagnetics: Maxwell's Equations Tailored to Numerical Simulations," [Online]. Available: http://www.compumag.org/jsite/images/stories/newsletter/ICS-01-08-2-Clemens.pdf (Accessed March 2015).

[29] M. T. Islam, M. R. I. Faruque, and N. Misran, "Reduction of Specific Absorption Rate (SAR) in the Human Head with Ferrite Material and Metamaterial," PIER, vol. 9, pp. 47–58, 2009.

[30] A. Zamanian and C. Hardiman, "Electromagnetic Radiation and Human Health: A Review of Sources and Effects," EMR & Human Health, pp. 16–26, 2005.

[31] H. C. Government of Canada, "Limits of Human Exposure to Radiofrequency Electromagnetic Energy in the Frequency Range from 3 kHz to 300 GHz," 2014.

[32] D. Finkenthal, B. Greco, R. Halsey, et al., "Introduction to Electromagnetic Spectrum," Technical Report, pp. 1–92 [Online]. Available: http://fusioned.gat.com/images/pdf/EMcurriculum.pdf (Accessed March 2017).

[33] I. Laakso, T. Uusitupa, and S. Ilvonen, "Comparison of SAR calculation algorithms for the finite-difference time-domain method," Phys. Med. Biol., vol. 55, pp. 421–431, 2010.

[34] K. S. Nikita, M. Cavagnaro, P. Bernardi, N. K. Uzunoglu, S. Pisa, E. Piuzzi, et al., "A study of uncertainties in modeling antenna performance and power absorption in the head of a cellular phone user," IEEE Trans. on Micro. Theory and Tech., vol. 48, pp. 2676–2685, 2000.

[35] L. Catarinucci and L. Tarricone, "Specific Absorption Rate (SAR) Numerical Evaluation: a Critical Discussion," Micro. Symp., pp. 1349–1352, 2007.

[36] J. Wang, O. Fujiwara, S. Watanabe, and Y. Yamanaka, "Computation with a parallel FDTD system of human-body effect on electromagnetic absorption for portable telephones," IEEE Trans. on Micro. Theory and Tech., vol. 52, pp. 53–58, 2004.

[37] K. Caputa, M. Okoniewski, and M. A. Stuchly, "An algorithm for computations of the power deposition in human tissue," IEEE Antennas and Propagation Magazine, vol. 41, pp. 102–107, 1999.

[38] L. Ae-Kyoung, and P. Jeong-Ki, "Study of the tissue volume for spatial-peak mass-averaged SAR evaluation," IEEE Trans. on Electromagnetic Compatibility, vol. 44, pp. 404–408, 2002.

[39] IEEE, "IEEE Recommended Practice for Measurements and Computations of Radio Frequency Electromagnetic Fields With Respect to Human Exposure to Such Fields,100 kHz-300 GHz," Revision of IEEE Std C95.3-1991, pp. 1–126, 2002.

[40] R. Otin and H. Gromat, "Specific absorption Rate Computations with a Nodal-based Finite Element Formulation," PIER, vol. 128, pp. 399–418, 2012.

[41] W. Minshen, L. Li, J. Chen, D. Jackson, W. Kainz, Q. Yihong, et al., "Evaluation and Optimization of the Specific Absorption Rate for Multiantenna Systems," IEEE Trans. on Electromagnetic Compatibility, vol. 53, pp. 628–637, 2011.

[42] L. Catarinucci, and L. Tarricone, " New algorithms for the Specific Absorption Rate numerical evaluation based on spherical averaging volumes," Progress In Electromagnetics Research, vol. 44, pp. 427– 445, 2012.

[43] IEEE, "IEEE Standard for Safety Levels With Respect to Human Exposure to Radio Frequency Electromagnetic Fields, 3 kHz to 300 GHz," Revision of IEEE Std C95.1-1991, pp. 1–238, 2006.

[44] D. Seabury, "An Update on SAR Standards and the Basic Requirements for SAR Assessment," Featured Article, pp. 1–8, 2005.

[45] NPL, "Measurement of SAR from body-mounted devices," [Online]. Available: http://www.npl.co.uk/electromagnetics/specific-absorption-rate/services/measurement-of-sar-from-body-mounted-devices (Accessed May 2017).

[46] D. T. Le, L. Hamada, and S. Watanabe, "A new measurement technique and experimental validations in determination SAR of N-antenna transmitters using scalar E-field probes," 9th European Conference on Antennas and Propagation (EuCAP), pp. 1–5, 2015.

[47] H. Li and B. K. Lau, "Efficient evaluation of specific absorption rate for MIMO terminals," Electronics Letters, vol. 50, pp. 1561–1562, 2014.

Chapter 3
Numerical Exposure Configurations

3.1 Introduction

The concept of controlling homes appliances through wireless links makes modern smart homes. These homes and exponential increase in use of wireless devices has raise concern over excessive exposure from these devices. Experimentally it's very difficult to realise different realistic exposure configurations or estimate EM absorption within the human body. For this purpose anatomical human models of various age groups used in numerical dosimetry.

In this chapter, numerical anatomical human models representing a sample of the population have been configured and modelled using an established commercially-available computation technique, namely CST Microwave Studio (MWS) [1]. These models have been simulated with very fine cartesian volume cells (voxels) resolutions of up to 2 mm to ensure adequate representation of each organ, and to satisfy the numerical stability requirements. The dielectric properties for all models were calculated based on Cole-Cole formulations [2], and the Nello Carrara Institute of Applied Physics (IFAC) online calculator [3], which is based on data reported in references [4–6]. Where no data were available for a particular tissue, adjustments and replacements were made to assign values from tissues with similar compositions.

Furthermore, age-dependent effects on dielectric properties were realised by utilising the novel age- and frequency-dependent (AFD) method. In this method, three different techniques are developed to calculate AFD dielectric properties. Relaxation parameters for Cole-Cole model were also produced and compared with different source and good agreement achieved to validate this method. This method utilises the measured data of animals (porcine/pigs) tissues using a curve-fitting techniques to map the AFD dielectric properties to their appropriate human equivalent ones [2, 7].

CST MWS widely used in the research community, and has been further validated and used in this study. Details of the validation studies as well as the modelling and selection of dielectric properties for all age groups are discussed in detail in this chapter.

3.2 Numerical Human Models

In this section modelling of voxel models are discussed in detail. The voxel models represent the complex structure of organs. Each organ have its own electrical properties and it absorb different level of energy when exposed to EM waves. A wide range of voxel models are available in literature [8]. However, in this section modelling of three different voxel models i.e. two adult and one child model discussed in detail and later used to study the SAR performance due to the exposure from wireless devices. The details about the voxel models are given in section.

3.2.1 Adult Voxel Models

Two adult voxel models (one female and one male) consider for EM evaluation. The female model is based on a voxelised 23-year-old female model, which is constructed from 791 slices along the body's long axis, with 294 × 124 voxels in the horizontal plane. By considering voxel dimensions of 1.9 mm, 2.0 mm, and 2.0 mm in the *x*, *y*, and z voxel axis respectively.

The resulting model has a height of 1.63 m and a weigh around 65 kg. These parameters are very close to the work presented in [9], which produced 1.63 m and mass of 60 kg. The difference in weight is attributed to the voxel dimensions and the mass densities used. Figure 3-1 shows a representation of the female model, with the opacity of the voxels varied to display the various body organs and tissue types. There were 40 different tissue types modelled in female model. Each of the tissue-voxel types were populated with their corresponding

dielectric parameters, calculated from IFAC database [3] as given in the Appendix A, Table A-1.

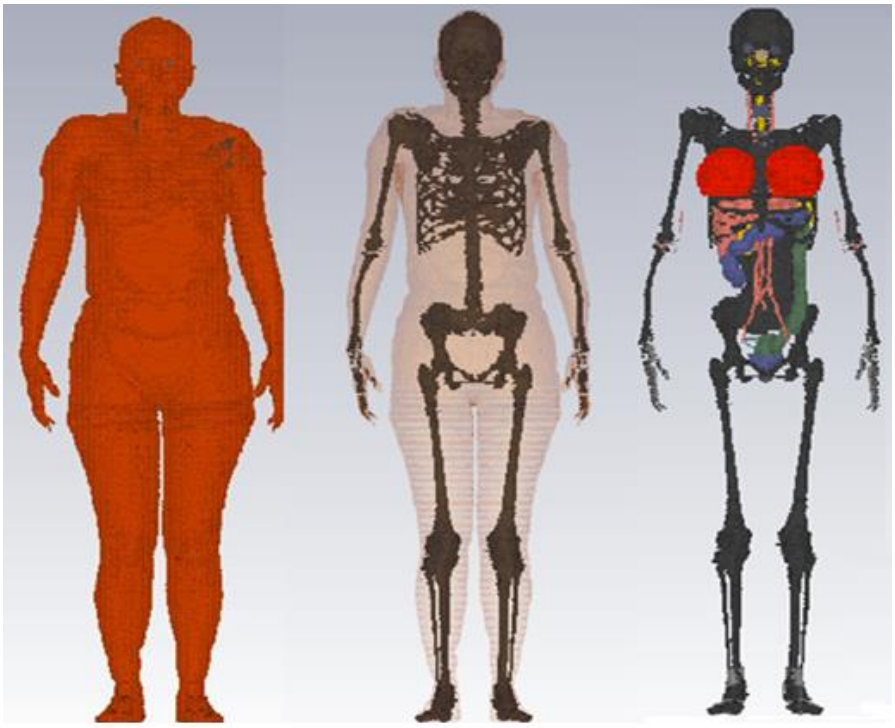

(a) **(b)** **(c)**

Figure 3-1. Volume rendered images of the female model; (a) The outside surface; (b) Skin and skeleton; (c) Skeleton with a few internal organs (Skin, Fat, and Muscle removed). Rendering resolution is 2 mm^3.

The adult 34-years old male model (shown in Figure 3-2) is based on a voxelised male model, which is constructed from 871 slices along the body's long axis, with 148 × 277 voxels in the horizontal plane. The computed male adult model represents a 1.76 m tall and weighs around 76 kg with voxel dimensions of 1.9 mm, 2.0 mm and 2.0 mm in each of the voxel axis. These dimensions are very close to work presented in reference [9], where the adult male has a height of 1.76 m and mass of 73 kg. The difference in weight is attributed to the mass densities used as mentioned in previous section. The dielectric properties of the 38 different tissue types included in male model were also calculated from the online database [3] as given in the Appendix A, Table A-2.

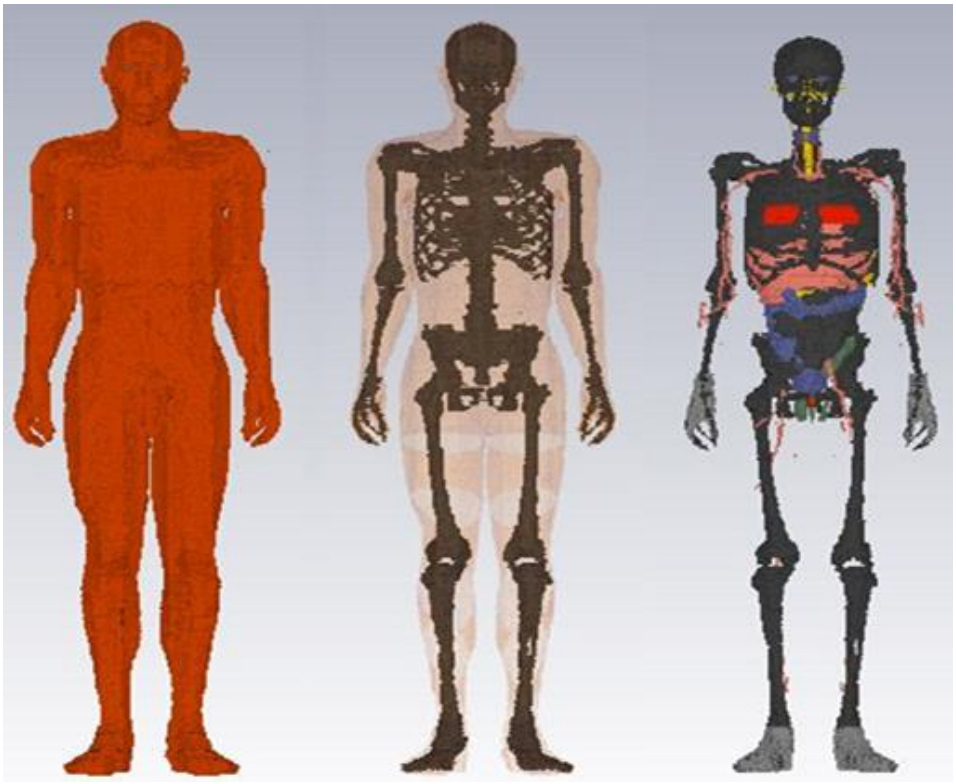

(a) **(b)** **(c)**

Figure 3-2. Volume rendered images of the male model; (a) The outside surface; (b) Skin and skeleton; (c) Skeleton with a few internal organs (Skin, Fat, and Muscle removed); Rendering resolution is 2 mm^3.

3.2.2 Child Voxel Model

The 7-year-old female child model (shown in Figure 3-3) is based on the ITIS Eartha virtual human model [8], representing 0.965 m tall and weigh of around 21.7 kg. The voxel dimensions are of 1.4 mm, 1.4 mm and 1.4 mm in *x*, *y*, and *z* axis. There are 300 × 122 voxels in each horizontal plane. A few refinements were made to the dielectric properties of the tissues to ensure that they are valid for the given age and for the operational frequencies of SMs such as 868 MHz and 2450 MHz. This female child model has 75 different tissue types that are given in the Appendix A, Table A-3. The dielectric properties of tissues used in each of the models have been determined from Cole-Cole models [2, 5, 7].

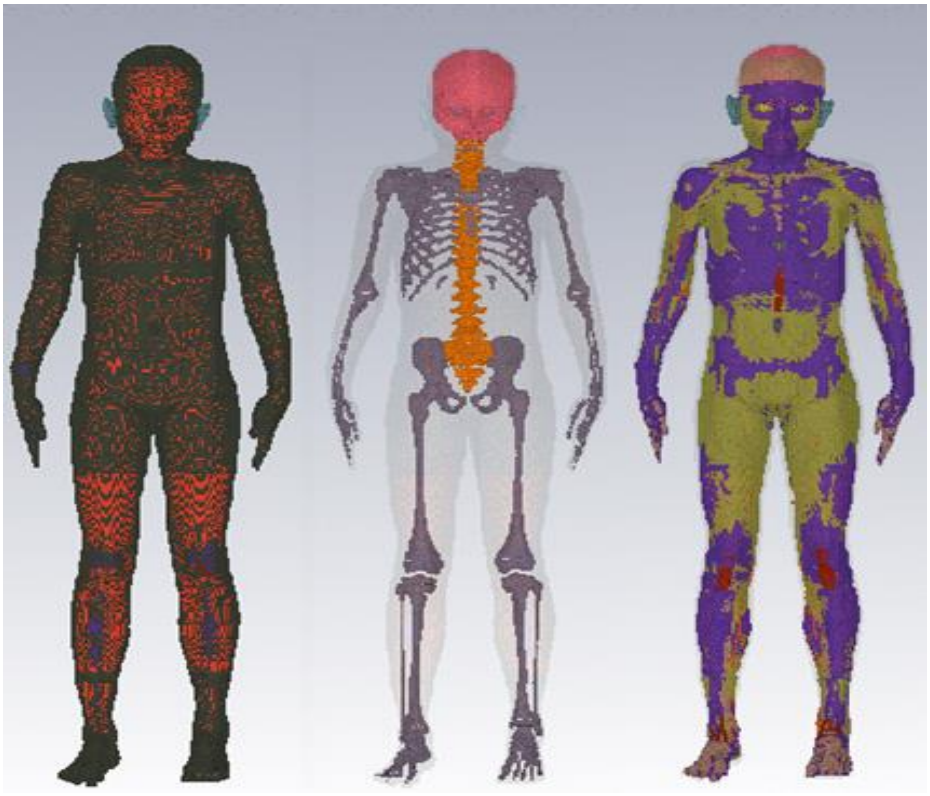

(a) **(b)** **(c)**

Figure 3-3. Volume rendered images of the female child model; (a) The outside surface; (b) Skin and skeleton; (c) Skeleton with a few internal organs (Skin, Fat, and Muscle removed); Rendering resolution is 1.4 mm^3.

The dielectric properties for the child model were calculated using novel age-dependent method that are calculated from 10, 50 and 250 kg pigs data [2]. Moreover, growth curve data for a 21.3 kg pig [10] were used to interpolate the dielectric properties for the child model, and the same method was applied for all tissues to get equivalent data for a 7-year-old child. In recent years, animals have been found to be similar to humans in terms of body organ development. According to reference [10], 4 week old pig is comparable to a 7-year-old child, and therefore data for a 21.3 kg pig was used to assign the dielectric properties for the child model.

3.3 Age-Dependent Tissue Properties

The frequency dependent nature of biological tissues has been well studied over the decades. Frequency-dependent dielectric properties of a wide range of tissues have become widely available following publication of the Cole-Cole dispersion models [4–6]. Due to lack of availability of age-dependent dielectric properties, most studies generally consider the

similar tissue properties for both adult and child models during the assessment of exposure from EMFs.

On the contrary, it is well-established that the water content level within the tissues of human body at different development stages (aging) become different. In literature, estimation methods based on empirical equations were used over a group of volunteers to show variations of total body water (TBW) as a function of age and weight as shown in Table 3-1 [11]. As a result of such differences in water contents, some studies have suggested that dielectric properties can be different, and this may lead to different levels of EM absorption due to the excessive EM exposure.

Table 3-1. Body water (kg) for young and elderly men, and elderly women from published equations; where TBW is total body water (Reproduce from [11]).

	Young Men (18-33 yrs)	**Elderly Men (67-89 yrs)**	**Elderly Women (67-89 yrs)**
TBW [Measured]	40.4 ± 1.4	34.8 ± 0.7	34.8 ± 0.7
TBW (Moore) [Age, Weight]	42.3 ± 0.8	37.0 ± 0.5	28.5 ±0.7
TBW (Pierson) [Age, Weight]	48.0 ± 1.4	41.4 ± 0.9	29.9± 1.1

It has been reported over the year's children absorbs higher levels of energy than adults when exposed to EMFs [12, 13]. Although frequency-dependent tissue properties were assigned to both adult and child in the references but factor of age-dependency wasn't anticipated. Accurate age-dependent dielectric properties are required in order to achieve more accurate energy deposition among different age groups when exposed to EMFs from different wireless sources.

3.3.1 Measured Tissue Properties

Human body organ growth and dielectric properties are comparable to animal's data. According to literature, data about the dielectric properties of biological tissues are gathered from mature animals. Few older studies stated the systematic changes in dielectric properties of brain tissues are due to the ageing effect [14, 15]. Some studies investigated the changes in dielectric properties of group of rat tissues including brain tissue as a function of age [9]. Several attempt were made in the past to demonstrate the similarities between human and rats on the basis of development of their organs [9, 16].

It is well-established that some tissues show variation in their dielectric properties as a function of age [2, 9, 17]. The water content level of the young age (child) tissue is higher than

adults [2, 9, 11, 18]. Miniature animal between 6 and 8 months of age, develops adult human sized organs and structure; as reported in reference [19]. In addition, the growth of pig organs such as heart and cardiovascular system, from birth to 4 months old age is analogous; in comparison with the growth of the same system in humans into the mid teen age. Similar comparisons were made to relate animal weight with human age as listed in **Error! Reference source not found.**.

It is therefore important to consider the effect of age-dependent properties (if any) on SAR assessment [12]. The importance of including age-relevant properties is also highlighted by the International Commission on Radiological Protection (ICRP) guidelines, which suggests the human organ mass changes as a function of age [20].

3.3.2 Age-dependent Human Dielectric Properties Extraction from Measured Data

Age-dependent dielectric properties of humans have been estimated based on the measured data for pigs of 10, 50 and 250 kg [2, 18]. The authors have supported their statement by running parallels between different developmental stages of animals and humans.

The 10, 50, and 250 kg animals were assumed to be their equivalent human 1-4 years old child, 11-13 years old teenage, and adult, respectively. Based on this approach, the measured dielectric data can be further utilised to predict the dielectric properties of a wider age groups.

To relate the animal weight with corresponding human age, pigs growth rate [10] is considered and theory from references [2, 18] was applied. So on the basis of growth rate, in terms of organ growth, comparisons made between human and animals weight as shown in **Error! Reference source not found.**. It was assumed that a 7 kg animal is equivalent to a 3-year old child. Similarly, 12.5 kg animal would be comparable to 5-6 years old humans.

Table 3-2. Human age predictions using animals weight [2, 10, 18].

Animal Weight (kg)	Human Ages (year)	Assumed age in this work
12.5	5-6	5.5
21.3	7-8	7.5
30.5	9-10	9.5
40.5	11-12	11.5
51.5	13-14	13.5
65	15-16	15.5
80	17-18	17.5
95	19-20	19.5
110	21-22	21.5

3.3.3 Novel Calculation Methods of Age-dependent Dielectric Properties

Three different novel empirical techniques were developed to predict age-dependent dielectric properties. These techniques were also validated accurately against available literature data. Dielectric properties were calculated in the frequency range of 0.4 – 10 GHz using the Cole-Cole parameters from [2]. In total 14 tissue properties were estimated as a function of age, and tissues were bone marrow, cornea, dura, fat, grey matter, intervertebral disc centre, intervertebral disc, long bone, skin, skull, spinal cord, tongue, and white matter.

Data about the different developmental stages of animal was reported in [2]. In order to correlate this data to a more precise equivalent human tissues, pig weights were used at three points to produce a curve with the best fit method. Animal brain growths were used from [10], to find equivalent developmental stage for humans. According to [2, 18], 4 weeks old pig could be a reasonable alternative to 3-years old child, in terms of organ growth and weight.

The curve fitting was applied in two distinguish ways in order to simplify the process of implementation i.e. single frequency age-dependent method and dispersive age-dependent method. The single frequency age-dependent theorem involves the basic idea of curve fitting technique at single frequency and in order to implement on wide frequency range huge number of equations to solve for both permittivity and conductivity. Whereas the dispersive age-dependent method is a simplified and generalised function of curve fitting which reduce the number of equations for wide frequency range (0.4 – 10 GHz). The details about both methods are explained in next sections.

3.3.3.1 Single Frequency Age-Dependent Method

In this method, curve fitting technique was applied on three points representing dielectric properties of 10 - 250 kg animal. To test the proposed method, a single frequency (1 GHz) has been chosen as an example, to generate two equations for permittivity and conductivity, on the basis of best fit method as shown in Figure 3-4 and Figure 3-5.

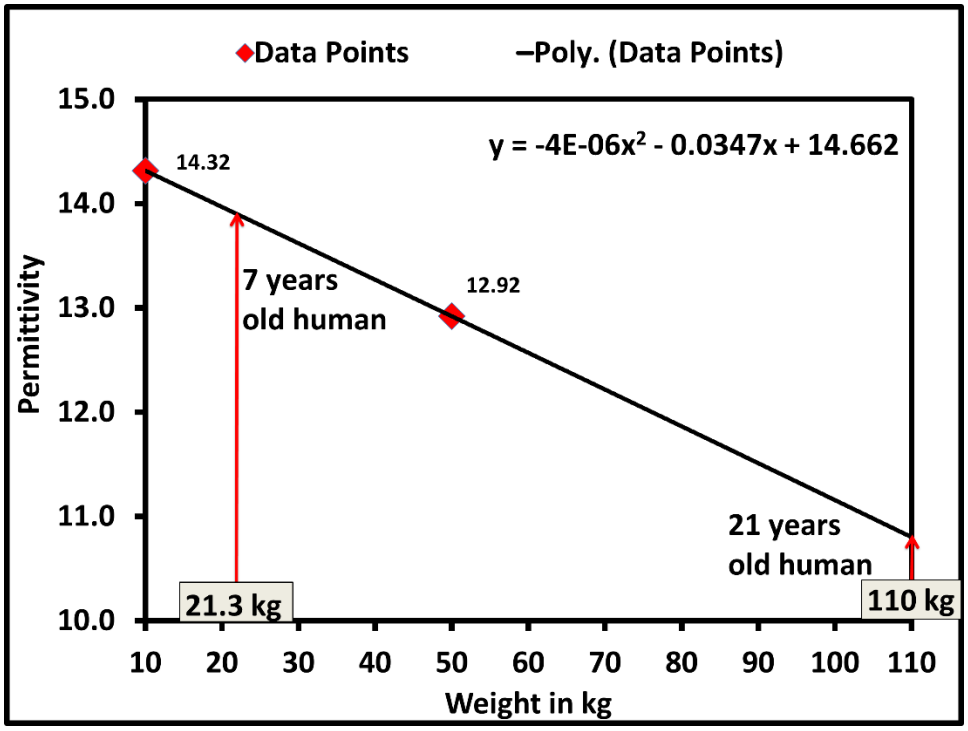

Figure 3-4. Permittivity of Fat at **1 GHz**.

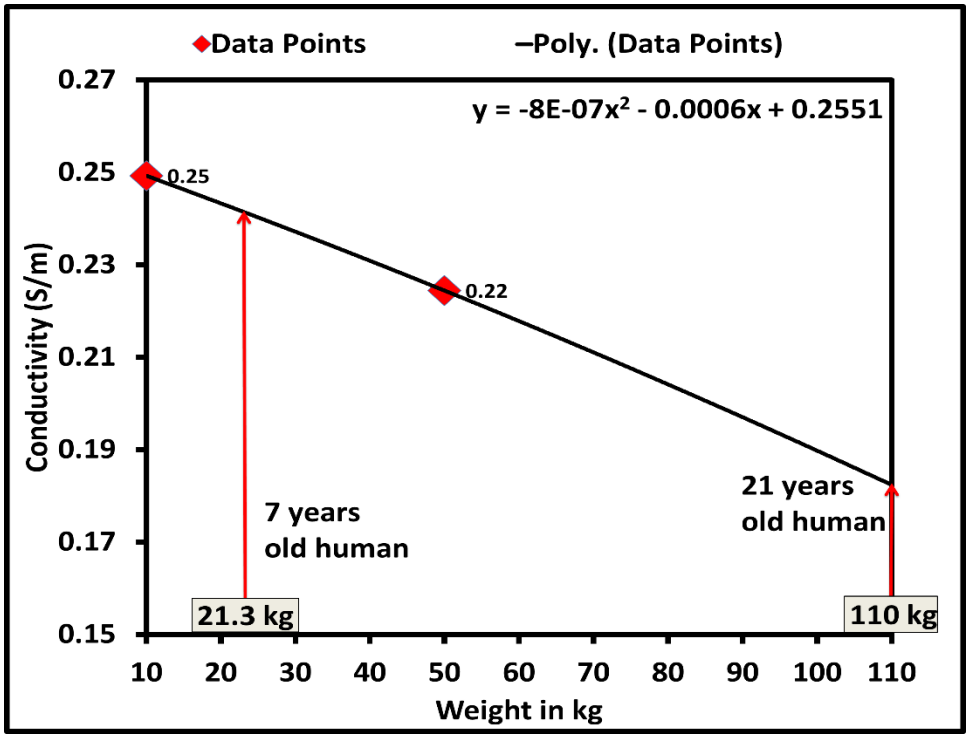

Figure 3-5. Conductivity of Fat at **1 GHz**.

Permittivity and conductivity of grey matter at 1 GHz can be obtained through the following equations:

$$y = -4 \times 10^{-6}x^2 - 0.0347x + 14.662 \qquad \text{(Equation 3.1)}$$

$$y = -8 \times 10^{-7}x^2 - 0.0006x + 0.2551 \qquad \text{(Equation 3.2)}$$

Where y is the permittivity at 1 GHz and x is weight of the pig. The weight of each pig corresponds to an equivalent human age. The above equation 3.1 yield values of 14.23 and 10.80 for permittivity of fat at 1 GHz relating to a 12.5 (5.5-years old human) and 110 kg pig (21.5-years old human), respectively. The difference in the permittivity values of fat tissue among the 5.5- and 21.5-years old human is approx. 24 %.

The conductivity values resultant from equation 3.2 are 0.25 and 0.18 Sm^{-1} of fat at 1 GHz relating to a 21.3 (5.5-years old human) and 110 kg pig (21.5-years old human), correspondingly. The difference in the permittivity values of fat tissue among the 5.5- and 21.5-years old human is approx. 28 %.

Curve fitting technique was further applied to the available animal data in order to generate complex mathematical equations for each tissue type and then human age equivalent animal weight applied to produce the dielectric properties of desire ages.

The current method is applicable to single frequency only. But in order to calculate tissue properties at wide frequency range, huge number of equations needs to be produce for both permittivity and conductivity values. Therefore, alternative method was introduced which reduces the complexity of this method. The simplified method, known as dispersive age-dependent method, provides the generalised equation for all tissues except bone marrow. The details about new method is explained in next section.

3.3.3.2 Dispersive Age-Dependent Method

The dielectric behaviour of both permittivity and conductivity of most tissues of animal can be describe with same empirical formula. The measured data about the bone marrow in [2] is based on 30 % and 50 % bone marrow. It is stated that bone marrow was measured at two distances from the end of the bone and the distribution of bone marrow type changes as a function of animal age. Therefore, its behaviours can't be described with same empirical equation as for other tissues.

It was noted that the permittivity value decreases as pig weight increases. On the contrary, conductivity follows the opposite trend. The generalised empirical formula for AFD dielectric properties defined as given below (equation 3.3), which can be used to verify the permittivity and conductivity of tissues within 0.4 to 10 GHz frequency range.

$$Y = A - Bx + C \qquad \text{(Equation 3.3)}$$

The dielectric properties of tissues can be calculated by putting the parameters from Table 3-3 in above equation. The parameter '*x*' is the weight of pig equivalent to human age. The table also include three set of data for a particular tissue which belongs from different frequencies.

Table 3-3. Parameters for age-dependent generalised expression (ID: Intervertebral Disc, IDC: Intervertebral Disc Centre).

Tissue	Frequency (GHz)	Permittivity			Conductivity		
		A	B	C	A	B	C
Cornea	0.4	$0.3x^2 \times 10^{-3}$	94.1×10^{-3}	57.61	$5 \times 10^{-6} x^2$	1.3×10^{-3}	0.95
	5	$0.3x^2 \times 10^{-3}$	98.1×10^{-3}	49.46	$2 \times 10^{-5} x^2$	7.2×10^{-3}	4.52
	10	$0.3x^2 \times 10^{-3}$	84.2×10^{-3}	41.88	$9 \times 10^{-5} x^2$	23.7×10^{-3}	10.65
Dura	0.4	$0.8x^2 \times 10^{-3}$	0.13	57.72	$4 \times 10^{-6} x^2$	2.3×10^{-3}	1.02
	5	$0.3x^2 \times 10^{-3}$	0.13	49.41	$2 \times 10^{-5} x^2$	6.2×10^{-3}	4.34
	10	$0.3x^2 \times 10^{-3}$	0.12	42.56	$5 \times 10^{-5} x^2$	17×10^{-3}	9.90
Fat	0.4	$-10^{-5} x^2$	33.9×10^{-3}	14.88	$-6 \times 10^{-7} x^2$	0.5×10^{-3}	0.21
	5	$4 \times 10^{-6} x^2$	31.1×10^{-3}	12.87	$3 \times 10^{-6} x^2$	4.3×10^{-3}	1.15
	10	$-10^{-5} x^2$	20.7×10^{-3}	10.68	$10^{-5} x^2$	11.9×10^{-3}	2.74
Grey Matter	0.4	$6 \times 10^{-5} x^2$	23×10^{-3}	53.61	$-3 \times 10^{-6} x^2$	-0.9×10^{-3}	0.82
	5	$6 \times 10^{-5} x^2$	20×10^{-3}	45.56	$4 \times 10^{-6} x^2$	0.6×10^{-3}	3.57
	10	$4 \times 10^{-5} x^2$	17×10^{-3}	40.10	$2 \times 10^{-6} x^2$	3.2×10^{-3}	7.93
ID	0.4	$0.8x^2 \times 10^{-3}$	0.25	62.15	$4 \times 10^{-5} x^2$	12.1×10^{-3}	1.39
	5	$0.7x^2 \times 10^{-3}$	0.23	51.92	$6 \times 10^{-5} x^2$	19.4×10^{-3}	5.10
	10	$0.6x^2 \times 10^{-3}$	0.22	44.28	$0.1x^2 \times 10^{-3}$	34.8×10^{-3}	11
IDC	0.4	$-0.2x^2 \times 10^{-3}$	26.5×10^{-3}	65.52	$9 \times 10^{-6} x^2$	2.4×10^{-3}	1.67
	5	$-0.3x^2 \times 10^{-3}$	52.3×10^{-3}	57.77	$-2 \times 10^{-5} x^2$	-3.2×10^{-3}	5.24
	10	$-0.3x^2 \times 10^{-3}$	36.9×10^{-3}	50.52	$0.1x^2 \times 10^{-3}$	-27.9×10^{-3}	11.70
Long Bone	0.4	$0.7x^2 \times 10^{-3}$	0.24	29.73	$10^{-6} x^2$	4.3×10^{-3}	0.37
	5	$0.6x^2 \times 10^{-3}$	0.19	22.60	$6 \times 10^{-6} x^2$	18.6×10^{-3}	2.20
	10	$0.5x^2 \times 10^{-3}$	0.16	18.94	$0.1x^2 \times 10^{-3}$	39.7×10^{-3}	4.50
Skin	0.4	$-9 \times 10^{-6} x^2$	35.8×10^{-3}	47.54	$-2 \times 10^{-6} x^2$	0.2×10^{-3}	0.64
	5	$5 \times 10^{-6} x^2$	34.3×10^{-3}	38.82	$-2 \times 10^{-5} x^2$	-3.8×10^{-3}	3.34
	10	$5 \times 10^{-5} x^2$	47×10^{-3}	33.41	$-5 \times 10^{-5} x^2$	-10.9×10^{-3}	7.27
Skull	0.4	$0.4x^2 \times 10^{-3}$	0.19	44.61	$2 \times 10^{-6} x^2$	2.3×10^{-3}	0.62
	5	$0.3x^2 \times 10^{-3}$	0.17	35.96	$3 \times 10^{-5} x^2$	14.9×10^{-3}	3.34
	10	$0.3x^2 \times 10^{-3}$	0.14	30.40	$8 \times 10^{-5} x^2$	36.3×10^{-3}	7.25
Spinal Cord	0.4	$0.3x^2 \times 10^{-3}$	0.13	39.05	$3 \times 10^{-6} x^2$	1.5×10^{-3}	0.50
	5	$0.3x^2 \times 10^{-3}$	0.11	32.69	$2 \times 10^{-6} x^2$	8×10^{-3}	2.50
	10	$0.3x^2 \times 10^{-3}$	99.2×10^{-3}	28.73	$5 \times 10^{-6} x^2$	19.5×10^{-3}	5.51
Tongue	0.4	$9 \times 10^{-5} x^2$	18.7×10^{-3}	55.84	$3 \times 10^{-6} x^2$	0.7×10^{-3}	0.89
	5	$7 \times 10^{-5} x^2$	12.1×10^{-3}	46.36	$10^{-6} x^2$	2.9×10^{-3}	4.42
	10	$4 \times 10^{-5} x^2$	6.8×10^{-3}	38.91	$3 \times 10^{-6} x^2$	5.8×10^{-3}	9.98
White Matter	0.4	$0.5x^2 \times 10^{-3}$	0.17	42.95	$7 \times 10^{-6} x^2$	2.4×10^{-3}	0.57
	5	$0.5x^2 \times 10^{-3}$	0.16	36.03	$4 \times 10^{-5} x^2$	11.9×10^{-3}	2.86
	10	$0.4x^2 \times 10^{-3}$	0.14	31.47	$10^{-4} x^2$	30.8×10^{-3}	6.36

It's worth mentioning that available online sources data corresponds to what human age is still unknown. An attempt is made by comparing animal data from reference [2] with available online sources [3, 21] at 2450 MHz (frequency chosen as an example) as shown in Table 3-4. It can be clearly seen in weight column that the dielectric properties from online sources doesn't belongs from same age groups.

Table 3-4. Comparison between measured animal [2] permittivity and conductivity with Gabriel et.al data [3, 21] at **2450 MHz**, Where animal weight (10, 50 and 250 kg) corresponds to the properties of animal at specified weight.

Tissue	**IFAC and ITIS [3, 21]**		**Peyman animal data [2]**		
	ε'	**σ (Sm^{-1})**	**ε'**	**σ (Sm^{-1})**	**Weight (kg)**
Bone Marrow 30 %	5.30	0.10	5.61	0.11	250
Cornea	51.61	2.30	52.91	2.04	10
Dura	42.03	1.67	41.93	2.17	250
Fat	5.28	0.11	5.61	0.12	250
Grey Matter	48.91	1.81	48.39	1.77	50
Intervertebral Disc	39.70	1.66	42.84	2.06	250
Long Bone (Cortical)	11.38	0.39	13.03	0.46	250
Skin (Dry)	38.00	1.46	41.26	1.60	50
Skull (Cancellous)	18.5	0.81	17.2	0.64	250
Spinal Cord	30.15	1.09	32.35	0.80	50
Tongue	52.63	1.80	52.37	2.05	250
White Matter	36.17	1.22	37.59	1.31	10

To generate tissue properties for a wide frequency range, three data set needs to be calculate at particular age in the first step. Then, resultant three data points of permittivity and conductivity from equation 3.6 can be further fitted or joined separately to generate the dielectric properties at any frequency point as shown in Figure 3-6. The error associated with this method as compared to single frequency age-dependent method is approx. 1 % and 10 % for permittivity and conductivity respectively.

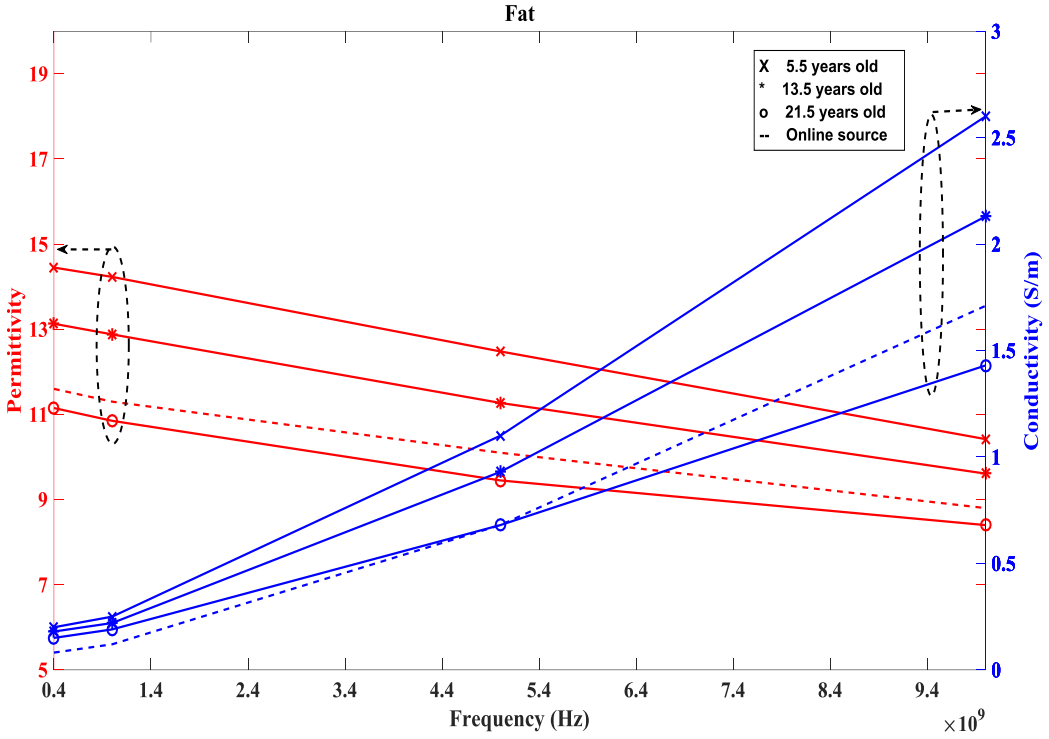

Figure 3-6. Comparison between age-dependent properties of fat tissue with online sources [3, 21], Online sources dielectric properties well match with 250 kg pig when comparing with [2] as shown in Table 3-4 and also confirms by this method.

The dielectric properties of fat have been calculated, as an example, at 3 different age groups (5.5, 13.5 and 21.5-years) over wide frequency range (0.4 – 10 GHz). In the Figure 3-6, permittivity values are represented in red colour and conductivity values are presented in blue colour. The comparison is made between the data from proposed method (dispersive age-dependent method) and available online sources [3, 21].The dielectric properties available on online sources was calculated from animals and human [22] and the factor of age dependences in measuring dielectric properties wasn't considered.

In Figure 3-6, 21.5-years old child dielectric properties (permittivity and conductivity) of fat tissue is very close to the online sources data which is in line with what Table 3-4 is predicting about the equivalence of fat tissue properties with 250 kg pig. In other words, fat tissue properties in online sources belongs from adult.

This novel age-dependent method also indicates that there is difference in dielectric properties among the different ages (see Figure 3-6). Fat tissues properties indicates that at 1 GHz for example the permittivity value of 5.5-years old child is approx. 24 % higher than 21.5-years old human. Similarly, the conductivity is also approx. 28 % higher as compared to 21.5-

years human. Similar comparison has been made among different ages with different tissues types and also compared with literature data (online sources) which are presented in Appendix A.

It has been noticed that age-dependent tongue tissue properties are not in line with Table 3-4 predictions. According to this study, 5.5-years old (equivalent to 12.5 kg pig) child data is closest to the available online source data whereas above table indicates that 250 kg pig is closest. The reason of such differences is unknown.

The percentage error has been calculated between single frequency and dispersive age-dependent methods in order to find the accuracy among the two methods. The error associated with permittivity and conductivity is well under one and ten percent respectively as mentioned before. It's worth mentioning that a very good agreement achieved between two methods.

Furthermore, Cole-Cole model have been applied in order to generate relaxation parameters which are AFD. The details about the implementation of Cole-Cole model are explained in next section.

3.3.2.3 Implementation of Cole-Cole Model on Age-Dependent Properties

According to the general relaxation theory, polar molecules in materials rearrange under the influence of applied E-field and contributing to the polarisation. This phenomenon is known as dielectric relaxation [23]. It is well established that dielectric relaxation process is always frequency-dependent. In accordance with frequency dependence, dielectric properties of a material are characterised by relaxation time constants.

The dielectric spectrum of biological tissues is composed of number of relaxation parameters. These parameters can be employed in well-known mathematically model known as Cole-Cole model or Cole-Cole expression [24] as given in equation 3.4.

$$\hat{\varepsilon}(\omega) = \varepsilon_{\infty} + \frac{\varepsilon_s - \varepsilon_{\infty}}{1 + (j\omega\tau)^{(1-\alpha)}} + \frac{\sigma_i}{j\omega\varepsilon_0} \qquad \text{(Equation 3.4)}$$

Where $\hat{\varepsilon}$ is the complex relative permittivity, τ_{relax} is the relaxation time, ε_s is static dielectric constant, σ_i is the ionic conductivity, $0 \leq \alpha \leq 1$ is an adjustable parameter and

indicating relaxation time distribution, and the Cole-Cole parameters have their usual significance.

Modelling the dielectric properties of tissues using equation 3.4 enables the incorporation in numerical assessments of human exposure to EMFs. In literature, the measured data about an animal was produced with the help of Cole-Cole expression [2]. However, relaxation parameters for AFD dielectric properties is also calculated using this method (Cole-Cole).

In equation 3.4 all parameters were fitted except for the ε_∞ values. The value chosen for ε_∞ was 3 which is based on assumption similar to that reported in reference [2]. The Cole-Cole model parameters of 14 tissue types for 5 to 22 years old human is represented in Table 3-5. It's worth mentioning that all the parameters values including τ_{relax}, α, ε_s and σ_i are very close as compared to reference [2].

Table 3-5. Cole-Cole parameters for the dielectric properties of human tissues as function of age.

Tissue/age	ε_s	τ_{relax} (ps)	σ_i (Sm^{-1})	α
Bone Marrow 30 %				
5.5 years	35.66	8.42	0.53	0.28
13.5 years	15.06	10.72	0.14	0.24
21.5 years	9.41	11.50	0.07	0.15
Bone Marrow 50%				
5.5 years	38.17	8.34	0.54	0.27
13.5 years	18.72	9.80	0.18	0.25
21.5 years	12.64	10.30	0.1	0.15
Cornea				
5.5 years	57.43	7.86	0.89	0.22
13.5 years	54.62	7.91	0.84	0.24
21.5 years	51.64	8.18	0.77	0.20
Dura				
5.5 years	57.43	7.86	0.89	0.22
13.5 years	54.62	7.91	0.84	0.24
21.5 years	51.64	8.18	0.77	0.20
Fat				
5.5 years	14.59	10.50	0.19	0.15
13.5 years	13.30	10.00	0.17	0.19
21.5 years	11.24	10.20	0.14	0.14
Grey Matter				
5.5 years	55.12	6.23	0.77	0.34
13.5 years	54.16	6.20	0.8	0.34
21.5 years	52.63	6.83	0.86	0.32
Intervertebral Disc				

5.5 years	60.78	7.81	1.17	0.28
13.5 years	52.99	9.18	0.71	0.26
21.5 years	46.28	10.80	0.0001	0.27
Intervertebral Disc Centre				
5.5 years	66.66	6.20	1.59	0.21
13.5 years	66.92	6.62	1.51	0.16
21.5 years	66.82	6.50	1.36	0.20
Long Bone				
5.5 years	28.79	14.00	0.27	0.38
13.5 years	20.97	18.50	0.11	0.38
21.5 years	12.91	18.50	0.08	0.36
Skin				
5.5 years	48.94	7.80	0.58	0.34
13.5 years	47.20	8.84	0.57	0.30
21.5 years	44.75	9.50	0.57	0.26
Skull				
5.5 years	43.94	8.84	0.53	0.33
13.5 years	37.37	9.37	0.45	0.35
21.5 years	29.39	10.50	0.33	0.33
Spinal Cord				
5.5 years	39.02	6.21	0.44	0.37
13.5 years	34.9	6.54	0.38	0.38
21.5 years	29.73	7.00	0.31	0.33
Tongue				
5.5 years	56.94	8.35	0.82	0.26
13.5 years	56.17	8.22	0.79	0.26
21.5 years	54.77	8.71	0.76	0.22
White Matter				
5.5 years	42.27	6.00	0.49	0.35
13.5 years	36.99	7.00	0.4	0.38
21.5 years	31.22	7.50	0.27	0.36

The parameters listed in above table are based on pure empirical equation (3.4). This study is not intended to identify the underlying mechanistic mechanism. Moreover, the data for each tissue type was fitted separately at each age. The parameters listed in above table, helps to calculate dielectric properties at any frequency (within 0.4 – 10 GHz) and age (5 – 22 years) without solving huge number of equations.

The relaxation parameters of bone marrow (as an example) are plotted in Figure 3-7 and values are fitted in order to show the trend with respect to the age of human. The static permittivity and ionic conductivity have been found main contributors in resultant dielectric properties while fitting the values in Cole-Cole expression.

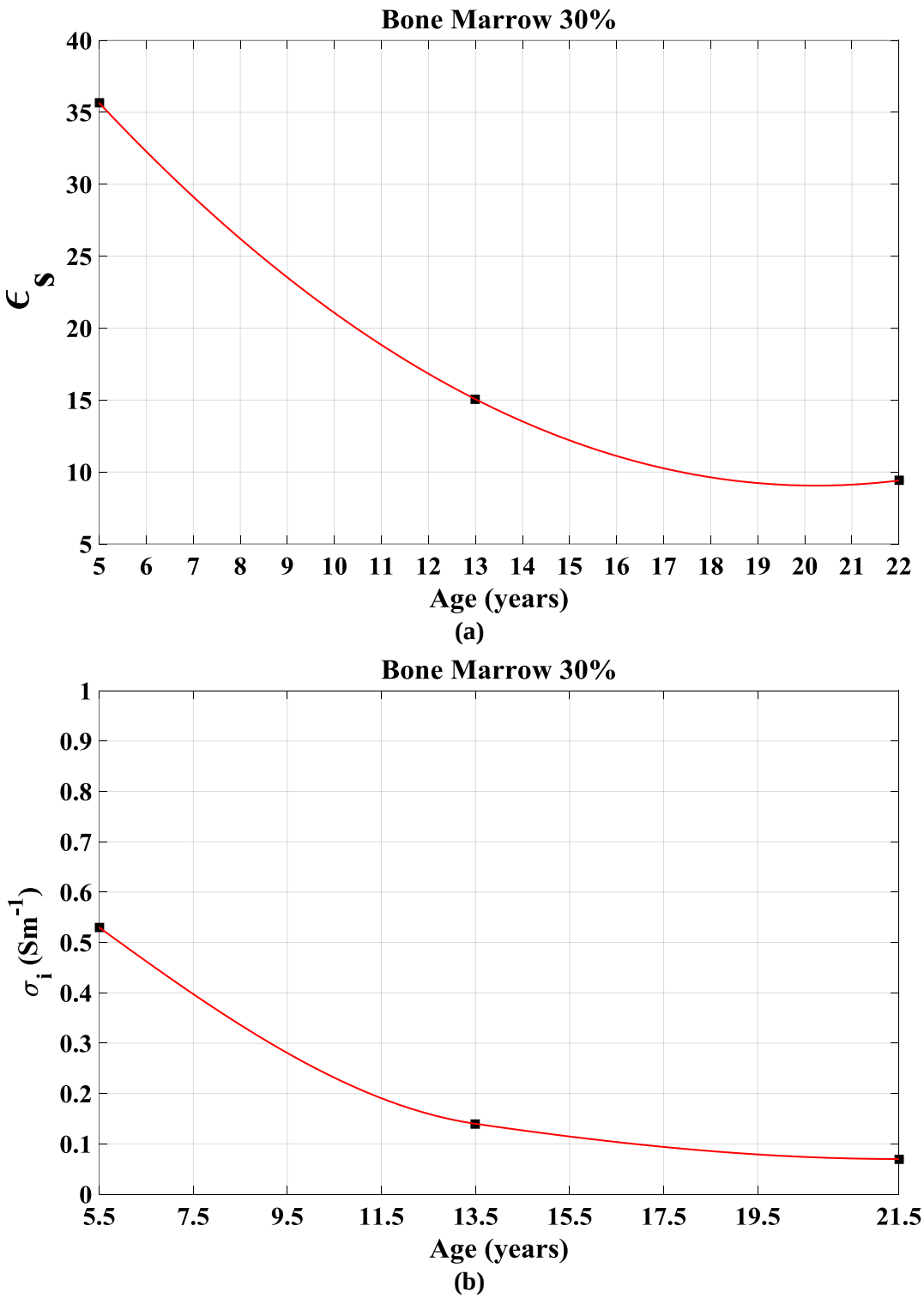

Figure 3-7. Age- dependent fitted values for relaxation parameters of Cole-Cole model of bone marrow 30 % tissue; (a) Static permittivity; (b) Ionic Conductivity

3.3.3.4 Accuracy among the Age-dependent Methods

Dielectric properties of biological tissues play a vital role in SAR assessment. These new age-dependent techniques allow to increase the accuracy of SAR assessment when humans of various age groups exposed to EMFs. The percentage error has been calculated based on values generated by single frequency and dispersive age-dependent methods. The single frequency method produces dielectric values at specific frequency point whereas the dispersive method generates over the whole frequency band (0.4 – 10 GHz). The values resultant from both methods compared at specific frequency and age. The error associated with dispersive age-dependent method is well under 1 % and 10% for both permittivity and conductivity respectively. The single frequency age-dependent method is more accurate than the dispersive age-dependent method and also from Cole-Cole model.

There is no consistent variation in dielectric properties w.r.t. age and frequency. The variation in dielectric properties among the different ages for example between 5.5- and 7.5-years old child is within 2–6 % and similar variation noticed when compare different age groups. The highest variation observed in tissue bone marrow 30 % was approx. 73 % in permittivity and 85 % in conductivity when compared 5.5-years old child with 21.5-years old human respectively. Some tissues dielectric properties increases with frequency and some shows the opposite trend. The uncertainty in tissue dielectric properties trend emphasises to consider the AFD properties in order to improve the accuracy in SAR assessment.

3.4 Numerical Validation

This section focuses on the validity and the accuracy of the methods and the numerical tools used to compute the EM propagation and the absorptions characteristics within the body. Experimental validation of the FDTD algorithm has been conducted by a number of researchers [26–35]. In previously mentioned references, authors have computed the whole body average specific energy absorption rate (SAR) distribution in a variety of models including children and adults after being exposed to wide range of frequencies from a plane wave source.

Different scenarios of plane wave exposure have been considered in [26, 27, 31, 33]. Plane wave exposure scenarios include model standing in free space (suspended) or on ground plane. In reference [33] analysis has been made on SAR distribution inside human models by changing the posture of the model when exposed to EM waves. In reference [27], SAR

assessment has been carried out on a sitting voxel model when exposed to variable frequencies using Wi-Fi devices. Plane wave exposures of voxel model and irradiation from antennas in the near field were studied for variety of exposure conditions. Similarly another study [34] estimates the SAR exposure to EMFs from the antennas for wireless devices (Wi-Fi and Bluetooth) using FDTD methods. These studies have demonstrated a good agreement between SAR distributions identified numerically and experimentally.

In this study, further validations have been conducted by comparing the results obtained using FIT algorithm against analytical and other commercial EM computation packages using some simple benchmarks [26–30, 35]. A description of the main validation procedure is presented in this section.

3.4.1 Comparison with an Analytical Benchmark

A theoretical calculation model has been used as a benchmark for validating the FIT software. This theoretical model is used for expressing the EMFs and SAR induced inside a lossy dielectric sphere by an incident plane-wave. The analytical solutions was based on exposing single layered, muscle-equivalent model spheres, with radii of 3 cm and 15 cm, to the plane wave of 1 GHz radiation [36]. Similar dielectric properties of muscle tissue were used in analytical and computational models [37]. The theoretically-predicted and computed SAR patterns are computed based on the patterns along the *x*, *y*, and *z* directions.

Plots of the normalised analytically-assessed SAR patterns along the major axes of a muscle-equivalent dielectric sphere (radius = 3 cm) is shown in Figure 3-8. The black solid lines shows the analytically solved SAR pattern along the three major axes X, Y, and Z [36]. Calculations are based on the plane waves of 1 GHz, with energy flux density of 1 $mWcm^{-2}$ and the WBSAR is 0.235 Wkg^{-1}. For the convenience of presentation, the distributed SAR values are normalised to the maximum SAR given for each figure. It was found that strong standing wave patterns (hot spots) exist in the sphere.

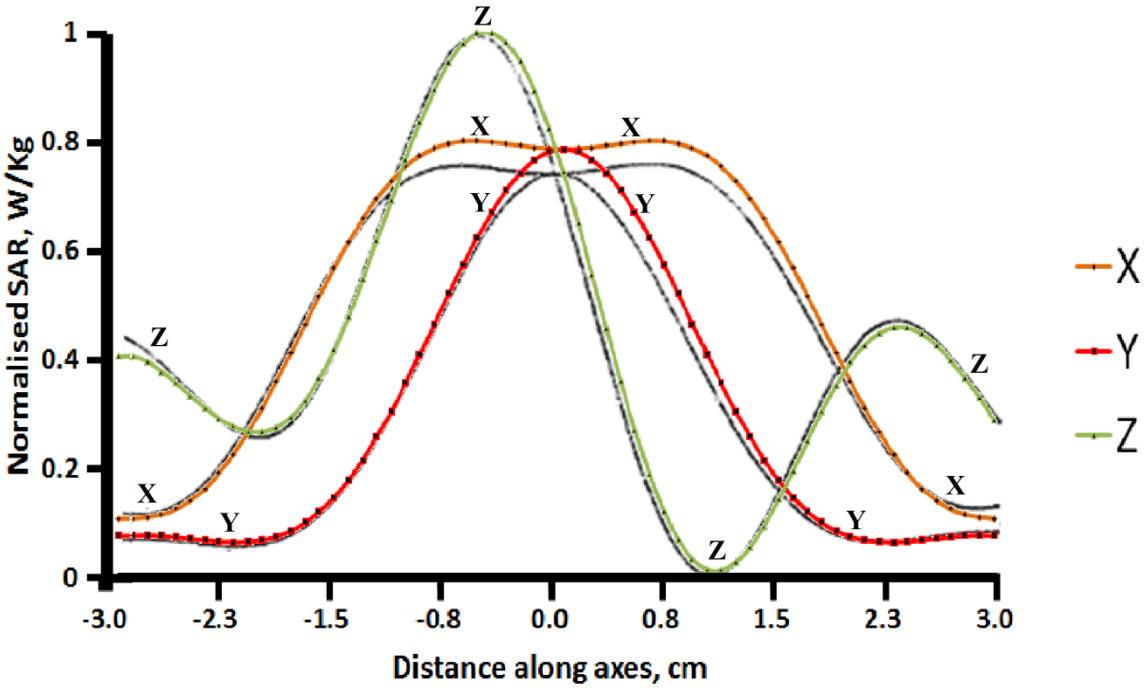

Figure 3-8. Plots of the normalised FIT-computed SAR patterns along the major axes of a muscle-equivalent dielectric sphere (Radius = 3 cm). Calculations are based on a plane wave source of **1 GHz**, with energy flux density of 1 $mWcm^{-2}$. WBSAR = 0.241 Wkg^{-1}.

Similarly, the computed SAR patterns inside the 3cm sphere using the CST MWS are also presented with coloured lines in Figure 3-8. The SAR values have also been normalised to the maximum value. The dense mesh has used for this studies, where total mesh cells was 1.7 million with 15 lines per wavelength (inside the dielectric) which satisfies the step size and stability conditions for this frequency. The sphere models have been separated from the PML layers by 10 cells representing free space in order to ensure better absorbing boundary condition (ABC) performance. One of the disadvantages of fixing the number of surrounding free-space cells is the variability in separation distance between the tested object and the ABC, specifically when varying the size of the cell.

Based on the figure, an excellent correlation has been observed among the overall SAR pattern which have been plotted from the analytical predictions and FIT (CST MWS) computations. It is noticed that the SAR values decreasing along the X, Y, and Z coordinates. However, these two graphs/results are in good comparison in order to validate this method. An excellent correlation has been observed among the overall estimated SAR, where error is found less than 3 %.

3.5 Chapter Summary

This chapter summarise, modelling of three different voxel models which were used to evaluate SAR due to exposure from wireless devices. Heterogeneous voxel models modelled using in-house modelling software package to handle voxels. Age- and frequency-dependent dielectric properties of 14 tissues have been calculated based on data fitting. The curve fitting techniques has been used and applied in three different methods on the available measured data of animals to predict the best fit dielectric properties for humans of various age groups. The Cole-Cole relaxation parameters has been also generated for all tissue type and very good agreement achieved with relaxation parameters of measured data.

Novel age-dependent methods are only applicable to extrapolate data for 5.5- to 21.5-years old humans within frequency range of 0.4 to 20 GHz. The age and frequency limitations are solely due to the lack of availability of animal growth data and measured data at higher frequencies correspondingly. The newly calculated data was then used to assess the induced SAR in a female child model [8] when exposed to a plane waves and smart meter devices in chapter 4. Moreover, the numerical tool (which is based on finite integration technique (FIT) method) was also validated by comparing the FIT calculations over a homogenous muscle-equivalent sphere with analytical Mie series solution for homogenous sphere.

References

[1] CST Microwave Studio - 3D EM simulation software 2016 version, [Online]. Available: https://www.cst.com/Products/CSTMWS (Accessed Jun 2016).

[2] A. Peyman and C. Gabriel, "Cole–Cole parameters for the dielectric properties of porcine tissues as a function of age at microwave frequencies," Phys. Med. Biol., vol. 55, pp. 413–419, 2010.

[3] IFAC, "Dielectric Properties of Body Tissues", [Online]. Available: http://niremf.ifac.cnr.it/tissprop/htmlclie/htmlclie.htm (Accessed Feb 2015).

[4] C. Gabriel, S. Gabriely, and E. Corthout, "The dielectric properties of biological tissues: I. Literature survey," Phys. Med. Biol., vol. 41, pp. 2231–2249, 1996.

[5] S. Gabriel, R. W. Lau, and C. Gabriel, "The dielectric properties of biological tissues: II. Measurements in the frequency range 10 Hz to 20 GHz," Phys. Med. Biol., vol. 41, pp. 2251–2269, 1996.

[6] S. Gabriel, R. W. Lau, and C. Gabriel, "The dielectric properties of biological tissues: III. Parametric models for the dielectric spectrum of tissues," Phys. Med. Biol., vol. 41, pp. 2271–2293, 1996.

[7] A. Peyman and C. Gabriel, "Dielectric properties of porcine glands, gonads and body fluids," Phys. Med. Biol., vol. 57, pp. 339–344, 2012.

[8] IT'IS, "High-Resolution Human Models for Simulations: Virtual Population," [Online]. Available: http://www.itis.ethz.ch/itis-for-health/virtual-population/human-models/ (Accessed Feb 2017).

[9] A. Peyman, A. A. Rezazadeh, and C. Gabriel, "Changes in the dielectric properties of rat tissue as a function of age at microwave frequencies," Phys. Med. Biol., vol. 46, pp. 1617–1629, 2001.

[10] The pig site, [Online]. Available: http://www.thepigsite.com/stockstds/17/growth-rate (Accessed Aug 2014).

[11] N.K. Fukagawa, L.G. Bandini, W.H. Dietz, and J.B. Young, "Effect of Age on Body Water and Resting Metabolic Rate," Journal of Gerontology: Medical Sciences, vol. 51, pp. 71–73 1996.

[12] J. F. Bakker, M. M. Paulides, A. Christ, N. Kuster, and G. C. V. Rhoon, "Assessment of induced SAR in children exposed to electromagnetic plane waves between 10 MHz and 5.6 GHz," Phys. Med. Biol., vol. 55, pp. 3115–3130, 2010.

[13] E. Piuzzi, P. Bernardi, M. Cavagnaro, S. Pisa, and J. C. Lin, " Analysis of Adult Child Exposure to uniform Plane Waves at Mobile Communication Systems Frequencies (900 MHz – 3 GHz)," IEEE Trans. on Electromagnetic Compatibility, vol. 53, pp. 38–47, 2011.

[14] M. Thurai, V. D. Goodridge, R. J. Sheppard, and E. H. Grant, "Variation with age of the dielectric properties of mouse brain cerebrum," Phys. Med. Biol., vol. 29, pp. 1133–1136, 1984.

[15] M. Thurai, M.C. Steel, R.J. Sheppard, and E.H. Grant, "Dielectric properties of developing rabbit brain at 37 degrees C," Bioelectromagnetics, vol. 6, pp 235–242, 1985.

[16] R. Quinn, "Comparing rat's to human's age: How old is my rat in people years?," Nutrition, vol. 21, pp. 775–777, 2005.

[17] A. Peyman, S. J. Holden, S. Watts, R. Perrott, and C. Gabriel, "Dielectric properties of porcine cerebrospinal tissues at microwave frequencies: in vivo, in vitro and systematic variation with age," Phys. Med. Biol., vol. 52, pp. 2229–2245, 2007.

[18] A. Peyman, C. Gabriel, E. H. Grant, G. Vermeeren, and L. Martens, "Variation of the dielectric properties of tissues with age: the effect on the values of SAR in children when exposed to walkie–talkie devices," Phys. Med. Biol, vol. 54, pp. 227–241, 2009.

[19] M. M. Swindle, A. Makin, A. J. Herron, F. J. Clubb, and K. S. Frazier, "Swine as Models in Biomedical Research and Toxicology Testing," Veterinary Pathology, vol. 49, pp. 344–356, 2012.

[20] J. Valentin, "Basic anatomical and physiological data for use in radiological protection: reference values: ICRP Publication 89," Annals of the ICRP, vol. 32, pp. 1–277, 2002.

[21] IT'IS Foundation Tissue Properties, [Online]. Available: http://www.itis.ethz.ch/virtual-population/tissue-properties/database/database-summary/ (Accessed Feb 2015).

[22] C. Gabriel, "Compilation of the dielectric properties of body tissues at RF and Microwave frequencies," Final Technical Report, 1996.

[23] W. Kuang and S. O. Nelson, "Low-frequency dieletric properties of biological tissues: A review with some insights," Trans. ASAE, vol. 41, pp. 173–184, 1998.

[24] A. Peyman, S. Holden, and C. Gabriel, "Dielectric Properties of Tissues at Microwave Frequencies," Technical Report, 2005.

[25] A. Hirata, K. Yanase, I. Laakso, K. H. Chan, O. Fujiwara, T. Nagaoka, et al., "Estimation of the whole-body averaged SAR of grounded human models for plane

wave exposure at respective resonance frequencies," Phys. Med. Biol., vol. 57, pp. 8427–8442, 2012.

[26] P. J. Dimbylow, "Fine resolution calculations of SAR in the human body for frequencies up to 3 GHz," Phys. Med. Biol., vol. 47, pp. 2835–2846, 2002.

[27] R. P. Findlay, and P. J. Dimbylow, "SAR in a child voxel phantom from exposure to wireless computer networks (Wi-Fi)," Phys. Med. Biol., vol. 55, pp. 405–411, 2010.

[28] J. F. Bakker, M. M. Paulides, A. Christ, N. Kuster, and G. C. v. Rhoon, "Assessment of induced SAR in children exposed to electromagnetic plane waves between 10 MHz and 5.6 GHz," Phys. Med. Biol., vol. 55, pp. 3115 – 3130, 2010.

[29] A. Christ, W. Kainz, E. G. Hahn, K. Honegger, M. Zefferer, E. Neufeld, et al., "The Virtual Family—development of surface-based anatomical models of two adults and two children for dosimetric simulations," Phys. Med. Biol., vol. 55, pp. 23–38, 2010.

[30] A. Hirata, O. Fujiwara, T. Nagaoka, and S. Watanabe, "Estimation of Whole-Body Average SAR in Human Models Due to Plane-Wave Exposure at Resonance Frequency," IEEE Trans. on Electromagnetic Compatibility, vol. 52, pp. 41–48, 2010.

[31] P. J. Dimbylow, "FDTD calculations of the whole-body averaged SAR in an anatomically realistic voxel model of the human body from 1 MHz to 1 GHz," Phys. Med. Biol., vol. 42, pp. 479–490, 1997.

[32] P. J. Dimbylow, and W. Bolch, "Whole-body-averaged SAR from 50 MHz to 4 GHz in the University of Florida child voxel phantoms," Phys. Med. Biol., vol. 52, pp. 6639–6649, 2007.

[33] R. P. Findlay, and P. J. Dimbylow, "Effects of posture on FDTD calculations of specific absorption rate in a voxel model of human body," Phys. Med. Biol., vol. 50, pp. 3825–3835, 2005.

[34] M. Martínez-Búrdalo, A. Martín, A. Sanchis, and R. Villar, "FDTD assessment of human exposure to electromagnetic fields from WiFi and bluetooth devices in some operating situations," BEMS, vol. 30, pp. 142–151, 2009.

[35] W. D. Hurt, J. M. Ziriax, and P. A. Mason, "Variability in EMF permittivity values: implications for SAR calculations," IEEE Trans. Biomed. Eng., vol. 47, pp. 396–401, 2000.

[36] H. S. HO, and A. W. Guy, "Development of Dosimetry For RF and Microwave Radiation-II Calculations of absorbed dose distribution in two sizes of muscle-equivalent spheres," Heal. Phys. J., vol. 29, pp. 317–324, 1974.

[37] H. P. Schwan, and G. M. Piersol, "The absorption of electromagnetic energy in body tissues," Amer. J. Phys. Med., vol. 33, pp. 371–404, 1954.

Chapter 4
Numerical and Practical Assessments of Communication Systems

4.1 Introduction

With the rapid move towards smart energy ecosystems, key components such as smart grids, smart homes (including smart appliances, gateways etc.) and smart meters (SMs) have relied on wireless technologies to maintain data communications. In the UK, the use of SMs for transmitting utility readings has attracted particular interest during the past few years. It is estimated that most household will have a SMs at home by 2020 [1]. SMs operate the home area network (HAN) mainly using a ZigBee standard [2], which is based on the IEEE-802.15.4 standard [3].

The IEEE-802.15.4 standard specifies two communication bands relevant to this study, 868 MHz in Europe and 2450 MHz worldwide. SMs lower band (868 MHz) frequency range partially lies under the Long Term Evolution (LTE) band GSM-850 [4]. SMs higher band (2450 MHz) operates within the Industrial Scientific and Medical (ISM) spectrum region.

The Department of Energy and Climate Change (DECC) has indicated that in-home display (IHD) devices are more likely to be placed near the communication hub (Comm-Hub) [5]. In general, it is expected that the distance between the Comm-Hub and IHD devices will be much less than 100 meters (m) in the vast majority of houses. There has been some concern

among the public about the installation of SMs in the home and exposure to the radio signals from the devices and thus World Health Organisation (WHO), announced the research agenda for RF fields [6].

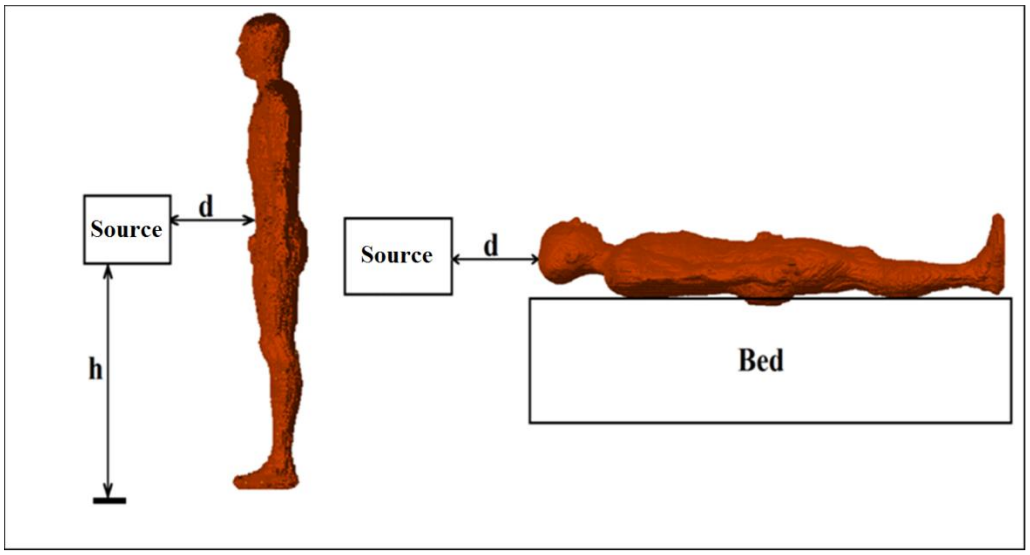

(a) **(b)**

Figure 4-1. Exposure scenarios where h = 1 m and d = 15 cm; (a) Human model is standing in front of source; (b) Human model is sleeping on bed.

The purpose of this study was to evaluate the EM absorption, due to SMs as shown in Figure 4-1, within numerical models representing a sample of the population: namely: a 7-years old female child [7, 8], a 23-years old female [9] and a 34-years old male [9]. Dielectric properties representing the various body organs were assigned with age- and frequency-dependent (AFD) values to ensure the consistency of the models with respect to their corresponding realistic targets. Furthermore, calculations were performed at a resolution of 2 mm and 1.4 mm for adults and child respectively at 868 MHz and 2450 MHz bands. The resulting induced averaged SAR, and the maximum SAR distributions have been compared with the exposure guidelines of the International Commission of Non-ionisation Radiation Protection (ICNIRP) [10].

4.2 Setup and Computational Methods

Time-domain algorithms were widely used in studies to calculate the EM power absorbed within human models [11–15]. The time-domain solution approach is capable of handling inhomogeneous, dispersive, and lossy dielectric mediums such as those found within the human body.

In this study, CST MWS uses the advanced FIT method which is equivalent to the FDTD method, but has some advantages in representing irregular structures. Both FDTD and FIT methods are inherently identical in the way they resolve Maxwell's equations in the differential and integral forms respectively. For geometries in which wave-object interaction has to be considered in the open regions the computational space has to be truncated by absorbing boundaries. PMLs absorbing boundaries have been used in order to minimise the unnecessary artificial reflections [14, 16–19].

Prior to the inclusion of the antenna in the exposure model, a set of validation simulations were completed using plane wave incident waves with vertical polarisation. Many studies have been conducted to calculate the plane wave exposure at various frequencies, as was discussed in recent studies [7, 11, 12, 14, 15, 20]. In this study calculations are performed for a plane wave with the standing human model suspended in air in one of the scenarios. The authors in one study [15] found slightly higher values for the isolated case as compared to the grounded case, where the plane wave was irradiating the isolated standing body from the front with the E-field component aligned vertically.

4.2.1 Cell Sizes and Stability Conditions

The FIT method follows the time evolution of a field interacting with body divided into voxels (grids). Selecting the largest cell size has been dictated by the minimum stability requirement, which is generally governed by a minimum of ten cells per wavelength within the highest dielectric region of the body [15, 16, 21].

The selection of cell sizes is also driven by the aim to provide satisfactory accommodation of the physical representation of the body and the computation efficiency. The minimum mesh cell requirement for female adult, male adult, and female child model was 28.84 million, 35.71 million, and 29.43 million mesh cells, respectively; based on the xyz dimensions of the models.

The maximum mesh cell size was limited to 4.13 mm and 1.49 mm at 868 MHz and 2450 MHz. In order to find cell size for models at these frequencies, tissue with the highest dielectric constant is used in the equation which is given below:

$$\lambda_b = \frac{c_0}{\frac{\sqrt{Highest\ dielectric\ value\ (Permittivity)}}{Frequency}} \qquad \text{(Equation 4.1)}$$

The above are worst-case requirements in small regions of the body where the permittivity is exceptionally high. It is worth noting that all of the numerical anatomical human models used in this study are represented with voxel dimensions equal or less than 2 mm. Further mesh refinements are then applied to reduce the computational cell sizes below these configurations to ensure accuracy and consistency with the numerical stability requirements as shown in Figure 4-2.

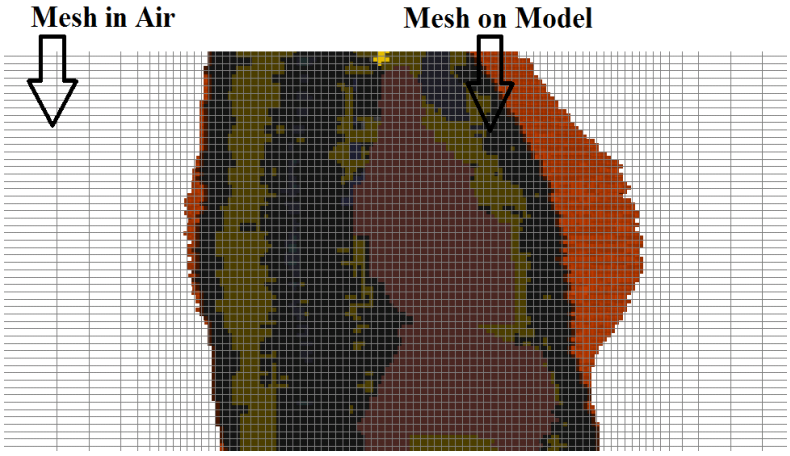

Figure 4-2. 240 million mesh generated by adopting the previously mentioned technique (FIT) in order to satisfying the stability condition.

4.3 Configuration of SM Antennas

In this section geometry of the antennas used in SMs is provided in detail. As mention before, SM operates in two different frequency bands 868 MHz in Europe and 2450 MHz in worldwide. Therefore, two antenna designed for this purpose. The 868 MHz antenna is based on meander line technique as shown in Figure 4-3. The size of the antenna is 60.20 mm (L) x 75 mm (W) x 0.40 mm (T). Both meander line parts of antenna was printed on FR4 substrate with thickness of 0.40 mm and permittivity of 4.4. This antenna parameters and dimensions are similar to antenna used in real SMs.

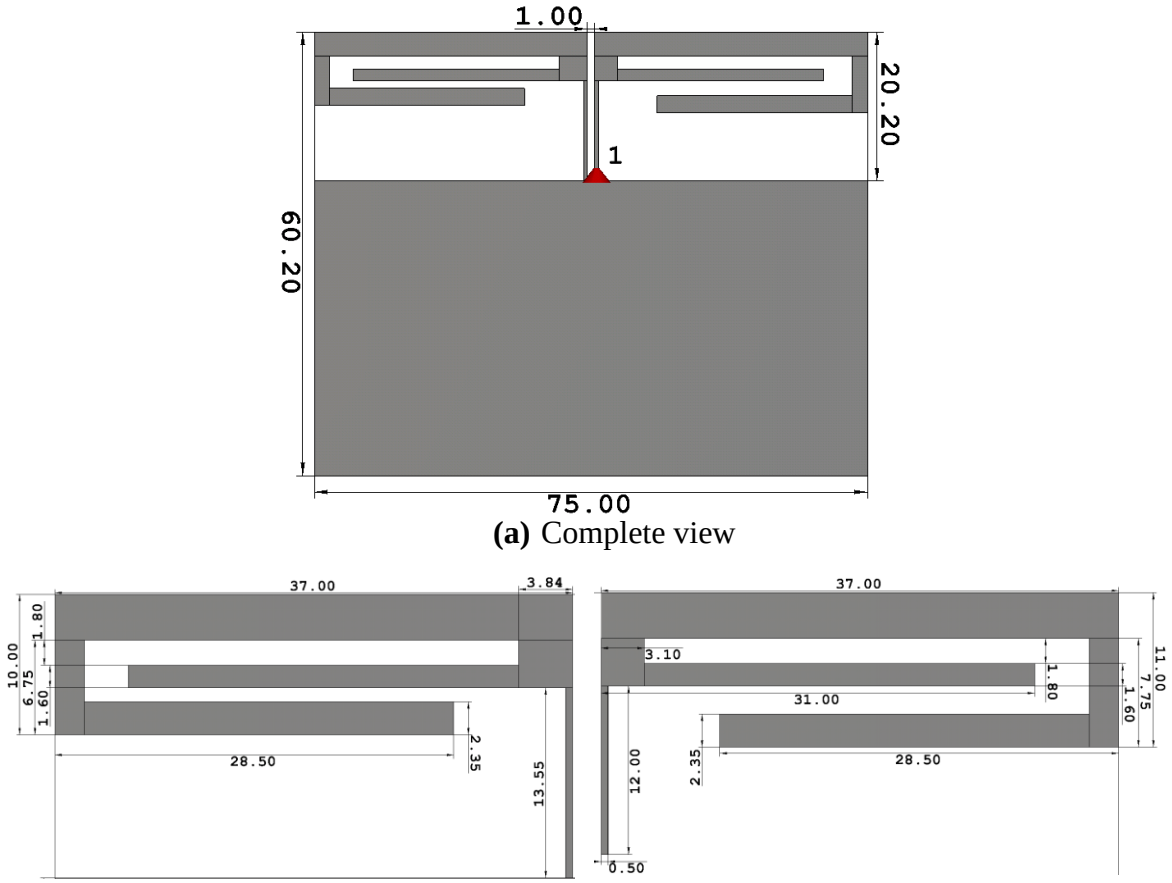

(a) Complete view

(b) Left top view **(c)** Right top view

Figure 4-3. Geometry of **868 MHz** antenna; All dimensions are in mm.

The S-parameters of 868 MHz antenna is given in Figure 4-4. The reflection coefficient (S11) of the antenna confirms that this antenna works on 868 MHz band and covers a frequency range between 846 to 884 MHz when return loss calculated below -6 dB. The radiation pattern of this antenna is presented in Figure 4-5. The far-field radiation pattern confirms that the 868 MHz antenna is omnidirectional. The total radiation efficiency and gain of the antenna is 97 % and 1.8 dB.

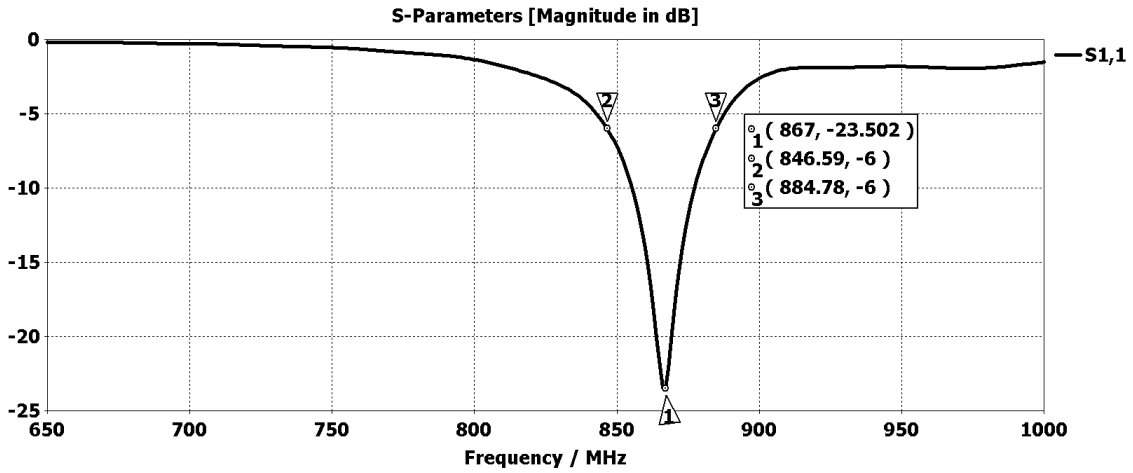

Figure 4-4. Computed S11 of **868 MHz** antenna.

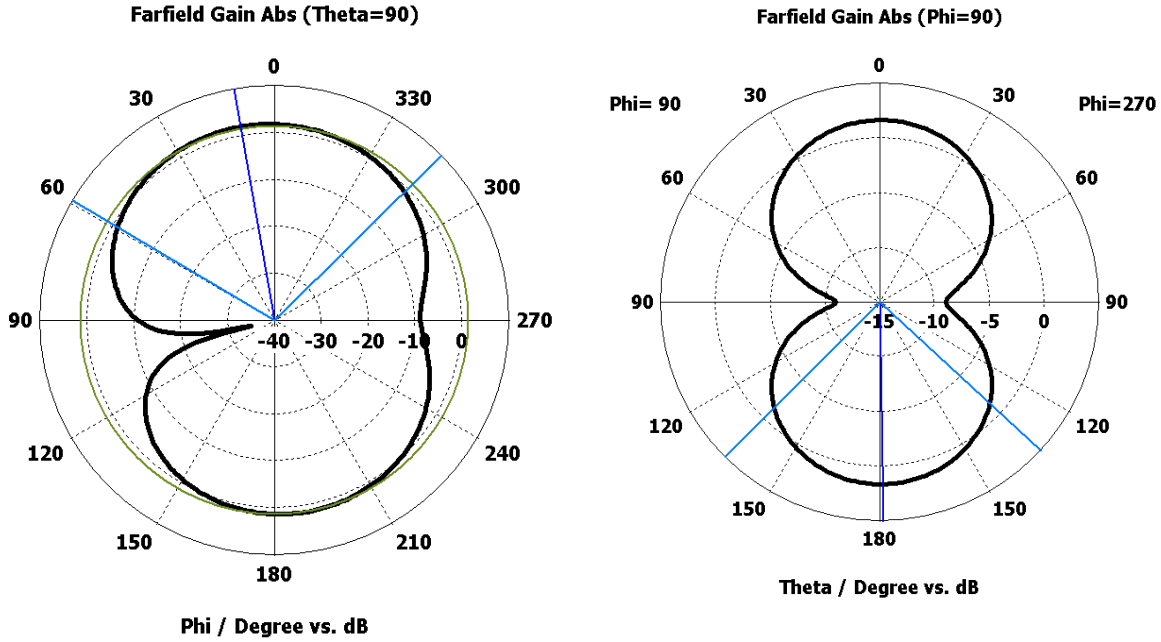

(a) At Theta is 90 (*z*-axis) **(b)** At Phi is 90 (*x*-axis)

Figure 4-5. Computed far-field radiation pattern of **868 MHz** antenna.

The 2450 MHz band antenna was designed with dimensions similar to antenna used in real SMs. The 2450 MHz antenna is designed based on PIFA antenna as shown in Figure 4-6. The size of the antenna is 99.0 mm (L) x 26 mm (W) x 0.40 mm (T). Both PIFA antenna similar part of antenna was printed on FR4 substrate with thickness of 0.40 mm and permittivity of 4.4.

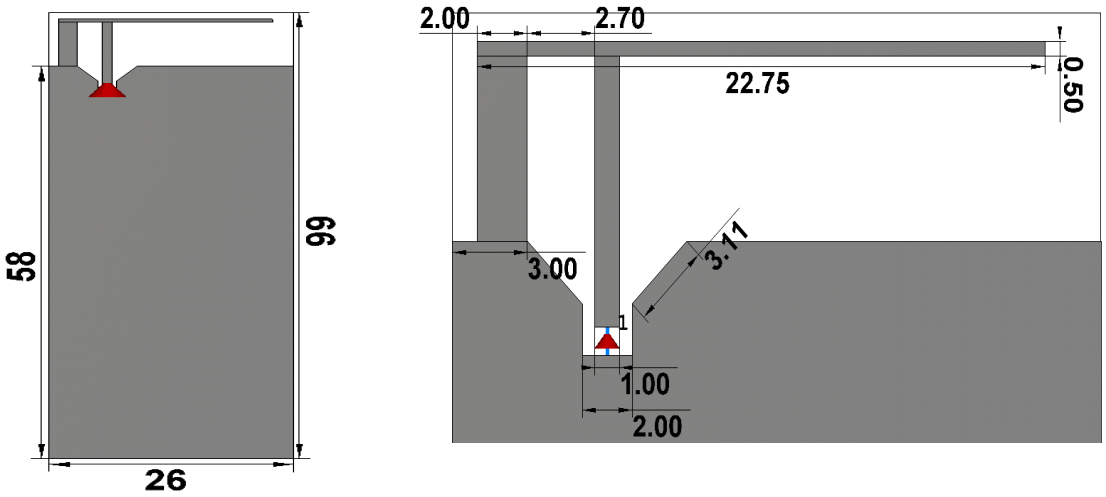

(a) Complete view **(b)** Close view

Figure 4-6. Geometry of **2450 MHz** antenna; All dimensions are in mm.

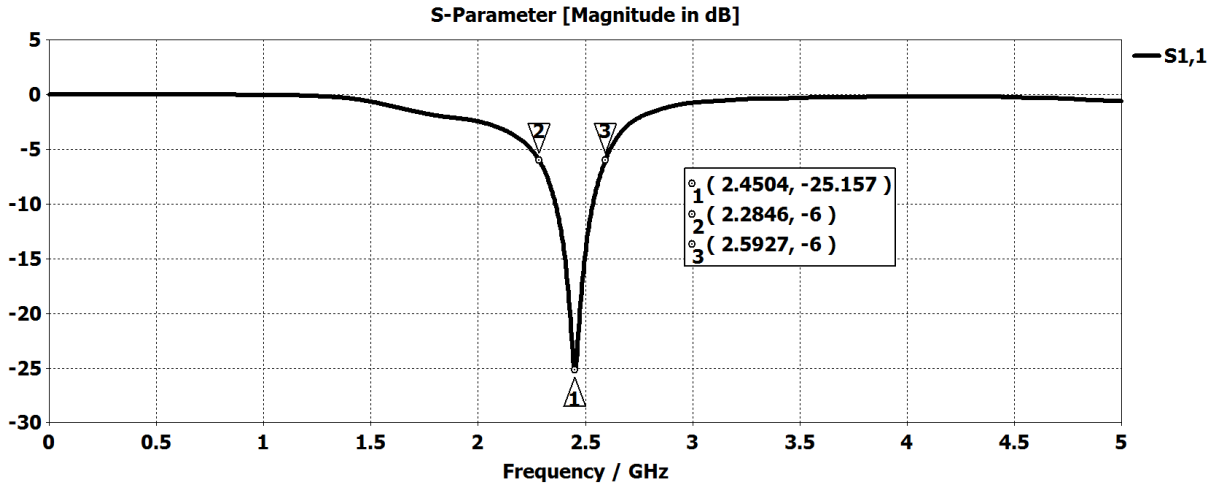

Figure 4-7. Computed S11 of **2450 MHz** antenna.

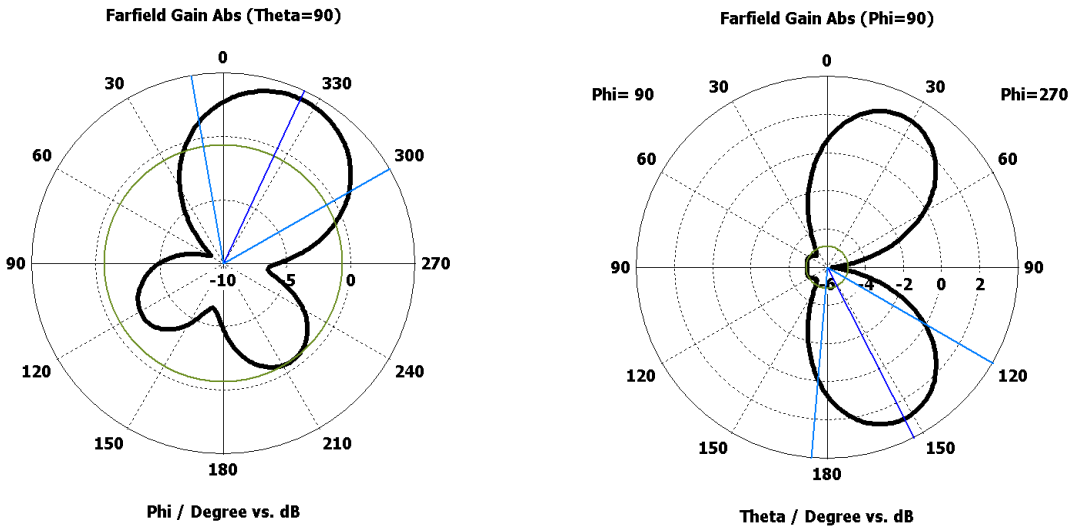

(a) At Theta is 90 (*z*-axis) (b) At Phi is 90 (*x*-axis)

Figure 4-8. Computed far-field radiation pattern of **868 MHz** antenna.

The S-parameters of 2450 MHz antenna is given in Figure 4-7. The S11 of the antenna confirms that this antenna works on 2450 MHz band and covers a frequency range between 2285 to 2593 MHz when return loss calculated below -6 dB. The radiation pattern of this antenna is presented in Figure 4-8. The far-field radiation pattern confirms that the 2450 MHz antenna is omnidirectional. The total radiation efficiency and gain of the antenna is 98 % and 4.28 dB.

4.4 Exposure Scenarios and SAR Calculations

The exposure of the models was analysed at two different frequencies, 868 MHz and 2450 MHz. The separation distances between the antennas and model was initially set to a typical value of 15 cm approx. while in the far-field, the models were exposed to a plane wave. Both standing and sleeping positions were considered for each model. In the standing position, the model was placed standing on a ground at a distance from the EM source (Figure 4-9 (a)).In the sleeping position, the model was placed at a certain height from the ground, in a horizontal position to mimic the sleeping position on a bed (Figure 4-9 (b)). In all cases, all relevant SAR calculations were computed and the results have been summarised.

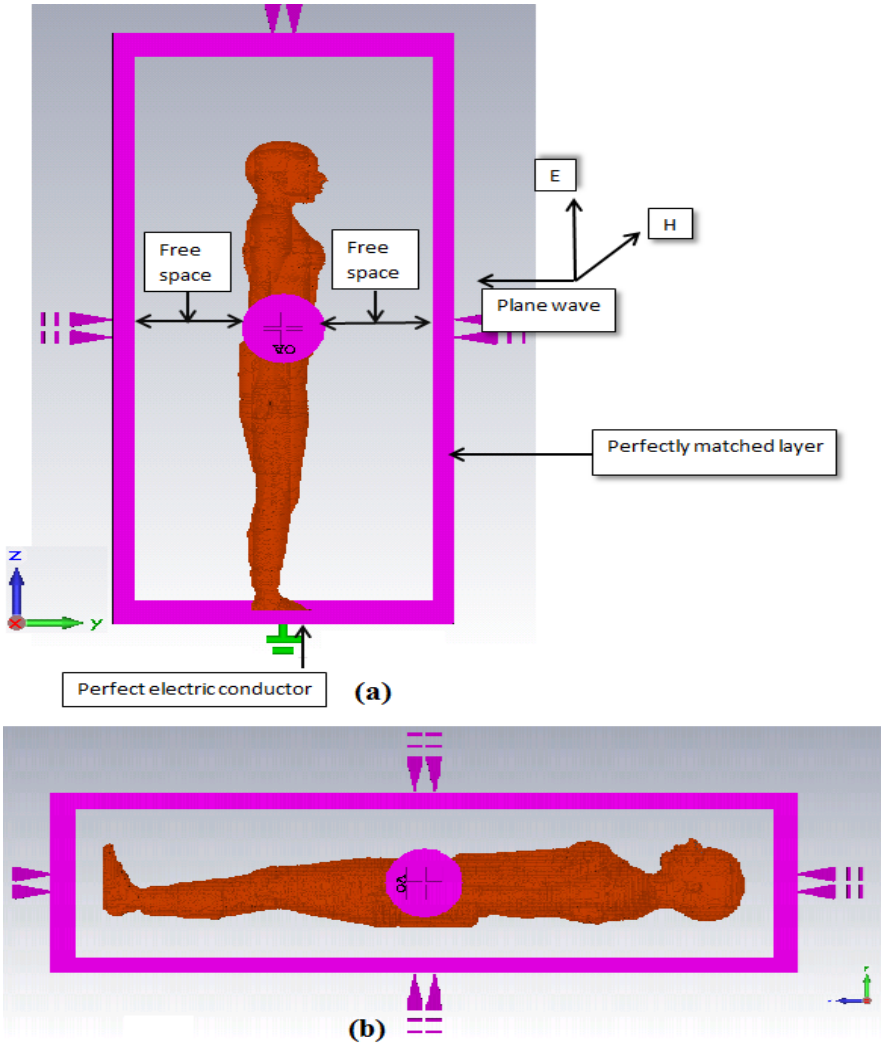

Figure 4-9. Plane wave exposure scenario of models; (a) When standing on ground plane and exposed from front to back; (b) When sleeping without ground plane and exposed from top to bottom; where extra free space ($\lambda/4$) is added around the body with chosen PMLs.

4.5 Plane Wave Exposure of Models

Plane wave exposure on human models is used to mimic the far-field conditions for sources located beyond 15 cm. Distance greater than 15 cm between the human model and SM antenna devices is large in terms of the computational volume and performing an assessment on human models with such a distance requires a great amount of computation power. Therefore, plane waves have been employed to realise exposure from far-field sources. Plane wave exposure is further divided into two different scenarios: when models are grounded and when models are isolated. Details of the plane wave exposure arrangement for the human models are given in the next sections.

4.5.1 Standing Models on a Ground Plane Exposed from Front to Back

Calculations of the field exposure were performed for a plane wave irradiating the model from the front with the E-field component aligned vertically. In the numerical computation tool employed, excitation power is dependent on the boundary size in plane-wave exposure condition, since the models were excited by a plane wave peak E-field strength of 1 V/m over the entire simulation area. Moreover, the excited field is doubled due to the perfect electrical conductor (PEC) boundary at the bottom plane acting as a mirror for the E-field.

The peak E-field strength is presented as a root mean square (rms) value, which is 1.414 V/m rms using the formula Vrms = 0.707 * Vpp [22]. However, the peak PD is 2.65 mWm^{-2} based on the assumption that 1 V/m is applied through free space (1^2 /377). For PEC ground boundary, the peak PD becomes four times higher than that of free space, based on the assumption that 2 V/m (due to mirroring effect of PEC/ground) is applied through free space (2^2/377). Therefore, the peak PD of the grounded models is 10.61 mWm^{-2}. The WBSAR values calculated for the grounded models at both frequencies are well under the basic restriction level described by the ICNIRP guidelines, as shown in Figure 4-10. The differences in WBSAR values mainly resulted from difference in average mass densities among the models.

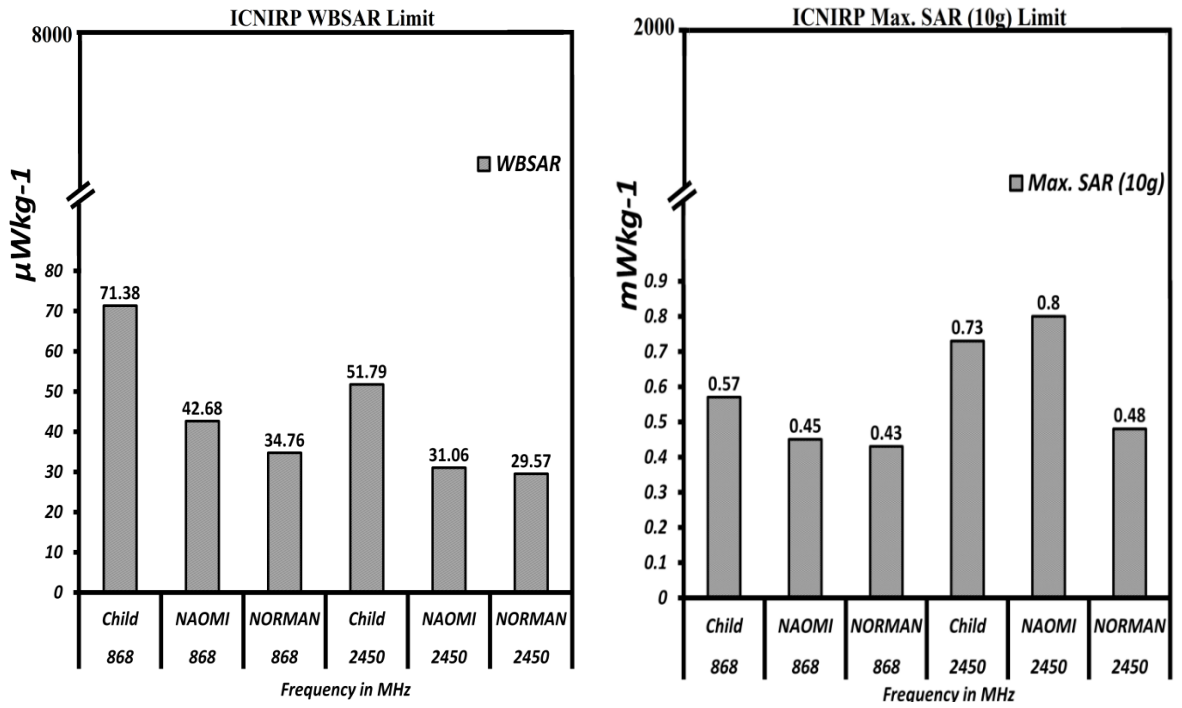

Figure 4-10. SARs distribution resulting from plane wave exposure; (a) WBSAR; (b) Max. SAR (10 g); when models are ***standing*** on PEC ground and exposed from front to back with 1 V/m peak ***plane wave***.

When models were exposed to a plane-wave under grounded conditions and 10 g averaging method applied, few hot spots (regions of locally enhanced absorption) were identified as shown in Figure 4-11 and Figure 4-12. The most affected parts of the child model at both frequencies are the anterior and posterior shin splints. For NAOMI, the plane wave exposure leads to most absorption in the wrist, ankle, nose, neck and fingers. In the case of NORMAN, similar parts of the body are affected, but also the eyes, groin and knees. The SAR distribution highlights the absorption maximum at thinner parts of the body e.g. wrist, ankle as indicated above. This could be due to the resonances appearing in such parts of body. It is interesting to notice that NAOMI max. SAR values are higher than child in plane wave exposure cases. These findings are in line with the findings given in this publication [23]. However, the SAR scale indicates that this effect is still negligible in comparison with guideline levels (Figure 4-10b).

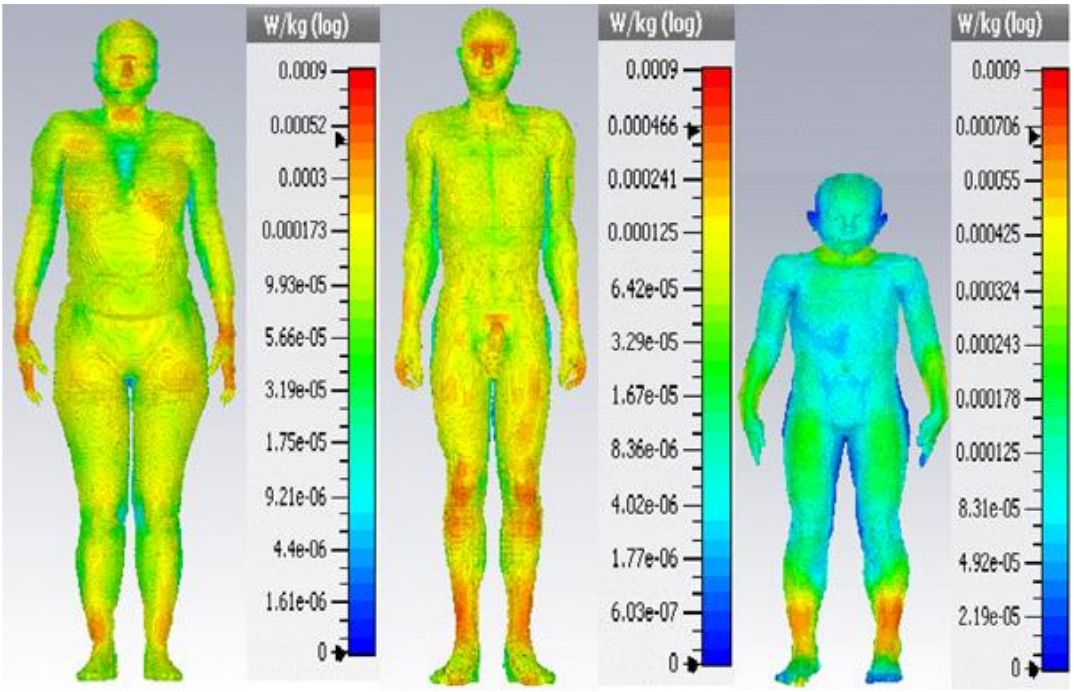

Figure 4-11. NAOMI, NORMAN and Child Max. SAR (10 g) distribution at **868 MHz**, when models are ***standing*** on PEC ground and exposed from front to back with 1V/m peak ***plane wave***.

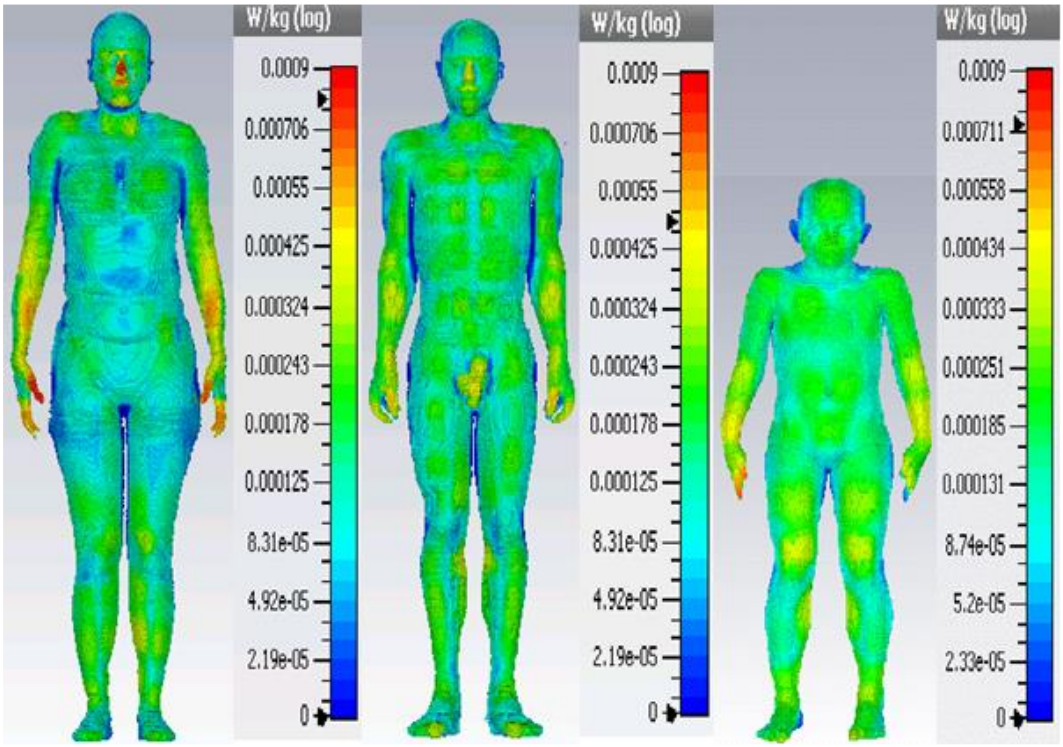

Figure 4-12. NAOMI, NORMAN and Child Max. SAR (10 g) distribution at **2450 MHz**, when models are ***standing*** on PEC ground and exposed from front to back with 1 V/m peak ***plane wave.***

4.5.2 Isolated Models in Sleeping Position Exposed from Top to Bottom

Calculations were performed for a plane-wave irradiating the model from top with E-field component aligned vertically under the isolated condition. In the case of isolation, the excitation power is set to 1 V/m peak value over the entire simulation area. Therefore, the peak PD of isolated models across the spectrum is 2.65 mWm^{-2}. When the models are isolated in air in a sleeping position, the WBSAR values for both frequencies are well under the basic restriction level described by ICNIRP guidelines as shown in Figure 4-13. The reason behind the difference in max. SAR values are same as explained in above section. However, a few hot spots are identified at both frequencies 868 MHz and 2450 MHz. The maximum absorption regions for all three models as shown in Figure 4-14 and Figure 4-15.

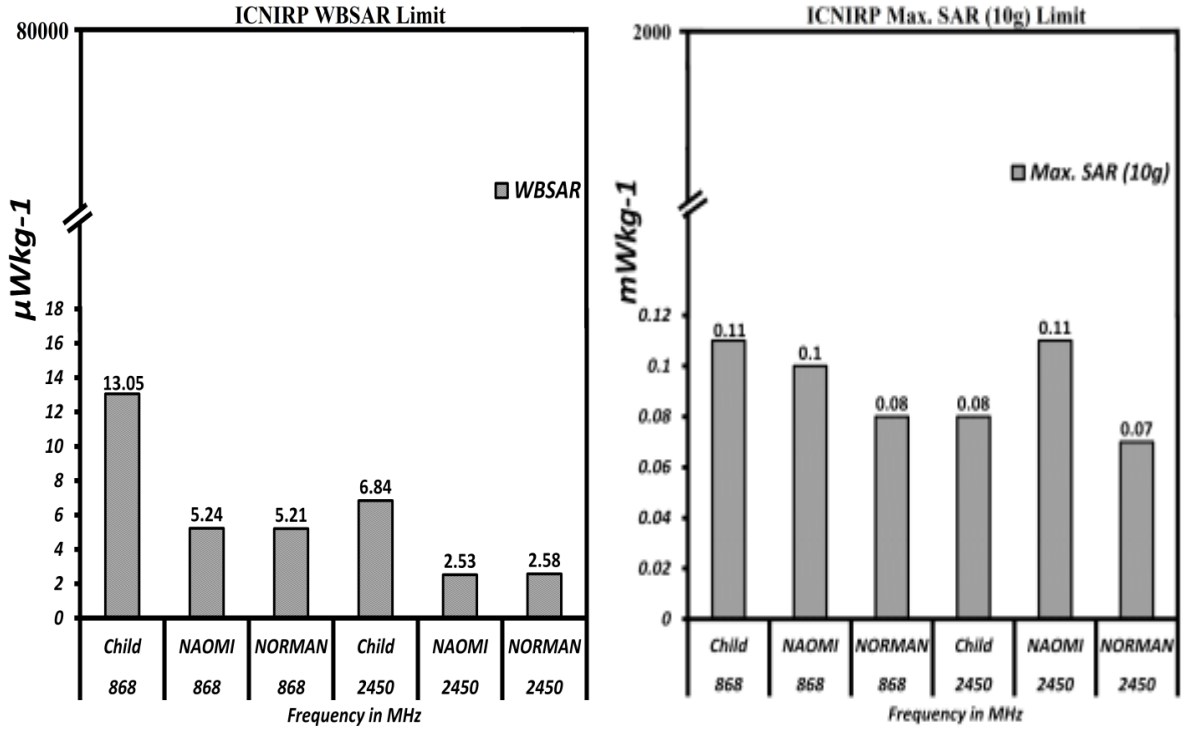

Figure 4-13. SARs distribution resulting from plane wave exposure; (a) WBSAR; (b) Max. SAR (10 g); when models are under ***sleeping*** condition and exposed from top to bottom with 1 V/m peak ***plane wave***.

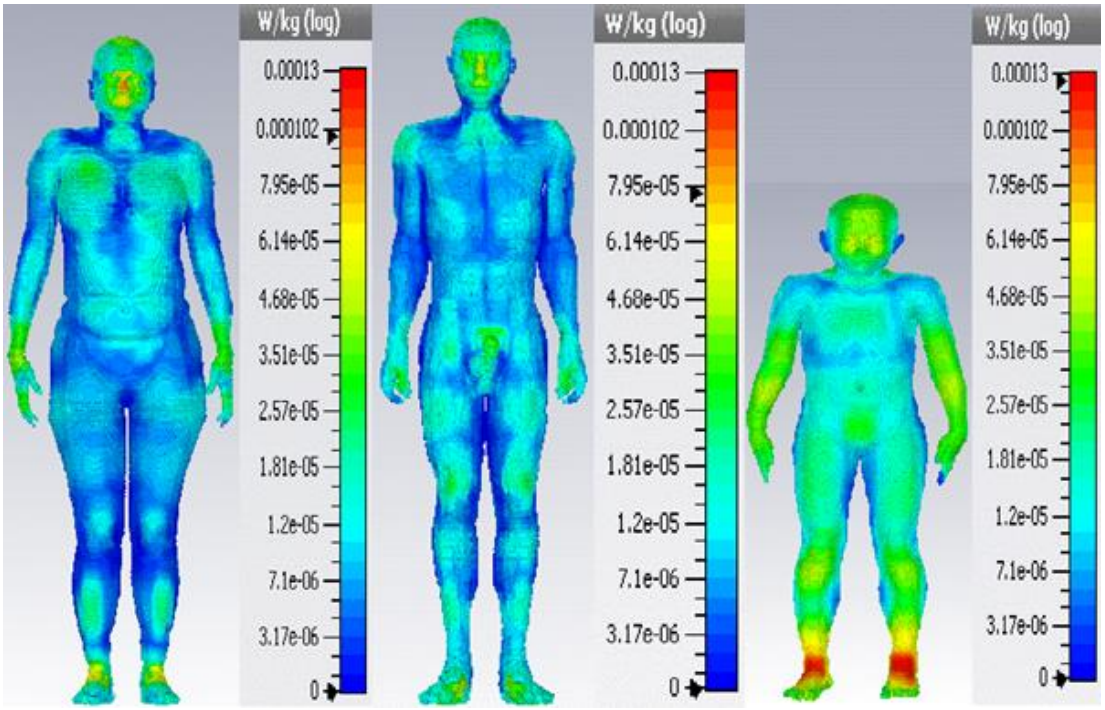

Figure 4-14. NAOMI, NORMAN and Child Max. SAR (10 g) distribution at **868 MHz**, when models are under ***sleeping*** condition and exposed from top to bottom with 1 V/m peak ***plane wave***.

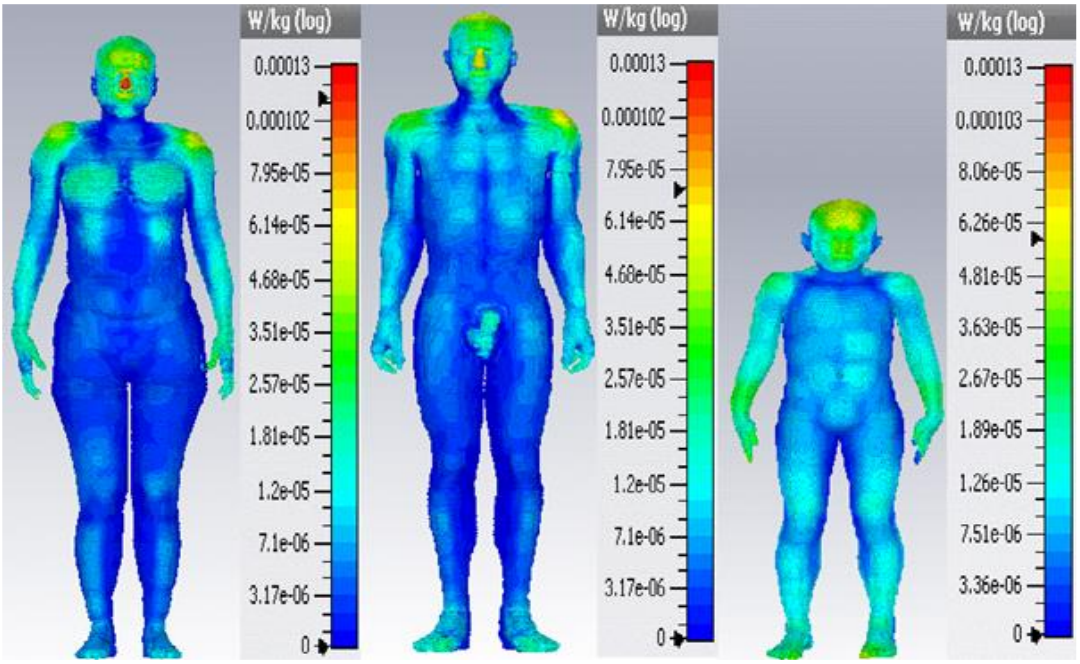

Figure 4-15. NAOMI, NORMAN and Child Max. SAR (10 g) distribution at **2450 MHz**, when models are under ***sleeping*** condition and exposed from top to bottom with 1V/m peak ***plane wave***.

4.6 Models Exposure with SM Device Antenna

This section describes the exposures resulting from modelled SM devices, as opposed to plane waves. A SM antenna is modelled in a plastic box with 2 mm thick walls, in order to mimic the real device. The SAR values have been normalised to an antenna output power of 1 W to allow for comparison with measured data described in the reference [24]. It is worth mentioning that 1 W is in fact approximately sixty five times higher than the maximum 15 mW power expected from SM devices during transmission.

Moreover, the PD in all cases calculated from measuring in *x* and *y*, *x* and *z* or *y* and *z* directions depends on the geometry of simulation box. After calculating the simulation box coordinates, area formulae are used to divide the output power by the calculated area in order to get the required PD in each scenario. The output powers from SM antenna at 868 MHz and 2450 MHz band are 0.7 W and 0.99 W, respectively due to the corresponding antenna radiating efficiency of 70 % and 99 %.

Due to the different voxel model sizes, boundary conditions (grounded or isolated) and exposure scenarios, the PD varies in each case. Therefore, for the standing position all three phantoms were modelled and assumed to be standing on ground with a distance between model and SM antenna set to 15 cm, as shown in Figure 4-16 (a). Similarly, for the sleeping position all three phantoms were modelled in a sleeping isolated position, with the distance between model and SM antenna set to 15 cm, as shown in Figure 4-16 (b).

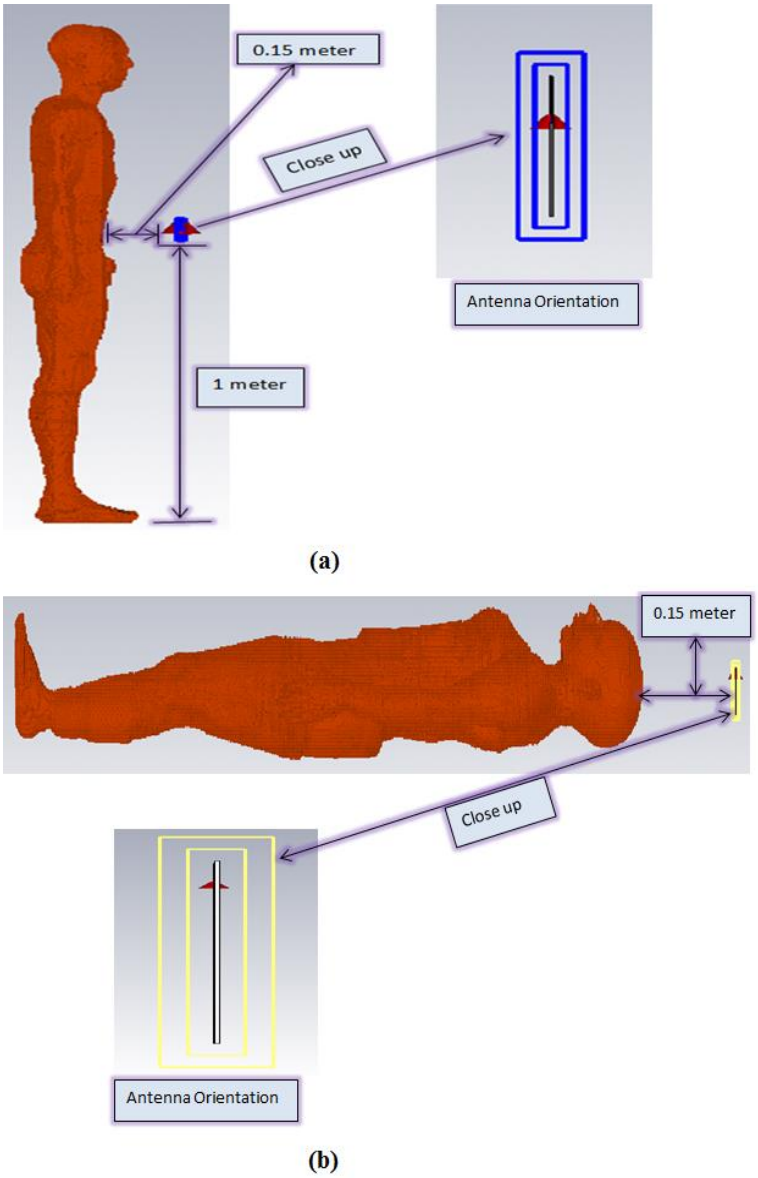

Figure 4-16. Exposure scenarios for models close to SM device antennas; (a) When standing on ground plane and exposed from front with respect to SM device antenna; (b) When sleeping without ground plane and exposed from top with respect to SM device antenna; where extra free space ($\lambda/4$) is added around the body with chosen PMLs.

4.6.1 Standing Models on a Ground Plane Exposed from Front to Back

Calculations were performed for a SM device antenna irradiating the grounded model from front side. When the models are grounded, the WBSAR values for both frequencies are well under the basic restriction level given in the guidelines, as shown in Figure 4-17.

At both frequencies, when the models are exposed under grounded conditions, a few hot spots are observed, as shown in Figure 4-18 and Figure 4-19. Because the height of a child model is smaller, when the SM device antenna is placed at 1 meter height from the ground, the

highest exposures are seen in the brain, eyes and forehead, at both frequencies. For both NAOMI and NORMAN, the exposure is relatively higher in the stomach area at both frequencies.

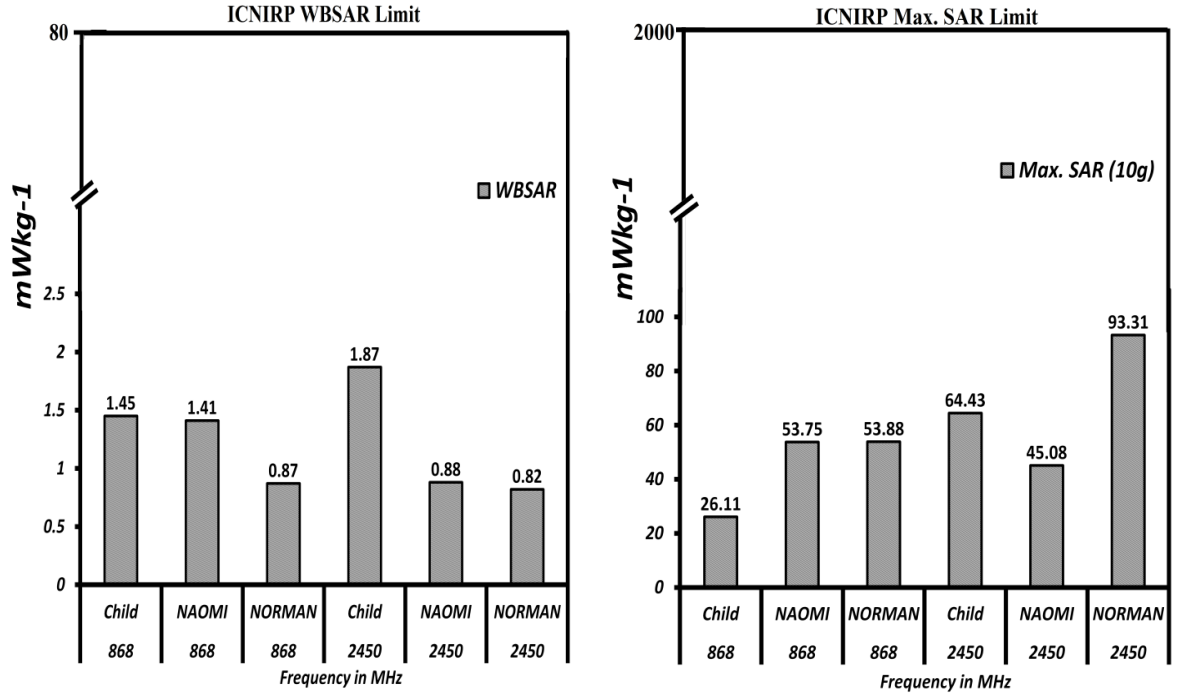

(a) **(b)**

Figure 4-17. SARs distribution resulting from exposure close to SM antennas; (a) WBSAR; (b) Max. SAR (10 g); when models are ***standing*** on PEC ground and exposed from front at 15 cm distance with 1 W input power at the ***SM antenna***.

The female model shows higher WBSAR levels than the male model, as shown in Figure 4-17. This could be due to the different distances between the body and SM antenna in the respective models. The distance was measured from the middle of feet and was set to approximately 15 cm. The tummy regions of both models are also different in shape so the differences in distance and body shape (especially in the tummy region) may explain the different SAR distributions (Figure 4-18 and Figure 4-19). In any case, the calculated SAR values are negligible in comparison with the ICNIRP guidelines.

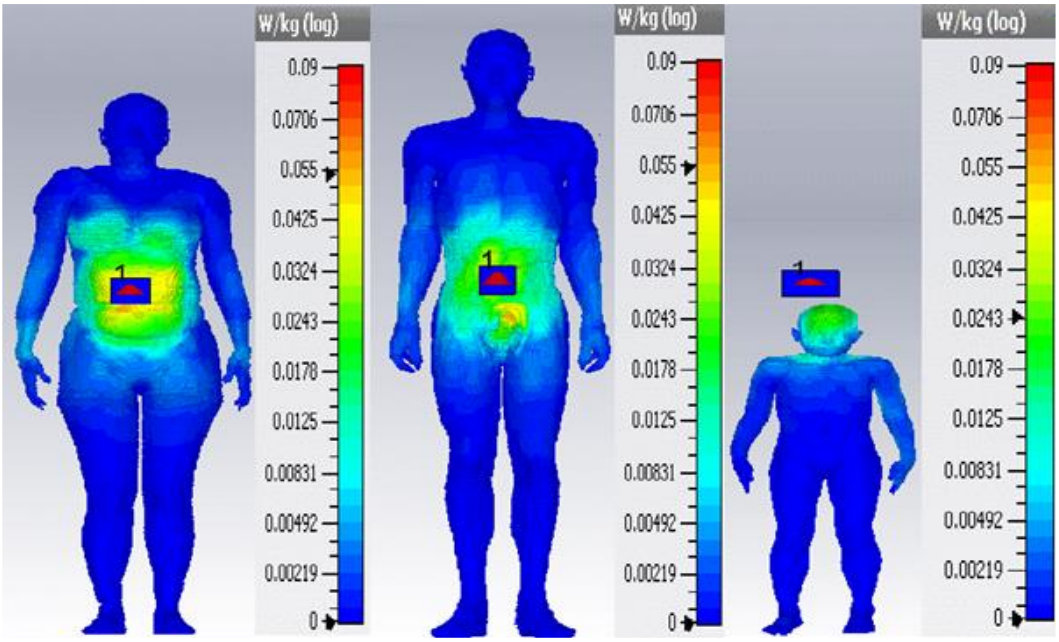

Figure 4-18. NAOMI, NORMAN and Child Max. SAR (10 g) distribution at **868 MHz**, when models are ***standing*** on PEC ground and exposed from front at 15cm distance with 1W input power at the ***SM antenna***.

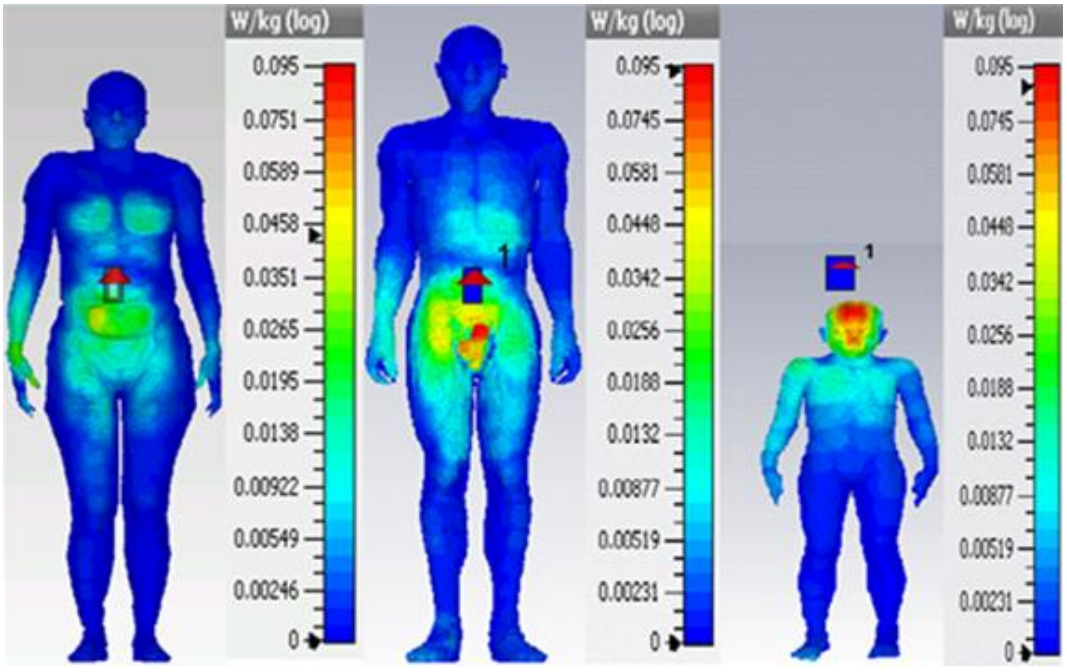

Figure 4-19. NAOMI, NORMAN and Child Max. SAR (10 g) distribution at **2450 MHz**, when models are ***standing*** on PEC ground and exposed from front at 15cm distance with 1W input power at the ***SM antenna***.

4.6.2 Models in Sleeping Position Exposed from Top to Bottom

Calculations were performed for a SM device antenna irradiating the model from top when the model is in a sleeping condition. In this scenario, all the WBSAR values for both frequencies are well under the basic restriction level defined in the guidelines, as shown in Figure 4-20 even though the output power from the modelled SM antennas were substantially above those from real devices. A few hot spots were identified in the skull at both frequencies, as shown in Figure 4-21 and Figure 4-22. In all cases of exposure, the highest SAR values occur in the brain, nose and eyes similar to the plane wave exposure scenario.

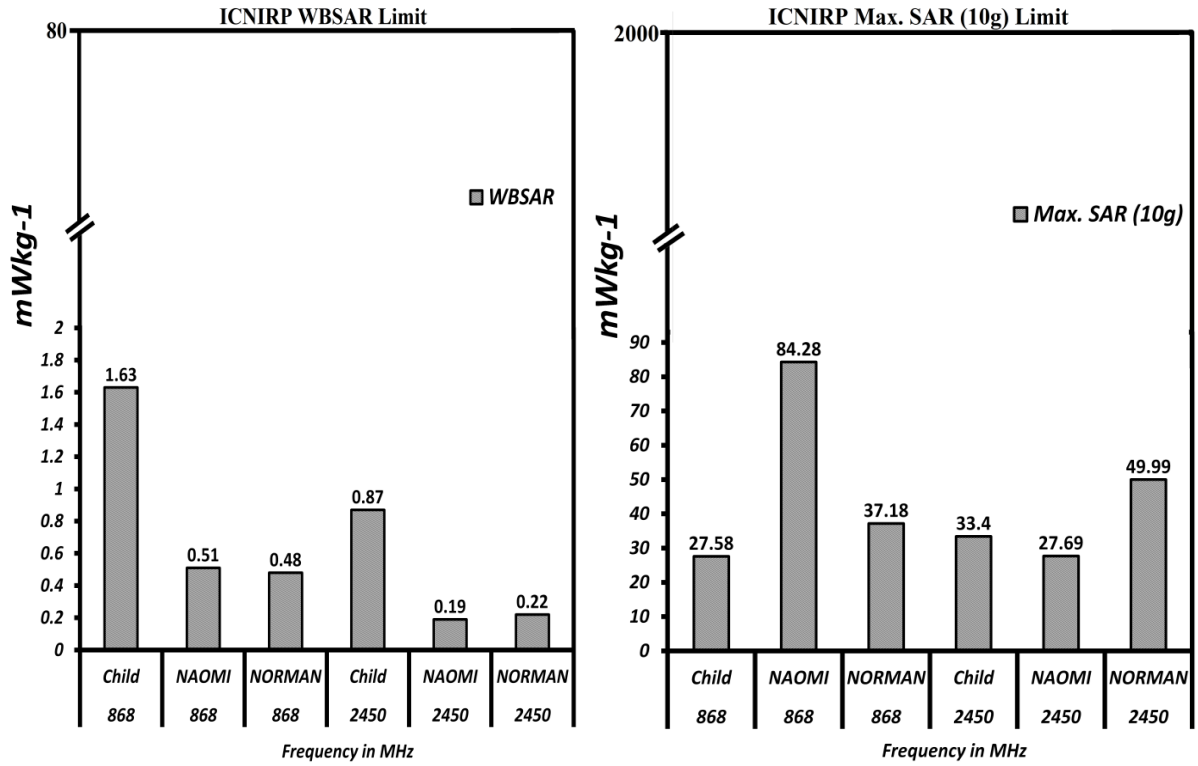

Figure 4-20. SARs distribution resulting from exposure close to SM antennas; (a) WBSAR; (b) Max. SAR (10g); when models are under ***sleeping*** condition and exposed from top at 15 cm distance with 1W input power of ***SM antenna***.

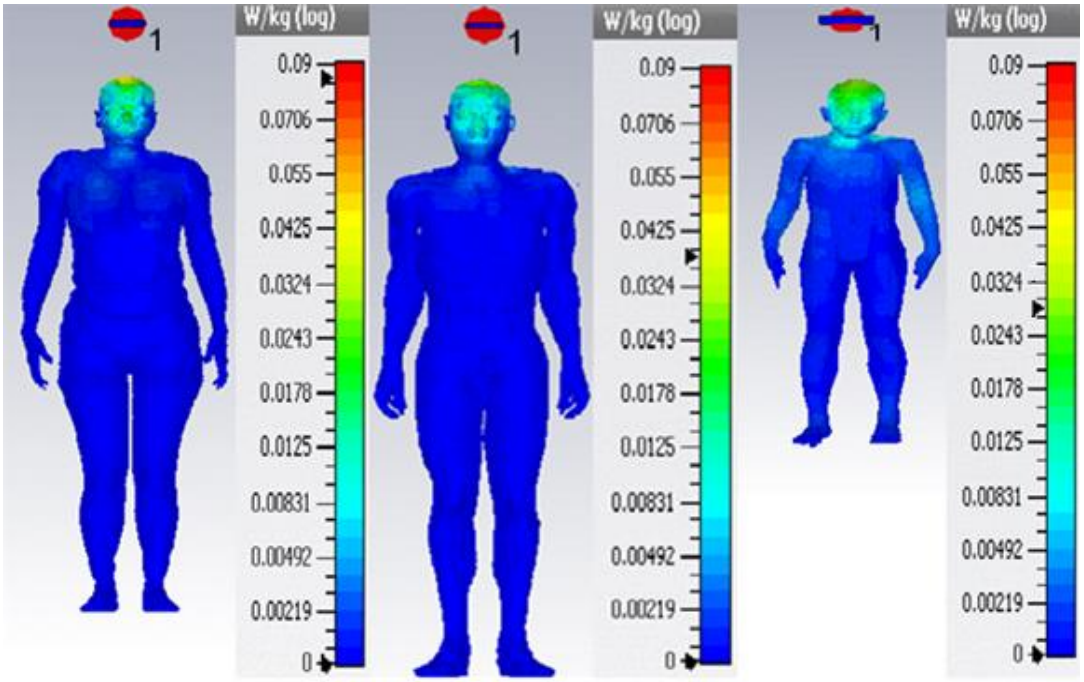

Figure 4-21. NAOMI, NORMAN and Child Max. SAR (10 g) distribution at **868 MHz**, when models are under ***sleeping*** condition and exposed from top at 15 cm distance with 1 W input power of ***SM antenna***.

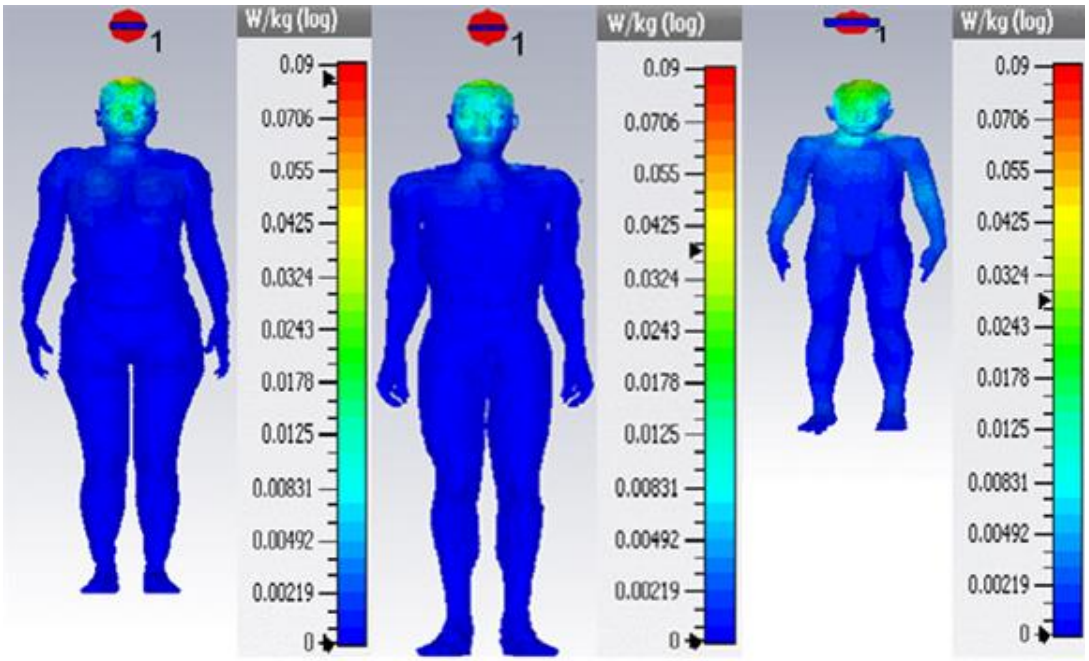

Figure 4-22. NAOMI, NORMAN and Child Max. SAR (10g) distribution at **2450 MHz**, when models are under ***sleeping*** condition and exposed from top at 15 cm distance with 1 W input power of ***SM antenna***.

4.7 Discussion

4.7.1 Review on Numerically Calculated SAR

In this study, human models of three different age groups were assessed to determine the induced WBSAR, and maximum (10 g averaged) SAR distributions when exposed to radio signals typical of those from SM HAN sources. SAR distributions have been assessed for 24 different scenarios, including standing and sleeping positions, when exposed at various distances from the signal source. Numerical simulations were carried out using validated, and well established computation tools, and through comparisons with similar configurations in earlier work [20].

The exposure configurations utilised high-resolution human models, which allowed for AFD tissue parameters. Dielectric properties of various tissues at different ages were assigned using a curve fitting technique applied to published measured data. Signal sources were simulated using realistic antenna designs to mimic the real sources at close distances, and plane waves to investigate far-field conditions of exposure.

Calculated WBSAR values in the present study are different from those published previously [20]. This is attributed to the difference in excitation parameters where the E-field of the signal in the previous study was set to 1 V/m rms, whereas in this study it is set to 1 V/m peak value which is equivalent to 1.41 V/m rms. Therefore, the WBSAR values for the grounded, plane wave exposure in the standing position scenario are expected to be twice as high as those reported in [20].

To confirm this, additional simulations were conducted on the NORMAN model standing on a grounded plane and exposed to a plane wave of 868 MHz and 2450 MHz as shown in Figure 4-23. An excitation E-field strength of 1 V/m (rms) resulted in a WBSAR value of approximately 17 μWkg^{-1} and 15 μWkg^{-1}, which is in line with other reported results.

When the model was exposed to double the amplitude of the excitation E-field strength, i.e. 2 V/m (rms), the resulting WBSAR is approximately 69 μWkg^{-1}, which is larger by a factor of four. This is due to the square of the doubled field, which is governed by the relationship ($|E|^{\wedge 2}$). Similarly, when the plane wave was excited with an 868 MHz signal with a peak amplitude of 1 V/m, the peak field is doubled in the presence of the metallic ground plane

resulting in a field strength of 1.414 V/m (rms). In this case, the power increases by a factor of 2 compared to the first case, giving a WBSAR value of around 35 μWkg^{-1}.

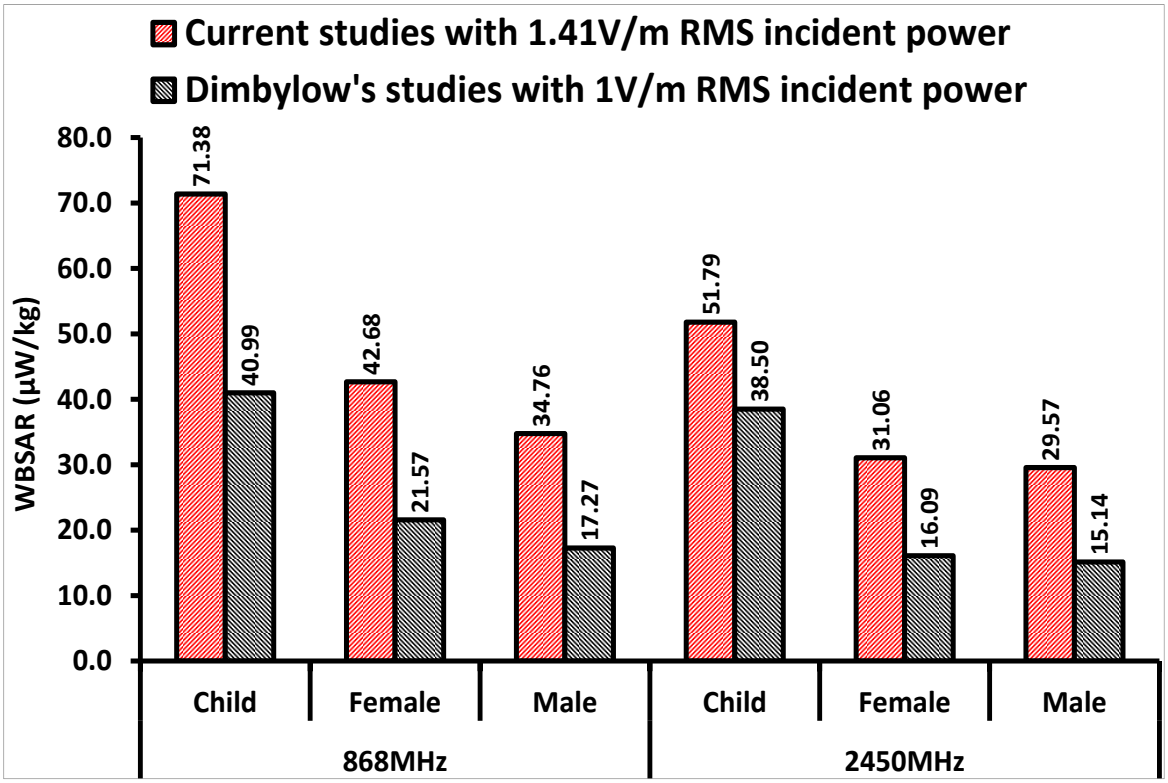

Figure 4-23. Comparison between current and previous studies, where 1 V/m (rms) and 1.41 V/m (rms) incident power used in current and earlier studies [20] when three models of different age groups are ***standing*** position and exposed by ***plane wave*** from front to back under grounded condition.

Similar differences were observed when the simulations were repeated at 2450 MHz. Within the bounds of the various configurations considered, higher SAR values were always observed for the child model, compared with the adult models. This is attributable to differences in the dielectric properties and the mass densities, which is in line with the observations reported in reference [24].

4.7.2 Comparison between Simulations and Measurements

In this section, comparisons were also made in this study between the simulated and measured E-fields and power densities as described in the companion paper [24]. Also, the SAR values predicted from the measured PD levels were assessed under a pessimistic assumption of plane wave equivalence. For the purpose of simulations, a computational domain representing an anechoic chamber with dimensions of 3.6 m × 2.4 m × 2.4 m was designed similar to that used in the laboratory measurement setup [24].

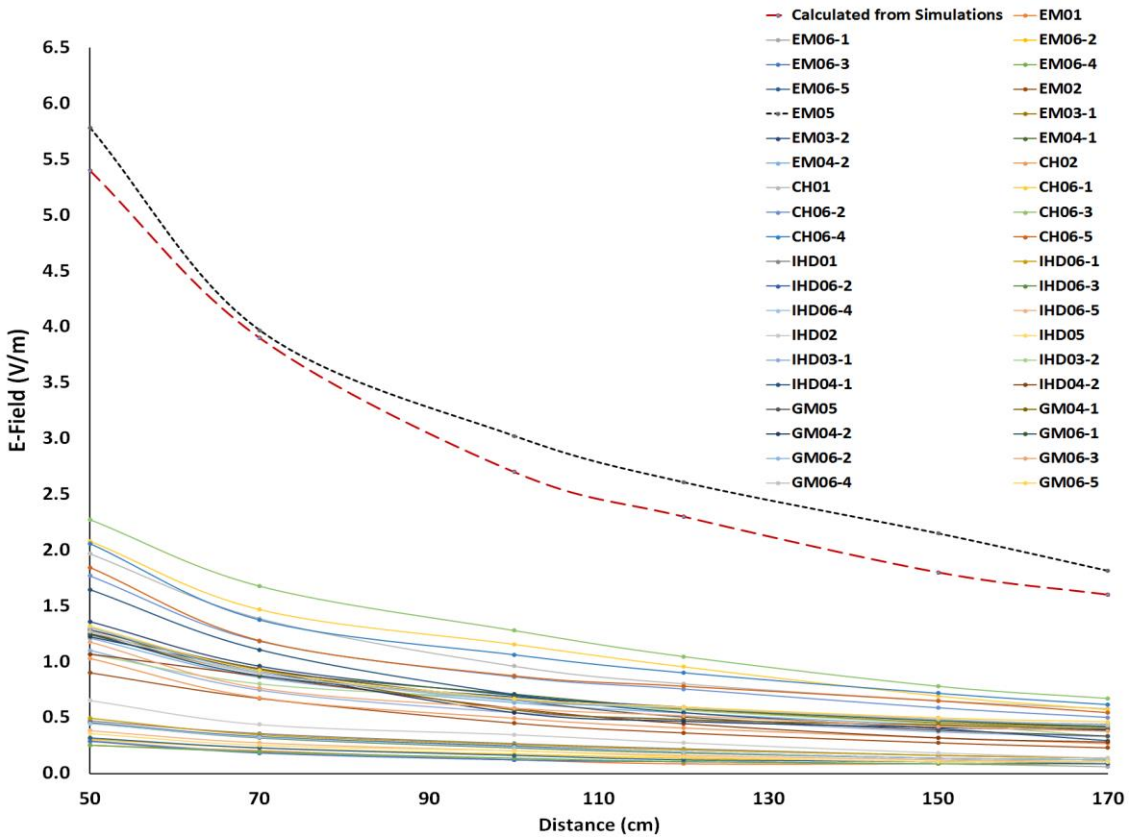

Figure 4-24. Comparison between simulated and measured ***E-Field*** from SM devices at **2450 MHz**. where EM, CH, IHD and GM represents Electricity Meter, Comms. Hub, In Home Display and Gas Meter, respectively. The measurements on a selection of SM devices provided by various manufacturers [24].

In free space, the E-fields and PD levels were calculated as a function of distance as shown in Figure 4-24 and Figure 4-25. It is worth mentioning that the maximum output power used in simulations and measurements was as 1 W and 15 mW, respectively. After normalising the simulated PDs to level similar to measured power densities, good agreement achieved between simulated and measured power densities for a particular device. The PD measured from IHD02 (device under the test ID) at 50 cm and 1 cm distance is 1.13 mWm^{-2} and 0.32 mWm^{-2} respectively, whereas the simulated PD after normalisation is 1.15 mWm^{-2} and 0.30 mWm^{-2} at 50 cm and 1cm, correspondingly as compared to measured power densities of IHD02 device. Measurements were performed on number of samples of SMs provided by the various manufacturers and utility companies device [24]. Therefore, there was some difference among the power densities in simulations with respect to measurements.

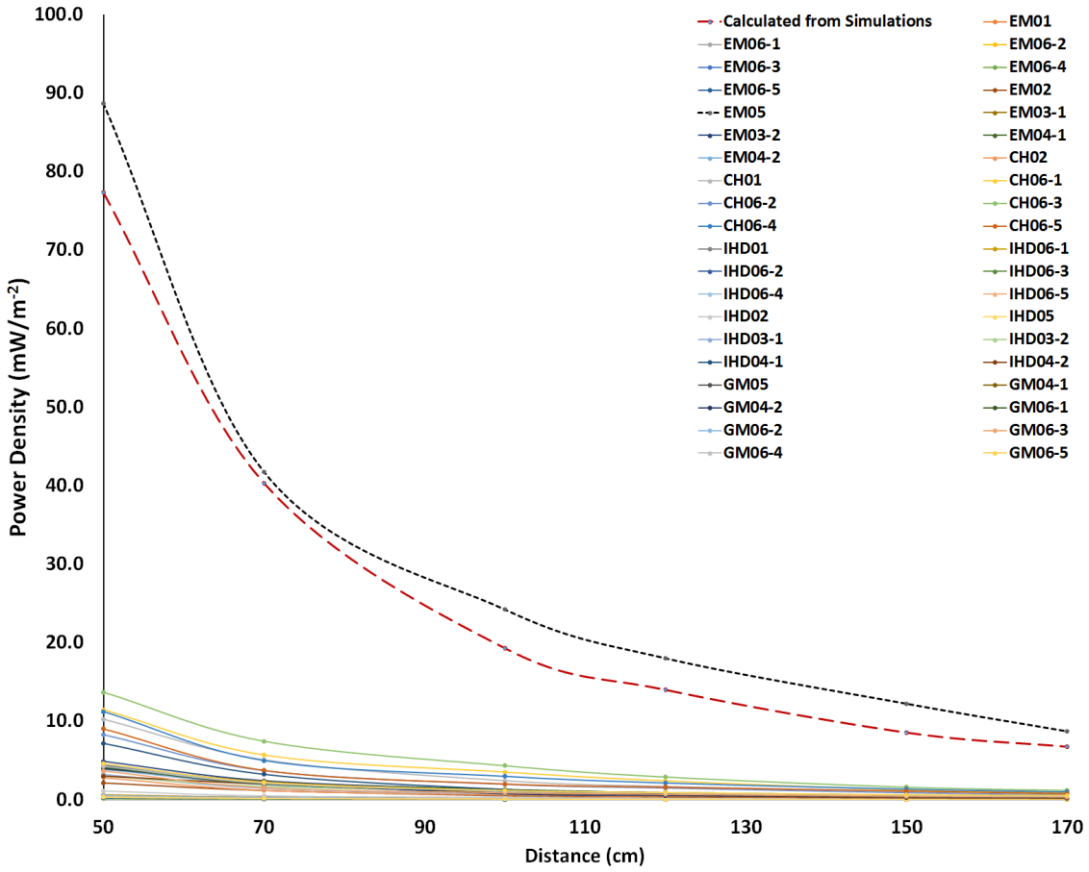

Figure 4-25. Comparison between simulated and measured ***PDs*** from SM devices at **2450 MHz**, where EM, CH, IHD and GM represents Electricity Meter, Comms. Hub, In Home Display and Gas Meter, respectively. The measurements on a selection of SM devices provided by various manufacturers [24].

Although, all simulations were performed at 15 cm distance using the SM antenna model, SAR values beyond that distance were assessed using plane wave equivalent configurations as described in plane wave exposure section. Simulated SAR values were normalised with respect to the simulated and measured power densities at 50 cm distance as shown in Table 4-1 and Table 4-2. These two tables depict the estimated WBSAR and maximum SAR (10 g) values respectively at the measured PD levels. The comparison between SAR values were restricted to maximum and average measured PD levels due to the large number of measurements on SM devices [24].

The maximum PD measured in the laboratory was 13.72 mWm^{-2} from CH06-3 (device under test ID) at a distance of 50 cm and in the 2450 MHz band, with exception of one of the "outlier device (EM05)" that had the PD of 88.71 mWm^{-2} [24]. The PD calculated in the numerical assessment part was 10.61 mWm^{-2} at 2450 MHz, when models were exposed to a plane wave under the standing configurations. The PD in simulations calculated based on the

size of bounding box which contains the voxel model. Therefore, the measured PD emitted from Comm-Hub device was found to be relatively higher as compared to simulations.

Table 4-1. Comparison between WBSAR values at **2450 MHz** band from simulated and measured power density levels at 50 cm distance.

Models Exposure Condition	**Simulated WBSAR (µWkg-1)**	**Simulated Power Density (mWm-2)**	**Normalised WBSAR to the input power density ($mWkg^{-1}$ per Wm^{-2})**	**Measured Power Density (mWm^{-2})**		**Predicted WBSAR (μWkg^{-1})**	
				Worst	**Average**	**Worst**	**Average**
Child Standing	51.79	10.61	4.88	88.71	5.93	432.90	28.94
NAOMI Standing	31.06	10.61	2.93	88.71	5.93	259.69	17.36
NORMAN Standing	29.57	10.61	2.79	88.71	5.93	247.23	16.53
Child Sleeping	6.84	2.65	2.58	88.71	5.93	228.98	15.30
NAOMI Sleeping	2.53	2.65	0.96	88.71	5.93	84.69	5.66
NORMAN Sleeping	2.58	2.65	0.97	88.71	5.93	86.37	5.77

The results show that the energy deposition is distributed differently for each model and this is due to differences in dimensions, frequency of interest, anatomical and dielectric properties, and exposure setup. The highest maximum SAR (10 g) values were observed when models were exposed to near field signals emitted from antennas operating at 868 MHz and 2450 MHz bands, in standing or sleeping position. In contrast and as expected, the highest WBSARs were observed when models were exposed to plane waves in standing or sleeping positions. The WBSAR value for NORMAN in standing position at 868 MHz is 34 μWkg^{-1}, falling to 29 μWkg^{-1} at 2450 MHz when exposed to a plane wave (see Figure 4-10).

Table 4-2. Comparison between maximum SAR values at **2450 MHz** from simulated and measured PD levels at 50 cm distance.

Models Exposure Condition	Simulated Max.SAR ($mWkg^{-1}$)	Simulated Power Density (mWm^{-2})	Normalised Max. SAR to the input power density ($mWkg^{-1}$ per Wm^{-2})	Measured Power Density (mWm^{-2})		Predicted Max. SAR ($mWkg^{-1}$)	
				Worst	Average	Worst	Average
Child Standing	0.73	10.61	0.07	88.71	5.93	6.10	0.41
NAOMI Standing	0.80	10.61	0.07	88.71	5.93	6.69	0.45
NORMAN Standing	0.48	10.61	0.05	88.71	5.93	4.01	0.27
Child Sleeping	0.08	2.65	0.03	88.71	5.93	2.68	0.18
NAOMI Sleeping	0.11	2.65	0.04	88.71	5.93	3.68	0.25
NORMAN Sleeping	0.07	2.65	0.03	88.71	5.93	2.34	0.16

On the other hand, the WBSAR value for NORMAN, when exposed from SM antenna sources in standing position, is 0.87 $mWkg^{-1}$ and 0.82 $mWkg^{-1}$ at the former and later frequency band, respectively (see Figure 4-17.). The differences are due to the differences in power densities. The PD is relatively high in all SMs antenna exposure configurations, mainly due to the relatively close distance (15 cm) considered in all SMs antenna exposure conditions, which is considered to reflect a worst-case scenario.

PDs were also calculated as a function of distance in both simulations and measurements where good agreement was achieved after normalisation. The estimated SAR values calculated for the measured PD levels are well below the guidelines. As PD decreases, the SAR values generally follow the same falling trend. The 1 W peak input power assigned to the SM antenna substantially overestimates what SMs are likely to emit (15 mW maximum limit).

Overall, in both simulations and measurements the SAR levels were found to be very low in comparison with the basic restriction levels advised by ICNIRP to protect human health. Similar observations were made in [26], where the exposure level from SM sources was found to much less than that resulting from mobile phones used in close proximity to the head for voice calls.

4.8 Chapter Summary

In this chapter, specific absorption rate (SAR) assessment performed using smart meter (SM) antenna and plane wave sources. The SM devices operate on two different frequency bands (868 and 2450 MHz) which are used for short range communication. The maximum input power for both bands vary, so in this study 1W input power considered as worst case scenario. The absorption of E-field within the human models from SM antennas and plane wave sources, are discussed in possible realistic scenarios. In total 24 different exposure scenarios study in this work. The results are critically analysed and also validated by comparison with earlier studies and measurements, and differences are explained in detail.

The SAR estimation is performed on three different models by using age- and frequency-dependent (AFD) tissue properties. The E-field and power density (PD) is calculated for each case when models are in standing or sleeping posture under grounded or isolated conditions. In nutshell, simulations described in this chapter demonstrate that the exposures incurred from SM devices produce whole body specific absorption rate (WBSAR) and max. SAR (10 g) values well below the exposure guideline limits. This was the case for all the exposure scenarios considered for all age groups, despite the overestimated emitted powers and the fact that continuously transmitted waves were used rather than the more realistic shorter duration signals that are characteristic of such devices.

References

[1] 2010 to 2015 government policy: household energy, [Online]. Available: https://www.gov.uk/government/policies/helping-households-to-cut-their-energy-bills/supporting-pages/smart-meters (Accessed Feb 2016).

[2] EETAsia. An introduction to ZigBee Smart Energy Profile 2.0, [Online]. Available: http://www.eetasia.com/ART_8800685052_590626_TA_a3e1e20e.HTM (Accessed Feb 2016).

[3] Demystifying 802.15.4 and ZigBee® (white paper), [Online]. Available: http://ftp1.digi.com/support/documentation/demystifyingzigbeeand802154.pdf (Accessed Feb 2016).

[4] LTE Frequency Bands & Spectrum Allocations, [Online] Available: http://www.radio-electronics.com/info/cellulartelecomms/lte-long-term-evolution/lte-frequency-spectrum.php (Accessed Feb 2016).

[5] Department of Energy and Climate Change: Smart Metering Implementation Programme, [Online]. Available: https://www.gov.uk/government/uploads/system/uploads/attachment_data/file/209840/SMIP_E2E_SMETS2_govt_consultation_response_part_2_final.pdf (Accessed Feb 2015).

[6] WHO Research Agenda for Radiofrequency Fields, [Online]. Available: http://apps.who.int/iris/bitstream/10665/44396/1/9789241599948_eng.pdf (Accessed Dec 2015).

[7] J. F. Bakker, M. M. Paulides, A. Christ, N. Kuster, and G. C. v. Rhoon, "Assessment of induced SAR in children exposed to electromagnetic plane waves between 10 MHz and 5.6 GHz," Phys. Med. Biol., vol. 55, pp. 3115 – 3130, 2010.

[8] ITIS. High-Resolution Human Models for Simulations: Virtual Population, [Online]. Available: http://www.itis.ethz.ch/itis-for-health/virtual-population/human-models/ (Accessed Dec 2015).

[9] P. Dimbylow, "Resonance behaviour of whole-body averaged specific energy absorption rate (SAR) in the female voxel model, NAOMI," Phys. Med. Biol., vol. 50, pp. 4053 – 4053, 2005.

[10] ICNIRP, "International Commission on Non-Ionizing Radiation Protection: Guidelines for limiting exposure to time-varying electric, magnetic and electromagnetic fields (up to 300GHz)," Heal. Phys. Soc., vol. 74, pp. 494 – 522, 1998.

[11] A. Hirata, K. Yanase, I. Laakso, K. H. Chan, O. Fujiwara, T. Nagaoka, et al., "Estimation of the whole-body averaged SAR of grounded human models for plane wave exposure at respective resonance frequencies," Phys. Med. Biol., vol. 57, pp. 8427 – 8442, 2012.

[12] R. P. Findlay, and P. J. Dimbylow, "SAR in a child voxel phantom from exposure to wireless computer networks (Wi-Fi)," Phys. Med. Biol., vol. 55, pp. 405 – 411, 2010.

[13] A. Hirata, O. Fujiwara, T. Nagaoka, and S. Watanabe, "Estimation of Whole-Body Average SAR in Human Models Due to Plane-Wave Exposure at Resonance Frequency," IEEE Trans. on Electromagnetic Compatibility, vol. 52, pp. 41 – 48, 2010.

[14] P. J. Dimbylow, "FDTD calculations of the whole-body averaged SAR in an anatomically realistic voxel model of the human body from 1 MHz to 1 GHz," Phys. Med. Biol., vol. 42, pp. 479 – 490, 1997.

[15] P. Dimbylow and W. Bolch, "Whole-body-averaged SAR from 50 MHz to 4 GHz in the University of Florida child voxel phantoms," Phys. Med. Biol., vol. 52, pp. 6639 – 6649, 2007.

[16] D. M. Sullivan, "*Electromagnetic simulation using the FDTD Method*," New York, 2000.

[17] Z. N. Chen, K. Hirasawa, K. W. Leung, and K. M. Luk, "A new inverted F antenna with a ring dielectric resonator," IEEE Trans. Veh. Technol., vol. 48, pp. 1029 – 1032, 1999.

[18] S. Yarasi, G. R. Kadambi, and T. Hebron, "Conformal shaped PIFAs for mobile communication applications," IEEE Ant. Prop. Soc. Int. Symp., pp. 82 – 85, 2003.

[19] K. R. Boyle, M. Udink, A. d. Graauw, and L. P. Ligthart, "A novel dual-fed, self-diplexing PIFA and RF front-end," IEEE Ant. Prop. Soc. Int. Symp., pp. 1935 – 1938, 2004.

[20] P. J. Dimbylow, "Fine resolution calculations of SAR in the human body for frequencies up to 3 GHz," Phys. Med. Biol., vol. 47, pp. 2835 – 2846, 2002.

[21] P. Dimbylow, W. Bolch, and C. Lee, "SAR calculations from 20 MHz to 6 GHz in the University of Florida newborn voxel phantom and their implications for dosimetry," Phys. Med. Biol., vol. 55, pp. 151 9 – 1530, 2010.

[22] Reference Designer Calculator, [Online]. Available: http://www.referencedesigner.com/rfcal/cal_04.php (Accessed Dec 2015).

[23] E. Piuzzi, P. Bernardi, M. Cavagnaro, S. Pisa, and J. C. Lin, " Analysis of Adult Child Exposure to uniform Plane Waves at Mobile Communication Systems Frequencies (900 MHz – 3 GHz)," IEEE Trans. on Electromagnetic Compatibility, vol. 53, pp. 38 – 47, 2011.

[24] A. Peyman, D. Addison, T. Mee, C. Goiceanu, M. Maslanyj, and S. Mann, " Exposure to electromagnetic fields from smart utility meters in GB; part I) laboratory measurements," Bioelectromagnetics, vol. 38, pp. 280 – 294, 2017.

[25] W. D. Hurt, J. M. Ziriax, and P. A. Mason, "Variability in EMF permittivity values: implications for SAR calculations," IEEE Trans. Biomed. Eng., vol. 47, pp. 396 – 401, 2000.

[26] Smart Meter and Cancer Risk Statement, [Online]. Available: http://www.health.gov.bc.ca/pho/SmartMeter-and-Cancer.html (Accessed Oct 2015).

Chapter 5
Numerical Exposure Assessments of Modern Mobile Systems

5.1 Introduction

The Long Term Evolution (LTE) technology use MIMO technique in order to improve current communication network in terms of providing better ways of reaching highest possible data rates. MIMO system refers to use multiple antennas at the transmitting and receiving terminals to improve the performance of a wireless communication link. MIMO technology is widely deployed in mobile handsets. The implementation of multiple antennas in mobile handset is a major challenge [1, 2].

The use of MIMO technology in LTE mobile handset has drawn many questions on whether such implementation may induce higher or lower specific absorption rate (SAR) peak level distributions within the human body. The multiple sources in one device may result certain patterns of higher or lower E-field values within the head region or other part of body because of the constructive and destructive nature of the emitted waves.

SAR assessment from traditional single antenna element for smart devices applications such as walkie-talkies, laptops, mobile handsets and Wi-Fi devices has been well studied over the years [3–7], but SAR study of MIMO antennas for mobile handsets are still under

investigation. For compact MIMO enabled mobile terminals, the strong coupling between multiple antenna elements can influence the SAR performance.

Similarly, the total radiation efficiency of mobile handset antenna also reduces when it interacts with mobile user. It can cause shifting of resonant frequency and mobile user absorbs the EM radiations emitted by mobile handset antennas. The mobile user's hand and head effects on a mobile handset terminal performance have been well studied in [8–10]. But this research mainly limited to mobile user effect on single element antenna.

Recently, another research was conducted to study the effects of mobile user hand and head on an adaptive four element antenna array for LTE MIMO mobile handset [11]. But this study mainly focus on user effects on the MIMO channel performance. A dual element MIMO antenna array with user hands effects has been studied in [12] for diversity performance at 2 GHz in mobile handset. SAR study on different mobile handset MIMO antennas for LTE applications [13] has been studied, but these studies mainly limited to use simple antennas i.e. PIFA antennas, with relatively simple MIMO configurations.

In this chapter, a thorough numerical modelling, supported by measurements, have been carried out in order to investigate the EM absorption within the human body caused by using the MIMO mobile handset antenna under the various operating modes. Previously designed MIMO mobile handset is used in this study [14]. Influence of various operating modes (standalone, simultaneous, beam steering) of MIMO antennas for mobile handsets on different parts of human body is studied by considering the size of mobile handset that is relatively similar to the currently available mobile handsets i.e. iphone devices.

SAR properties are studied due to exposure from a new design of MIMO antennas for mobile handset which operates on GSM/UMTS/LTE (1.9 GHz), WLAN (2.45 GHz) and LTE (2.1 GHz, 2.6 GHz) bands. Both body-worn assessment configurations using flat phantom and calling mode testing configurations using homogeneous voxel model is investigated. For compliance, standard assessment methods have been used in this study in order to compare the resultant SAR values due to the exposure from MIMO mobile handset with FCC and ICNIRP guidelines (see section 2.2 Public Electromagnetic Exposure Limit Guidelines for more details about guidelines).

5.2 Configuration of LTE MIMO Antenna

According to 3GPP LTE release 11 [15] a two element MIMO antenna with dual transmitters is required in LTE mobile handsets. The geometry of the predesigned dual element LTE MIMO antenna is shown in Figure 5-1. The size of each antenna element is 50 mm (L) x 24 mm (W) x 0.035 mm (T). Each antenna element is printed on FR4 substrate with the thickness of 0.80mm and a permittivity of 4.4.

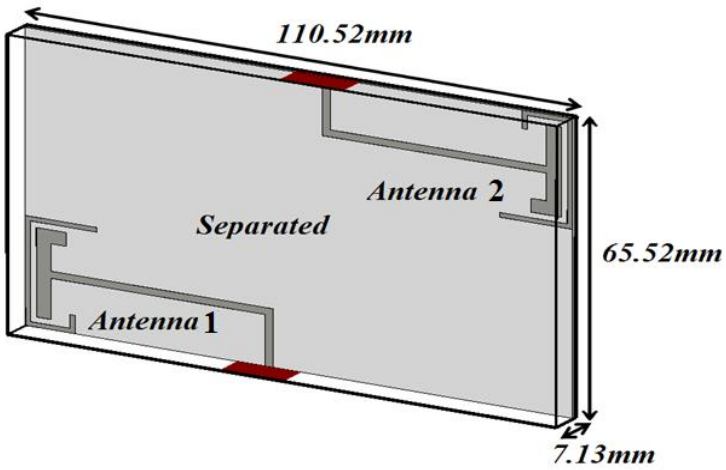

Figure 5-1. Geometry of the predesigned dual element LTE MIMO antenna with mobile handset body; (110.52 mm x 65.52 mm x 7.13 mm).

In this chapter, dual element MIMO antenna is encapsulated in a plastic casing (teflon) in order to consider the realistic mobile handset configuration. Due to the limitation of software and measurement equipment components such as battery and screen are disregarded. Nevertheless, these components affect the behaviour and performance of antenna and also the SAR estimation. The total thickness of the mobile handset body including the MIMO antenna is 7.13 mm which is equivalent to the iPhone S6 specification [16].

MIMO antenna total length is 110.52 mm which is slightly on shorter side in comparison with iPhone S6 (138 mm). However, the width is in good comparison with 65.52 mm and 67.1 mm of current mobile handset and iPhone S6, respectively. The S-parameters of two element LTE MIMO antennas in free space is given in Figure 5-2.

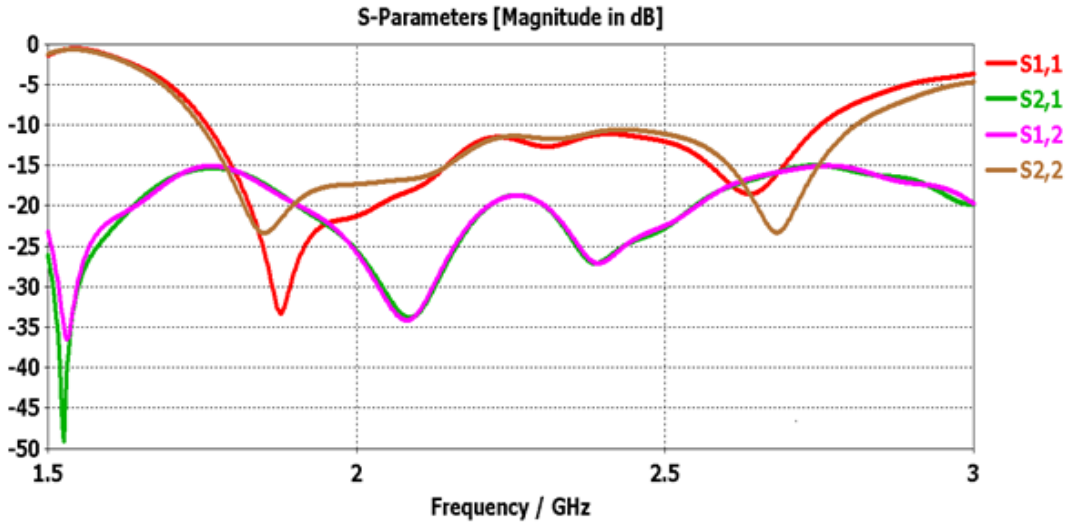

Figure 5-2. Computed S-parameters are measured below -6 dB in free space (cover 1.9 GHz, 2.1 GHz, 2.45GHz and 2.6 GHz band where the isolation is well below -15 dB).

5.2 Selection of Tissue Properties

In this study, two-third muscle-equivalent homogenous tissue properties assigned to both models including male head and flat phantom. According IEEE Std. 1528-2013 (section 1.4.1.3), homogenous liquid tissue properties should be used rather than multi-layered or high-density solid, in order to practical evaluate SAR with E-field probes [21]. In literature, three layer (skin, fat, and muscle) human-body model and two-third muscle-equivalent model produce the same effect on antenna performance and have been used for SAR assessment [22].

Moreover, the selection of two-third muscle-equivalent tissues properties (including mass density) is based on comparison with the two-third muscle-equivalent tissue properties (excluding mass density), muscle tissue properties only, and heterogeneous tissues properties. For this purpose, male voxel model exposed with plane wave in free space from front to back by applying all four previously mention tissue properties configurations and SAR values were calculated as shown in Figure 5-3.

The selection of lower frequency (866 MHz) for this validation is based on the understanding that lower frequency requires less computation time and resources. It can be clearly seen that from Figure 5-3, after allocating two-third muscle-equivalent tissue properties (excluding mass density) and muscle tissue properties to male model in each case produce underestimated SAR values as compared to heterogeneous male model. Therefore, two-third muscle-equivalent models (including mass density) were found more suitable alternative of

heterogeneous model. Although two-third muscle-equivalent (including mass density) produce approx. 25 % over estimated result, but the selection of tissue properties is in line with IEEE Std. 1528-2013 (section 1.4.1) [21].

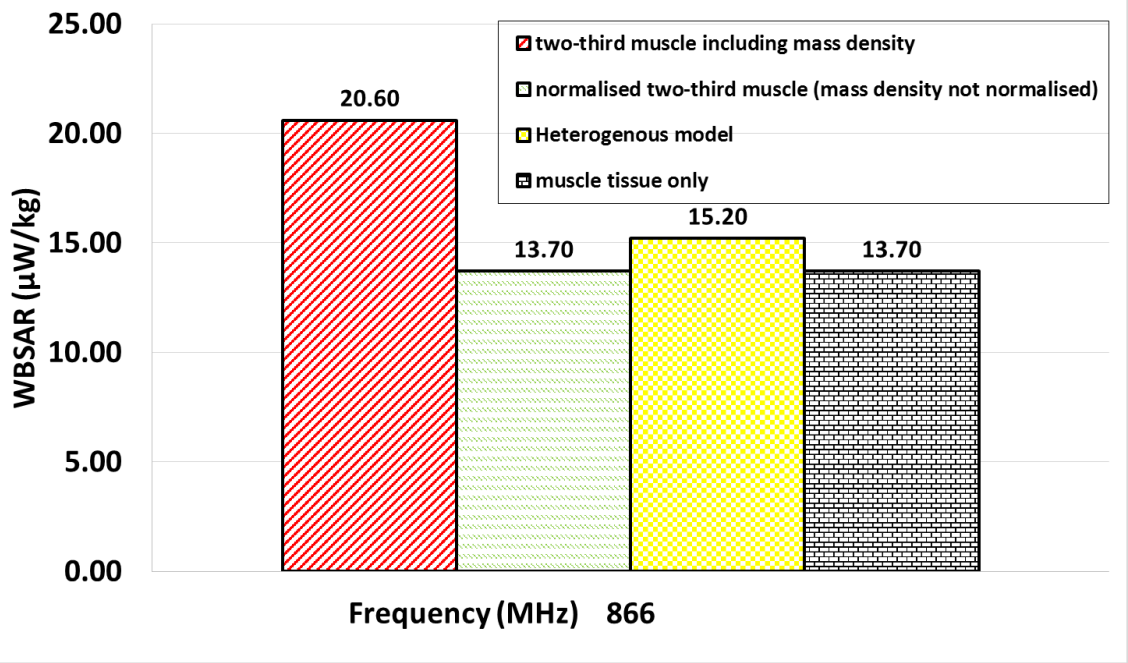

Figure 5-3. Validation of dielectric choice; Where male model exposed with plane from front to back and WBSAR values calculated; (two-third muscle including and excluding mass density means mass density is two-third and mass density value is same as in literature, respectively).

5.3 SAR Assessment on MIMO Modes

In this section, SAR performance of dual element MIMO antenna for mobile handsets investigated in three operating modes, when excited with accepted power of 24 dBm (0.25W). According to FCC, mobile handsets need to be tested for SAR compliance in both calling mode and body-worn cases [17]. Therefore, SAR performance is investigated in both recommended configurations. SAR assessment in calling mode is performed by using head model and body-worn case is simplified with flat phantom as has been used over the years [13, 18–20]. The list of MIMO modes of mobile handset for SAR evaluation is listed below:

1. Standalone or Single Input Single Output (SISO) Mode.
2. Simultaneous/ MIMO/Spatial Diversity Mode.
3. Beam-staring Mode (estimation of SAR for different relative phases between antenna ports).

5.3.1 SAR Assessment on Standalone Mode

MIMO enabled devices needs to comply with standards and guidelines, same as single element antenna of mobile handset, provided by international organisations for limiting human exposure to EM RF fields. MIMO technique is already implemented in the current LTE network and it is mostly employed in the downlink. Multiple antennas used in downlink as compare to uplink. LTE MIMO enabled mobile handsets consists of two or more antennas as explained in 3GPP release 11 [15], but the SAR performance of MIMO antennas are quite complicated as compare to single element antenna. MIMO antennas SAR performance is usually investigated in two generic modes such as SISO and MIMO mode.

In standalone or SISO mode only one antenna operates at a times. The standalone mode realised by one antenna element is excited and other terminated by 50 ohms (Ω) load. SAR assessment in standalone mode is performed in two cases:

- Standalone SAR performance investigation in calling mode
- Standalone SAR performance investigation in body-worn case

5.3.1.1 Standalone SAR in Calling Mode

SAR assessment is performed on all four frequency bands namely: 1.9 GHz, 2.1 GHz, 2.45 GHz and 2.6 GHz. The mobile handset antenna set next to the human head model in calling mode configuration. The mobile handset body surface touches the left check, which is an assessment requirement set by the international guidelines providing organisations [17, 21] as shown in Figure 5-4. It is worth mentioning the international guidelines emphasises that every mobile handset should be tested in more realistic scenarios.

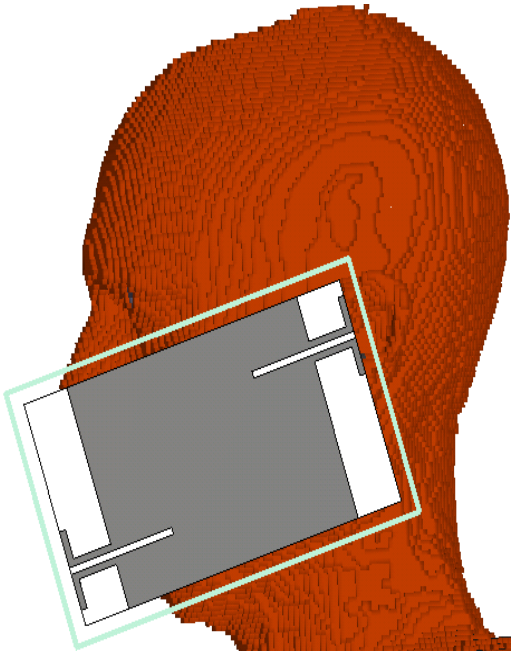

Figure 5-4. Calling positon of a mobile handset without hands.

According to FCC, each transmitting antenna element must be located within 25 mm distance from the surface or edge when mobile handset antennas support hotspot mode operations. Both antenna elements were designed and fabricated in line with FCC requirements [14]. In this current design of MIMO antenna for mobile handset, one antenna element is placed on lower bottom facing the lower left cheek and other antenna element is placed far end of ground plane in order to minimise coupling as shown in Figure 5-1.

After setting up the assessment configuration, standalone mode is tested in all four frequency bands. Both FCC and ICNIRP guidelines were used for comparison with current findings. It is worth mentioning that Europe follow the ICNIRP guidelines which are relax in term of basic restrictions limits. But in other part of the world mostly follow FCC standard which are stricter in setting basic restrictions limits. Therefore, results are evaluated using two different averaging methods namely: 10 g (ICNIRP) and 1 g (FCC) as shown in Figure 5-5.

When MIMO mobile handset antenna-1 (port 1) operates in standalone mode, relatively higher level of EM absorption noticed in lower frequency bands. In the literature, it has been found, generally increasing the ground plane size can reduce the EM absorption on human body [13, 23, 24]. But in this study, antenna-2 (port 2) of MIMO mobile handset is on far end, and facing jaw, and nose part of head model. Strangely maximum SAR from antenna-2 is higher than antenna-1 at 2.6 GHz band as shown in Figure 5-5 (b). Interestingly both antenna

elements are excited from the middle of ground plane on either side of mobile handset as shown in Figure 5-1.

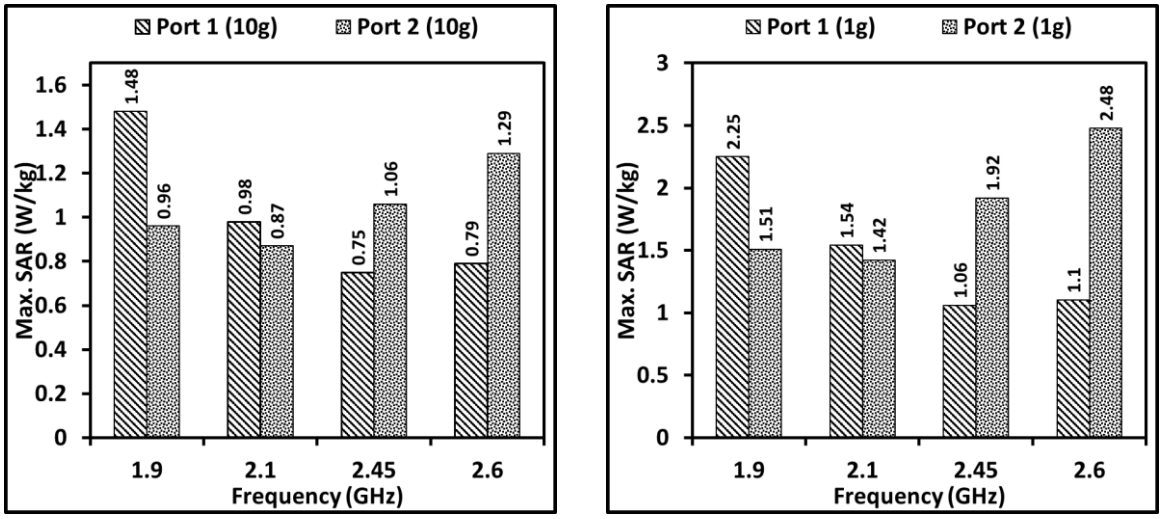

Figure 5-5. Standalone maximum SAR results in calling mode from a MIMO mobile handset antenna; (a) Maximum SAR exposure results in a 10 g cube with maximum limit is 2 Wkg^{-1}; (b) Maximum SAR in 1 g cube with maximum limit is 1.6 Wkg^{-1}.

SAR distribution resultant from exposure from antenna-1 and antenna-2 in standalone mode is represented in Figure 5-6 and Figure 5-7. One of the possible source of higher maximum SAR values is feeding point. Antenna-2 feeding point is very close to the top left cheek where the maximum SAR is observed at 2.6 GHz. Another important factor to consider is the gain of antenna elements and field distribution including E- and H-fields at different frequencies which results in different level of maximum SAR values. In addition, it has been noticed that the chassis mode of antenna-1 is stronger at low frequencies. But for antenna-2 chassis mode is stronger at higher frequencies. Therefore, higher maximum SAR values are observed at low and high frequencies from antenna-1 and antenna-2, respectively.

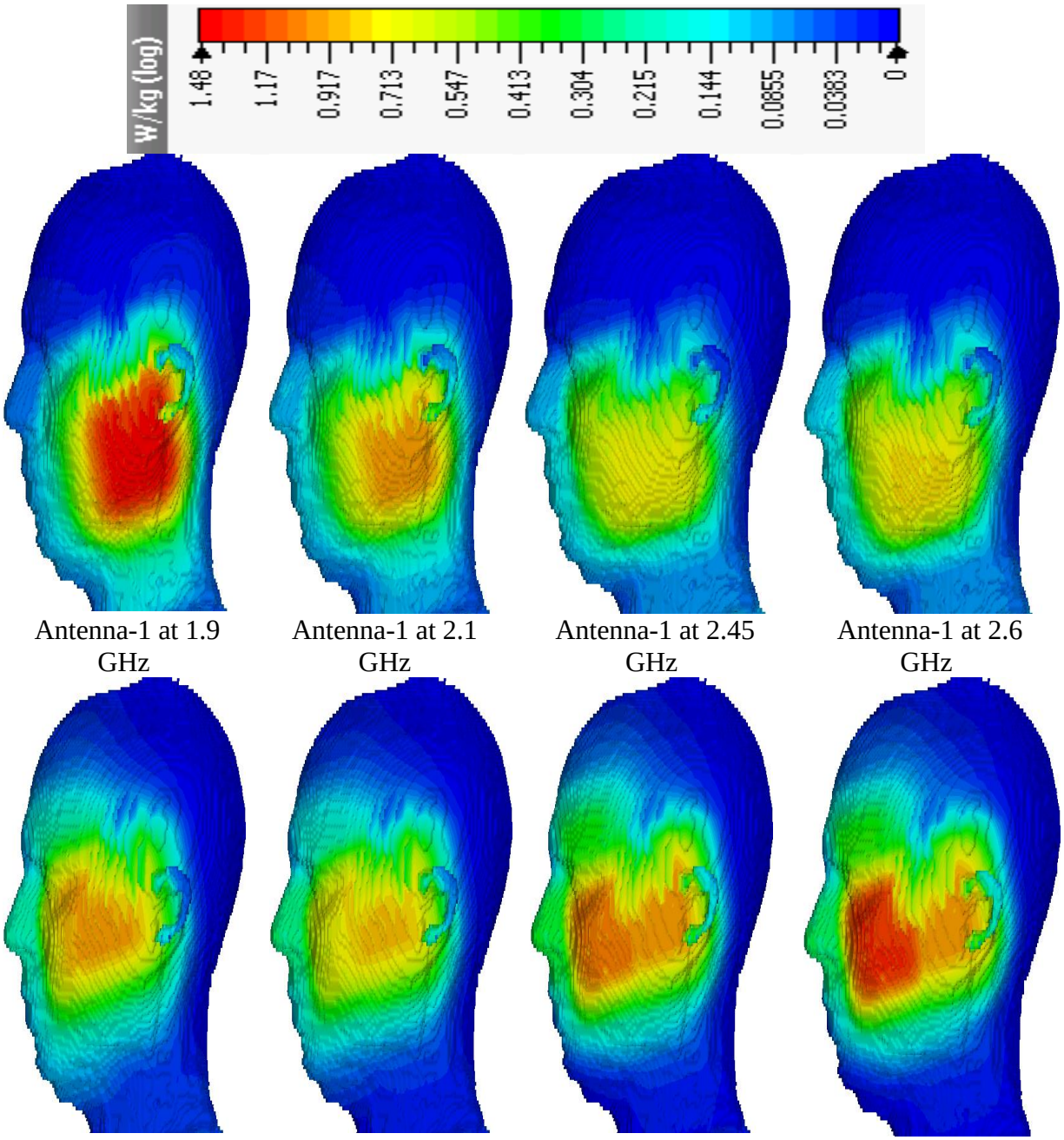

Figure 5-6. Maximum SAR distribution in calling mode over 10 g cube from MIMO mobile handset antenna when operating in standalone mode at four frequency bands.

Maximum SAR values are calculated in 10 g (as shown in Figure 5-6) and 1 g (as shown in Figure 5-7) cube due to different averaging method as mention before. In the case of 10 g cube averaging method, maximum SAR values found very close to basic restriction level. The highest maximum SAR values noticed at 1.9 GHz band which is 1.48 Wkg^{-1}. It is worth mentioning that the basic restrictions limit for general public set by ICNIRP over 10 g cubes is 2 Wkg^{-1} and the maximum SAR value at 1.9 GHz band is very close to that limit.

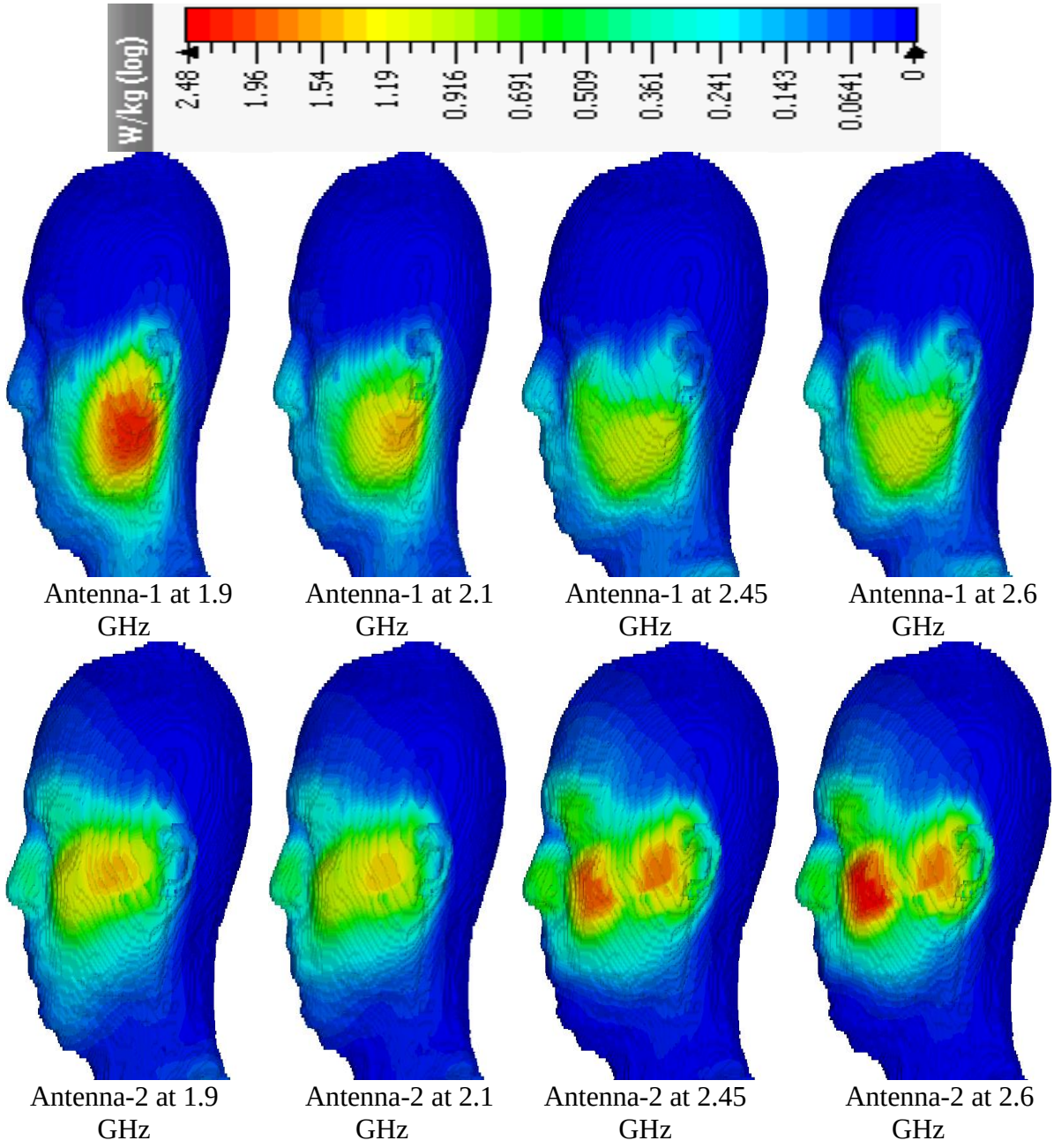

Figure 5-7. Maximum SAR distribution in calling mode over 1 g cube from MIMO mobile handset antenna when operating in standalone mode at four frequency bands.

On the other hand when the SAR estimation is performed over 1 g cube, the absorption levels found much higher than the FCC basic restriction levels. The highest maximum SAR values are again noticed at 1.9 and 2.6 GHz band from antenna-1 and antenna-2 respectively. Identical SAR distribution behaviour of MIMO mobile handset antenna noticed when averaging performs over 1 g cube (as shown in Figure 5-7) in comparison with when averaging performs over 10 g cube (as shown in Figure 5-6). The estimated SAR values are 2.25 Wkg^{-1} and 2.48 Wkg^{-1} at 1.9 GHz from antenna-1 and 2.6 GHz from antenna-2, correspondingly. The

results indicates that maximum SAR (1g) values are above the FCC guidelines, which is in line with reference [20].

5.3.1.2 Standalone SAR in Body-Worn Configuration

Standalone mode is further investigated in body-worn configuration. Flat phantoms have been used to simplify the SAR estimation from mobile handsets. These muscle equivalent phantoms are usually used to consider the mobile handset effects on trunk and limbs of human body. Due to the limitation of measurements in complex heterogeneous model, flat phantom become a better choice as preferred in international guidelines (IEEE-1528 std).

In body-worn assessment configuration, flat phantom dimensions are set to 150 mm x 364 mm x 398 mm (as shown in Figure 5-8) with two-third muscle-equivalent properties assigned to it. The size of flat phantom is kept relatively larger due to bigger form factor of MIMO mobile handset. According to international standards and literature there is no minimum size requirement for flat phantom but size is usually set larger than mobile handset body in order to study the SAR performance. In one of recent studies body-worn case is assessed with 225 mm x 150 mm x 150 mm flat phantom dimensions [18].

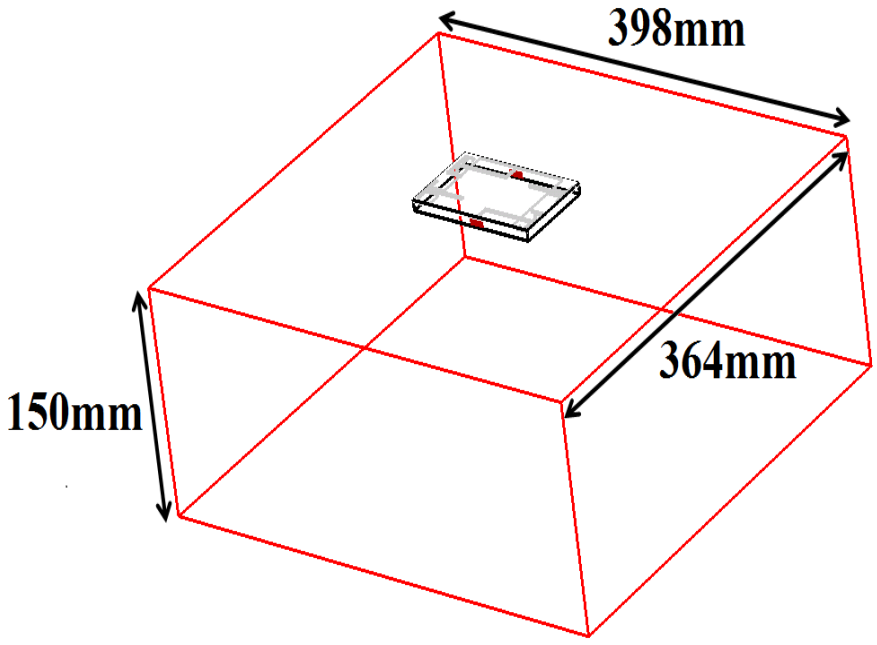

Figure 5-8: Flat muscle-equivalent model with separation distance of 5 mm from MIMO mobile handset antenna with dimensions of 398 mm x 364 mm x 150 mm.

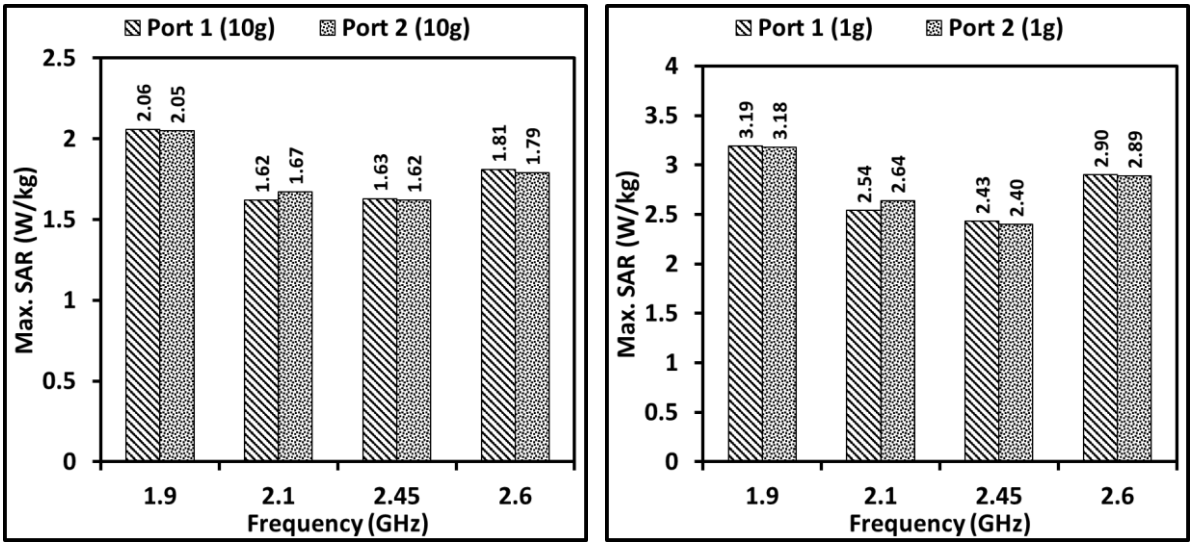

Figure 5-9. Standalone maximum SAR results in body-worn mode from a MIMO mobile handset antenna; (a) Maximum SAR exposure results on 10 g cube with maximum limit is 2 Wkg^{-1}; (b) Maximum SAR on 1 g cube with maximum limit is 1.6 Wkg^{-1}.

In body-worn exposure scenario, the distance between MIMO mobile handset antenna and flat phantom is set to 5 mm corresponds to the worst body exposure scenario. Although in recent studies 3 mm distance is tested in body-worn case [18, 19]. But FCC standards define 5-10 mm distance between the antenna and flat phantom when analysing hotspot mode or body worn case [17].

When MIMO mobile handset set to operate in standalone mode in body-worn case, the EM absorption level on flat phantom from antenna-1 and antenna-2 is almost identical as shown in Figure 5-9. It can be seen maximum SAR values are significantly higher than the recommended limits and these findings are in line with reference [20]. It has been noticed that efficiency of both antennas hugely effected by the presence of flat phantom in near vicinity. The efficiency of both antennas reduces approximately by 60 %.

It is quite evident from both calling mode and body-worn exposure that highest level of SAR values were found at lower frequencies (1.9 GHz) in majority of scenario except when 1 g averaging performed at 2.6 GHz band from antenna-2. This difference is due to two different averaging methods used and also the gain of antenna wasn't similar. It is worth mentioning that chassis mode almost has identical effect on flat phantom when MIMO mobile handset operates in standalone mode. However, the behaviour of chassis mode changes with human body shape (as noticed in calling mode exposure).

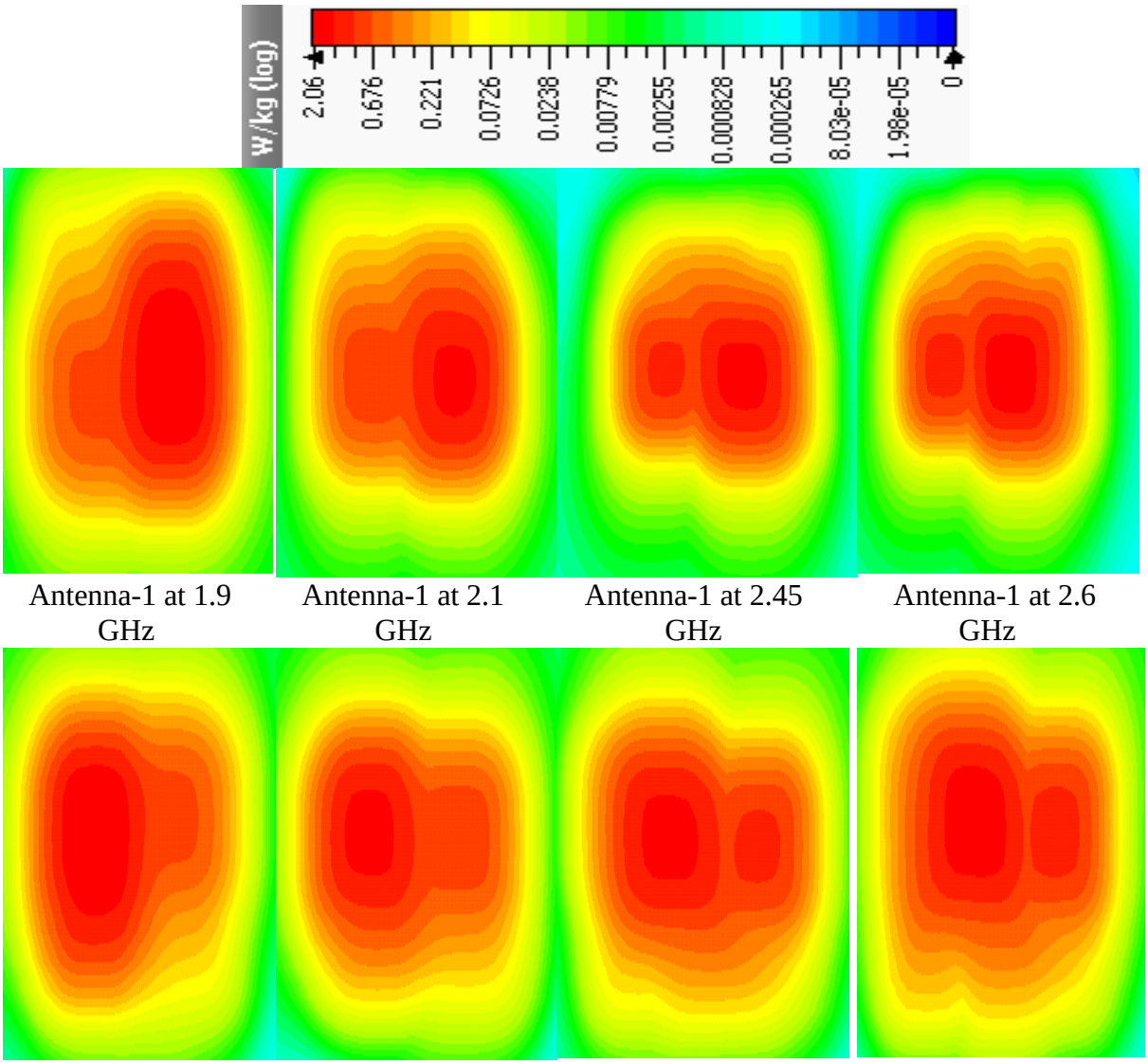

Figure 5-10. Maximum SAR distribution in body-worn mode over 10 g cube from MIMO mobile handset antenna when operating in standalone mode at four frequency bands.

The maximum SAR distribution indicates that MIMO mobile handset antenna in standalone mode is vulnerable for health in the close proximity of human body as shown in Figure 5-10 and Figure 5-11. When SAR estimation performed over 10 g and 1 g cube, EM absorption levels within the flat phantom found much higher than the basic restriction limits. It is also evident that maximum SAR is higher in body-worn case (flat phantom) as compared to calling mode scenario.

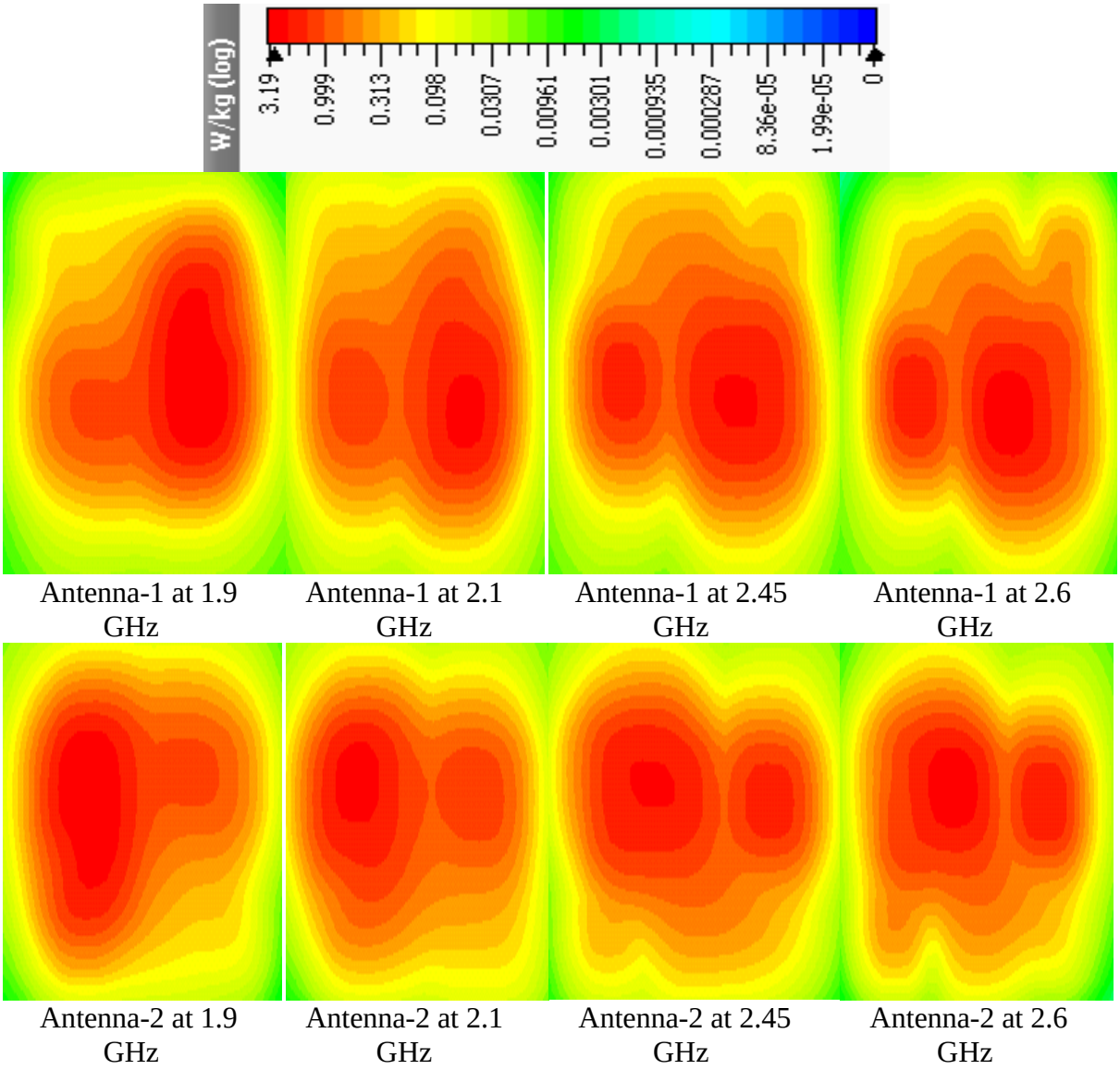

Figure 5-11. Maximum SAR distribution in body-worn mode over 1 g cube from MIMO mobile handset antenna when operating in standalone mode at four frequency bands.

5.3.2 SAR Assessment on Simultaneous Mode

Another mode of MIMO technology is simultaneous excitation mode or MIMO mode. The MIMO mode is completely different from SISO mode. In this mode multiple antennas operates simultaneously. The SAR assessment is performed when MIMO mobile handset antenna set to operates in simultaneous excitation mode. The SAR estimation is divided in two different configuration i.e. calling mode and body-worn exposure scenarios.

5.3.2.1 Simultaneous SAR in Calling Mode

In this assessment configuration, MIMO mobile handset antenna was placed next to the head model in calling mode similar to standalone calling mode configuration as shown in

Figure 5-4. The MIMO mobile handset antenna set to operates in simultaneous excitation mode on four different frequency bands. SAR estimation was performed when both antennas of MIMO mobile handset operate simultaneously on same frequency band. The calculated maximum SAR values over 10 g cube was found lower than the maximum SAR values calculated over 1 g cube as shown in Figure 5-12. The maximum SAR values were also found much lower than the basic restriction limits. Highest maximum SAR values observed at 1.9 GHz over both averaging methods (10 g and 1 g). These finding are in line what was reported in previous standalone calling mode exposure configuration. It is worth mentioning that maximum SAR value on 1 g cube was found much higher than the basic restriction level at 1.9 GHz band.

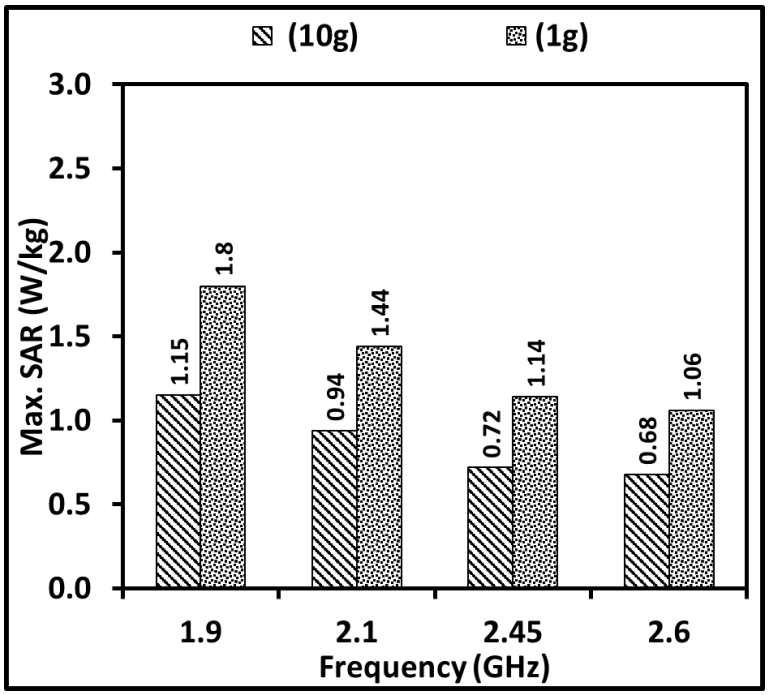

Figure 5-12. Maximum SAR results in calling mode from a MIMO mobile handset antenna in simultaneous excitation mode; Maximum SAR exposure results over 10 g and 1g cube with maximum limits are 2 Wkg^{-1} and 1.6 Wkg^{-1}, respectively.

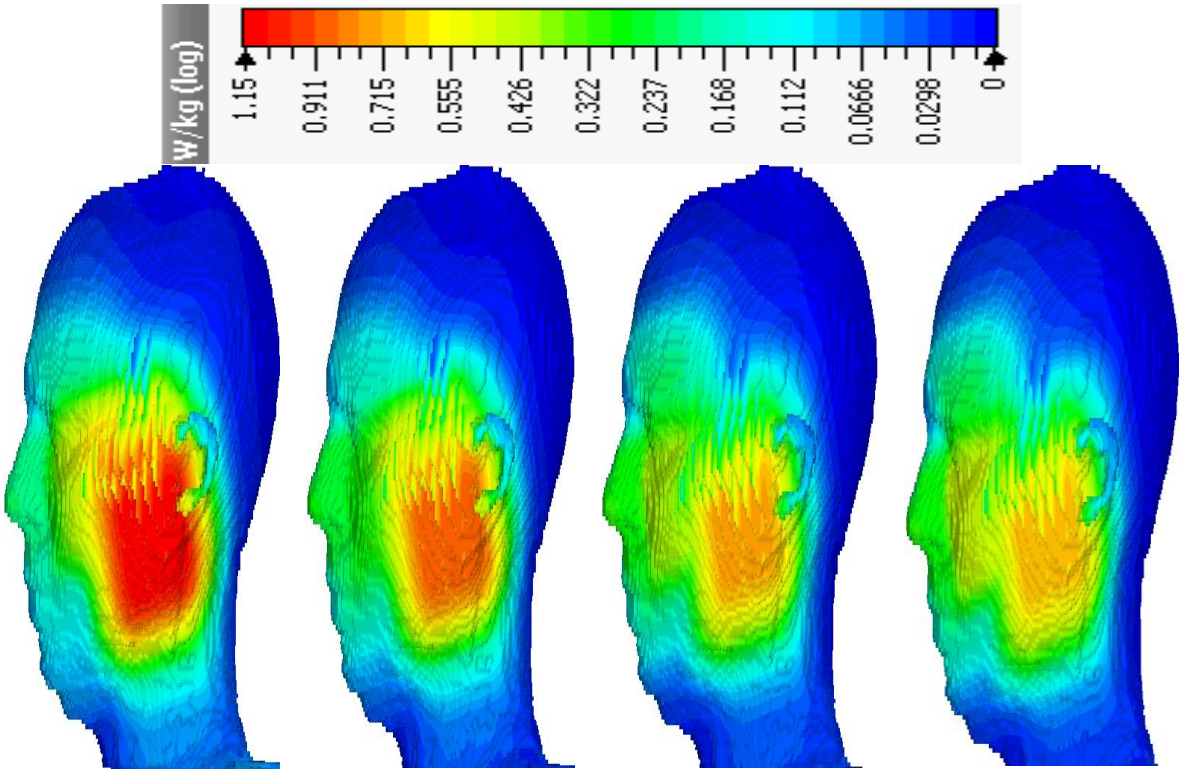

(a) 1.9 GHz **(b)** 2.1 GHz **(c)** 2.45 GHz **(d)** 2.6 GHz

Figure 5-13. Maximum SAR distribution in calling mode over 10 g cube from MIMO mobile handset antenna when operating in simultaneous excitation mode at four frequency bands.

It has been noticed that when MIMO mobile handset operates in simultaneous mode power distributes among its antenna elements. So power distribution among '*n*' antenna elements can be mathematically represented by:

$$P_n = R_n P_{total} \qquad \text{(Equation 5.1)}$$

Where P_n is the power in '*n*' antenna element, P_{total} is the total power in the system, and R_n is a real constant with range between $0 \leq R_n \leq 1$. R_n is dependent on the total power of system and can be calculated for each antenna elements by equation given below:

$$R_n = \frac{1}{N} \qquad \text{(Equation 5.2)}$$

Where N is the total number of antenna elements in the system.

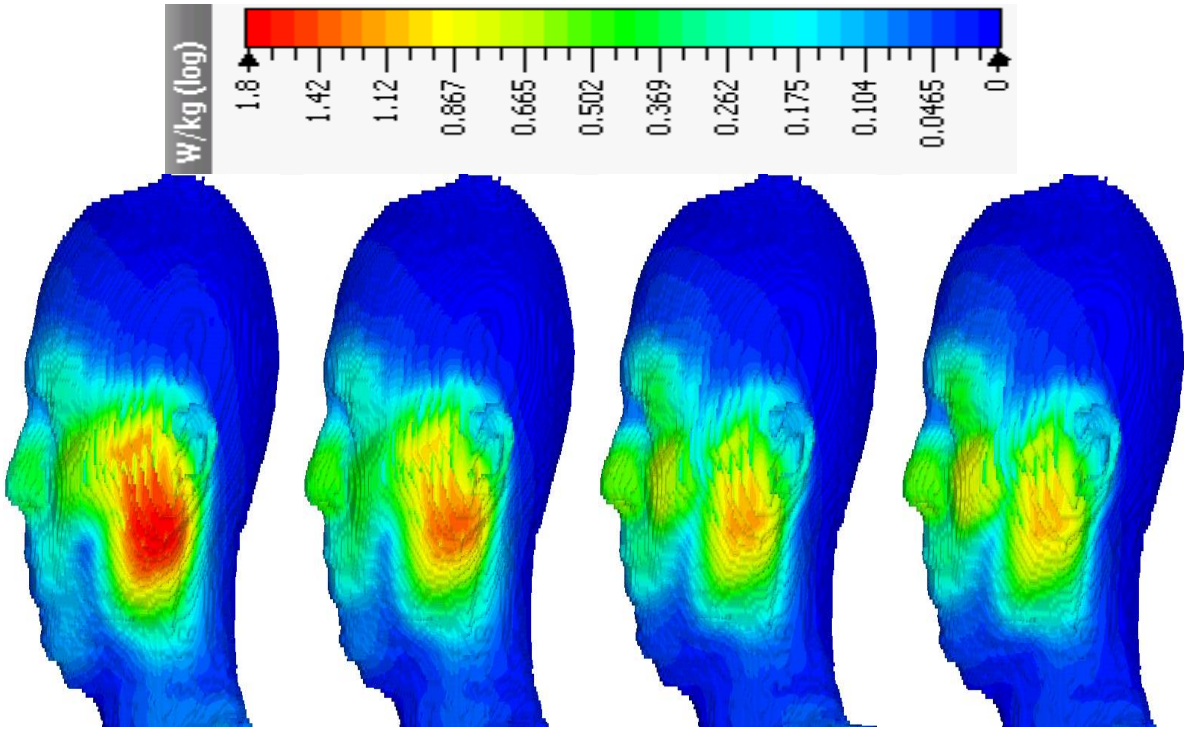

(a) 1.9 GHz **(b)** 2.1 GHz **(c)** 2.45 GHz **(d)** 2.6 GHz

Figure 5-14. Maximum SAR distribution in calling mode over 1 g cube from MIMO mobile handset antenna when operating in simultaneous excitation mode at four frequency bands.

On the other hand, in standalone mode each antenna element radiates separately with maximum power. Therefore, relatively less absorption noticed in simultaneous excitation mode. Figure 5-13 and Figure 5-14 shows maximum SAR distribution in simultaneous excitation mode. It was found that chassis mode plays crucial role in getting high maximum SAR values such as at 1.9 GHz band. H-field distribution is another important factor in getting higher SAR values. H-field on ground plane of MIMO mobile handset is a main source of inducing SAR. Due to strong chassis mode at 1.9 GHz band maximum SAR distribution is concentrated along the body of mobile handset which is causing highest absorption in terms of SAR values.

5.3.2.2 Simultaneous SAR in Body-Worn Configuration

In this assessment configuration body-worn exposure scenario is investigated on flat phantom, when MIMO mobile handset antenna operates in simultaneous excitation mode. The mobile handset antenna place 5 mm above the flat phantom as shown in Figure 5-8. The MIMO mobile handset antenna set to radiates at its maximum power levels and SAR values are then calculated as shown in Figure 5-15. Similar trend of SAR distribution observed on flat phantom

in comparison with calling mode exposure scenario under same operating mode (MIMO mode). The highest maximum SAR values was found in lower frequency band i.e. 1.9 GHz and maximum SAR values follows the falling trend with increase in frequency.

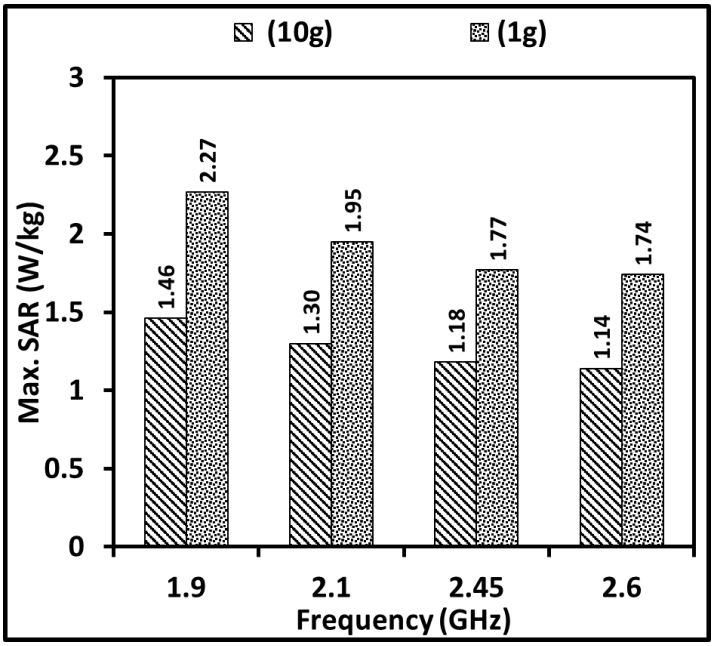

Figure 5-15. Maximum SAR results in body-worn mode from a MIMO mobile handset antenna in simultaneous excitation mode; Maximum SAR exposure results over 10 g and 1 g cube with maximum limits are 2 Wkg^{-1} and 1.6 Wkg^{-1}, respectively.

SAR estimation was performed on both 10 g and 1 g cube in order to compare the compliance with international standards. It was found that maximum SAR values over the 10 g cube are very close but under the basic restriction limits for general public exposure set by ICNIRP as shown in Figure 5-15. On the other hand, maximum SAR values over 1 g cube at all four frequency bands were found higher than the maximum permissible limit set by the FCC. SAR distribution is almost identical from both antenna elements and evenly distributed when averaging performed over 10 g and 1 g cube. The EM absorption levels were found much in 1 g cube as compared to 10 g cube as shown in Figure 5-16 and Figure 5-17.

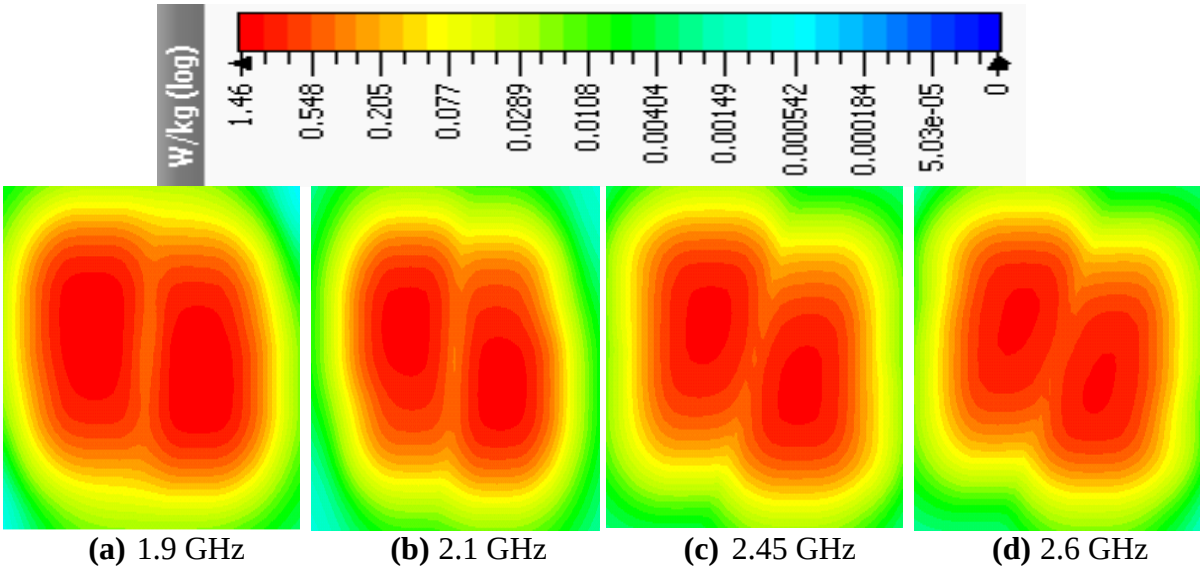

(a) 1.9 GHz **(b)** 2.1 GHz **(c)** 2.45 GHz **(d)** 2.6 GHz

Figure 5-16. Maximum SAR distribution in body-worn mode over 10 g cube from MIMO mobile handset antenna when operating in simultaneous excitation mode at four frequency bands.

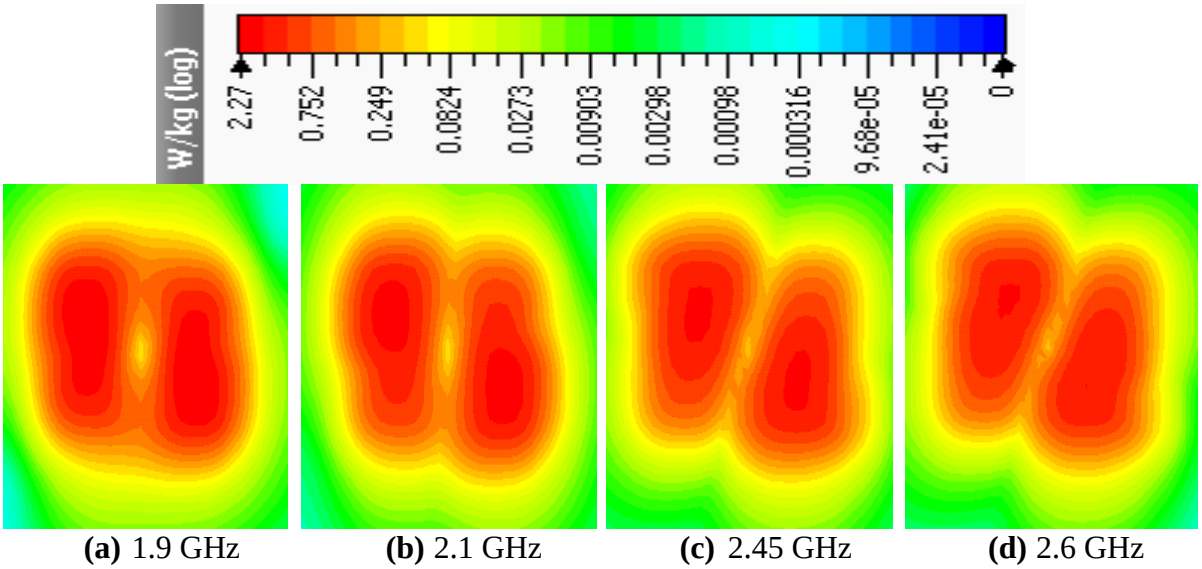

(a) 1.9 GHz **(b)** 2.1 GHz **(c)** 2.45 GHz **(d)** 2.6 GHz

Figure 5-17. Maximum SAR distribution in body-worn mode over 1 g cube from MIMO mobile handset antenna when operating in simultaneous excitation mode at four frequency bands.

5.3.3 SAR Assessment on Beam Steering Mode

In this section, concept of beam steering is realised on MIMO mobile handset antenna. Beam steering on MIMO technology is relatively quiet new concept [21]. For devices with two or more antenna elements operates on same frequency bands. The total E-field, thus SAR, is not only dependent on magnitude of energy absorption inside the body but also relies on the relative phases of signals transmitted from multiple antenna elements [25]. It is because the

total E-field is a vector summation of individual E-fields from two or more antenna elements. In order to calculate SAR of such device (MIMO) with such configuration, SAR needs to evaluate at every relative phase combination of the antennas.

In this assessment configuration, excessive exposure from MIMO mobile handset antenna in beam steering mode was realised by introducing relative phases among the antenna elements of MIMO device sweeping from 0 deg. to 360 deg. with 45 deg. phase step. The phase step kept larger to reduce the number of simulations. Moreover, this concept can only be valid in simultaneous excitation mode, when two or more MIMO antenna elements operate simultaneously on same frequency band.

5.3.3.1 SAR Assessment in Calling Mode using Beam Steering

The assessment configuration kept same used in previous two modes. MIMO mobile handset antenna place next to the left cheek as shown in Figure 5-4. The mobile handset set to operate in simultaneous excitation mode and 45 deg. phase shift is introduced at antenna-2 while keeping the antenna-1 without any phase shift or 0 deg. phase shift. This type of configuration has considerable impact on SAR reduction and at the same time it could be a cause of higher SAR values.

In the Figure 5-18 and Figure 5-19, SAR values were estimated at 1.9 GHz and 2.1 GHz band by employing above mentioned configuration. It was noticed that by introducing phase shift at antenn-2 maximum SAR values significantly reduce (as shown in Figure 5-18). Lowest SAR values obtained when 180 deg. phase shift introduced at 1.9 GHz band. Similarly, lowest SAR values were also observed when phase shift of approx. 135 deg. and 225 deg. introduced into the system at 2.1 GHz band (as shown in Figure 5-19).

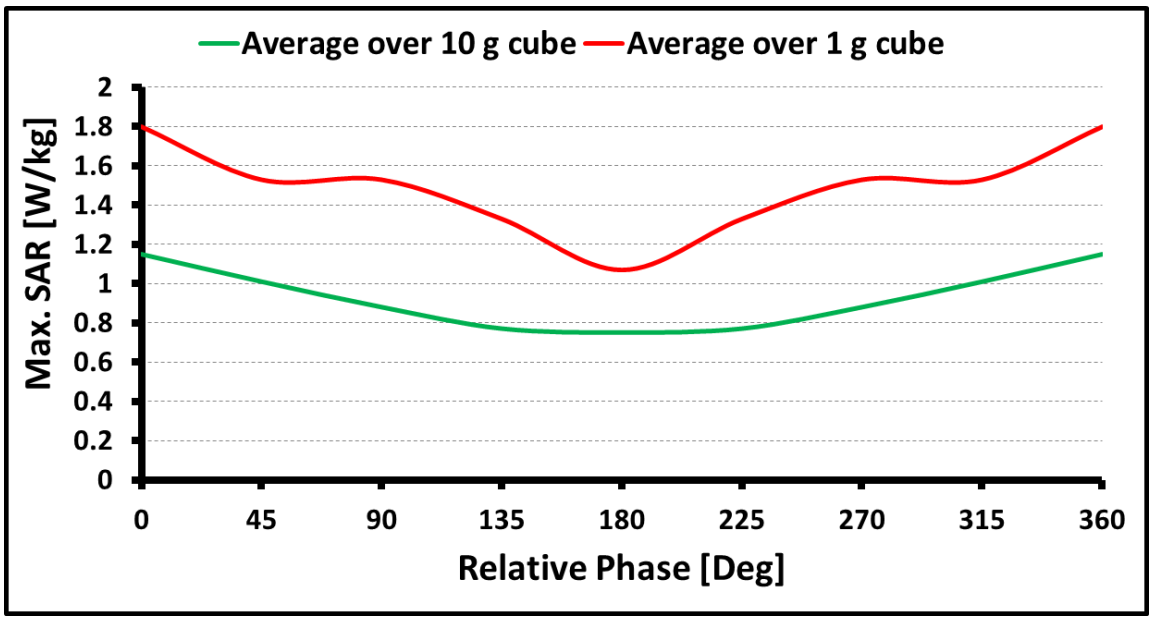

Figure 5-18. Maximum SAR values at **1.9 GHz** band in calling mode with combination of relative phases of both antennas in simultaneous excitation mode when averaged over 1 g and 10 g cube.

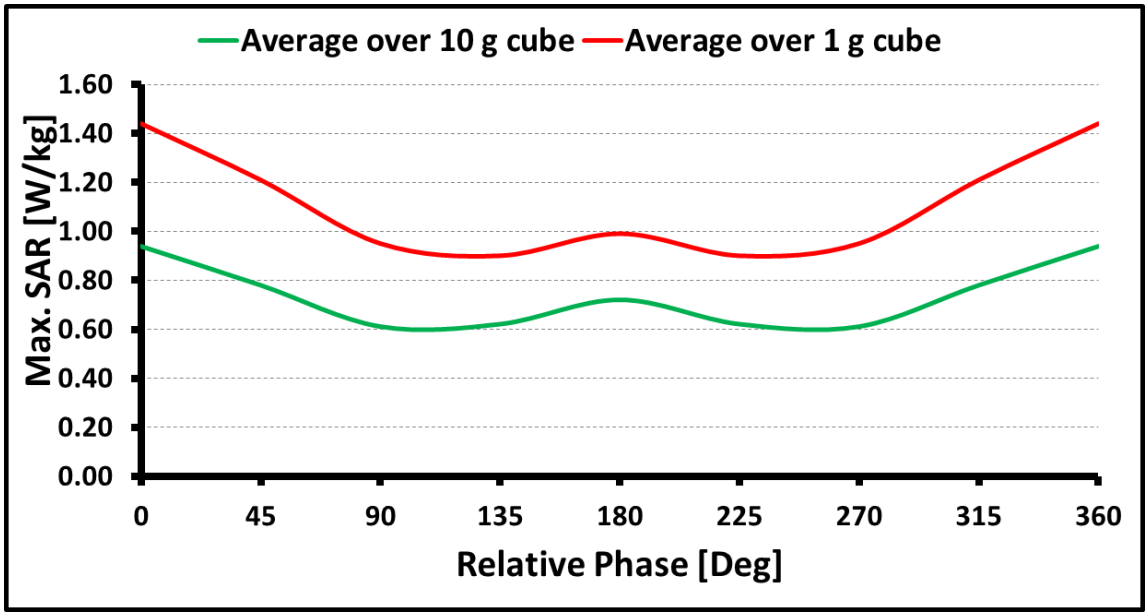

Figure 5-19. Maximum SAR values at **2.1 GHz** band in calling mode with combination of relative phases of both antennas in simultaneous excitation mode when averaged over 1 g and 10 g cube.

Similarly, when phase shift introduced at 2.45 GHz and 2.6 GHz band in calling mode highest maximum SAR values were identified at 180 deg. phase shift in both frequency bands as shown in Figure 5-20 and Figure 5-21. It also worth mentioning that the lowest EM absorption found between 0 to 45 deg. and 315 to 360 deg. phase shift at previous mention frequency band.

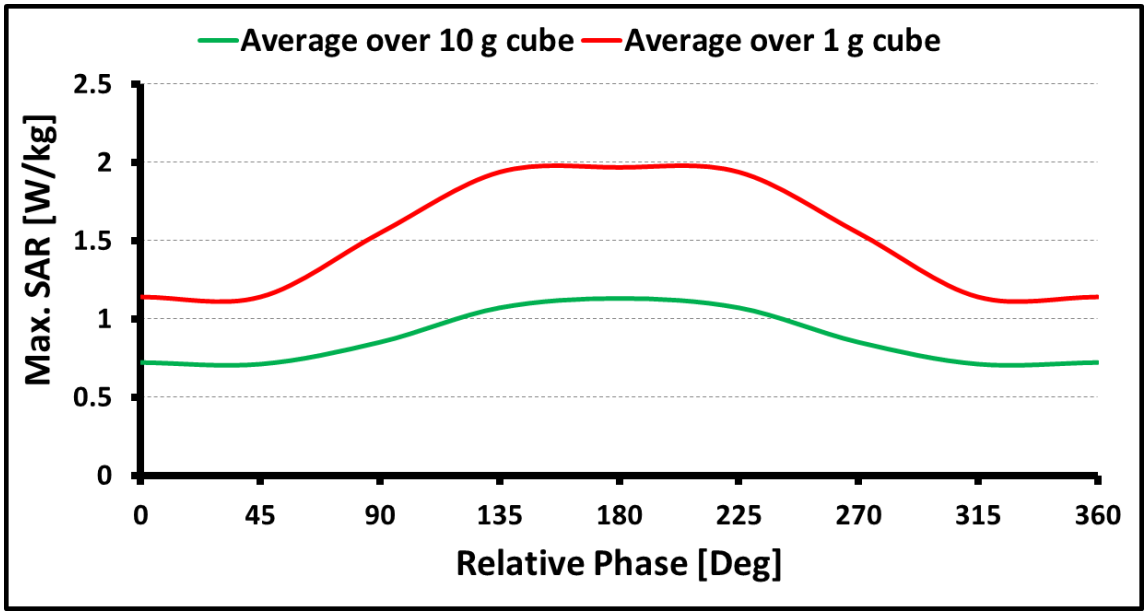

Figure 5-20. Maximum SAR values at **2.45 GHz** band in calling mode with combination of relative phases of both antennas in simultaneous excitation mode when averaged over 1 g and 10 g cube.

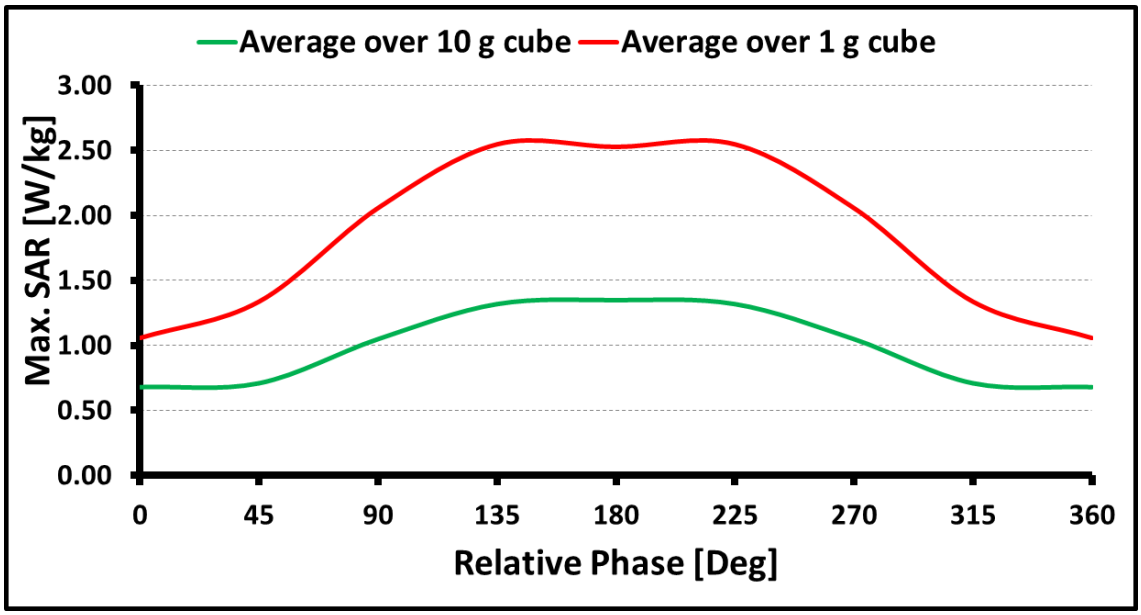

Figure 5-21. Maximum SAR values at **2.6 GHz** band in calling mode with combination of relative phases of both antennas in simultaneous excitation mode when averaged over 1 g and 10 g cube.

5.3.3.2 SAR Assessment in Body-Worn mode using Beam Steering

In this test configuration, phase shift modulation scheme is investigated on flat phantom using MIMO mobile handset antenna. The mobile handset was set 5 mm away from the flat phantom with dimension shows in Figure 5-8. The MIMO mobile handset antenna set to operates in simultaneous excitation mode at previously mention frequency bands with its

maximum power. 45 deg. phase shift was introduced at antenna-2 while keeping antenna-1 unchanged.

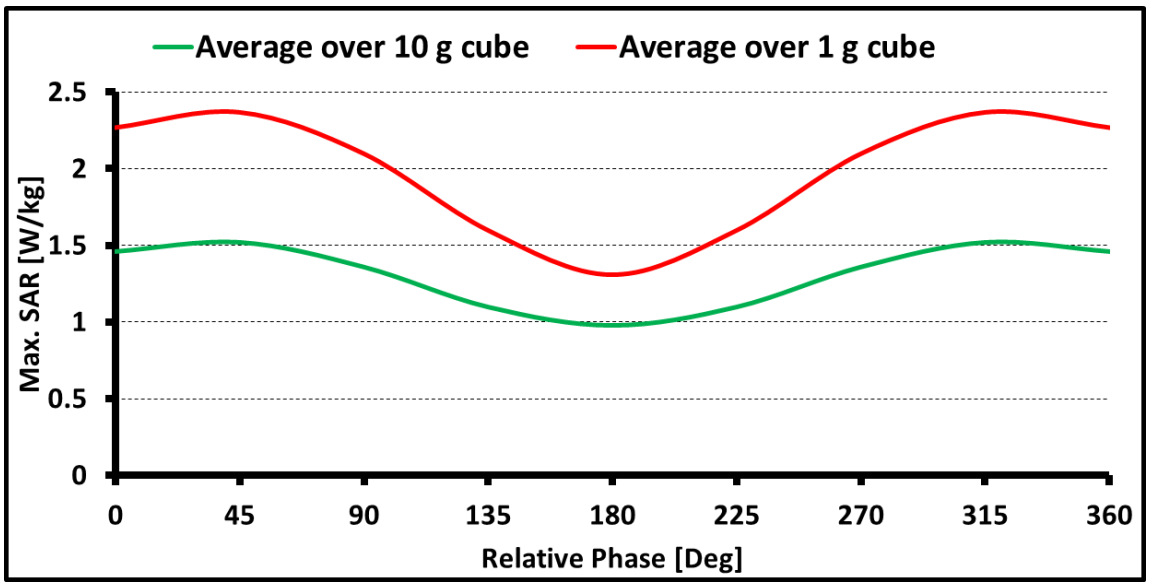

Figure 5-22. Maximum SAR values at **1.9 GHz** band in body-worn mode with combination of relative phases of both antennas in simultaneous excitation mode when averaged over 1 g and 10 g cube.

After introducing the phase shaft at 1.9 GHz and 2.1 GHz band, maximum SAR values follows the same pattern as noticed in calling mode exposure configuration when relative phase of 45 deg. introduced into the system (MIMO mobile handset antenna). At 1.9 GHz band, lowest SAR values observed when phase shift is 180 deg. and highest SAR values detected when phase shift is 45 and 315 deg. (as shown in Figure 5-22). At 2.1 GHz band, lowest SAR values noticed when phase shift is 180 deg. in body-worn mode as shown in Figure 5-19. In comparison with calling mode configuration at same frequency band (2.1 GHz), lowest SAR values found at 135 and 225 deg. as shown in Figure 5-23.

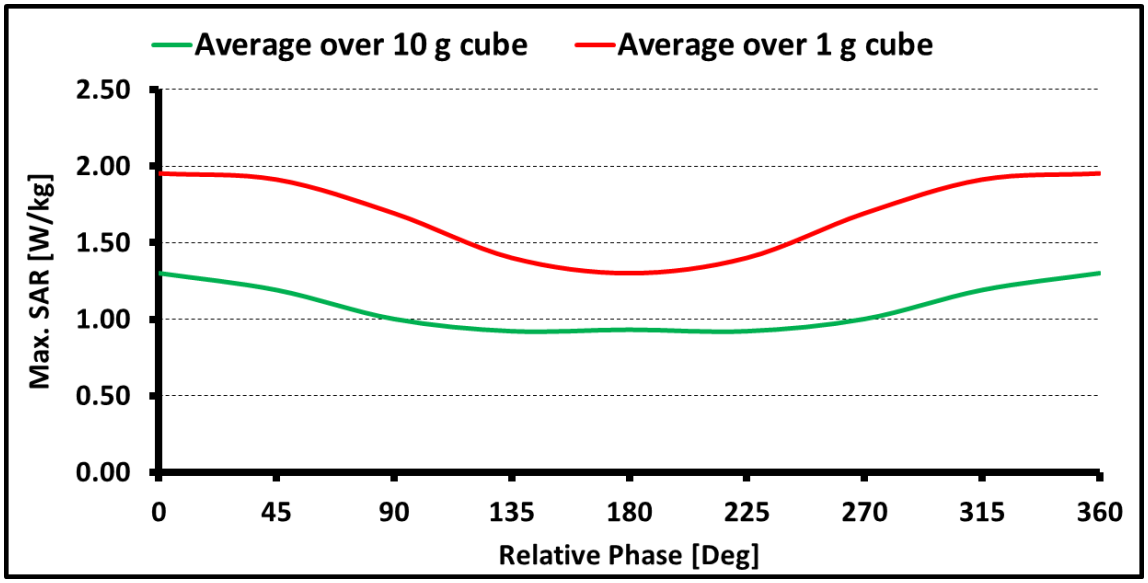

Figure 5-23. Maximum SAR values at **2.1 GHz** band in body-worn mode with combination of relative phases of both antennas in simultaneous excitation mode when averaged over 1 g and 10 g cube.

Similarly, when phase shift of 135 and 225 deg. introduced at 2.45 GHz and 2.6 GHz band in body-worn mode, highest maximum SAR values observed on both frequency bands. At former frequency band (2.45 GHz) the change in maximum SAR values is very small or negligible between 0 to 360 deg. phase shifts as shown in Figure 5-24. In comparison with calling mode exposure configuration at 2.45 GHz band, maximum SAR values change abruptly between 0 to 360 deg. phase shifts (see Figure 5-20). At later frequency band (2.6 GHz), highest maximum SAR values in body-worn mode were observed when phase shift is 135 and 225 deg. as shown in Figure 5-25. Similar SAR values were also noticed at 2.6 GHz band in calling mode configuration on same angles i.e. 135 and 225 deg. (as shown in Figure 5-21).

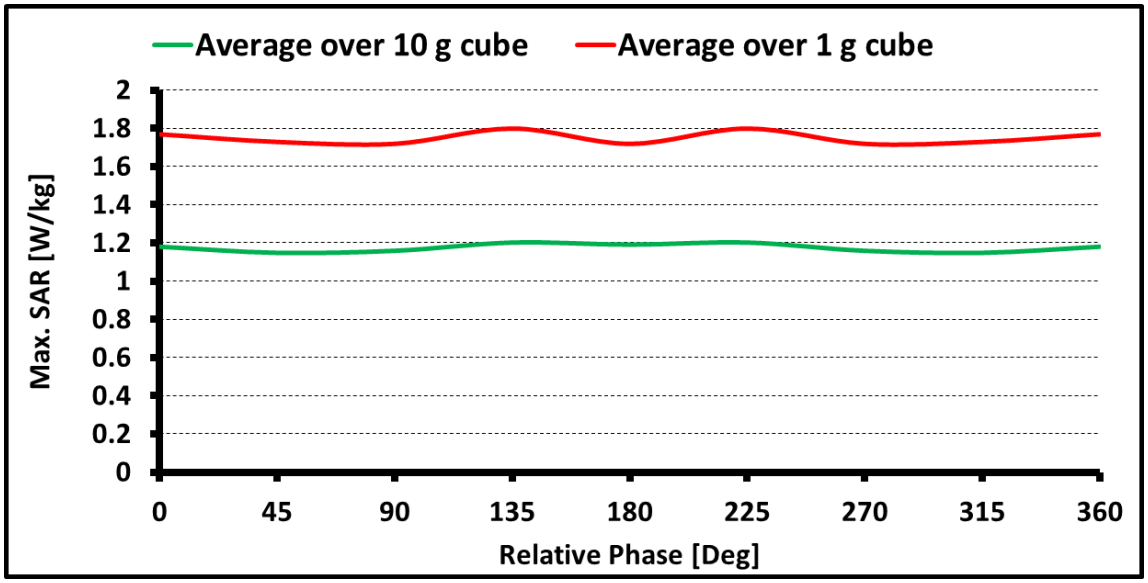

Figure 5-24. Maximum SAR values at **2.45 GHz** band in body-worn mode with combination of relative phases of both antennas in simultaneous excitation mode when averaged over 1 g and 10 g cube.

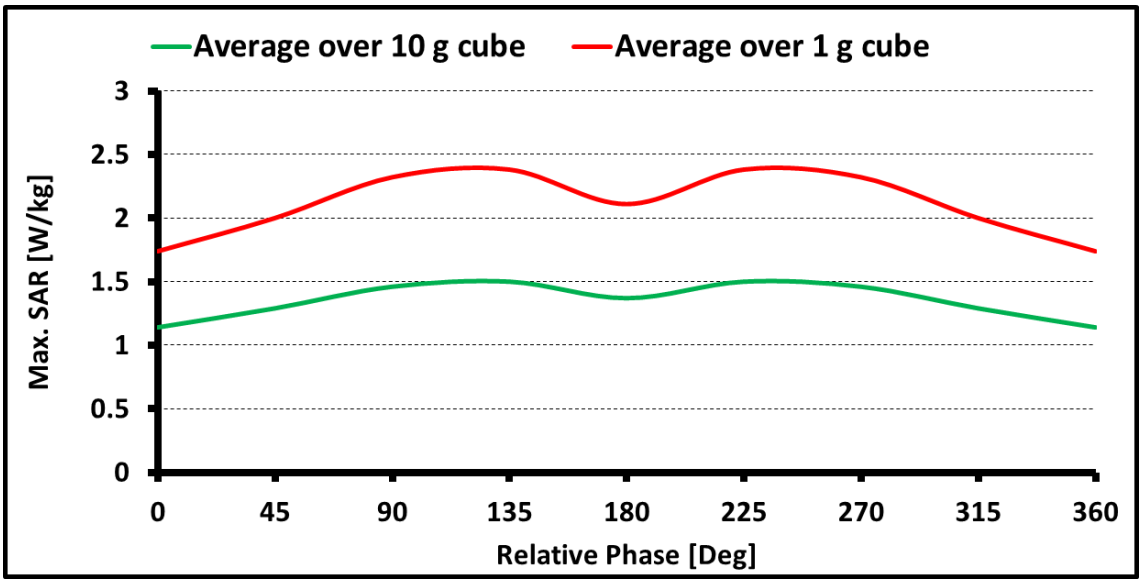

Figure 5-25. Maximum SAR values at **2.6 GHz** band in body-worn mode with combination of relative phases of both antennas in simultaneous excitation mode when averaged over 1 g and 10 g cube.

It is worth mentioning that comparatively lower SAR values observed in body-worn assessment configuration as compared to calling mode exposure scenario when relative phases were introduced in MIMO mobile handset antenna. The EM absorption levels in calling mode can reach approx. up to 2.5 Wkg^{-1} over 1 g cube which is almost twice higher than the basic restriction levels set by FCC for public. However, maximum SAR values found much lower than the basic restriction level provided by ICNIRP when averaging performed over 10 g cube.

5.4 Comparison between Measurements and Simulations

In this section, comparison were made between the simulated and measured transmission coefficient (S21) in order to validate the different MIMO configuration findings from previous sections. For this purpose, a monopole probe was designed in CST MWS. The monopole probe was designed using coaxial cable (RG402) to operate at 2.45 GHz band. The outer, dielectric and inner diameter of coaxial cable was 3.58, 2.97 and 0.91 mm respectively. The prototype of monopole probe and dimension are given in Figure 5-26.

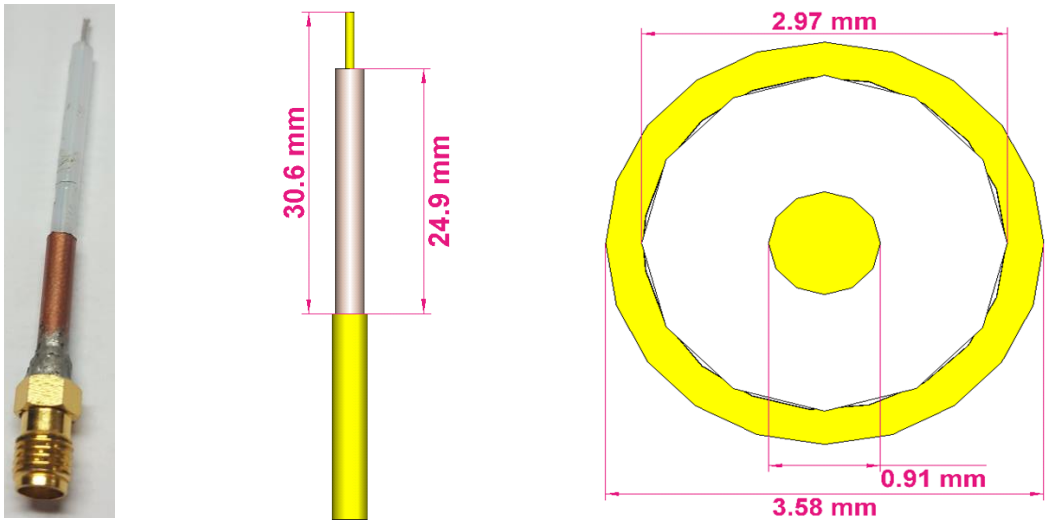

(a) Prototype **(b)** Side view (c) Top view

Figure 5-26. Dimensions of monopole probe; where it radiates $\lambda/4$ wavelength at **2.45 GHz**.

The comparison between simulated and measured S-parameters are given in Figure 5-27. The measured S-parameters indicates monopole probe operates between 2.1 GHz to 2.55 GHz band which cover the WLAN band. All the S-parameters was calculated below -6 dB. The monopole probe radiate at $\lambda/4$ wavelength. After validating the probe, it was later used to scan the MIMO mobile handset antenna when operating at 2.45 GHz band in order to calculate S21 at different location on mobile handset antenna.

In the experimental setup, S21was calculated by scanning the MIMO mobile handset antenna in far-field. The measurements were conducted in far-field due to the reason that proposed monopole probe doesn't operate well in near-field due to its bad isolation with MIMO mobile handset antenna. Therefore, far-field measurements were conducted to validate the findings of this study.

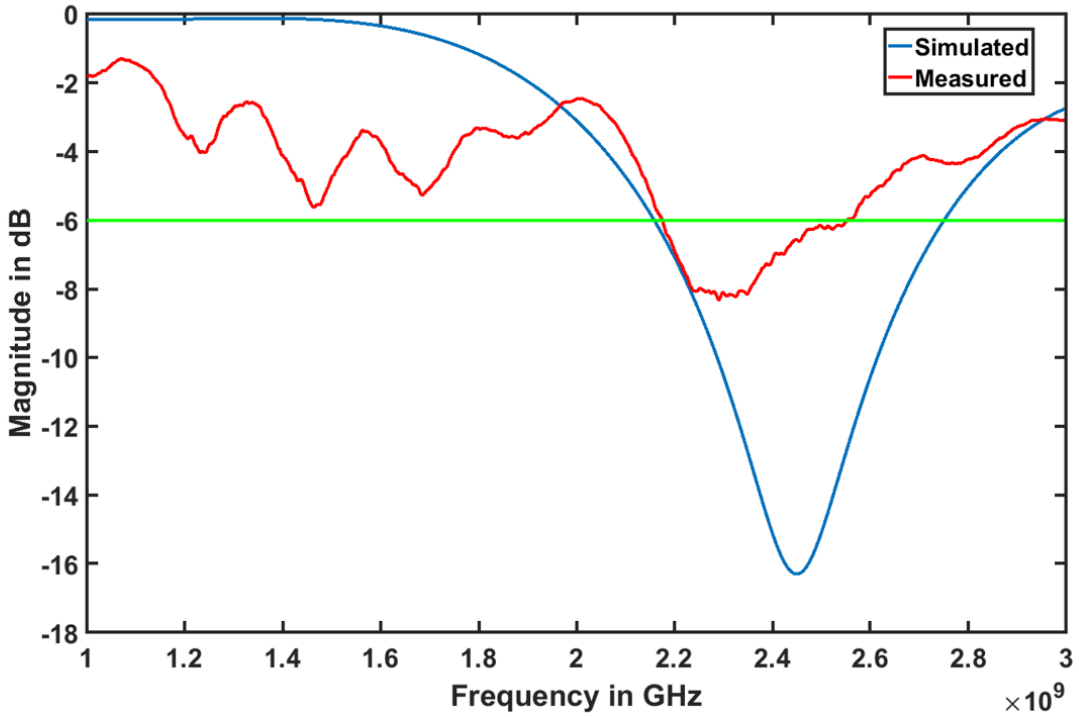

Figure 5-27. Comparison between simulated and measured S11 of E-field monopole probe when operating at **2.45 GHz**. The S11 was calculated below -6 dB and covers frequency range between 2.1 to 2.55 GHz.

For this purpose, Rohde and Schwarz 24 port VNA was calibrated using electronic calibration kit in order to remove any error if there is any in the cables or system. One port of MIMO mobile handset antenna was connected with VNA and other port was terminated with 50-ohm load. In this way MIMO mobile handset antenna SISO mode configuration was realised. The monopole probe was connected with other port of VNA. The probe was placed on automatic position system in order to scan the MIMO mobile handset antenna in number of steps. The experiment setup is shown in Figure 5-28. Similar configuration was used in simulation as shown in Figure 5-29 in order to do fare comparison.

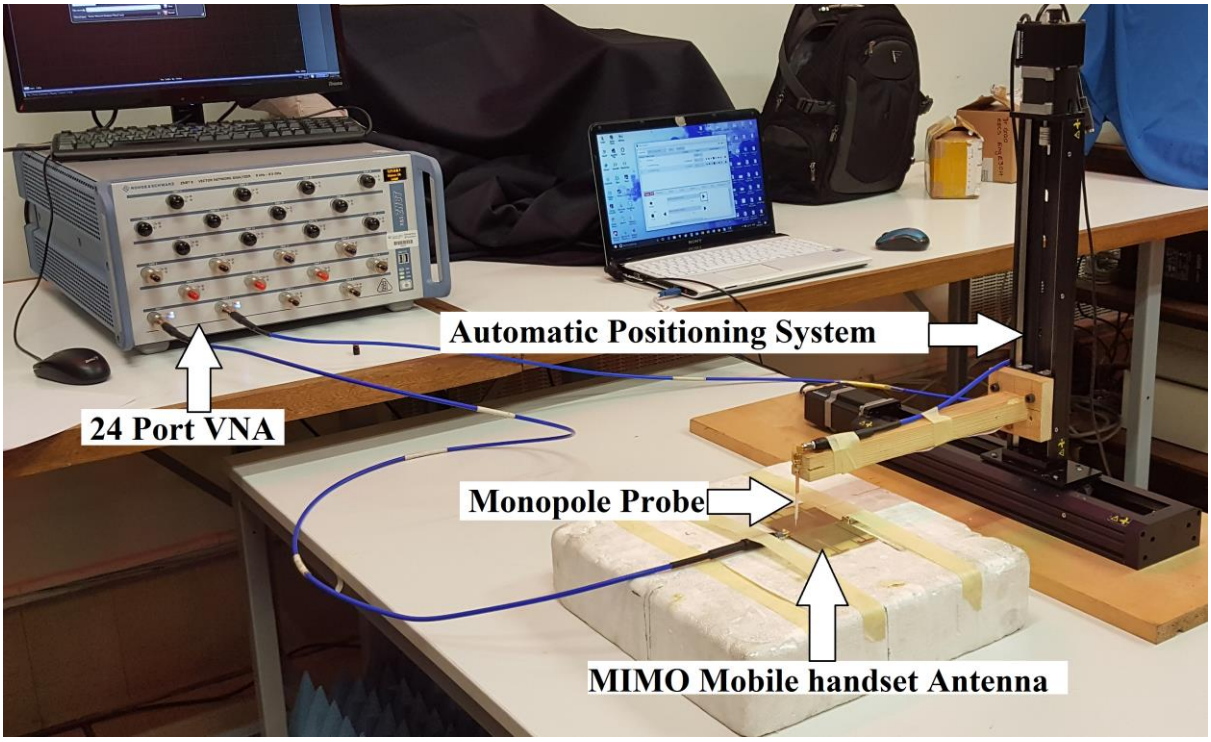

Figure 5-28. Experimental setup of MIMO mobile handset antenna scanning using monopole probe.

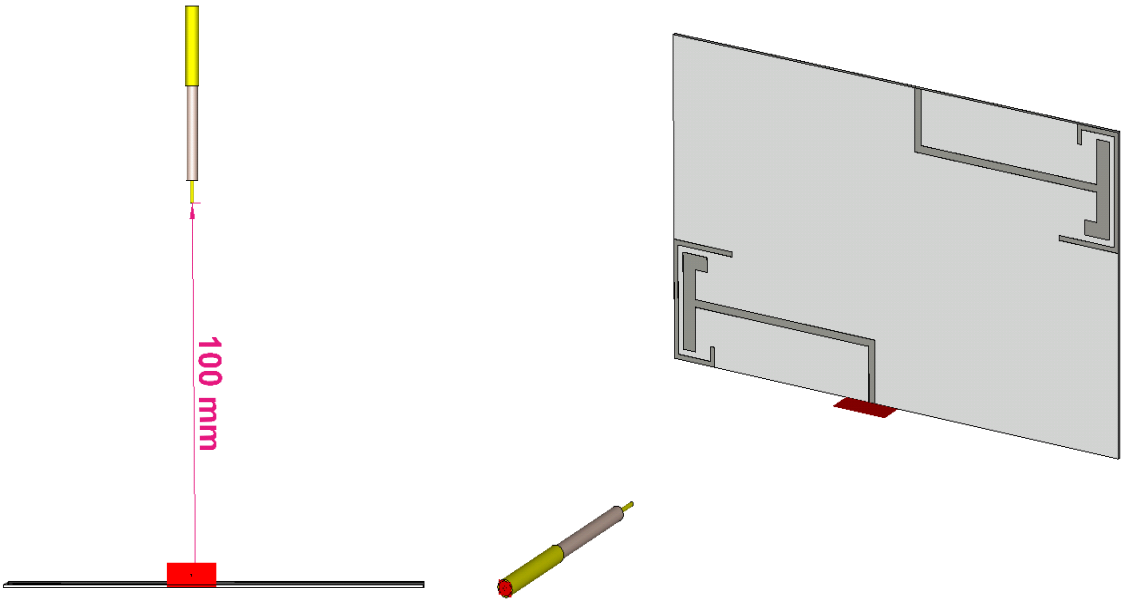

(a) Front view (b) Prospective view

Figure 5-29. Simulation setup of MIMO mobile handset antenna scanning using monopole probe; where the distance between the monopole probe and MIMO mobile handset was set to 10 cm.

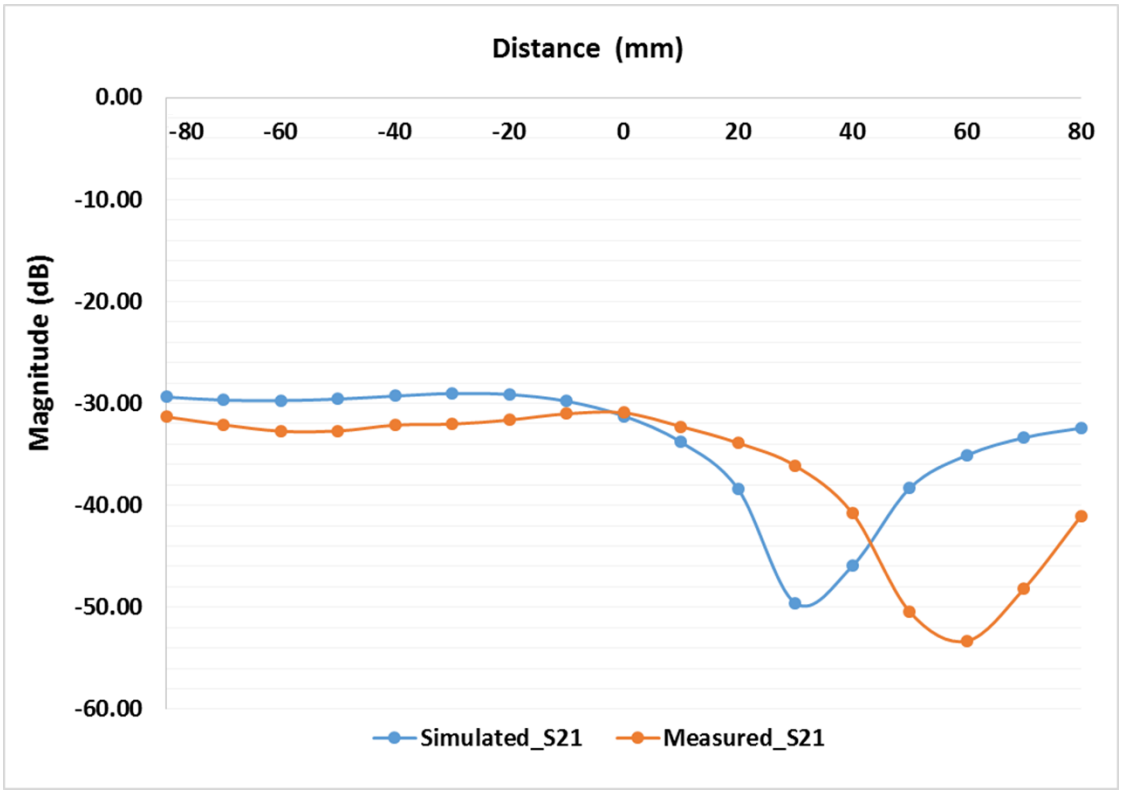

Figure 5-30. Comparison between simulated and measured S21 in far-field. S21 calculated at 17 different point on MIMO mobile handset; where 0 mm distance represents location at the centre of the MIMO mobile handset by keeping 10 cm distance between both probe and antenna.

The S21 was collected by moving the monopole probe in 10 mm steps on either side of MIMO mobile handset (positive *x*-axis and negative *x*-axis), where 0 mm distance represents the probe location at the centre of the MIMO mobile handset antenna. The calculated S21 in numerical simulations matches fairly well with measurements as shown in Figure 5-30. There was slight shift noticed in measurements which is due to very poor fabrication of monopole probe as can be seen in Figure 5-26. The monopole probe was fabricated with hands including the cutting of solid materials etc. Therefore, such differences are expected to be appear in measurements.

5.5 Chapter Summary

In this chapter, specific absorption rate (SAR) assessment from MIMO mobile handset is investigated. The MIMO mobile handset has various operating mode such as standalone mode, simultaneous excitation mode and also new phase modulation schemes can be employed in order to achieve better signal strength and gain. The SAR estimation is performed at all three modes of MIMO mobile handset in three exposure configurations such as calling mode and body-worn case by setting the MIMO mobile handset at its maximum power. It was found that standalone mode produce higher SAR values as compared to simultaneous excitation mode. The maximum SAR values in standalone mode are significantly higher than the recommended limits and these findings are in line with reference [20]. The main source of higher SAR values is the fields around the feeding point in the standalone mode.

On the other hand, H-fields distribution on ground plane is stronger in simultaneous excitation mode which is main source of SAR values in this mode. The phase modulation scheme predicts the lowest and highest SAR values can be achieved. It's also worth mentioning that in most cases SAR values are much higher than the basic restriction levels set by international organisations such as International Commission on Non-Ionising Radiation Protection (ICNIRP), Federal Communications Commission Office (FCC). Furthermore, CST Microwave Studio (MWS) also further validated by calculating the Transmission Coefficient (S21) between MIMO mobile handset and monopole probe, and fairly good agreement achieved between simulated and measured S21.

References

[1] LTE-Advanced, [Online]. Available: http://www.3gpp.org/technologies/keywords-acronyms/97-lte-advanced (Accessed Jan 2017).

[2] J. Lee, J. K. Han, J. Zhang, "MIMO Technologies in 3GPP LTE and LTE-Advanced," J. on Wireless Communication and Networks, doi:10.1155/2009/302092, 2009.

[3] K. L. Wong, M. R. Hsu, W. Y. Li, S. W. Su, and A. Chen, "Study of the Bluetooth headset antenna with the user's head," Microwave and Optical Technology Letters, vol. 49, pp. 19–23, 2007.

[4] R. P. Findlay, and P. J. Dimbylow, "SAR in a child voxel phantom from exposure to wireless computer networks (Wi-Fi)," Phys. Med. Biol., vol. 55, pp. 405– 411, 2010.

[5] A. Peyman, C. Gabriel, E. H. Grant, G. Vermeeren, and L. Martens, "Variation of the dielectric properties of tissues with age: the effect on the values of SAR in children when exposed to walkie–talkie devices," Phys. Med. Biol, vol. 54, pp. 227 – 241, 2009.

[6] A. K. Lee, S. E. Hong, J. H. Kwon, and H. D. Choi, "SAR Comparison of SAM Phantom and Anatomical Head Models for a Typical Bar-Type Phone Model," IEEE Trans. on Electromagnetic Compatibility, vol.57, pp. 1281 – 1284, 2015.

[7] A. Tateno, K. Tanaka, T. Nagaoka, S. Watanabe, K. Saito, M. Takahashi, et al., "Comparison of SAR in human body radiated from mobile phone and tablet computer," Int. Symposium on Electromagnetic Compatibility, pp. 186 – 189, 2014.

[8] W. Yu, S. Yang, C. L. Tang, and D. Tu, "Accurate Simulation of the Radiation Performance of a Mobile Slide Phone in a Hand-Head Position," IEEE Antennas and Propagation Magazine, vol. 52, pp. 168 – 177, 2010.

[9] J. Ilvonen, O. Kivekas, J. Holopainen, R. Valkonen, K. Rasilainen, and P. Vainikainen, "Mobile Terminal Antenna Performance With the User's Hand: Effect of Antenna Dimensioning and Location," IEEE Antennas and Wireless Propagation Letters, vol. 10, pp. 772 – 775, 2011.

[10] M. Pelosi, O. Franek, M. B. Knudsen, G. F. Pedersen, and J. B. Andersen, "Antenna Proximity Effects for Talk and Data Modes in Mobile Phones," IEEE Antennas and Propagation Magazine, vol. 52, pp. 15 – 27, 2010.

[11] S. Zhang, K. Zhao, Z. Ying, and S. He, "Adaptive Quad-Element Multi-Wideband Antenna Array for User-Effective LTE MIMO Mobile Terminals," IEEE Trans. on Antennas and Propagation, vol. 61, pp. 4275 – 4283, 2013.

[12] A. A. H. Azremi, J. Ilvonen, R. Valkonen, J. Holopainen, O. Kivekas, C. Icheln, et al., "Coupling Element-Based Dual-Antenna Structures for Mobile Terminal with Hand Effects," Int. J. Wireless information Networks, vol. 18, pp. 146 – 157 2011.

[13] K. Zhao, S. Zhang, Z. Ying, T. Bolin, and S. He, "SAR Study of Different MIMO Antenna Designs for LTE Application in Smart Mobile Handsets," IEEE Trans. on Antennas and Propagation, vol. 61, pp. 3270 – 3279, 2013.

[14] S. Shoaib, I. Shoaib, N. Shoaib, X. Chen, and C. G. Parini, "MIMO Antennas for Mobile Handsets," IEEE Antennas and Wireless Propagation Letters, vol. 14, pp. 799 – 802, 2015.

[15] 3GPP Release 11: Understanding the Standards for HSPA+ and LTE-Advanced Enhancements, [Online]. Available: http://www.5gamericas.org/files/9014/0759/2350/3GPP_Release_11-_ES_Final_.pdf (Accessed Dec 2015).

[16] Apple iPhone 6 (s), [Online]. Available: http://www.apple.com/uk/iphone-6s/specs/ (Accessed Feb 2016).

[17] Federal Communications Commission, "SAR Evaluation Considerations for Handsets with Multiple Transmitters and Antennas," Draft Laboratory Division Publication Report, Oct 2012.

[18] H. Li, A. Tsiaras, B. Derat, and B. K. Lau, "Analysis of SAR on flat phantom for different multi-antenna mobile terminals," European Conference on Antennas and Propagation (EuCAP), pp. 1989 – 1993, 2014.

[19] H. Li and B. K. Lau, "Efficient evaluation of specific absorption rate for MIMO terminals," Electronics Letters, vol. 50, pp. 1561 – 1562, 2014.

[20] H. Li and B. K. Lau, "Simple assessment of Specific Absorption Rate (SAR) for MIMO terminals," IEEE Int. Symposium on Antennas and Propagation & USNC/URSI National Radio Science Meeting, pp. 1228 – 1229, 2015.

[21] IEEE, "IEEE Recommended Practice for Determining the Peak Spatial-Average Specific Absorption Rate (SAR) in the Human Head from Wireless Communications Devices: Measurement Techniques," IEEE Std. 1528 – 2013 (Revision of IEEE Std 1528 – 2003), pp. 1 – 246, 2013.

[22] J. Tak, Kyeol Kwon, S. Kim, and J. Choi, "Dual-Band On-Body Repeater Antenna for In-on-On WBAN Applications," Int. J. Ant. Prop., pp. 1 – 12, 2013.

[23] ICNIRP, "International Commission on Non-Ionizing Radiation Protection: Guidelines for limiting exposure to time-varying electric, magnetic and electromagnetic fields (up to 300 GHz)," Heal. Phys. Soc., vol. 74, pp. 494 – 522, 1998.

[24] M. R. Islam and M. Ali, "Ground Current Modification of Mobile Terminal Antennas and Its Effects," IEEE Antennas and Wireless Propagation Letters, vol. 10, pp. 438 – 441, 2011.

[25] D. T. Le and V. H. Chu, "Analyses on the maximum local specific absorption rate of multiple antenna devices in different measurement planes," International Conference on Advanced Technologies for Communications (ATC), pp. 496 – 500, 2015.

Chapter 6
Numerical Exposure Assessments of Communication Systems at Higher Frequencies

6.1 Introduction

With the enormous increase in internet users, demands for high data rate from wireless and portable devices dramatically increased from last few years. Wireless devices manufacturers are facing huge challenge how to overcome the global large bandwidth requirements. 4G mobile communication systems or formally called Long Term Evolution (LTE) enable systems operates under 6 GHz frequency band. There is well-established assessment guidelines for devices that operates under 6 GHz [1] and 10 GHz [2] to keep the exposure levels under the basic limits and to minimise the public concern about over exposures.

5G wireless mobile communication systems expected to use frequency bands at millimetre waves (mmWs) range [3]. The mmW frequency band ranges from 30 GHz to 100 GHz, which is a part of radio frequency (RF) spectrum. The possible use of these higher frequency bands impose new challenges in terms of EM exposure assessment. The mmW radiations are non-ionising and the major concern is heating of tissues at these frequencies. Due to lack of availability of assessment methods, governments currently rely on standards that developed before the exponential increase in use of wireless communication devices.

Several attempts made in the past to investigate the effects of mmW exposure on human body. Majority of previous studies investigates the thermal effect caused by exposure from mmWs frequencies [4–8]. These studies uses different techniques such as thermocouple, magnetic resonance thermal imager and various analytical solutions to estimate the temperature variations within the human body. Theoretical analysis on the steady state temperature elevation using bioheat equation is also very challenging as it depends on many parameters such as thermal conductivity, blood flow, thermal and tissues thickness parameters. A complete literature review has been done in references [9–11], which provide basic knowledge about the mmWs behaviour in terms of transmission and reflection at the skin tissue interface and dielectric properties of skin are also provide over the wide frequency range.

Due to the shallow penetration depth in biological material at mmW frequencies, most of the energy is absorbed within few millimetres of the skin. This makes challenging for conventional E-field probe to estimate EM absorption on skin surface. Therefore, SAR levels were found significantly higher in comparison with those at microwave frequencies with same incident power density (IPD) [9–11]. International guidelines providing agencies recommend to use power density (PD) as a basic restriction limit to reduce the excessive exposure at higher frequencies (above 6 [1] and 10 GHz [2]). But devices operating in near- or far-field do not take account for field distribution or power absorption in the tissues, they only consider density of power travelling towards the tissue [9]. Therefore, PD may not likely be useful as SAR or temperature for assessing safety at higher frequencies.

In this chapter, numerical SAR assessment is performed on human head-equivalent cube models (HHECM) and human eye-equivalent cube models (HEECM) between 2 to 30 GHz in order to find out how SAR can be used as useful in limiting the over exposure at mmWs. For this purpose EM wave penetration depth is used to identify the absorption levels with the help of SAR inside the body from the surface.

6.2 Exposure Configuration

There is a well-established and well-accepted thermal heating effect due to the mmW exposure. The primary target, at mmWs, organs or biological tissues are human eyes and skin. Human skin thickness varies from 0.5 mm on eyelids to 4 mm on the heels of feet [10, 12]. Skin is the largest tissue among the other human tissues and organ. It is well understood that

tissues with high concentration of water absorb more energy. Therefore, eyes and skin are major concern at mmW frequency range.

For this purpose, single-layer (skin only), multi-layer (skin, fat and muscle) HHECM and HEECM was exposed with plane wave and SAR values were calculated. The IPD was set to 2.65 mWm^{-2} for all exposure scenarios. The exposure configuration of single- and multi-layer model is shown in Figure 6-1.

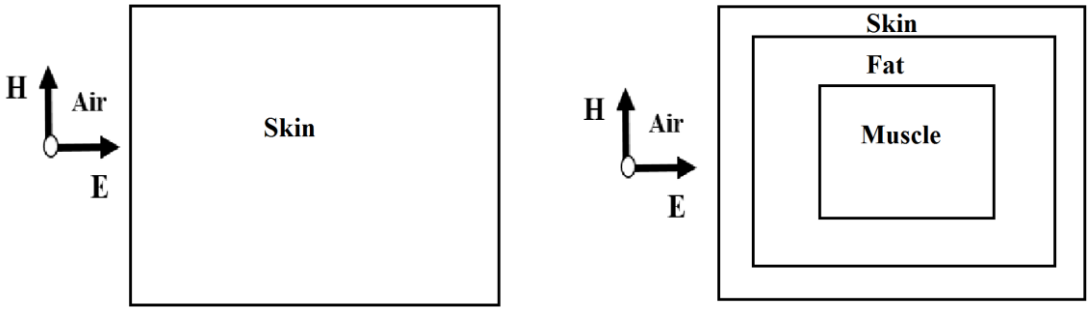

(a) (b)

Figure 6-1. Plane wave exposure configuration of (a) Single-layer skin-equivalent cube model (b) Multi-layer skin, fat and muscle-equivalent cube model.

Dielectric properties of tissues such as dry- and wet-skin, fat and muscle were calculated over the wide frequency range from 2 GHz to 30 GHz using the Debye model. First order equation of Debye model is given below:

$$\varepsilon(\omega) = \varepsilon_{\infty} + \frac{\varepsilon_s - \varepsilon_{\infty}}{1+i\omega\tau} + \frac{\sigma}{i\omega\varepsilon_0} \qquad \text{(Equation 6.1)}$$

All relaxation parameters of Debye model calculated based on curve fitting technique. The dielectric properties namely permittivity and conductivity graphs are presented in Appendix B, Figure B-1 and Figure B-2.

6.3 Plane Wave Exposure Assessment of E-field absorption within Skin using SAR as a function of Frequency

In this assessment configuration, dry- and wet-skin tissue dielectric properties was assigned to a single-layer HHECM in two separate cases. The HHECM was designed in CST microwave studio and the dimensions was set to 120 x 170 x 180 mm^3 as sown in Figure 6-2.

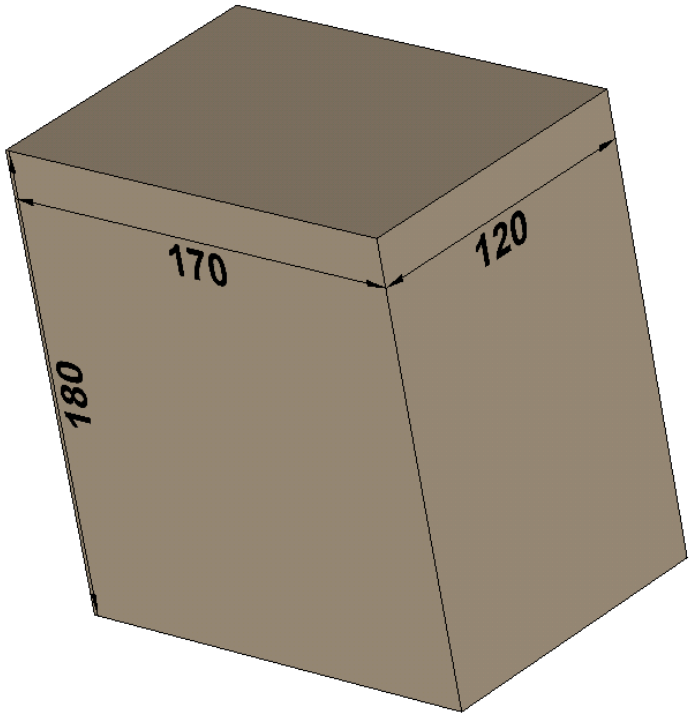

Figure 6-2. 3-D view of HHECM, where all dimensions are in mm.

The model was exposed with plane wave (as shown in Figure 6-1 (a)) in free space at various frequencies (2 GHz, 6 GHz, 10 GHz, 12 GHz, 16 GHz, 20 GHz, 24 GHz, 28 GHz and 30 GHz), where the E- and H-field components was aligned perpendicular and parallel to the cube model respectively. Standard boundary conditions was considered. The purpose of choosing cube volume was to investigate the EM absorption levels inside the model with respect to its surface. The cube SAR was numerically calculated and iterative computation on its central sub-volume was applied to calculate SAR values to assess the depth at which the wave have no longer effect on SAR performance.

6.3.1 Comparisons of SAR levels on Dry-Skin and Wet-Skin

After exposing the HHECM with plane wave resultant SAR values are compared in both dry- and wet-skin cases at previously mentioned frequencies. Initially SAR was numerically calculated in whole cube model then SAR values were also calculated in its sub-volume (as shown in Figure 6-3) in order to investigate the EM waves penetration depth.

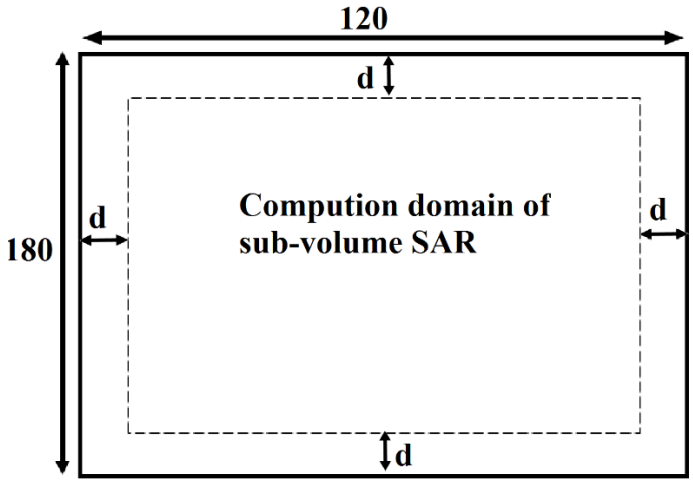

Figure 6-3. Sub-volume dimensions of HHECM; where "d" is the variable distance from the cube surface, where all dimensions are in mm.

SAR values were calculated in sub-volume after reducing the HHECM size by setting "d" 1 mm, 2.5 mm, 5 mm, 10 mm, 20 mm and 50 mm from the surface of model from all sides. The size reduces from all sides in order to keep the consistency of thickness of human skin. Similar reduction method applied to rest five cases.

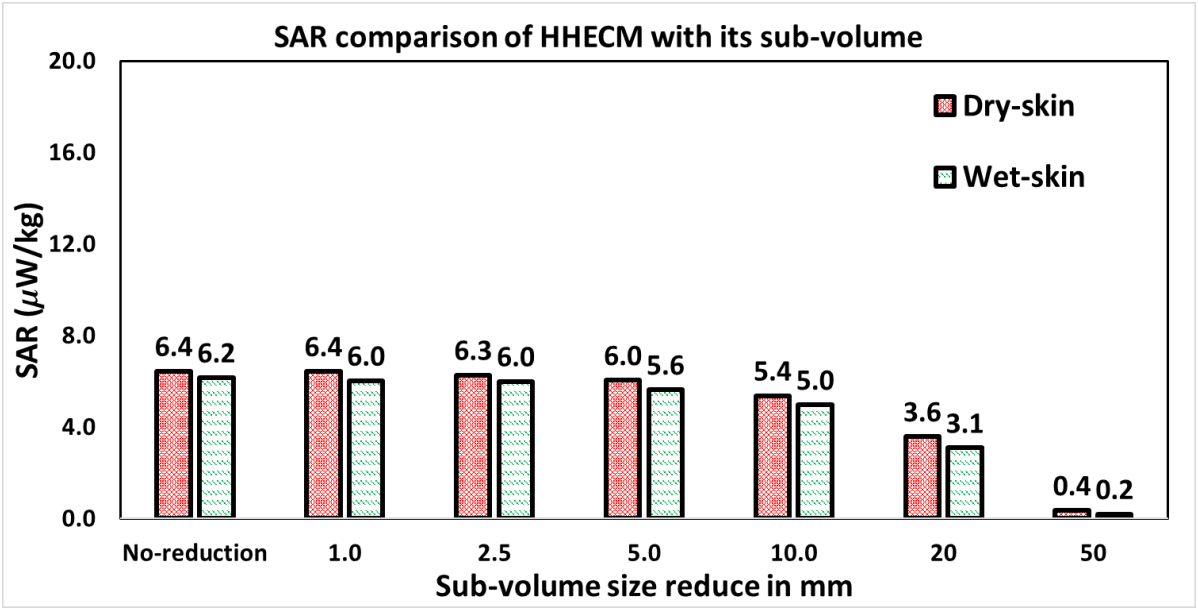

Figure 6-4. Comparison of SAR values of dry- and wet-skin HHECM with its sub-volume resultant from plane wave exposure at **2 GHz**, where no-reduction key word on *x*-axis of graph represents the SAR in whole cube volume. It can be seen that the wave at this frequency doesn't exceed 50 mm from the HHECM surface.

It is quite evident from Figure 6-4, there is clear difference among the EM absorption levels within the dry- and wet-skin cases. The WBSAR values of HHECM (no-reduction) and its sub-volume cases (when size reduced by considering "d" is 1 mm, 2.5 mm and 5 mm) are almost similar in both dry- and wet-skin cases, which is due to the deeper penetration of EM

waves at 2 GHz. It means that EMFs absorbs not only on the surface of skin but deep inside the body. Approx. 57 % and 50 % energy absorbs within 20 mm of skin from the surface in dry- and wet cases correspondingly.

Another important fact is less absorption noticed in wet-skin as compared to dry-skin exposure scenarios. It is usually noticed that when wet-skin exposed to EM waves, it absorbs more energy but the dry-skin has shown higher absorption levels at all frequency bands that are considered in this study. The possible reason behind this trend could be due to the very minor difference in dielectric properties.

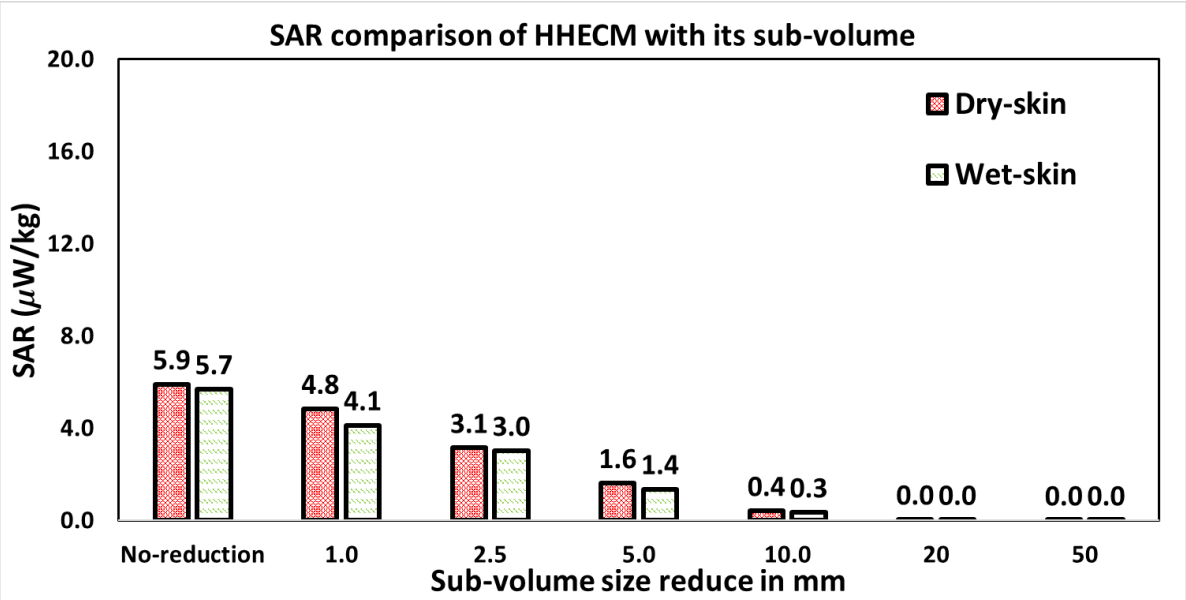

Figure 6-5. Comparison of SAR values of dry- and wet-skin HHECM with its sub-volume resultant from plane wave exposure at **6 GHz**, where no-reduction key word on *x*-axis of graph represents the SAR in whole cube volume. It can be seen that the wave at this frequency doesn't exceed 10 mm from the HHECM surface.

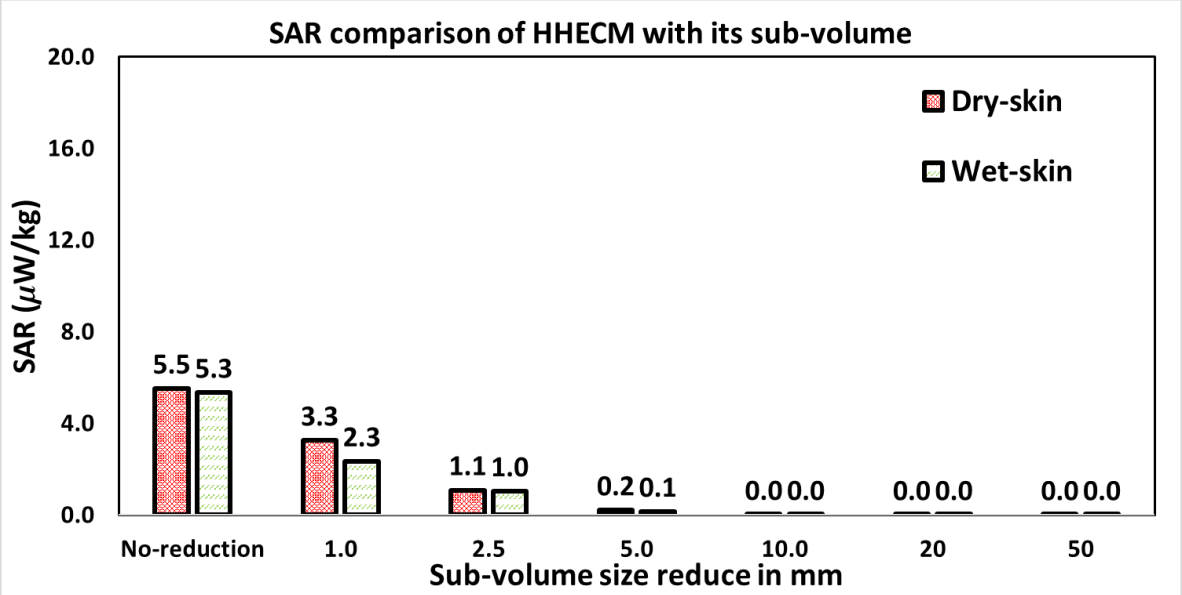

Figure 6-6.Comparison of SAR values of dry- and wet-skin HHECM with its sub-volume resultant from plane wave exposure at **10 GHz**, where no-reduction key word on *x*-axis of graph represents the SAR in whole cube volume. It can be seen that the wave at this frequency doesn't exceed 5 mm from the HHECM surface.

EM waves penetration depth decrease quickly as frequency gradually increases as can be seen in Figure 6-5, Figure 6-6 and Figure 6-7. The difference between the WBSAR values of HHECM (no-reduction case) at 6 GHz with its sub volume cases when box phantom size reduced by considering "d" is 1 mm and 2.5 mm, are within 20 % and 48 % respectively (as shown in Figure 6-5). Almost 50 % energy absorbed within the 2.5 mm of skin from surface and rest energy absorbs within 2.5 mm to 5 mm skin. The energy absorption within skin is negligible approaching to almost zero after 5 mm distance from skin surface to deep inside the HHECM.

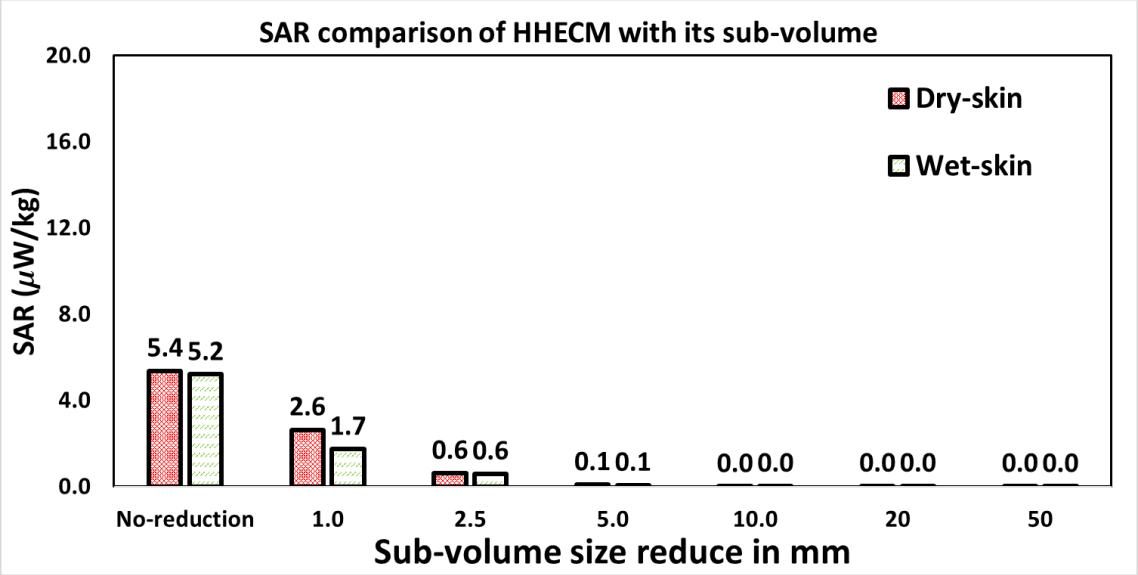

Figure 6-7. Comparison of SAR values of dry- and wet-skin HHECM with its sub-volume resultant from plane wave exposure at **12 GHz**, where no-reduction key word on *x*-axis of graph represents the SAR in whole cube volume. It can be seen that the wave at this frequency doesn't exceed 5 mm from the HHECM surface.

At 10 and 12 GHz, 80 % and 90 % of energy absorbed within the 2.5 mm skin from surface, respectively (as shown in Figure 6-6 and Figure 6-7). The remaining 20 % and 10 % energy absorbs between 2.5 mm and 5 mm skin at both frequency bands correspondingly. On the other hand, energy absorption within the wet-skin shows the similar behaviour in comparison with dry-skin case.

E-field values calculated based on the resulted SAR values in both dry- and wet-skin scenarios as shown in Figure 6-8 and Figure 6-9, respectively. It can be clearly seen that E-field absorption levels are much higher and its penetration depth is deeper at lower frequencies (2 GHz). E-field absorption level and its penetration depth gradually decreases with the increase in frequency which is approx. zero at 10 mm distance from the surface of skin at 12 GHz in both dry- and wet-skin cases (as shown in Figure 6-8 and Figure 6-9).

The graph presented in Figure 6-16 represents the penetration of EM waves within the HHECM with respect to frequency. It can be clearly seen that EM absorption within the dry- and wet-skin equivalent cube model doesn't exceed 5 mm at 12 GHz. Further simulations was conducted to investigate EM absorption levels on dry-skin only above 12 GHz. It was found that almost 100 percent of energy absorbs within 1.5 mm of skin from its surface above 16 GHz. All the SAR values resultant from plane wave exposure at 12 GHz to 30 GHz are presented in Appendix B.

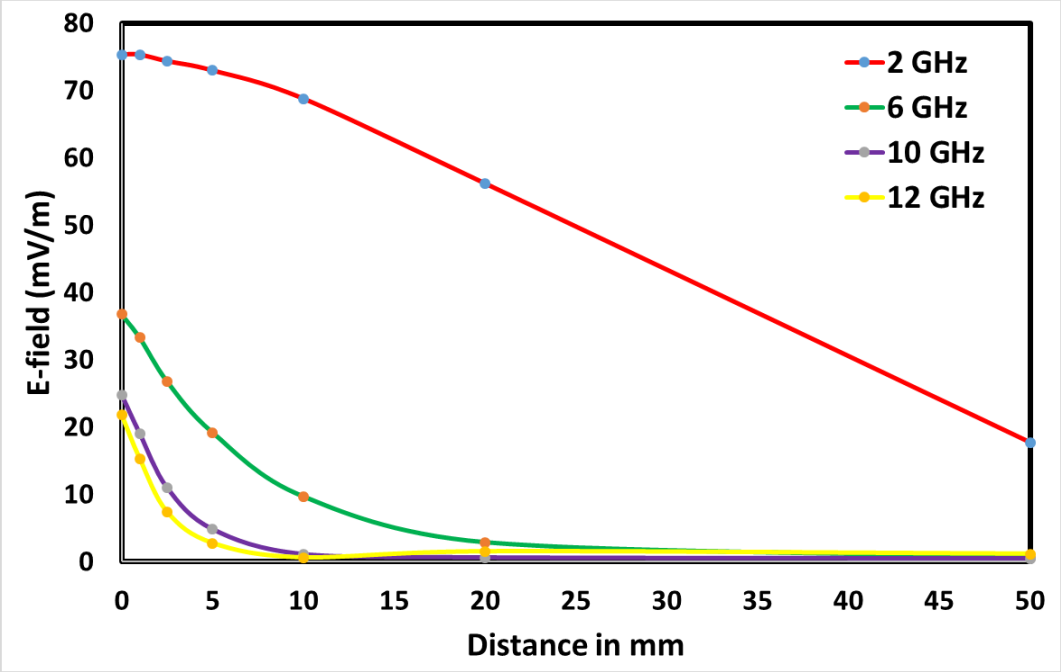

Figure 6-8. E-field absorption within the dry-skin from surface to 50 mm deep inside the HHECM.

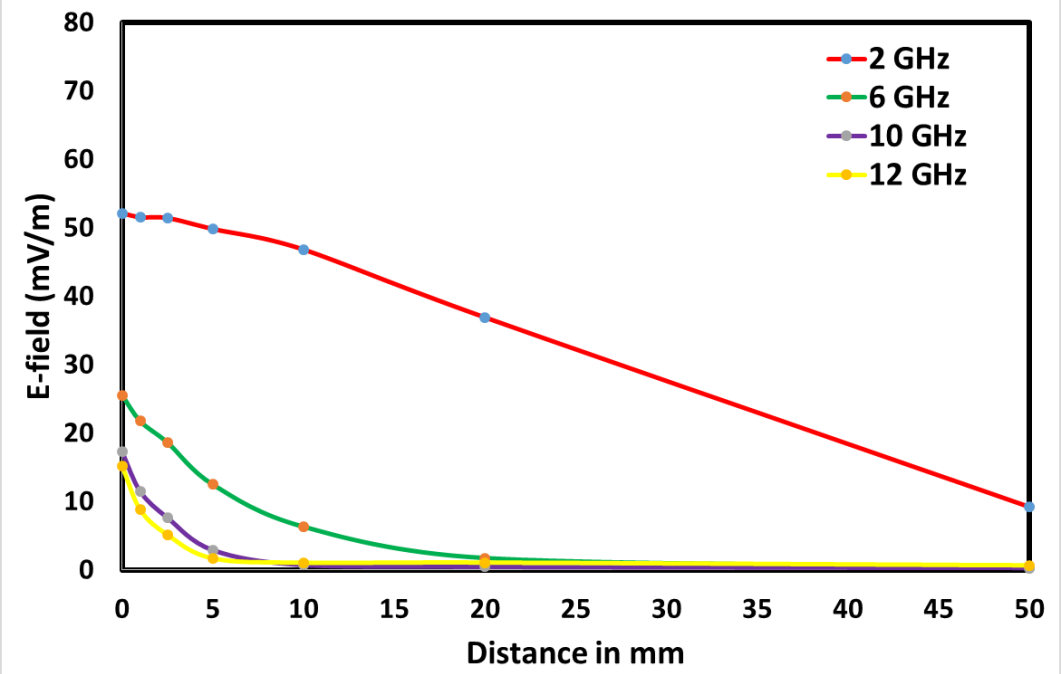

Figure 6-9. E-field absorption within the wet-skin from surface to 50 mm deep inside the HHECM.

6.4 Plane Wave Exposure Assessment of E-field absorption within Multi-Layer Model using SAR as a function of Frequency

In this assessment configuration, three-layer dry-skin, fat and muscle-equivalent HHECM was exposed by plane wave source (as shown in Figure 6-1), where the E- and H-field components was aligned perpendicular and parallel to the cube model respectively. Standard boundary conditions was applied. All tissue properties were produced using Debye first order relaxation model. The choice of dry-skin instead wet-skin in multi-layered model was based on higher absorption levels observed when exposed with plane wave in single-layer HHECM.

The multi-layer model has same dimensions as single-layer model as shown in Figure 6-2. In this multi-layer configuration skin and fat thickness was set 4 mm and 25 mm, respectively and remaining cube was considered as muscle. The choice of thickness of skin, fat and muscle is based on data available in literature [13, 14]. The multi-layer model is composed of three cube. The outer most cube is skin, middle cube is fat and inner cube is muscle. The composition of three-layer model is shown in Figure 6-10.

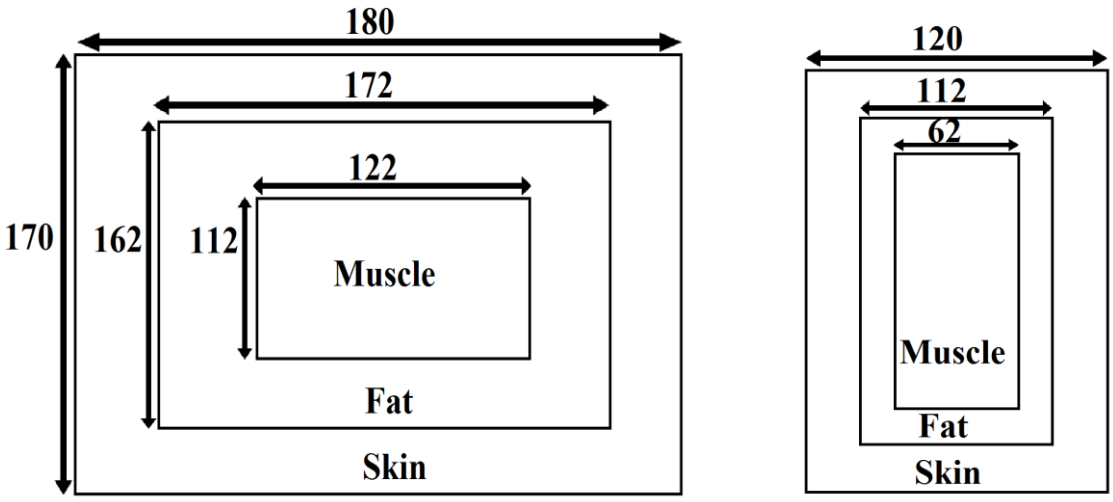

(a) Front view (b) Side view

Figure 6-10. Dimensions of multi-layer HHECM; The outer, middle and inner cube represents skin, fat and muscle respectively, where all dimensions are in mm.

6.4.1 Comparisons of SAR levels on Dry-Skin and Multi-layer Model

After exposing the HHECM with plane wave resultant SAR values are compared in both dry-skin and multi-layered model at previously mentioned frequencies. Initially SAR was numerically calculated in whole cube model then SAR values were also calculated in its sub-

volume (as shown in Figure 6-3) in order to investigate the EM waves penetration depth. The SAR calculation method is exactly the same as performed in single-layer model. Due to huge number of mesh cells generated in this multi-layer configuration. Therefore, simulations were only conducted up to 12 GHz.

SAR values were also calculated in its sub-volume same as single-layer exposure configuration, sub-volume size achieved by reducing the HHECM size by considering "d" is 1 mm, 2.5 mm, 5 mm, 10 mm, 20 mm and 50 mm from the surface of model from all sides. The size reduces from all sides in order to keep the consistency of thickness of human skin. Similar reduction method applied to rest five cases. Higher SAR values are observed in dry-skin as compared to multi-layer model as shown in Figure 6-11.

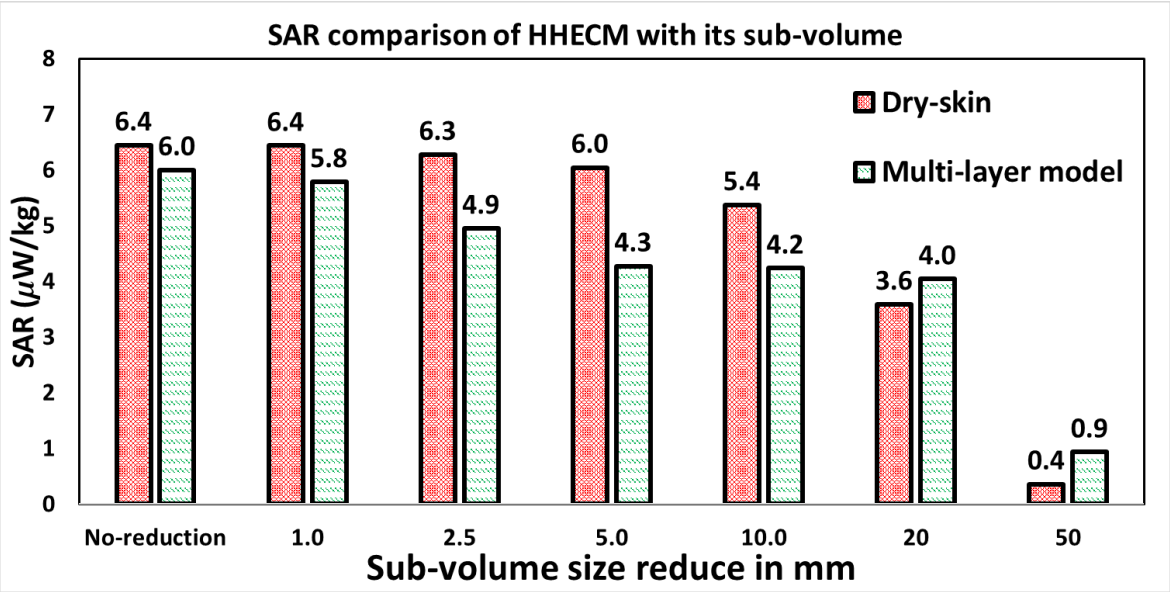

Figure 6-11.Comparison of SAR values of dry-skin and multi-layer HHECM with its sub-volume resultant from plane wave exposure at **2 GHz**, where no-reduction key word on *x*-axis of graph represents the SAR in whole cube volume. It can be seen that the wave at this frequency doesn't exceed 50 mm from the HHECM surface.

It is understandable that single-layer skin equivalent exposure cases has shown slightly over estimated SAR values as compared to multi-layer cases. But interestingly multi-layer model has shown higher absorption levels in 20 mm and 50 mm reduction cases. The EMFs absorption level at 20 mm distance from surface of skin is approx. 77 % and 57 % in multi-layer model and dry-skin respectively. It is worth mentioning theoretically penetration depth of EM waves in multi-layer model is higher. Therefore, absorption levels are significantly higher as compared to dry-skin at 2 GHz.

EM absorption levels are significantly higher in multi-layer model and in its sub-volume as compared to dry-skin cases at 6 GHz (as shown in Figure 6-12). Approx. 10 – 20 % higher SAR values noticed in multi-layer model and in its sub-volume in comparison with dry-skin. In multi-layer model approx. 50 % and 20 % of energy absorbs within 2.5 mm and 10 mm cases from its surface correspondingly.

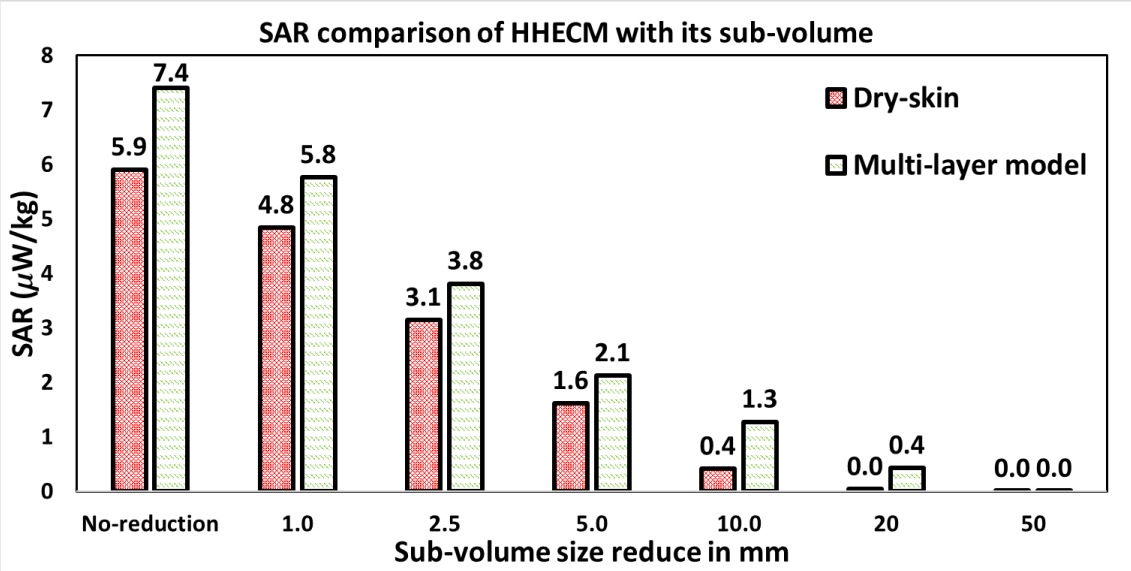

Figure 6-12.Comparison of SAR values of dry-skin and multi-layer HHECM with its sub-volume resultant from plane wave exposure at **6 GHz,** where no-reduction key word on *x*-axis of graph represents the SAR in whole cube volume. It can be seen that the wave at this frequency doesn't exceed 20 mm from the HHECM surface.

At 10 and 12 GHz, approx. 57 % and 48 % energy absorbs within 1 mm from the surface of multi-layer model respectively (as shown in Figure 6-13 and Figure 6-14). It can be clearly seen that at both frequencies more than 90 % of energy absorbs within 2.5 mm of multilayer model and similar behaviour noticed in dry-skin. It is worth mentioning that above 2 GHz higher SAR values found in multi-layer model as compared to single-layer model.

This could be the reason why international guidelines providing organisation such as FCC/ IEEE/ ICNIRP emphasis to use dielectric properties for homogenous model that can provide slightly over estimated SAR values as compared to heterogeneous model. Moreover, this finding is in line with the reference [6, 8, 9], where higher level of temperature variation observed in multi-layer models as compared to single-layer model at 60 GHz. So it can be concluded that as you go higher in the frequency homogenous models may not be suitable for SAR assessments or in other words for temperature variations. Multilayer models might be the only option left to consider to accurately assess the EM absorption levels either using by SAR or temperature variation.

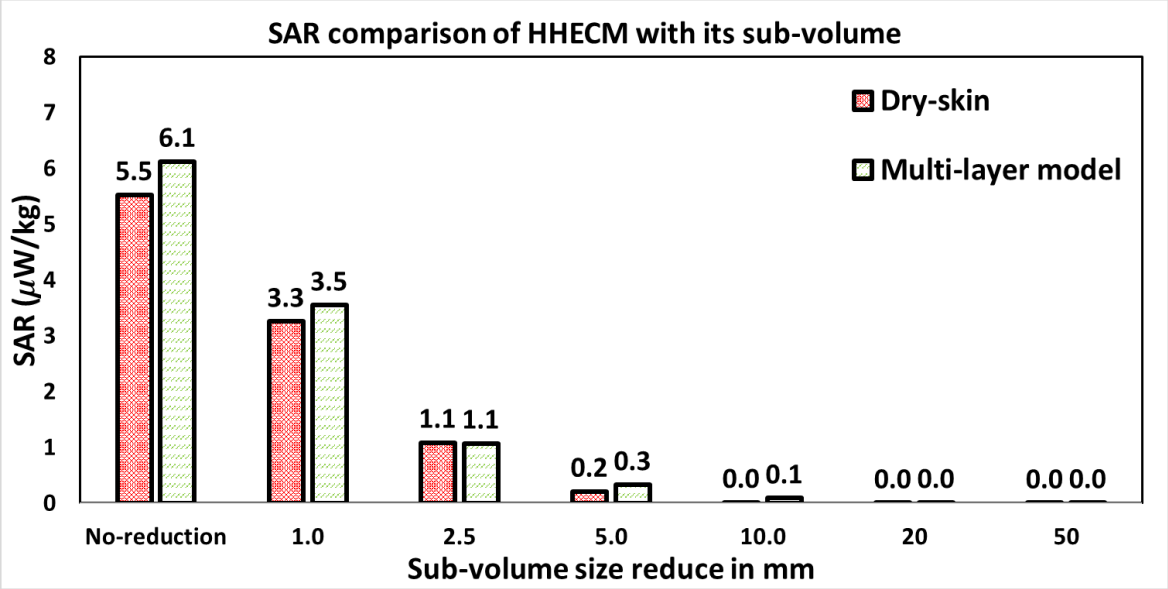

Figure 6-13.Comparison of SAR values of dry-skin and multi-layer box phantom with its sub-volume resultant from plane wave exposure at **10 GHz**, where no-reduction key word on x-axis of graph represents the SAR in whole cube volume. It can be seen that the wave at this frequency doesn't exceed 10 mm from the HHECM surface.

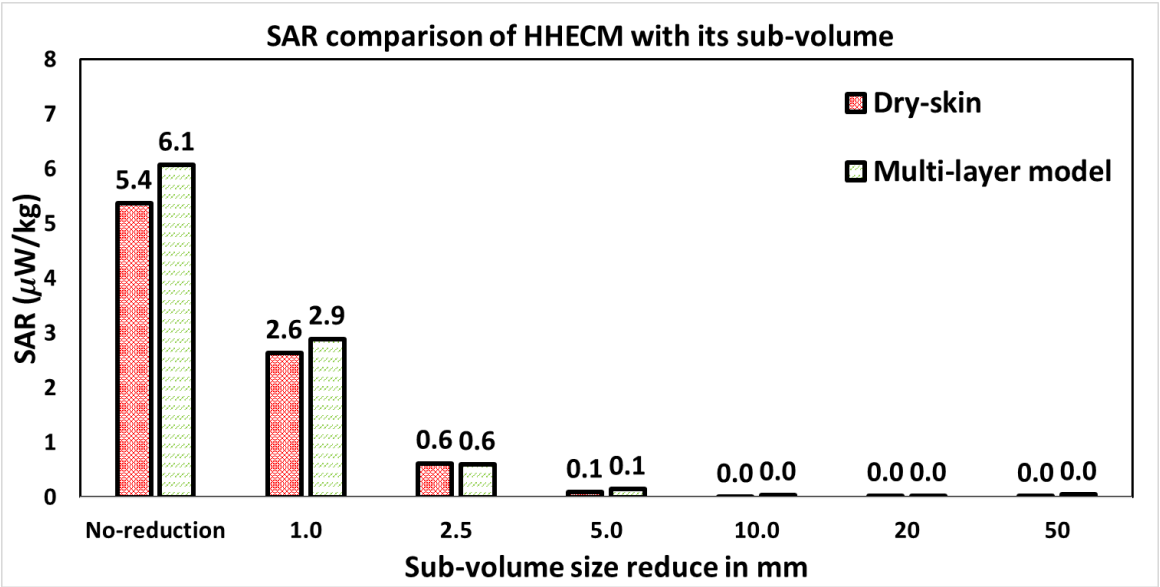

Figure 6-14.Comparison of SAR values of dry-skin and multi-layer box phantom with its sub-volume resultant from plane wave exposure at **12 GHz,** where no-reduction key word on *x*-axis of graph represents the SAR in whole cube volume. It can be seen that the wave at this frequency doesn't exceed 5 mm from the HHECM surface.

E-field values calculated based on the resulted SAR values in multi-layer model as shown in Figure 6-15. It can be clearly seen that E-field absorption levels are much higher and its penetration depth is deeper at lower frequencies (2 GHz). E-field absorption levels reaches to 0 mV/m at 20 mm distance from the surface of HHECM at 12 GHz. The graph presented in Figure 6-16 represents the penetration of EM waves within the HHECM with respect to frequency. It can be clearly seen that EM absorption within multi-layer HHECM is much higher

between 2 to 10 GHz as compared to dry- and wet-skin equivalent cube model. But interestingly EM absorption levels in both exposure configuration doesn't exceed 5 mm at 12 GHz.

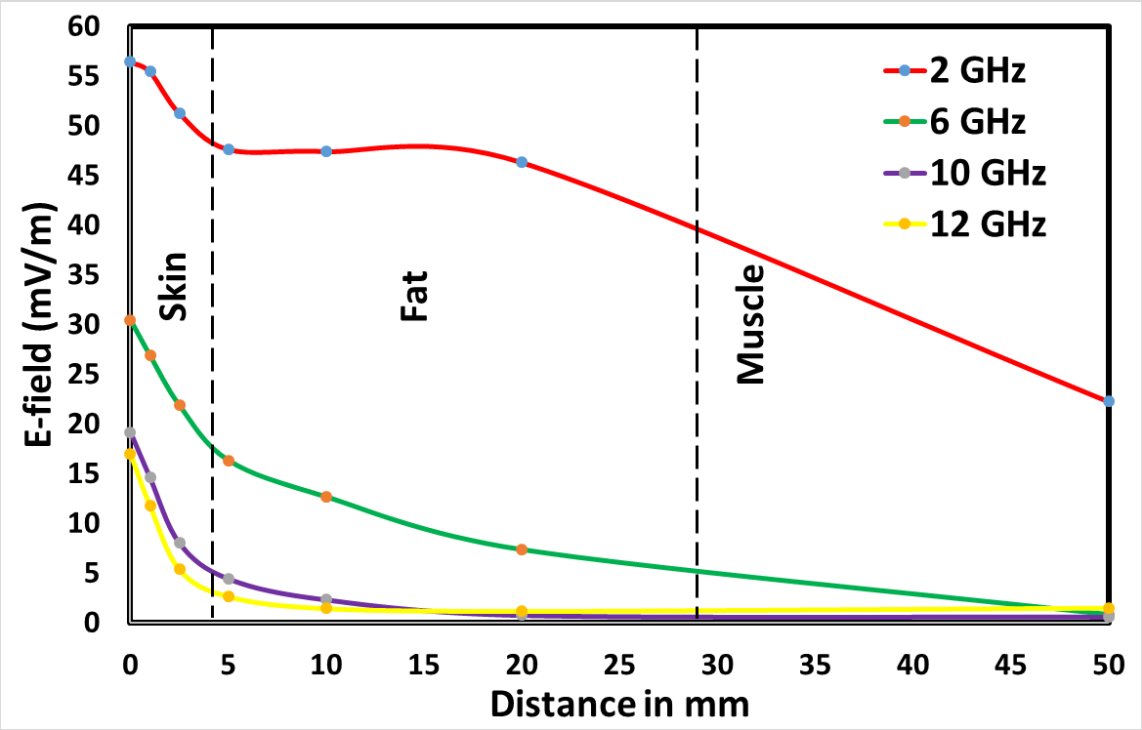

Figure 6-15. E-field absorption within the multi-layer model (dry-skin, fat, muscle) from surface to 50 mm deep inside the HHECM.

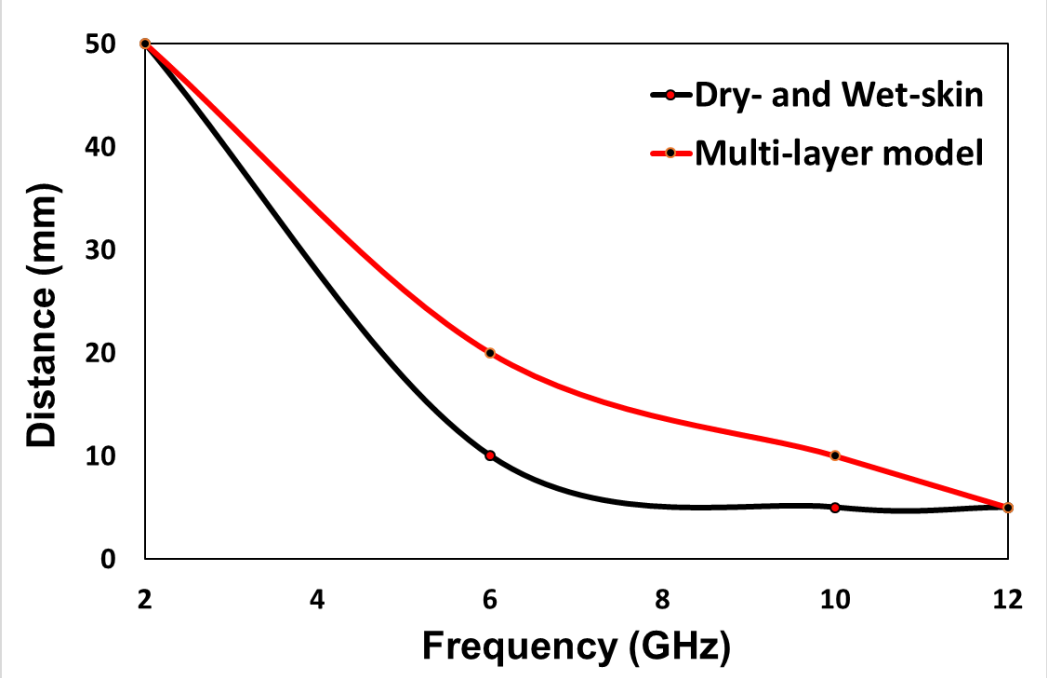

Figure 6-16. Comparison of maximum penetration depth of EM waves within dry- and wet-skin equivalent HHECM and multi-layer HHECM from its surface.

6.5 Plane Wave Exposure Assessment of E-field absorption within Eye using SAR as a function of Frequency

In this assessment configuration, HEECM was exposed with plane wave source in free space, where the E- and H-field components was aligned perpendicular and parallel to the cube model respectively. The HEECM dimensions was set to 24 mm^3 [20, 21] and standard boundary condition was applied. The cube model is composed of two tissue layers i.e. outer and inner layers. The outer layer thickness was set to 1 mm^3 and cornea tissue properties was assigned to it. Similarly inner layer thickness was set to 23 mm^3 and vitreous humor tissue properties was assigned to it (as shown in Figure 6-17. The electrical properties of both tissues calculated using Debye first order relaxation model.

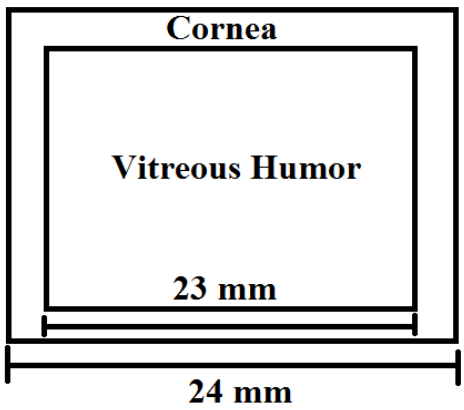

Figure 6-17. HEECM composition with its dimensions.

6.5.1 Comparisons of SAR levels on HEECM and Multi-layer Model

The SAR values are calculated in both HEECM and multi-layered model (size normalised to HEECM equivalent) between 10 GHz to 30 GHz. Initially SAR was numerically calculated in whole cube model then SAR values were also calculated in its sub-volume (as shown in Figure 6-3) in order to investigate the EM waves penetration depth. The SAR calculation method is exactly the same as performed in previous sections. Simulations were only conducted up to 30 GHz due to fact that penetration depth of EM waves is within 2.5 mm of distance from its surface in the case of HEECM. The SAR results at 30 GHz are discussed in next section and results from 10 GHz to 28 GHz are presented in Appendix B. Due to fact that same phenomenon of penetration depth noticed as discussed in previous sections.

SAR values were also calculated in HEECM and multi-layer model (HEECM equivalent) sub-volumes same as single-layer and multi-layer exposure configuration. At 30 GHz, it can be clearly seen that approx. 95 % and 90 % of energy absorbs with 1 mm from the surface of HEECM and multi-layer model respectively (as shown in Figure 6-18). It was initially assumed that HEECM will show the higher SAR values as compared to multi-layer model due to the fact that eye tissues have high concentration of water. Interestingly multi-layer model shows higher SAR values as compared to HEECM. There were some higher SAR values found deep inside the multi-layer model at 5 mm and 10 mm distance from its surface. This is due to the fact that at 30 GHz huge number of mesh cells are required to improve the accuracy of SAR estimation.

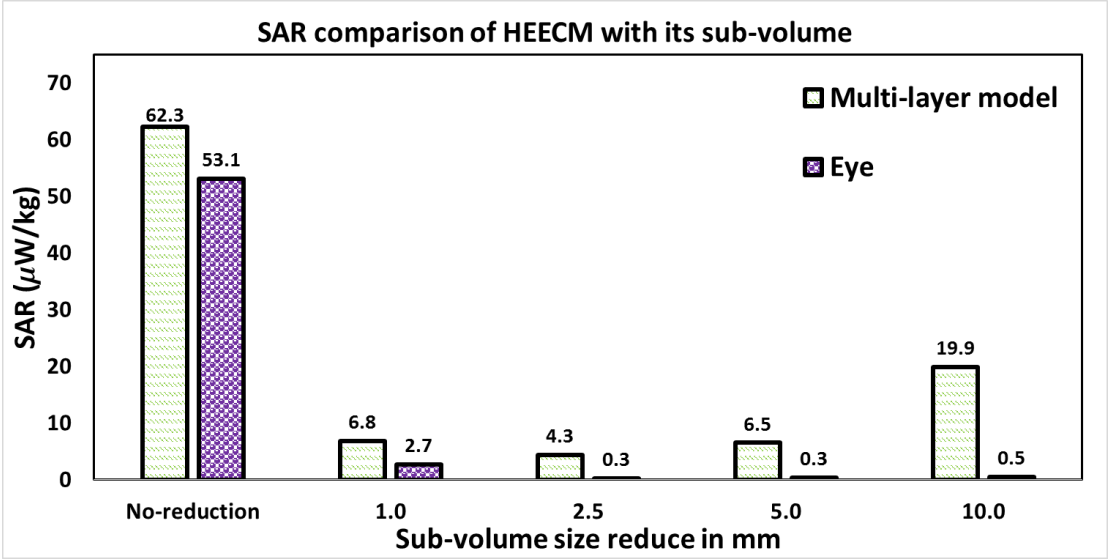

Figure 6-18. Comparison of SAR values of HEECM and multi-layer model (size normalised to HEECM equivalent) with its sub-volume resultant from plane wave exposure at **30 GHz**, where no-reduction key word on *x*-axis of graph represents the SAR in whole cube volume. It can be seen that the wave at this frequency doesn't exceed 2 mm or less from the HEECM surface.

In addition, maximum SAR values were also calculated in both HEECM and multi-layer model between 10 to 30 GHz frequency ranges (as shown in Figure 6-19). Due to the shallow penetration depth of EM waves and small size of human eye (human eye weights 14 g), maximum SAR values were averaged over 0.1 g cube instead of 1 or 10 g cube. There is approx. 33 % and 10 % higher maximum SAR values found in eye and multi-layer model respectively at 10 GHz as compared to 30 GHz. It is worth mentioning that maximum SAR values between 16 to 30 GHz found 3 to 5 % higher in multi-layer model in comparison with eye.

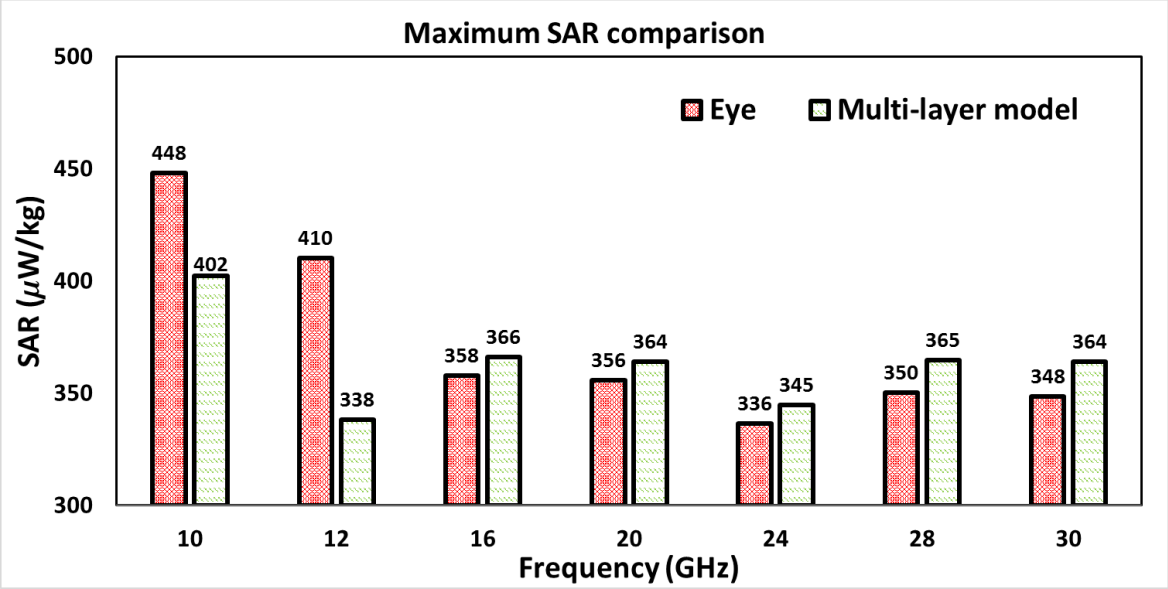

Figure 6-19. Comparison of maximum SAR values between HEECM and multi-layer model (size normalised to HEECM equivalent) resultant from plane wave exposure. The maximum SAR values calculated in 0.1 g cube.

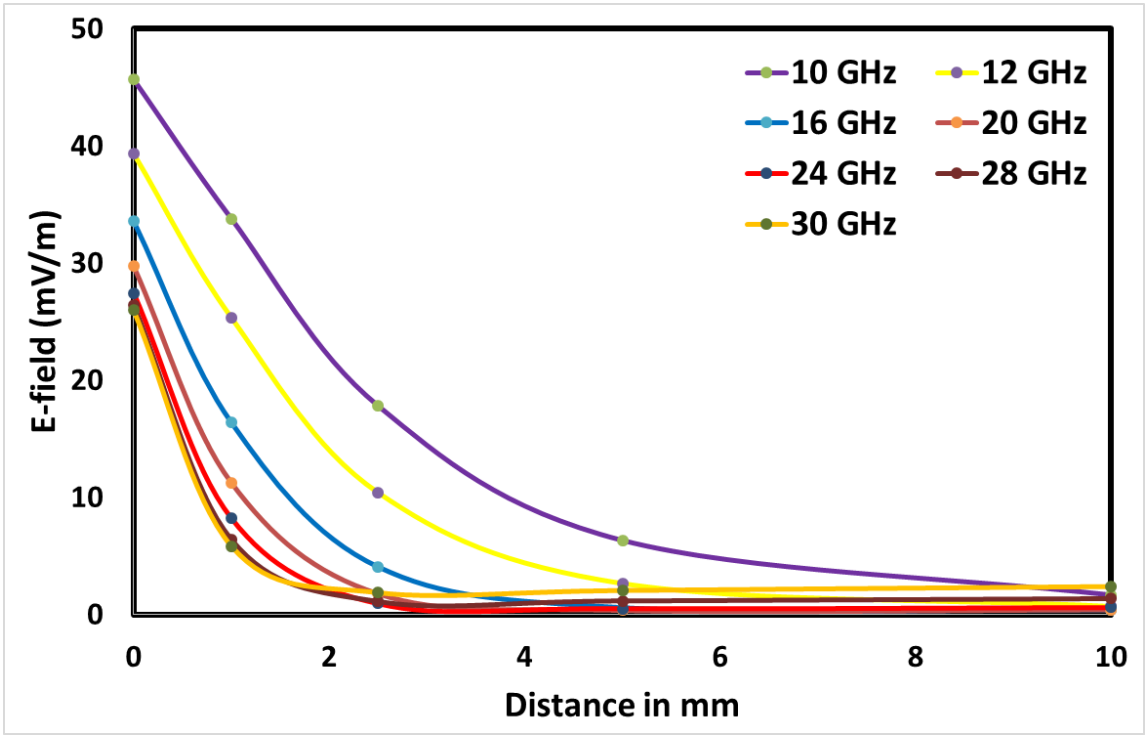

Figure 6-20. E-field absorption within the eye from surface to 50 mm deep inside the HEECM.

E-field values calculated based on the resulted SAR values in eye as shown in Figure 6-20. It can be clearly seen that E-field absorption levels are much higher and its penetration depth is deeper at lower frequencies (10 GHz). E-field absorption level gradually decreases with the increase in frequency which is approx. 2 mV/m at 10 mm distance from the surface of

HEECM at 30 GHz. The graph presented in Figure 6-21 represents the penetration of EM waves within the HEECM with respect to frequency. It can be clearly seen that between 16 GHz to 30 GHz the penetration depth EM waves is within 2 to 3 mm from the surface of HEECM.

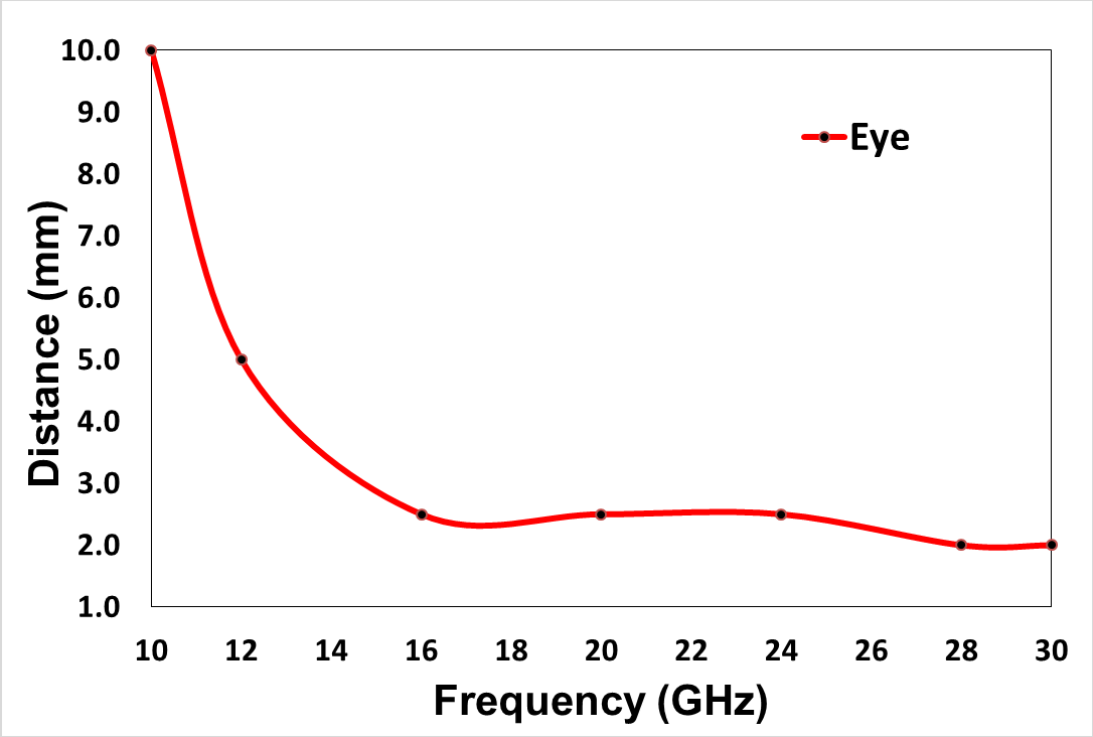

Figure 6-21. Maximum penetration depth of EM waves within eye from the surface of HEECM.

However, it has been previously mentioned that present regulations at mmWs provide safety limits in term of IPD. But without providing any specific methodologies and evaluations guidelines for exposure under near-field configurations. In this chapter, a method is provided to calculate the SAR within few millimetre of biological material. Recently an empirical method is provide in reference [22] to calculate IPD using the SAR and penetration depth. The equation for IPD calculation is given below [22]:

$$\text{IPD } [\text{W/m}^2] = \frac{\rho.\delta.SAR\ (0)}{2.(1-|\Gamma|^2)} \qquad \text{(Equation 6.1)}$$

Where "ρ" is the mass density, "δ" is the penetration depth, SAR (0) is the SAR at the skin surface and "Γ" is the reflection coefficient.

The numerical technique is presented in this chapter to calculate SAR (within few millimetre of any biological material) and penetration depth which can be very useful in

predicting IPD levels with some accuracy. It is worth mentioning that SAR assessment at the surface of any biological material is extremely difficult and challenging due to the cube averaging method.

6.7 Chapter Summary

This chapter presents the review on current understanding of the biological effects caused by exposure from mmW frequencies. International guidelines providing agencies recommend to use power density (PD) as a basic restriction threshold to limit the human body excessive exposure above 6 and 10 GHz for Federal Communications Commission Office (FCC) and International Commission on Non-Ionising Radiation Protection (ICNIRP), respectively. The difficulty is how SAR can be applicable when average volume is different and also due to the shallow penetration depth at mmWs. For the purpose of understanding SAR assessment is performed numerically from 2 to 30 GHz in single- and multi-layer human head-equivalent cube model (HHECM), and human eye-equivalent cube model (HEECM) in order to investigate penetration depth using SAR and the absorption levels within few millimetre from the surface of exposed biological material.

HHECM and HEECM was exposed with plane wave and incident power density (IPD) was set to 2.65 mWm^{-2} in all exposure scenarios. SAR values are also calculated in its sub-volume domain to investigate the depth at which the EM waves have no longer effect on SAR estimation in both homogenous and heterogeneous cases. It is concluded that approximately 90 % of energy absorbs within 1 mm of skin above 30 GHz in homogenous cases. It is worth mentioning that multi-layer model (size normalised to HEECM) has shown higher SAR values compared to HEECM above 16 GHz.

References

[1] ICNIRP, "International Commission on Non-Ionizing Radiation Protection: Guidelines for limiting exposure to time-varying electric, magnetic and electromagnetic fields (up to 300GHz)," Heal. Phys. Soc., vol. 74, pp. 494 – 522, 1998.

[2] R. F. Cleveland, D. M. Sylvar, and J. L. Ulcek, "Evaluating Compliance with FCC Guidlines for Human Exposure to Radiofrequency Electromagnetic Fields," Federal Communication Commission Office of Engineering & Technology, Washington D.C., pp. 1 – 52, 2001.

[3] T. S. Rappaport, S. Sun, R. Mayzus, H. Zhao, Y. Azar, K. Wang, et al., "Millimeter Wave Mobile Communications for 5G Cellular: It Will Work!," IEEE Access, vol. 1, pp. 335 – 349, 2013.

[4] S. I. Alekseev, M. C. Ziskin, and E. E. Fesenko, "Problems of using a thermocouple for measurements of skin temperature rise during the exposure to millimeter waves," Biophysics, vol. 56, pp. 561 – 565, 2011.

[5] L. Alon, W. S. Sloovinsky, G. Y. Cho, and T. S. Rappaport, "mmWaves Exposure assessment using magnetic resonance thermal imaging," presented at the BioEM, Monterey conference, 2015.

[6] A. Kanezaki, S. Watanabe, A. Hirata, and H. Shirai, "Theoretical Analysis for Temperature Elevation of Human Body Due to Millimeter Wave Exposure," International Biomedical Engineering Conference in Cairo, pp. 1 – 4, 2008.

[7] A. Kanezaki, A. Hirata, S. Watanabe, and H. Shirai, "Effects of dielectric permittivities on skin heating due to millimeter wave exposure," Biomedical Engineering, vol. 8, pp. 1 – 9, 2009.

[8] A. Kanezaki, A. Hirata, S. Wantanabe, and H. Shirai, "Parameter variation effects on temperature elevation in a steady-state, one-dimensional thermal model for millimeter wave exposure of one- and three-layer human tissue," Phys. Med. Biol., vol. 55, pp. 4647 – 4659, 2010.

[9] T. Wu, T. S. Rappaport, and C. M. Collins, "Safe for Generations to Come: Considerations of Safety for Millimeter Waves in Wireless Communications," IEEE Microwave Magazine, vol. 16, pp. 65 – 84, 2015.

[10] A. Guraliuc, M. Zhadobov, and R. Sauleau, "Beyond 2020 heterogeneous wireless network with millimeter-wave small-cell access and backhauling," Miwaves, 2014.

[11] M. Zhadobov, N. Chahat, R. Sauleau, C. L. Quement, and Y. L. Drean, "Millimeter-wave interactions with the human body: State of knowledge and recent advances," International J. of Microwave and Wireless Technologies, vol. 3, pp. 237 – 247, 2011.

[12] R. Y. Ha, K. Nojima, W. P. Adams, and S. A. Brown, "Analysis of Facial Skin Thickness: Defining the Relative Thickness Index," Plastic and Reconstruction Surgery, vol. 115, pp. 1769 – 1773, 2005.

[13] S. H. Lee, D. Kim, M. Y. Baek, H. Tchah, Y. S. Kim, E. Ryoo, et al., "Abdominal Subcutaneous Fat Thickness Measured by Ultrasonography Correlates with Hyperlipidemia and Steatohepatitis in Obese Children," Pediatric Gastroenterology, Hepatology & Nutrition, vol. 18, pp. 108 – 114, 2015.

[14] D. Black, J. Vora, M. Hayward, and R. Marks, "Measurement of subcutaneous fat thickness with high frequency pulsed ultrasound: comparisons with a caliper and a radiographic technique," Clinical Physics and Physiological Measurement, vol. 9, pp. 57 – 64, 1988.

[20] Diameter of a human eye, [Online]. Available: https://hypertextbook.com/facts/2002/AniciaNdabahaliye1.shtml (Accessed Aug 2017).

[21] Human eye, [Online]. Available: https://application.wiley-vch.de/books/sample/3527403809_c01.pdf (Accessed Aug 2017).

[22] A. R. Guraliuc, M. Zhadobov, R.Sauleau, L. Marnat, and L. Dussopt, " Near-Field User Exposure in Forthcoming 5G Scenarios in the 60-GHz band," IEEE Trans. on Antenna and Propagation, DOI:10.1109/TAP.2017.2754473.

Chapter 7
Conclusion and Future Work

7.1 Conclusion

In this thesis, numerical dosimetry techniques have been used to investigate the interaction of EMFs with sample of population. The outcome of these will provide insight and guidance to the experimental studies.

Dielectric properties of biological tissues play a vital role in determining the absorption levels within the human body after the exposure from EM waves. For this purpose, novel age- and frequency- dependent (AFD) technique has been developed and validated against the available online source data. The curve fitting techniques has been used and applied in three different methods on the available animals measured data to predict the best fit dielectric properties for humans of various age groups. This method is capable of differentiating tissue properties based on frequency (0.4 to 10 GHz) and age (5 to 22 years old human). The Cole-Cole relaxation parameters has been also generated for all tissue type and very good agreement achieved with relaxation parameters of measured data of animals.

The new age-dependent techniques allow to increase the accuracy of specific absorption rate (SAR) assessment. EM wave's exposure from state of art wireless devices such as smart meters (SMs), MIMO mobile handset, and 5G devices has been investigated in detail. The RF

electromagnetic fields (EMFs) exposure from SM devices were assessed in both near-and far-fields exposure configurations. SM antenna's and plane wave source was used for the near-field and far field assessments respectively. Voxel based human models of three different age groups were used for this purpose to determine the induced whole-body averaged and maximum (10 g-averaged) SAR distributions due to exposure to radio signals emitted by SM devices. The SAR profiles have been assessed for 24 different scenarios including standing and sleeping position, when exposed from various distances from the signal source.

Numerical simulations were carried out using validated, and peer reviewed computation tools based on finite integration technique (FIT), and through comparisons with similar configurations with earlier work. Simulations have shown that all exposure cases have produced whole-body specific absorption rate (WBSAR) and maximum SAR values well below the exposure guideline limits, despite the overestimated emitted powers, and the fact that continuous waves were used rather than the realistic shorter duration sessions. Results have also shown that the energy deposition was distributed differently depending on the model (dimensions as well as anatomical and dielectric differences), frequency and exposure setup.

Relatively higher maximum SAR values have been observed when models exposed with SM antenna at 868 MHz and 2.45 GHz band in standing position or in sleeping position. Higher SAR values have been observed when child model exposed under various scenarios in comparison with adult models, due to the difference in the dielectric properties and the mass densities. This is in line with the observations reported in reference [1]. Moreover, E-field and PDs were also calculated in all exposure scenarios and compared with measured data [2]. The SAR levels were predicted based on power density (PD) levels observed in measurement by normalising the simulation results. SAR levels were found to be very low in comparison with the basic restriction levels advised by ICNIRP to protect human health. Similar observations were found in reference [3], where the exposure level from the source was much less than that resulting from mobile phone usage.

Similarly, the EM exposure from MIMO mobile handset antenna has been also evaluated. In the recent past, many attempts have been made to investigate the performance of MIMO antennas in mobile handset. But generally studies restrict to simple antenna designs and assessment techniques. Nevertheless, some studies have been very good in providing knowledge of ground variation effect in terms of SAR.

In this MIMO study, relatively new assessment configuration have been employed to analyse the SAR performance of MIMO mobile handset antenna. To serve this purpose, three different exposure scenarios have been examined in this thesis. Due to the various operating modes of MIMO antennas for mobile handset, it is very important to investigate all modes with improved techniques. MIMO mobile handset three basic modes investigated in two exposure scenarios i.e. body worn and calling mode scenarios. The calling mode scenarios are further classified in two exposure scenarios in order to satisfy the different international guidelines assessment requirement. Male human head model was used in SAR evaluation from MIMO mobile handset.

Numerical simulations were conducted using the human head models under various exposure scenarios. Two-third muscle-equivalent tissue properties were assigned to male model due to the fact that it is having the similar effect as the compared to heterogeneous models and found more suitable as it provide slight over estimation which is in line with IEEE-1528 [4] recommendations. The international guidelines especially IEEE-1528 also supports to use single layer model in SAR testing as it reduces the complication in measurements. The SAR evaluation was performed on four frequency bands namely: 1.9, 2.1, 2.45 and 2.6 GHz.

Comparing the maximum SAR values of MIMO mobile handset antennas from international guidelines, relatively very high values has been observed. The basic restriction levels exceed in most cases when MIMO mobile handset antenna operates in standalone mode under various configurations. Moreover, the beam steering concept indicates the worst possible maximum SAR absorption configuration but at the same time it also provides the better techniques to reduce the absorption significantly.

Due to the higher SAR absorption levels in standalone and beam steering operating modes in both body worn and calling mode cases. The maximum SAR values resultant from MIMO mobile handset exposure were found slightly on higher side in comparison with basic restriction levels set by International Commission on Non-Ionising Radiation Protection (ICNIRP) and Federal Communications Commission Office (FCC) to protect human health. Moreover, CST Microwave Studio (MWS) was further validated by calculating the S21 between MIMO mobile handset and monopole probe in simulation and compared with measured S21, and fairly good agreement achieved between simulation and measurements.

International guidelines providing agencies recommend to use power density (PD) as a basic restriction threshold to limit the human body excessive exposure above 6 and 10 GHz for FCC and ICNIRP, respectively. The difficulty is how SAR can be applicable when average volume is different and also due to the shallow penetration depth at mmWs. Therefore, SAR distribution was evaluated on human head- and eye-equivalent cube models in homogenous and heterogeneous scenarios in order to investigate the absorption levels deep inside the body from the surface of biological material. For this purpose, human head-equivalent cube model (HHECM) and human eye-equivalent cube model (HEECM) was exposed with plane wave and incident PD was set to 2.65 mWm^{-2} in all exposure scenarios. SAR values were also calculated in its sub-volume domain to investigate the depth at which the EM waves have no longer effect on SAR estimation in both homogenous and heterogeneous cases.

7.2 Key Contributions

The major contributions in this thesis are detailed as follows:

- Novel AFD methods include Cole-Cole model based parameters were also proposed in order to calculate dielectric properties of biological tissues, which was later used in SM study to enhance the accuracy in SAR assessment.
- SAR distribution on sample of population was assessed in 24 different SM exposure configurations by using state of art SM wireless device antenna which will be used in real SMs. Both standing and sleeping exposure scenarios were evaluated in near- and far-fields at two different frequencies. The numerical simulations were validated by comparing the simulated and measured PDs levels.
- SAR distribution on voxel-based head model (NORMAN) was assessed in two different MIMO mobile handset configurations (calling and body worn cases). Three different operating modes of MIMO system studied in detail and recommendations provided which can be helpful in designing antenna with lower SAR levels. The outcome of numerical simulations were validated by comparing the simulated and measured S21 parameters by developing monopole sensor which act as a receiver.
- Demonstrated the use of SAR distribution on HHECM and HEECM in far-fields to identify SAR values within few millimetre of biological material and the penetration depth of EM waves at mmWs. It was concluded that approximately 90 % of energy absorbs with 1 mm of skin above 30 GHz.

7.3 Future Work

The work presented in this thesis covers a small but important part of this area. In the light of drawn conclusion and limitations of the work presented, further research could be carried out in the following aspects:

Numerical Modelling of Human Body

- High resolution (less than 2 mm) voxel based models are require to further investigate the absorption levels within the human body with more realistic exposure configuration for SMs and MIMO systems in order to increase the accuracy of energy absorption levels where more than one system are working in near proximity of human body.

Animal data for Age-dependent Tissue Properties

- At present, animal dielectric data with respect to their weight is available in very small quantities and for very few tissue types. In order to calculate dielectric tissue properties with respect to age new weight based data about all animal tissue types are required to further apply the novel ag-dependent method to produce age-dependent tissue properties of provide age groups.
- Similarly, after the availability of dielectric data about all tissues properties of animal it is then possible to further apply this novel method to predict the data available in literature about the dielectric tissue properties belongs from which age group.

Complex MIMO Configurations

- Numerical dosimetry can be further investigated with more complex and realistic MIMO configurations on sample of population which provide deep analysis how this technology behaves in term of energy exposure levels with different age groups by considering the fact there is a huge impact of changing the position of mobile terminal.

Assessment method beyond 10 GHz

- New averaging method is required to validate SAR assessment at higher frequency as PD doesn’t take account of penetration depth.
- New 5G technology may impose new challenges in assessment due to inclusion of one or more AP such as transmitter and receiver in near vicinity of human body.

References

[1] W. D. Hurt, J. M. Ziriax, and P. A. Mason, "Variability in EMF permittivity values: implications for SAR calculations," IEEE Trans. Biomed. Eng., vol. 47, pp. 396–401, 2000.

[2] A. Peyman, D. Addison, T. Mee, C. Goiceanu, M. Maslanyj, and S. Mann, " Exposure to electromagnetic fields from smart utility meters in GB; part I) laboratory measurements," Bioelectromagnetics, vol. 38, pp. 280 – 294, 2017.

[3] Smart Meter and Cancer Risk Statement, [Online]. Available: http://www.health.gov.bc.ca/pho/SmartMeter-and-Cancer.html (Accessed Dec 2014).

[4] IEEE, "IEEE Recommended Practice for Determining the Peak Spatial-Average Specific Absorption Rate (SAR) in the Human Head from Wireless Communications Devices: Measurement Techniques," IEEE Std. 1528 – 2013 (Revision of IEEE Std 1528 – 2003), pp. 1 – 246, 2013.

Appendix A

Table A-1. Dielectric properties of 40 different tissue types assigned to NAOMI at **868 MHz** and **2450 MHz**, where the dielectric data is chosen from various sources to improve accuracy of assessment.

Tissue Types	Frequency 868MHz		Frequency 2450MHz		Mass Density [kgm^{-3}]	Source
	Relative Permittivity	Conductivity [Sm^{-1}]	Relative Permittivity	Conductivity [Sm^{-1}]		
Adrenal Gland	50.5	1.00	48.2	1.77	1028	Peyman (2012)
Air(except lungs)	1.0	0.0	1.0	0.0	1	IFAC
Background	1.0	0.0	1.0	0.0	0	IFAC
Bile	70.3	1.83	68.4	2.79	928	IFAC
Blood	61.5	1.52	58.3	2.54	1050	IFAC
Bone cancellous	20.9	0.33	18.6	0.80	1178	IFAC
Bone Cortical	12.5	0.14	11.4	0.39	1908	IFAC
Brain	46.0	0.76	42.6	1.49	1043	IFAC
Breast fat	25.9	0.49	24.5	0.93	911	IFAC & Peyman (2010)
Cartilage	42.8	0.77	38.8	1.75	1100	IFAC
Cerebrospinal fluid	68.7	2.40	66.3	3.45	1007	IFAC
duodenum	65.2	1.17	62.2	2.20	1030	IFAC
Eye lens	46.6	0.78	44.6	1.50	1076	IFAC
Eye sclera	55.4	1.15	52.6	2.03	1032	IFAC
Fallopian ovaries	50.7	1.27	44.7	2.26	1048	IFAC
Fat	5.5	0.05	5.3	0.10	911	IFAC
Gall bladder	59.2	1.25	57.6	2.05	1071	IFAC
Heart muscle	60.1	1.21	54.8	2.25	1081	IFAC
kidney	59.0	1.37	52.8	2.42	1066	IFAC
Liver	47.0	0.84	43.1	1.68	1079	IFAC
Lower Large Intestine	59.7	2.15	54.4	3.17	1000	IFAC
Lunch	65.2	1.17	62.2	2.20	1088	IFAC
Lung	22.1	0.45	20.5	0.80	394	IFAC
Muscle	55.1	0.93	52.7	1.73	1090	IFAC
Oesophagus	65.2	1.17	62.2	2.20	1040	IFAC
Pancreas	59.8	1.03	57.2	1.96	1087	IFAC

Skin	41.6	0.86	38.0	1.46	1109	IFAC
Small intestine	59.7	2.15	54.4	3.17	1030	IFAC
Spinal cord	32.6	0.56	30.2	1.09	1075	IFAC
Spleen	57.4	1.26	52.5	2.05	1089	IFAC
Stomach	65.2	1.17	62.2	2.20	1088	IFAC
Tendon	45.9	0.71	43.1	1.68	1142	IFAC
Thymus	59.8	1.03	57.2	1.96	1023	IFAC
Thyroid gland	59.8	1.03	57.2	1.96	1050	IFAC
Upper Large Intestine	59.7	2.15	54.4	3.17	1000	IFAC
Urinary Bladder	59.2	1.25	18.0	0.68	1035	IFAC
Urine	68.7	2.01	67.8	2.83	1035	Peyman (2012)
Uterus	61.2	1.26	57.8	2.24	1105	IFAC
Vagina	50.7	1.27	44.7	2.24	1048	IFAC
Vitreous Humour	68.9	1.63	68.2	2.47	1005	IFAC

Table A-2. Dielectric properties of 38 different tissue types assigned to NORMAN at **868 MHz** and **2450 MHz**, where the dielectric data is chosen from various sources to improve the accuracy of the assessment.

Tissue Types	**Frequency 868MHz**		**Frequency 2450MHz**		**Mass Density [kgm^{-3}]**	**Source**
	Relative Permittivity	**Conductivity [Sm^{-1}]**	**Relative Permittivity**	**Conductivity [Sm^{-1}]**		
Adrenal gland	50.5	1.00	48.2	1.77	1028	Peyman (2012)
Air (except lungs)	1.0	0.00	1.0	0.00	1	IFAC
Background	1.0	0.00	1.0	0.00	0	IFAC
Bile	70.3	1.83	68.4	2.79	928	IFAC
Blood	61.5	1.52	58.3	2.54	1050	IFAC
Bone cancellous	20.9	0.33	18.6	0.80	1178	IFAC
Bone cortical	12.5	0.14	11.4	0.39	1908	IFAC
Brain	45.9	0.76	42.6	1.49	1046	IFAC
Breast fat	25.9	0.49	24.5	0.93	911	IFAC & Peyman (2010)
Cerebrospinal fluid	68.7	2.40	66.3	3.45	1007	IFAC
Duodenum	65.2	1.17	62.2	2.20	1030	IFAC
Eye lens	46.6	0.78	44.6	1.50	1076	IFAC
Eye sclera	55.4	1.15	52.6	2.03	1032	IFAC
Fat	5.5	0.05	5.3	0.10	911	IFAC
Gall bladder	59.2	1.25	57.6	2.05	1071	IFAC

Heart muscle	60.1	1.21	54.8	2.25	1081	IFAC
kidney	59.0	1.37	52.8	2.42	1066	IFAC
Liver	47.0	0.80	43.1	1.70	1079	IFAC
Lower Large Intestine	59.7	2.15	54.4	3.17	1000	IFAC
Lunch	65.2	1.17	62.2	2.20	1088	IFAC
Lung	22.1	0.45	20.5	0.80	394	IFAC
Muscle	55.1	0.93	52.7	1.73	1090	IFAC
Oesophagus	65.2	1.17	62.2	2.20	1040	IFAC
Pancreas	59.8	1.03	57.2	1.96	1087	IFAC
Prostate	60.7	1.20	57.6	2.16	1045	IFAC
Skin	41.6	0.86	38.0	1.46	1109	IFAC
Small Intestine	59.7	2.15	54.4	3.17	1030	IFAC
Spinal cord	32.6	0.56	30.2	1.09	1075	IFAC
Spleen	57.4	1.26	52.5	2.05	1089	IFAC
Stomach	65.2	1.17	62.2	2.20	1088	IFAC
Tendon	45.9	0.71	43.1	1.68	1142	IFAC
Testis	60.7	1.20	57.6	2.16	1082	IFAC
Thymus	59.8	1.03	57.2	1.96	1023	IFAC
Thyroid gland	59.8	1.03	57.2	1.96	1050	IFAC
Upper Large Intestine	59.7	2.15	54.4	3.17	1000	IFAC
Urinary bladder	59.2	1.25	18.0	0.68	1035	IFAC
Urine	68.7	2.01	67.8	2.83	1035	Peyman (2010)
Vitreous Humour	68.9	1.63	68.2	2.47	1005	IFAC

Table A-3. Dielectric properties of 75 different tissue types of Eartha at **868 MHz** and **2450 MHz**, where the dielectric data is chosen from various sources for accurate assessment (IE21P: Interpolation Equations from 21.3kg pig).

Tissue Names	**Frequency 868MHz**		**Frequency 2450MHz**		**Mass Density [kgm^{-3}]**	**Assumptions**	**Source**
	Relative Permittivity	**Conductivity [Sm^{-1}]**	**Relative Permittivity**	**Conductivity [Sm^{-1}]**			
Adrenal gland	50.5	1.00	48.2	1.77	1028	Adrenals	IFAC
Air internal	1.0	1.00	1.0	0.00	1	Air (except lungs)	IFAC
Artery	61.5	1.52	58.3	2.54	1050	Blood	IFAC
Bladder	59.2	1.25	18.0	0.68	1035	Bladder	IFAC
Blood vessel	61.5	1.52	58.3	2.54	1050	Blood	IFAC
Bone	22.6	0.35	20.1	0.85	1908	Long bone	IE21P

Brain grey matter	44.6	0.86	41.8	1.49	1043	50% grey & White matter= Brain	IE21P
Brain white matter	44.6	0.86	41.8	1.49	1043	50% grey & White matter= Brain	IE21P
Bronchi	42.1	0.76	39.7	1.45	1102	Bronchi	IT'IS
Bronchi lumen	1.0	0.00	1.0	0.00	1	Bronchi lumen	IT'IS
Cartilage	42.8	0.77	38.8	1.75	1100	Cartilage	IFAC
Cerebellum	49.7	1.25	44.8	2.10	1045	Cerebellum	IT'IS
CSF	68.7	2.40	66.3	3.45	1007	CSF	IFAC
Commissura anterior	39.0	0.58	36.2	1.21	1041	Commissura anterior	IT'IS
Commissura posterior	39.0	0.58	36.2	1.21	1041	Commissura Posterior	IT'IS
Connective tissue	45.9	0.71	43.1	1.68	1027	Connective tissue	IT'IS
Cornea	54.5	1.07	51.6	3.54	1051	Cornea	IE21P
Diaphragm	55.1	0.93	52.7	1.74	1090	Diaphragm	IT'IS
Ear cartilage	42.8	0.77	38.8	1.75	1100	Cartilage	IFAC
Ear skin	45.50	0.79	42.2	1.64	1109	Skin	IE21P
Eye lens	46.6	0.78	44.6	1.50	1076	Eye Lens	IT'IS
Eye Sclera	55.4	1.15	52.6	2.03	1032	Eye Sclera	IT'IS
Eye vitreous humour	68.9	1.63	68.2	2.47	1005	Eye Vitreous Humour	IT'IS/IFAC
Fat	14.0	0.23	13.3	0.46	911	Fat	IE21P
Gallbladder	59.2	1.25	57.6	2.05	1071	Gallbladder	IFAC
Heart lumen	61.5	1.52	58.3	2.54	1050	Heart lumen	IT'IS
Heart muscle	60.1	1.21	54.8	2.25	1081	Heart muscle	IT'IS
Hippocampus	44.6	0.86	41.8	1.49	1043	Brain	IE21P
Hypophysis	59.8	1.03	57.2	1.97	1053	Hypophysis	IT'IS
Hypothalamus	59.8	1.03	57.2	1.97	1053	Hypothalamus	IT'IS
Intervertebral disc	55.1	1.28	51.4	2.29	1100	Intervertebral disc	IE21P
Kidney cortex	58.9	1.37	52.7	2.43	1049	Kidney cortex	IT'IS

Kidney medulla	58.0	1.37	52.7	2.43	1044	Kidney medulla	IT'IS
Large intestine	58.1	1.07	53.9	2.04	1088	Large intestine	IT'IS
Large intestine lumen	55.1	0.93	52.7	1.74	1045	Large intestine lumen	IT'IS
Larynx	42.8	0.77	38.8	1.75	1100	Larynx	IT'IS
Liver	47.0	0.80	43.1	1.70	1079	Liver	IFAC
Lung	22.1	0.45	20.5	0.80	394	Lung	IFAC
Mandible	12.5	0.14	11.4	0.39	1908	Mandible	IT'IS
Marrow red	11.3	0.22	10.3	0.45	1029	Marrow red	IT'IS
Medulla oblongata	49.7	1.25	44.8	2.10	1046	Medulla oblongata	IT'IS
Meniscus	42.8	0.76	38.8	1.76	1100	Meniscus	IT'IS
Midbrain	49.7	1.25	44.8	2.10	1046	Midbrain	IT'IS
Mucosa	55.1	0.93	52.7	1.74	1102	Mucosa	IT'IS
Muscle	55.1	0.9	52.7	1.7	1090	muscle	IFAC
Nerve	32.6	0.56	30.1	1.09	1075	Nerve	IT'IS
Oesophagus	65.2	1.17	62.2	2.20	1040	Oesophagus	IFAC
Oesophagus lumen	1	0.0	1.0	0.0	1	Oesophagus lumen	IT'IS
Ovary	50.7	1.27	44.7	2.26	1100	Fallopian ovaries	IFAC
Pancreas	59.8	1.03	57.2	1.96	1087	Pancreas	IFAC
Patella	45.9	0.71	43.1	1.68	1142	Tendon	IFAC
Pharynx	1.0	0.0	1.0	0.0	1	Pharynx	IT'IS
Pineal body	59.8	1.03	57.2	1.97	1053	Pineal body	IT'IS
Pons	49.7	1.25	44.8	2.10	1046	Pons	IT'IS
SAT(Subcutaneous Fat)	11.3	0.10	10.8	0.26	911	Subcutaneous fat	IT'IS
Skin	45.50	0.79	42.2	1.64	1079	Skin	IE21P
Skull	39.3	0.71	36.1	1.43	1850 [36]	Skull	IE21P
Small intestine	59.7	2.15	54.4	3.17	1030	Small intestine	IFAC
Small intestine lumen	55.1	0.93	52.7	1.74	1045	Small intestine lumen	IT'IS
Spinal cord	66.30	1.76	63.1	2.71	1075	Spinal cord	IE21P
Spleen	57.4	1.26	52.5	2.05	1089	Spleen	IFAC
Stomach	65.2	1.17	62.2	2.20	1088	Stomach	IFAC
Stomach lumen	55.1	0.93	52.7	1.74	1045	Stomach	IT'IS
Teeth	12.5	0.1	11.4	0.39	2180	Tooth	IT'IS

Tendon Ligament	45.9	0.71	43.1	1.68	1142	Tendon	IFAC
Thalamus	52.9	0.92	48.9	1.81	1045	Thalamus	IT'IS
Thymus	59.8	1.03	57.2	1.96	1023	Thymus	IFAC
Tongue	54.2	1.03	50.9	2.01	1090	Tongue	IT'IS
Trachea	42.1	0.76	39.7	1.45	1080	Trachea	IT'IS
Trachea lumen	1.0	0.0	1.0	0.0	1	Trachea lumen	IT'IS
Ureter\Urethra	44.9	0.68	42.5	1.44	1102	Ureter\ Urethra	IT'IS
Uterus	61.2	1.26	57.8	2.25	1105	Uterus	IT'IS
Vagina	59.7	2.15	54.4	3.17	1088	Vagina	IT'IS
Vein	61.5	1.52	58.3	2.54	1050	Blood	IFAC
Vertebrae	55.1	1.28	51.4	2.29	1100	Interverte bral disc	IE21P

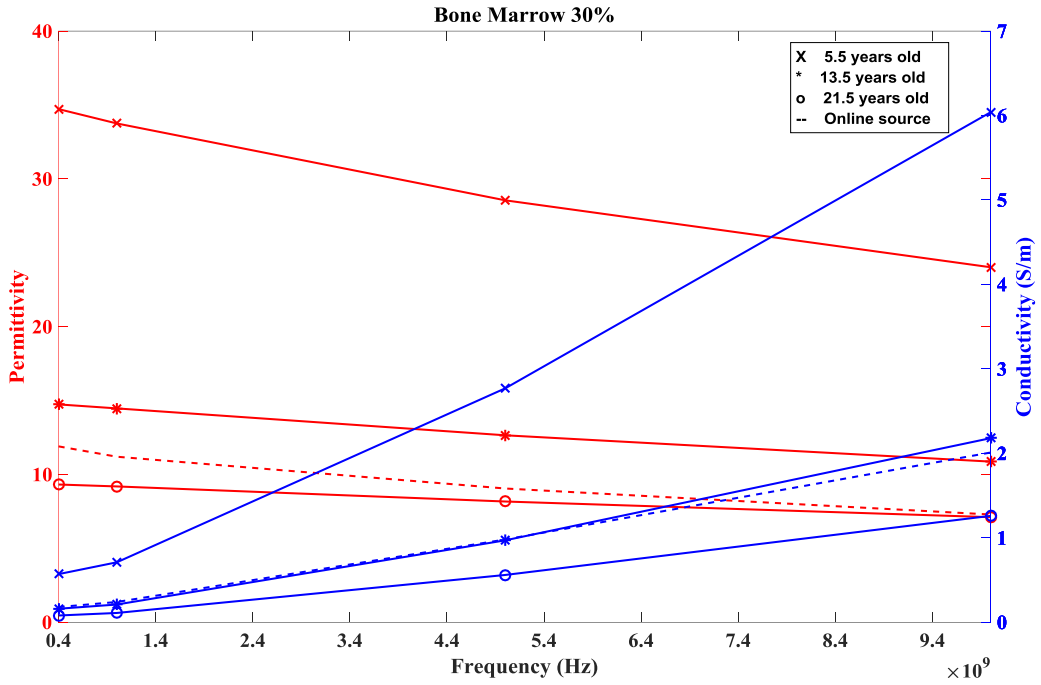

Figure A-1. Comparison between age-dependent properties of bone marrow 30% tissue with online sources [2, 3], Online sources dielectric properties well match with 250 kg pig when comparing with [20] as shown in Table 3-4 and also confirms by this method

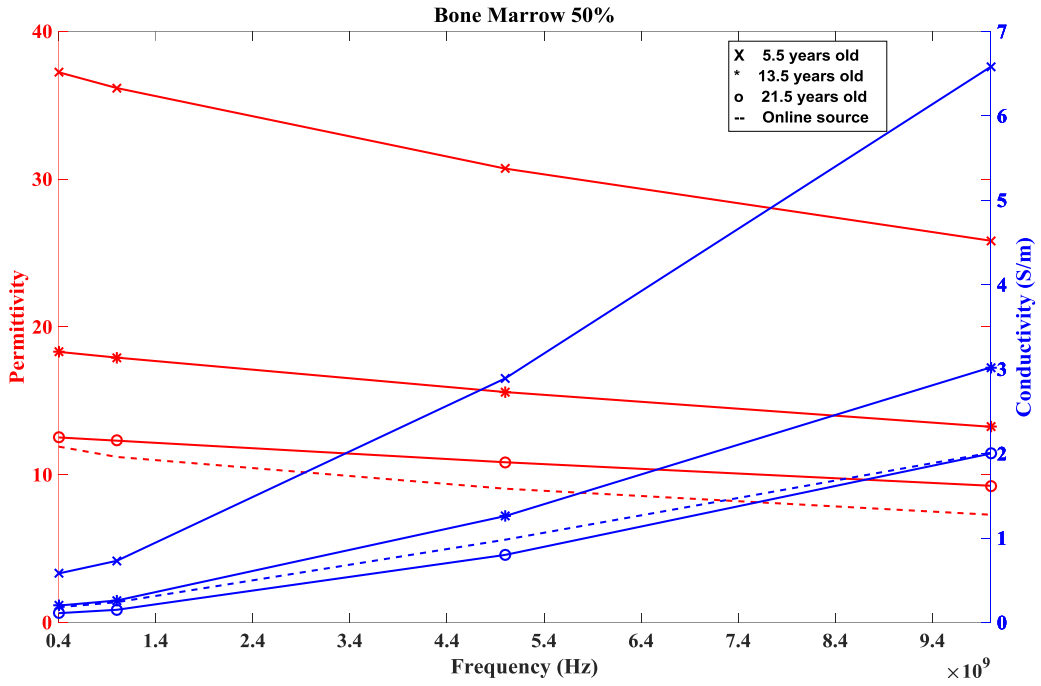

Figure A-2. Comparison between age-dependent properties of bone marrow 50% tissue with online sources [2, 3], Online sources dielectric properties well match with 250 kg pig when comparing with [20] as shown in Table 3-4 and also confirms by this method

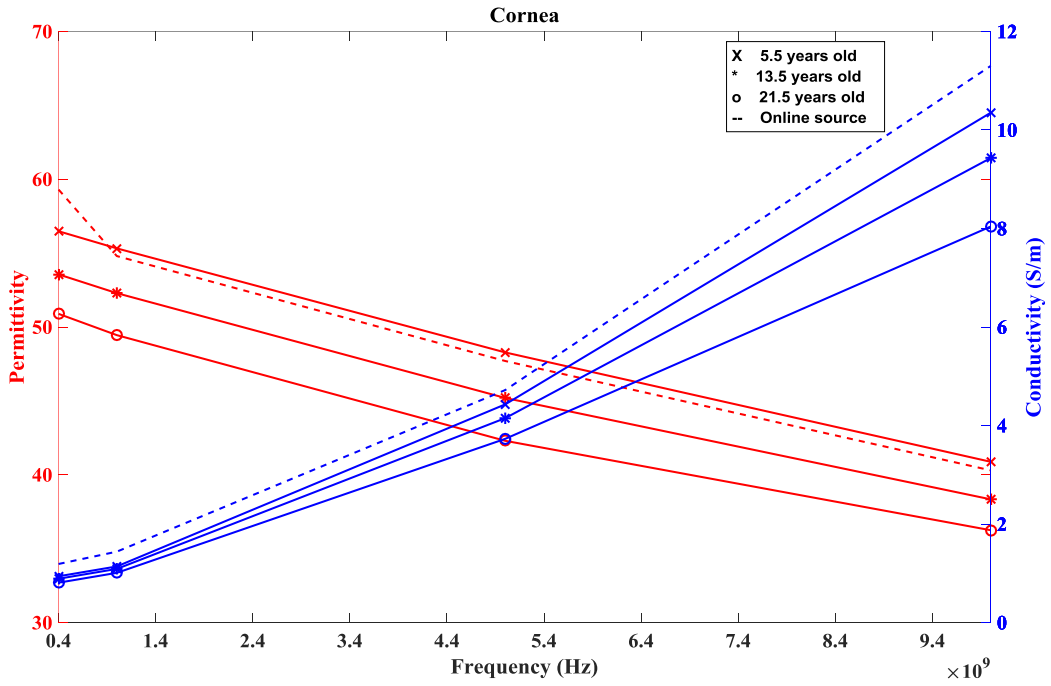

Figure A-3. Comparison between age-dependent properties of cornea tissue with online sources [2, 3], Online sources dielectric properties well match with 10 kg pig when comparing with [20] as shown in Table 3-4 and also confirms by this method.

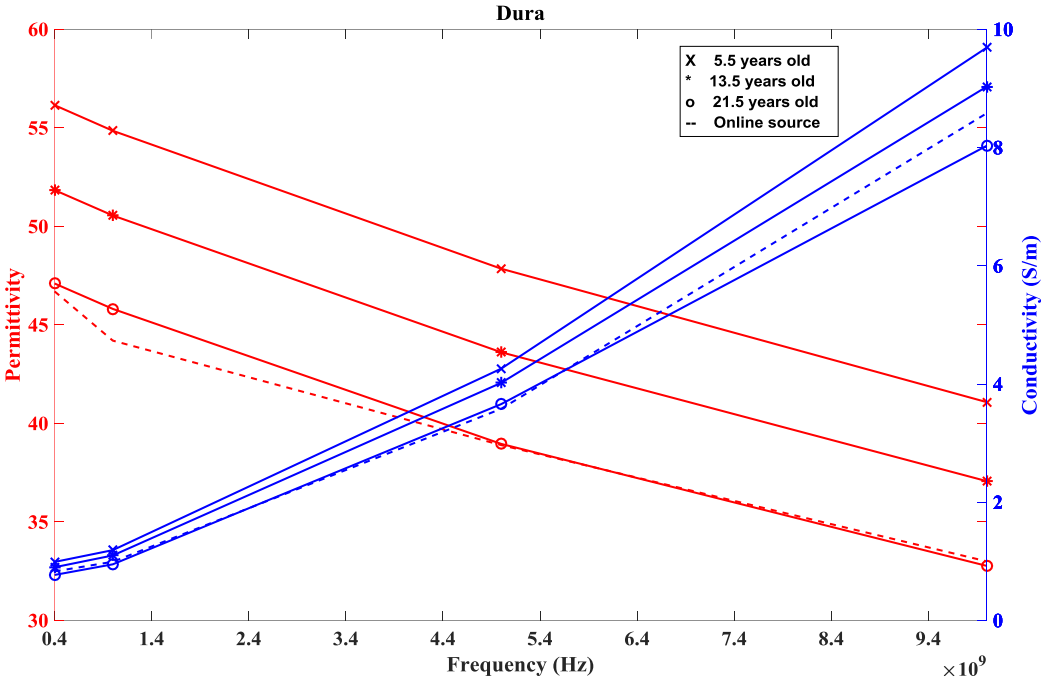

Figure A-4. Comparison between age-dependent properties of dura tissue with online sources [2, 3], Online sources dielectric properties well match with 250 kg pig when comparing with [20] as shown in Table 3-4 and also confirms by this method.

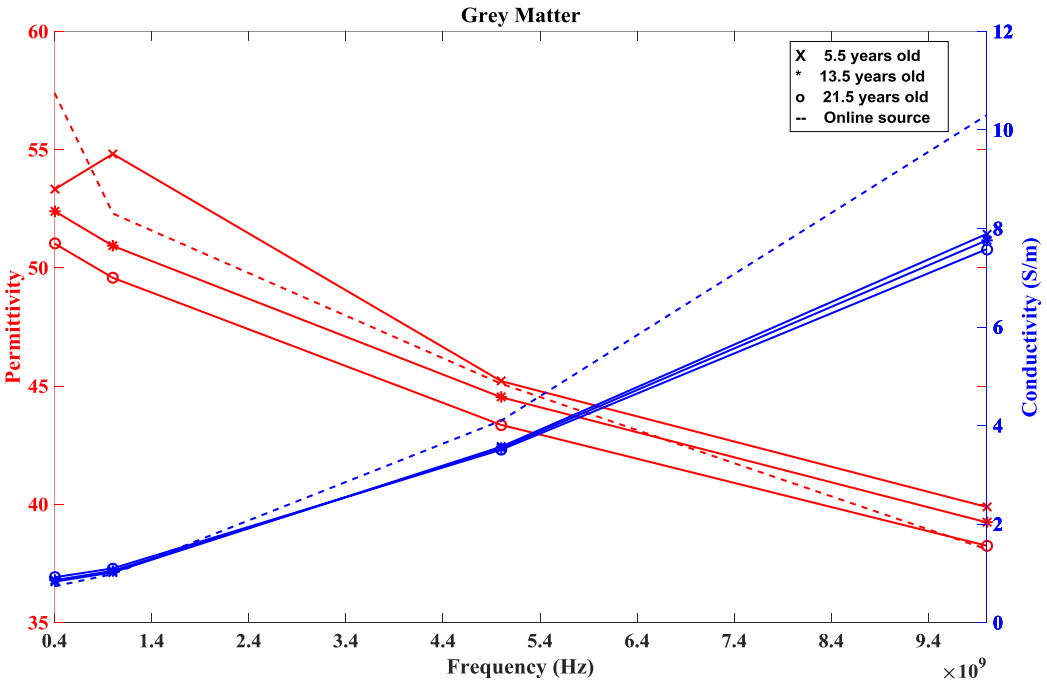

Figure A-5. Comparison between age-dependent properties of gray matter tissue with online sources [2, 3], Online sources dielectric properties well match with 50 kg pig when comparing with [20] as shown in Table 3-4 and also confirms by this method.

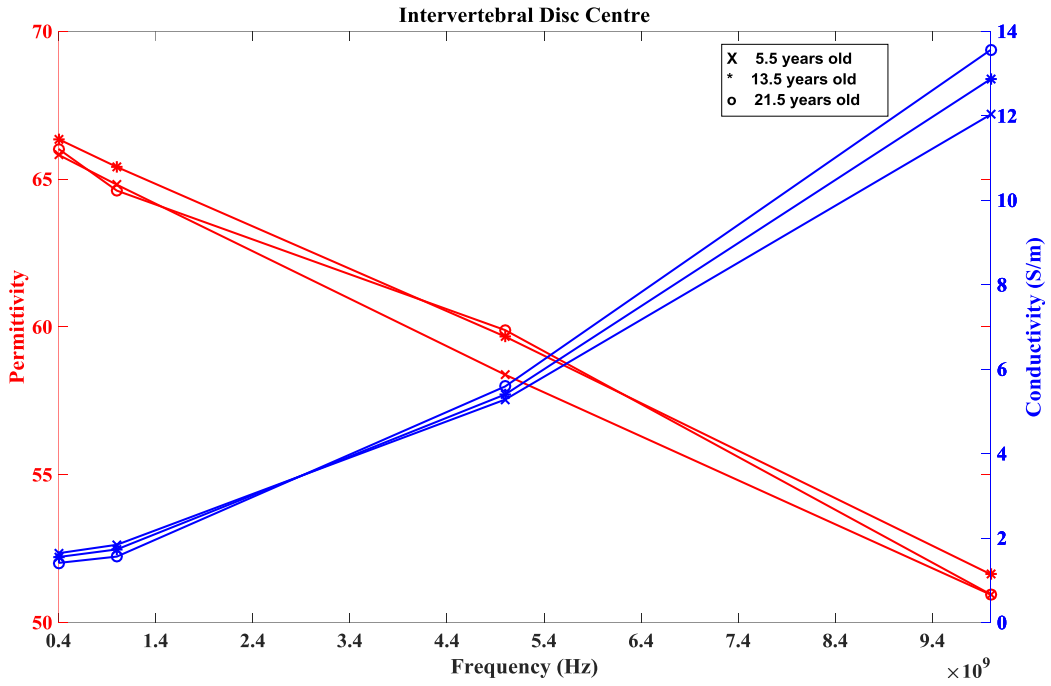

Figure A-6. Age-dependent properties of intervertebral disc centre. Due to lack of availability of online source data comparison is not available of this tissue.

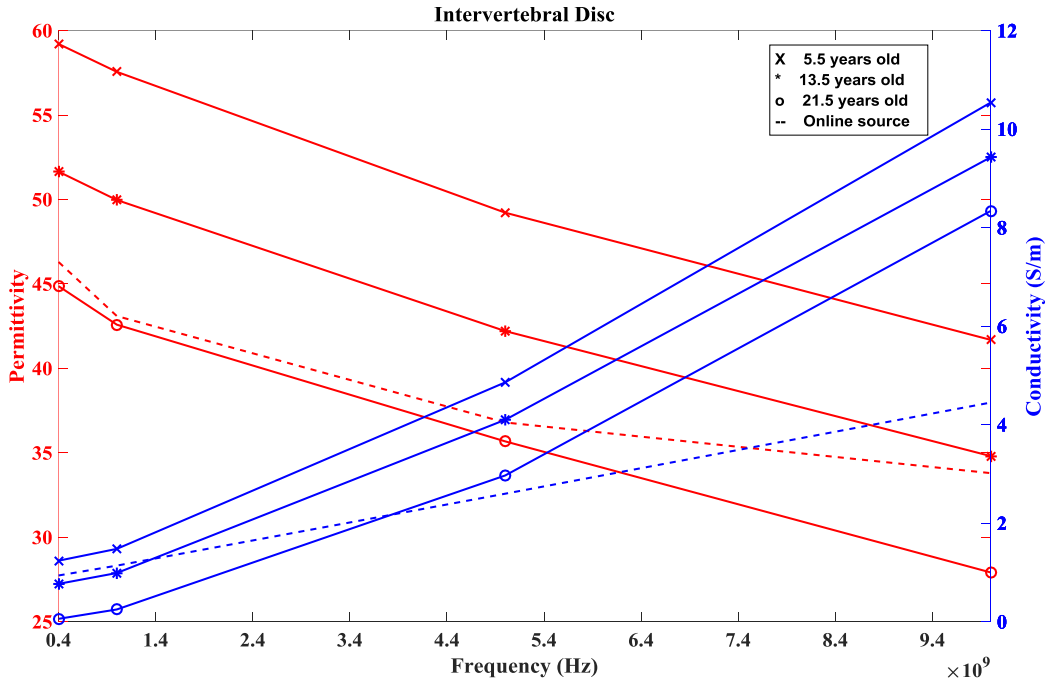

Figure A-7. Comparison between age-dependent properties of intervertebral disc tissue with online sources [2, 3], Online sources dielectric properties well match with 250 kg pig when comparing with [20] as shown in Table 3-4 and also confirms by this method.

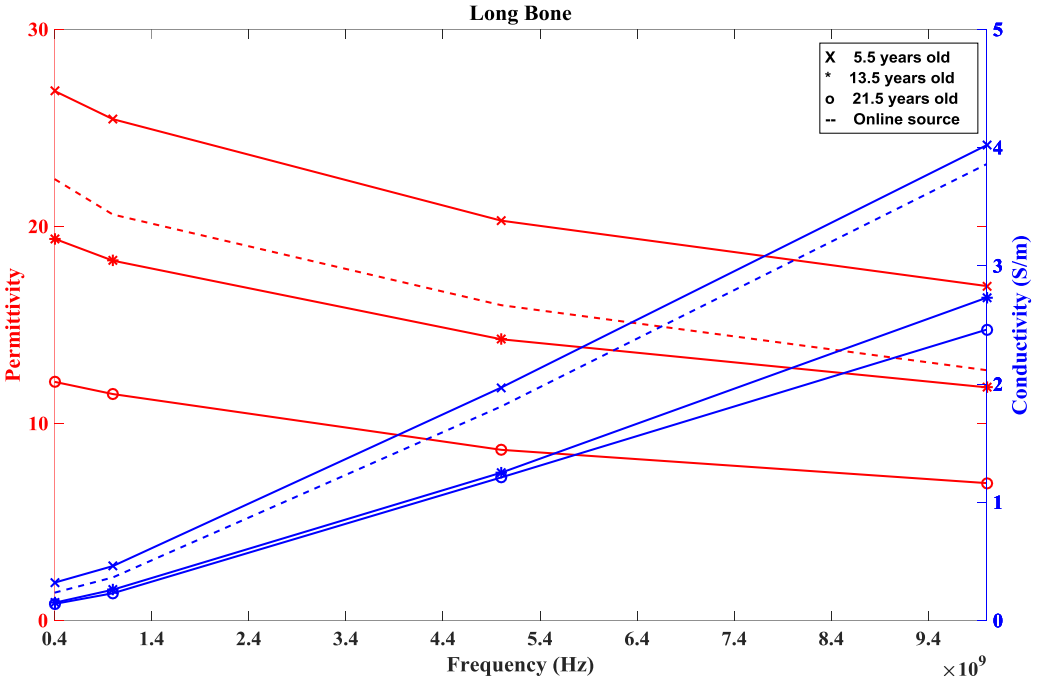

Figure A-8. Comparison between age-dependent properties of long bone tissue with online sources [2, 3], Online sources dielectric properties well match with 250 kg pig when comparing with [20] as shown in Table 3-4 and also confirms by this method.

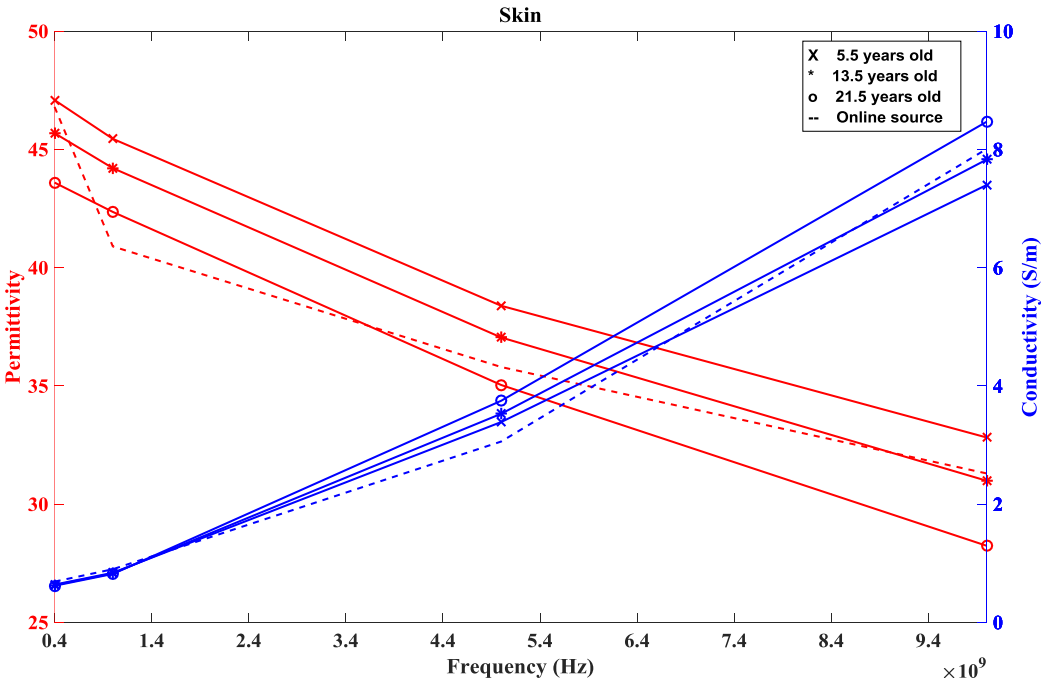

Figure A-9. Comparison between age-dependent properties of skin tissue with online sources [2, 3], Online sources dielectric properties well match with 50 kg pig when comparing with [20] as shown in Table 3-4 and also confirms by this method.

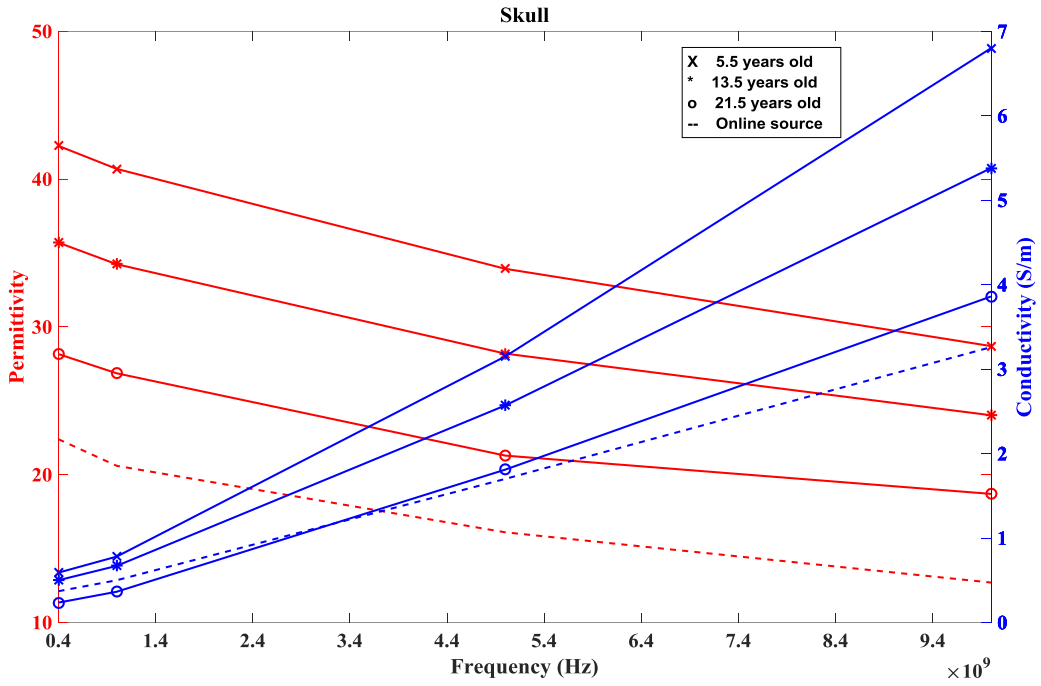

Figure A-10. Comparison between age-dependent properties of skull tissue with online sources [2, 3], Online sources dielectric properties well match with 250 kg pig when comparing with [20] as shown in Table 3-4 and also confirms by this method.

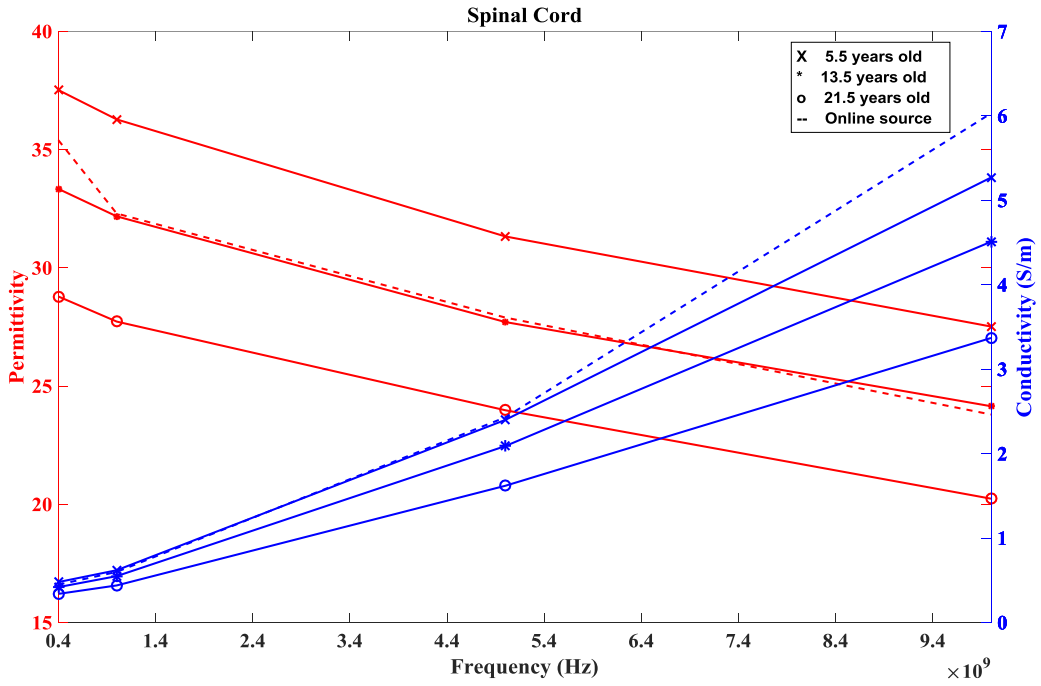

Figure A-11. Comparison between age-dependent properties of spinal cord tissue with online sources [2, 3], Online sources dielectric properties well match with 50 kg pig when comparing with [20] as shown in Table 3-4 and also confirms by this method.

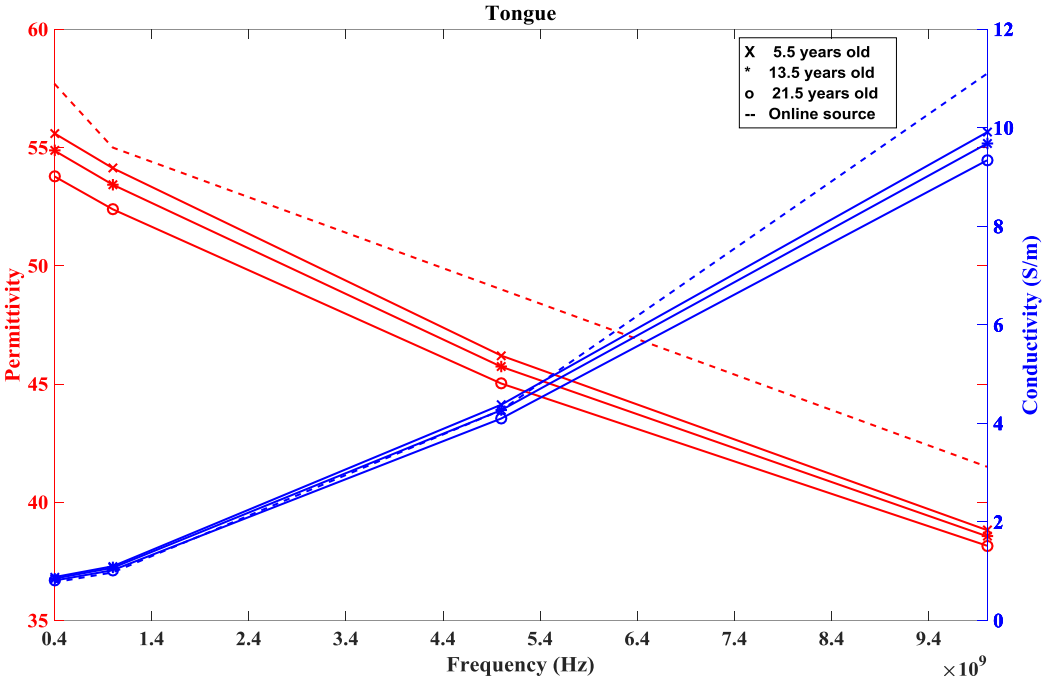

Figure A-12. Comparison between age-dependent properties of tongue tissue with online sources [2, 3], Online sources dielectric properties well match with 250 kg pig when comparing with [20] as shown in Table 3-4 and also confirms by this method.

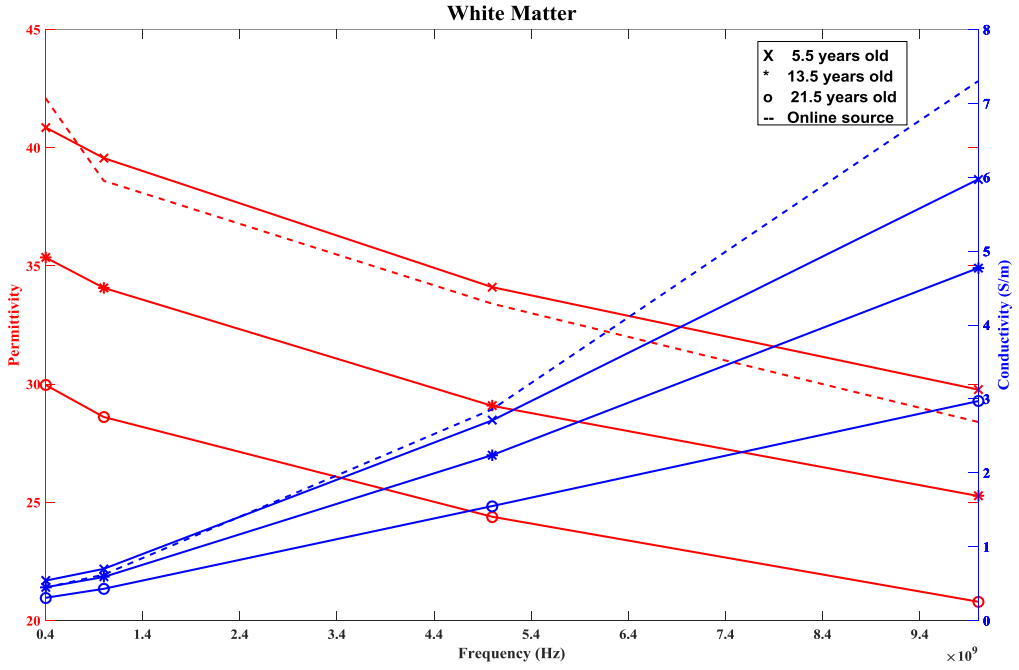

Figure A-13. Comparison between age-dependent properties of white matter tissue with online sources [2, 3], Online sources dielectric properties well match with 10 kg pig when comparing with [20] as shown in Table 3-4 and also confirms by this method.

Appendix B

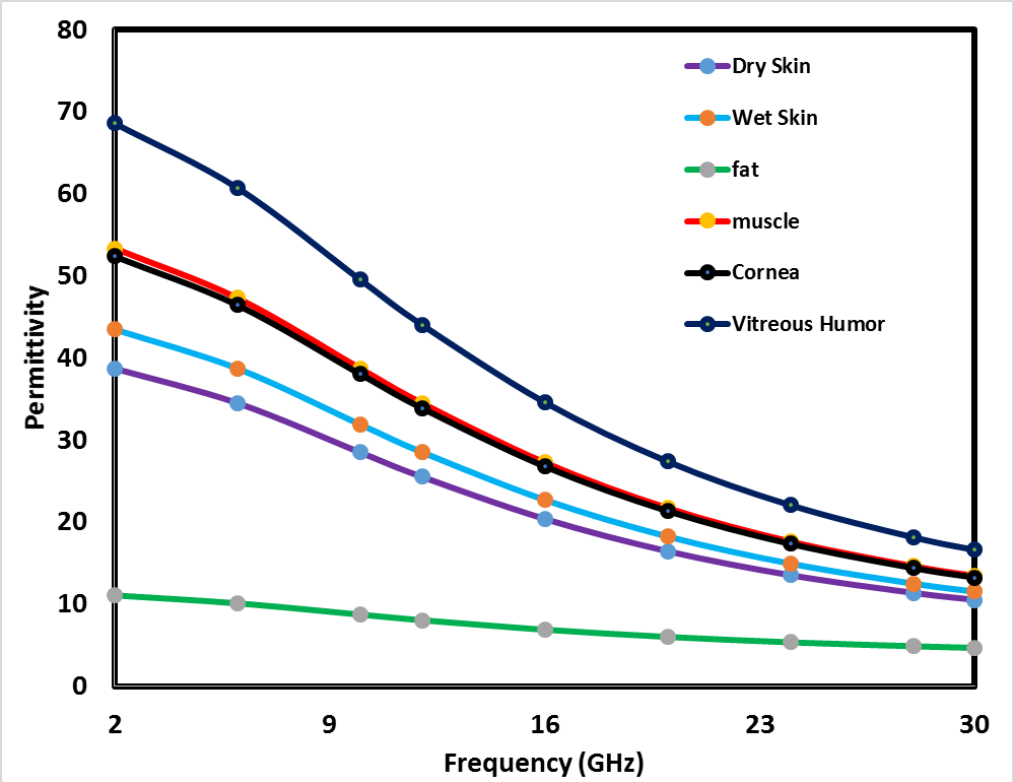

Figure B-1. Debye model fitted permittivity values of dry- and wet-skin, fat, muscle, cornea, vitreous humor.

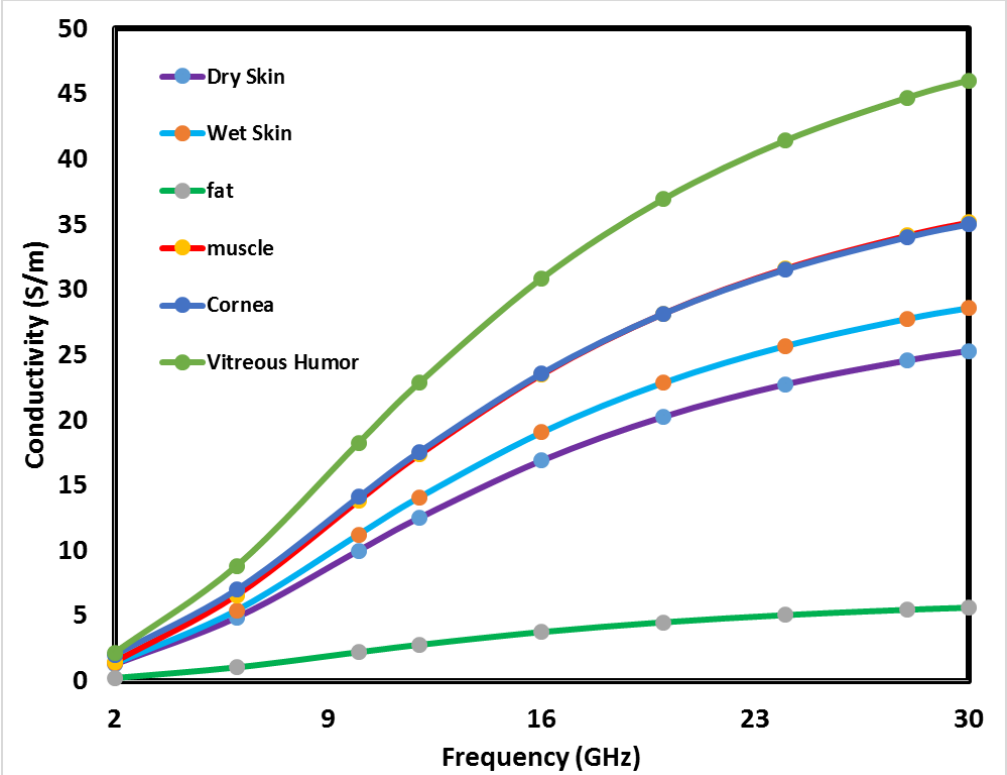

Figure B-2. Debye model fitted conductivity values of dry- and wet-skin, fat, muscle.

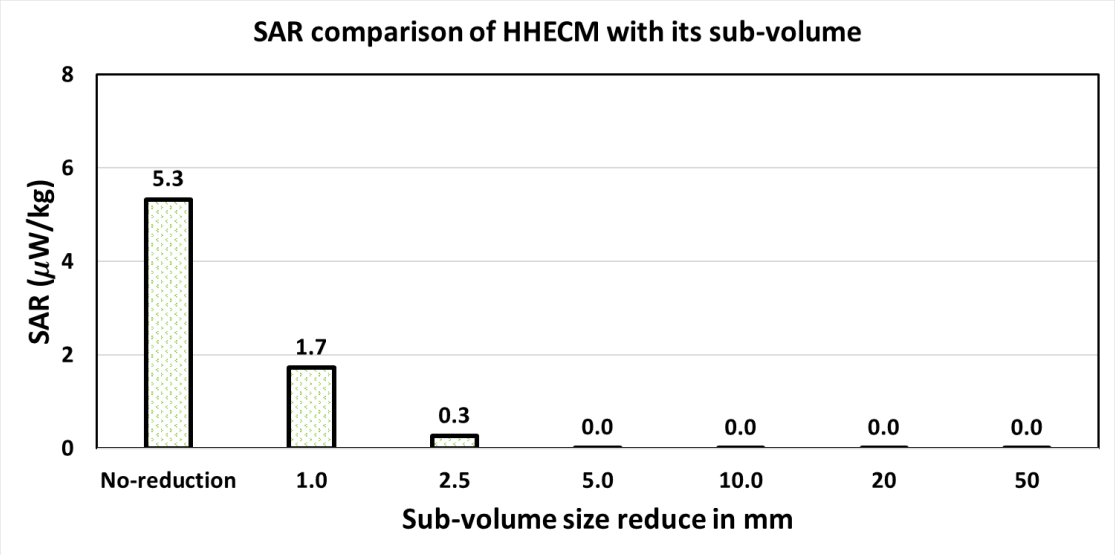

Figure B-3. Comparison of SAR values of dry-skin equivalent HHECM with its sub-volume resultant from plane wave exposure at **16 GHz**.

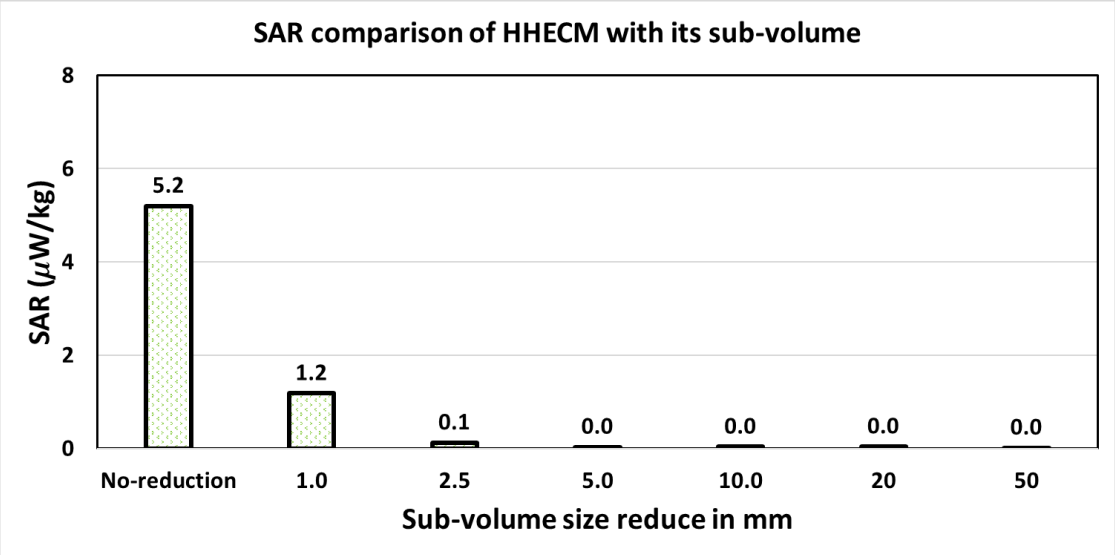

Figure B-4. Comparison of SAR values of dry-skin equivalent HHECM with its sub-volume resultant from plane wave exposure at **20 GHz**.

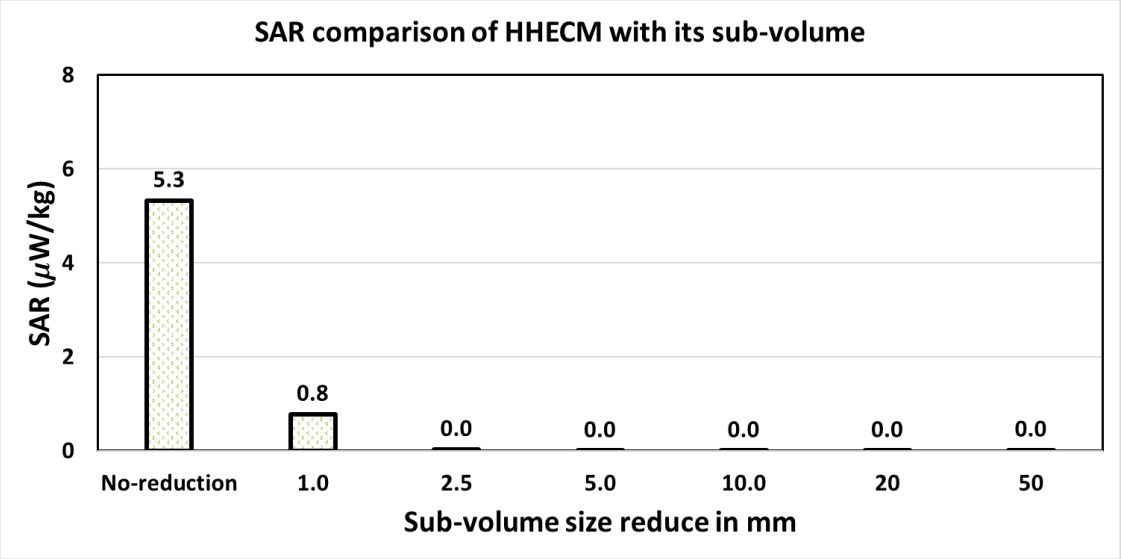

Figure B-5. Comparison of SAR values of dry-skin equivalent HHECM with its sub-volume resultant from plane wave exposure at **24 GHz**.

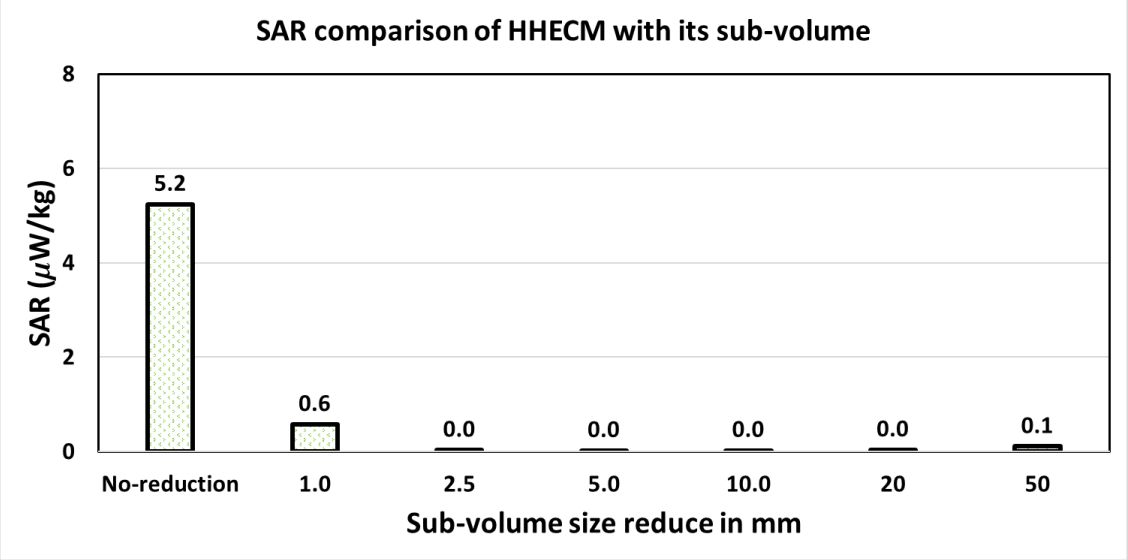

Figure B-6. Comparison of SAR values of dry-skin equivalent HHECM with its sub-volume resultant from plane wave exposure at **28 GHz**.

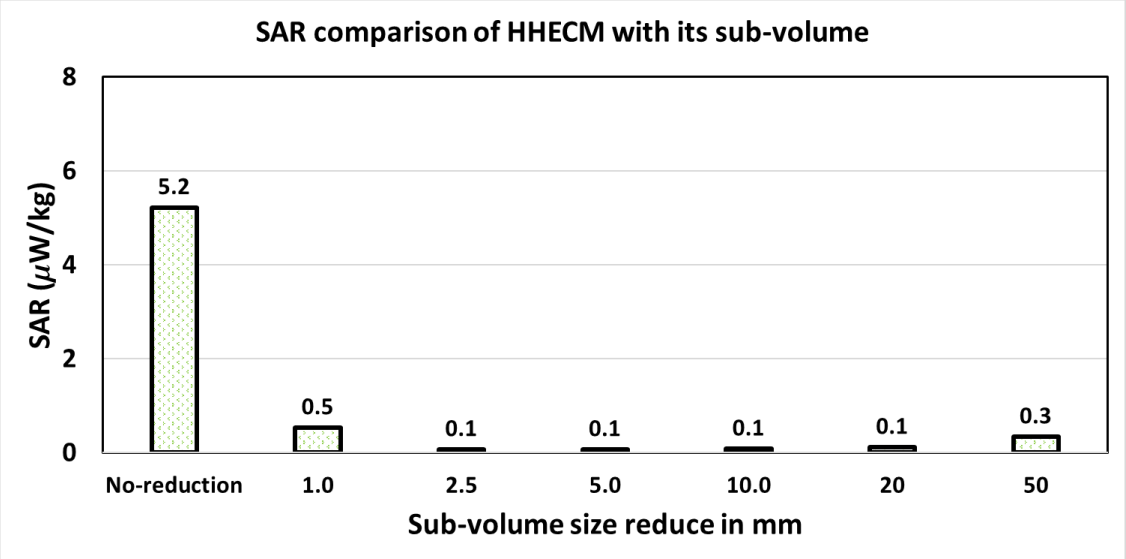

Figure B-7. Comparison of SAR values of dry-skin HHECM with its sub-volume resultant from plane wave exposure at **30 GHz**.

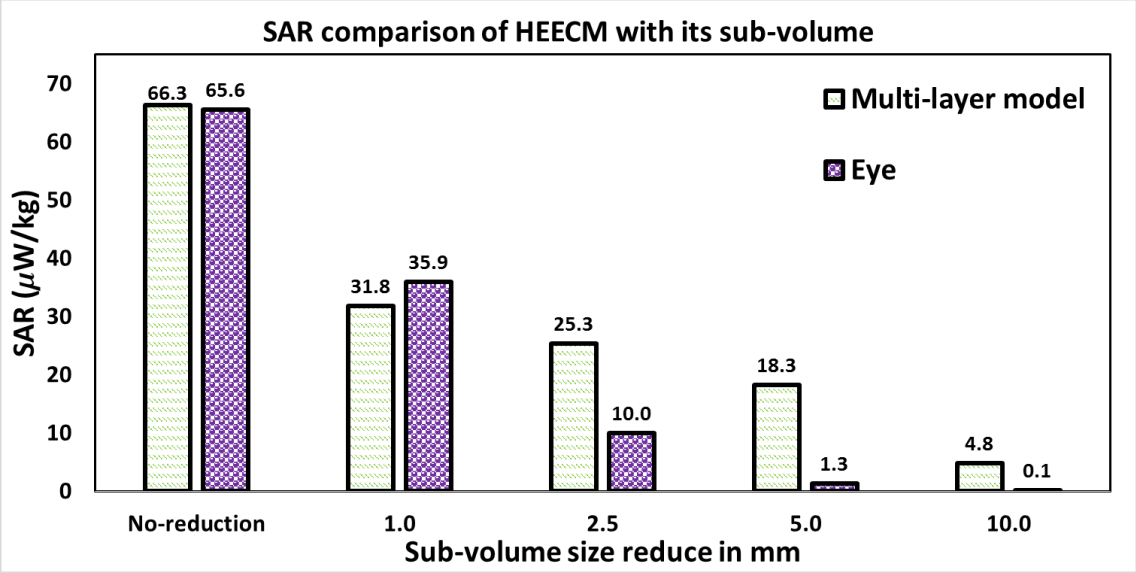

Figure B-8. Comparison of SAR values of HEECM and multi-layer model (size normalised to HEECM equivalent) with its sub-volume resultant from plane wave exposure at **10 GHz**, where no-reduction key word on *x*-axis of graph represents the SAR in whole cube volume. It can be seen that the wave at this frequency doesn't exceed 5 mm from the HEECM surface.

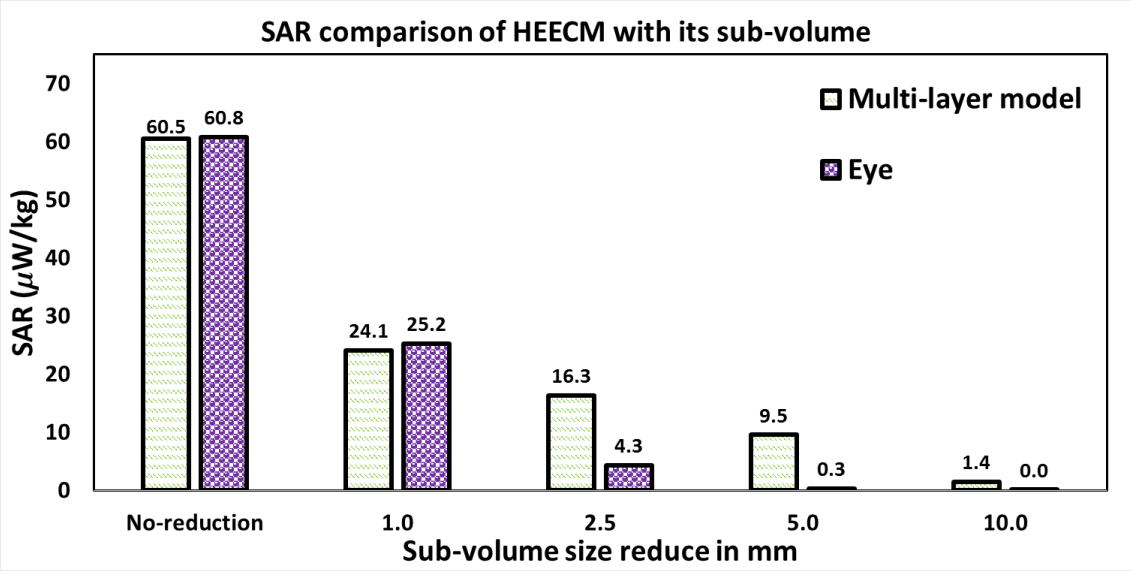

Figure B-9. Comparison of SAR values of HEECM and multi-layer model (size normalised to HEECM equivalent) with its sub-volume resultant from plane wave exposure at **12 GHz**, where no-reduction key word on *x*-axis of graph represents the SAR in whole cube volume. It can be seen that the wave at this frequency doesn't exceed 5 mm from the HEECM surface.

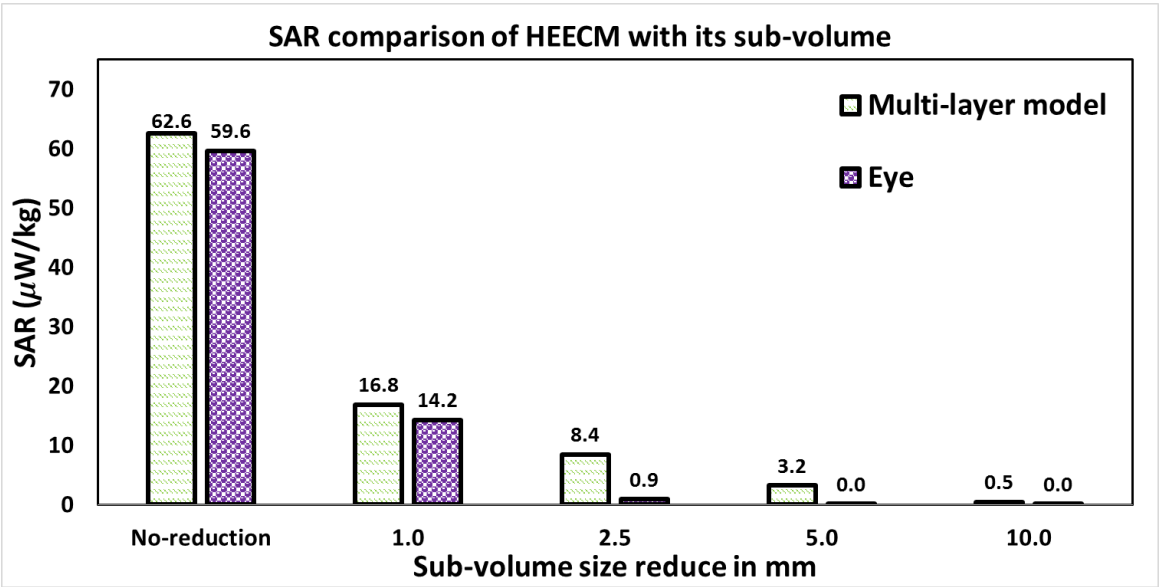

Figure B-10. Comparison of SAR values of HEECM and multi-layer model (size normalised to HEECM equivalent) with its sub-volume resultant from plane wave exposure at **16 GHz**, where no-reduction key word on *x*-axis of graph represents the SAR in whole cube volume. It can be seen that the wave at this frequency doesn't exceed 2.5 mm from the HEECM surface.

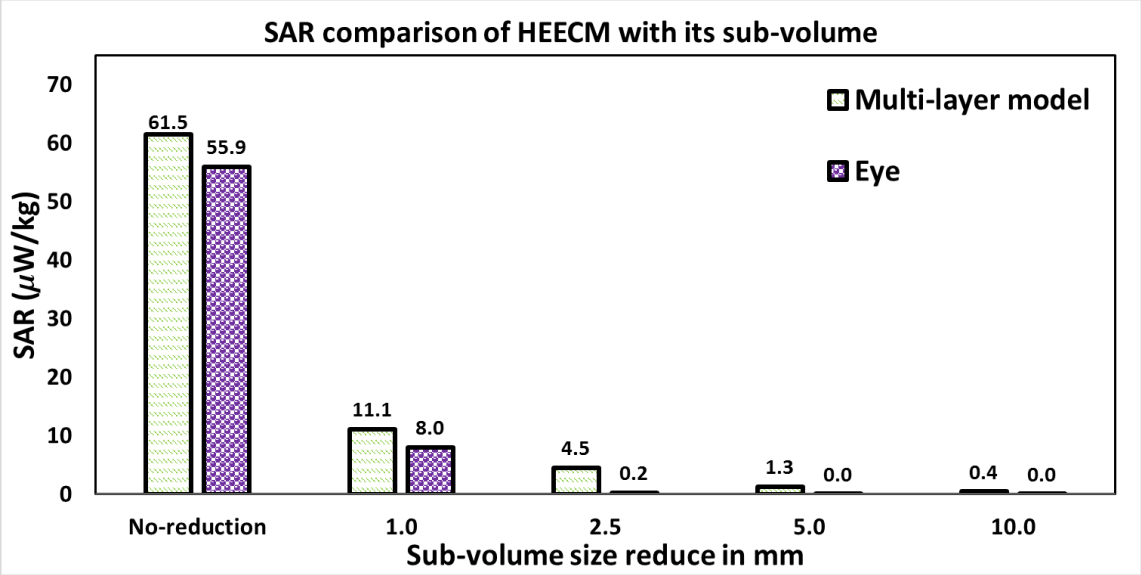

Figure B-11. Comparison of SAR values of HEECM and multi-layer model (size normalised to HEECM equivalent) with its sub-volume resultant from plane wave exposure at **20 GHz**, where no-reduction key word on *x*-axis of graph represents the SAR in whole cube volume. It can be seen that the wave at this frequency doesn't exceed 2.5 mm from the HEECM surface.

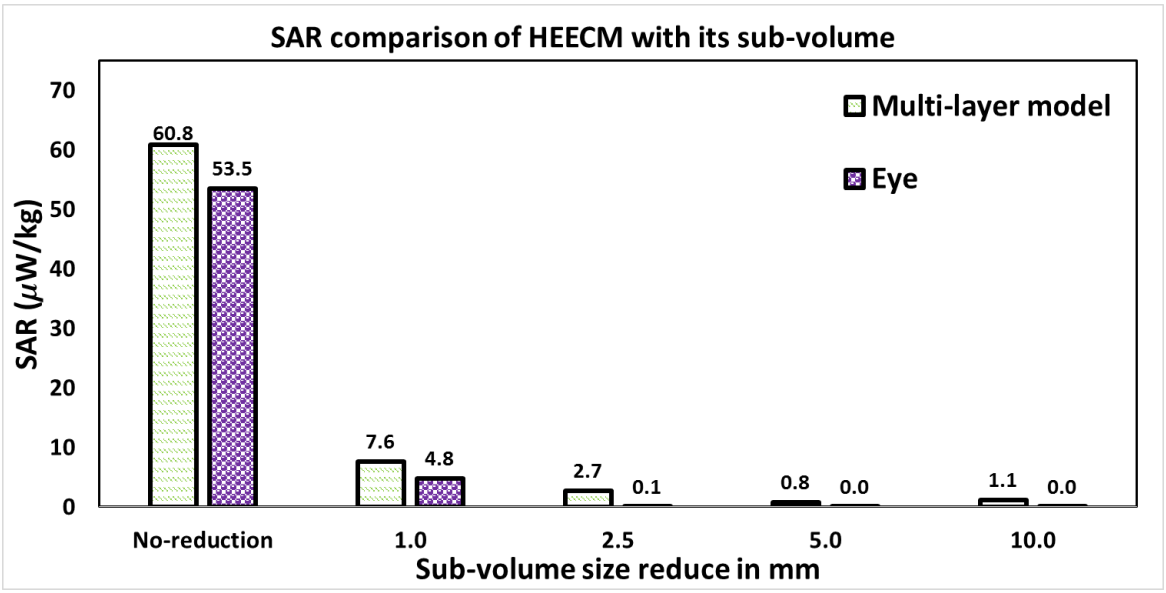

Figure B-12. Comparison of SAR values of HEECM and multi-layer model (size normalised to HEECM equivalent) with its sub-volume resultant from plane wave exposure at **24 GHz**, where no-reduction key word on *x*-axis of graph represents the SAR in whole cube volume. It can be seen that the wave at this frequency doesn't exceed 2.5 mm from the HEECM surface.

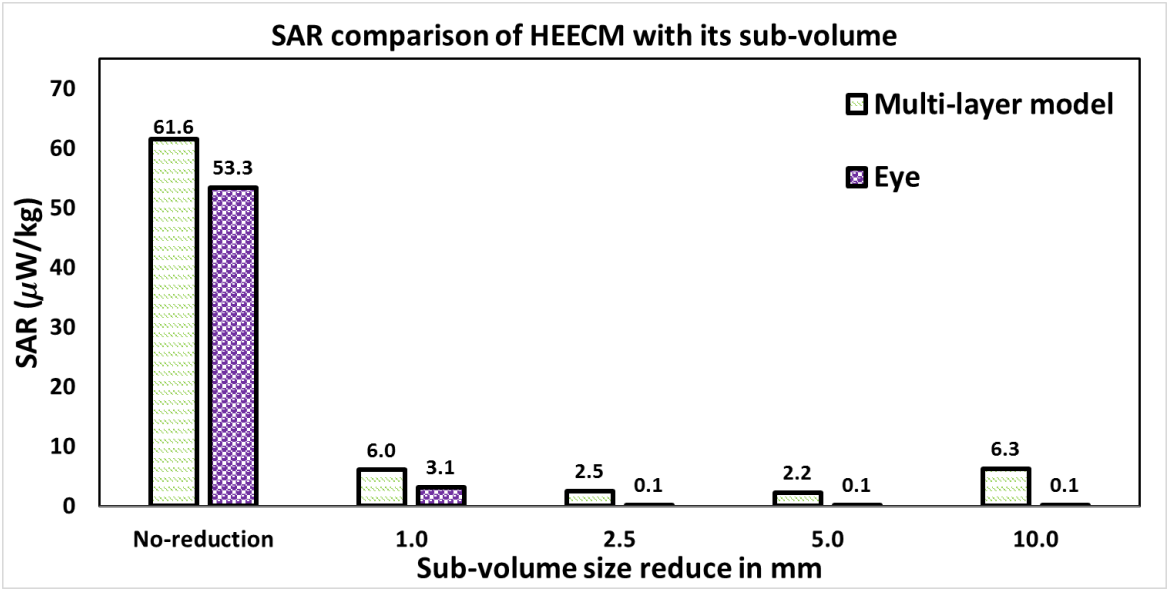

Figure B-13. Comparison of SAR values of HEECM and multi-layer model (size normalised to HEECM equivalent) with its sub-volume resultant from plane wave exposure at **28 GHz**, where no-reduction key word on *x*-axis of graph represents the SAR in whole cube volume. It can be seen that the wave at this frequency doesn't exceed 2.5 mm from the HEECM surface.